MEASUREMENT OF ANGULAR AND MOMENTUM DISTRIBUTIONS OF CHARGED PARTICLES WITHIN AND AROUND JETS IN Pb+Pb AND pp COLLISIONS AT $\sqrt{S_{\mathrm{NN}}} = 5.02$ TeV WITH ATLAS AT THE LHC

BY

AKSHAT PURI

DISSERTATION

Submitted in partial fulfillment of the requirements
for the degree of Doctor of Philosophy in Physics
in the Graduate College of the
University of Illinois at Urbana-Champaign, 2019

Urbana, Illinois

Doctoral Committee:

Professor Matthias Grosse Perdekamp, Chair
Assistant Professor Anne Marie Sickles, Director of Research
Professor Lance Cooper
Assistant Professor Bryce Gadway

ABSTRACT

Heavy ion collision experiments have been centered around studying the extreme state of matter formed in such collisions, the quark-gluon plasma. There have been efforts to measure and characterize this state of matter for almost two decades, first at the Relativistic Heavy Ion Collider and subsequently at the Large Hadron Collider. While there have been different approaches to study it, correlated particle showers called jets have found a special place as a probe of the QGP. Arising from highly energetic collisions between partons, jets are formed early enough in heavy ion collisions that they experience the formation of the QGP and its evolution. They are modified from what they would be in a vacuum, and studying these modifications can give insight into the properties of the QGP as well as the strong interaction.

Jet measurements can focus on a variety of observables like yields, momenta, or fragmentation patterns, each with its own limitations and advantages. This thesis presents a measurement of the angular distribution of charged particles around the jet axis as measured by the ATLAS detector for Pb+Pb and pp collisions with a center of mass energy of $\sqrt{s_{\mathrm{NN}}} = 5.02$ TeV. Comparing the measurement in the two systems shows that charged particles carrying a transverse momenta p_{T} of less than 4 GeV have a broader distribution in Pb+Pb collisions, while those with $p_{\mathrm{T}} > 4$ GeV have a narrower distribution. Furthermore, there is an enhancement for particles with $p_{\mathrm{T}} < 4$ GeV in Pb+Pb collisions, with the enhancement increasing up to 2 for $r < 0.3$ from the jet axis, and remaining constant for $0.3 < r < 0.6$. Charged particles with $p_{\mathrm{T}} > 4$ GeV show a small enhancement in the jet core for $r < 0.05$, and are increasingly suppressed up to 0.5 for $r < 0.3$. This depletion remains constant for $0.3 < r < 0.6$.

For my Mother, Father, and Brother

Acknowledgments

First and foremost, I would like to thank my advisor, Professor Anne Sickles. Her encouragement and support helped me grow not only as a researcher but also as a person. Our discussions ranged from physics to food and made my time in graduate school rewarding and enjoyable. I feel extremely lucky to be her student and could not have asked for a better advisor.

I would like to extend a big thank you to Martin Rybar, the post doctoral researcher in our group. His constant support not only in my research but also as a friend was invaluable. Whether it was discussing how the ATLAS detector works or playing Red Alert and getting a beer after work, he was a huge positive presence in graduate school and I will miss working with him.

Other people I wish to thank include

- My research group members Michael Phipps, Yakov Kulinich, Sebastian Tapia, Virginia Bailey, Tim Rinn, Anabel Romero, and Xiaoning Wang, for sitting through numerous meetings and practice talks and for providing feedback on my work.
- My doctoral committee members Matthias Grosse Perdekamp, Bryce Gadway, Lance Cooper, and Aida X El-Khadra.
- The Heavy-Ion Group, in particular Martin Spousta, Aaron Angerami, Dennis Perepelitsa, Peter Steinberg, and Brian Cole, for a variety of discussions that broadened my physics knowledge.
- The ATLAS Collaboration and the large team of people including Iwona Grabowska-Bold, Benjamin Nachman, Mario Martinez, Chiara Roda, Thomas Le Compte, Filippo Ceradini, Matteo Bauce, Gideon Bella, Maxwell Charles Baugh, Evgenii Baldin, Abi Soffer, Yuya Kano, Yann Coadou, Jiangyong Jia, Guillaume Unal, and David Stoker, who read numerous drafts of my research paper and provided crucial feedback.

Outside of my research, I would like to extend gratitude towards my ballroom dance team. I joined the team when I first started in graduate school and it very quickly became the center of my social life. I would

like to especially thank my dance partner Anna Kalinowski for the dances that let me get away from work and for her patience and support when I was not available for practice because of my research. I would also be remiss if I did not mention my dance coaches over the years: Kato Lindholm, Alex Tecza, Kirsti Roslender, Frank Gillitzer and Peter Minkov.

I would like to acknowledge the love and support from my friends, including but certainly not limited to Parul Agrawal, John Hadley, Bridget Regan, David Meldgin, Varun Badrinath, Yana Garmash, Anna Vardanyan, Katie Bolan, Timothy Chin, Mike Antoline, Michelle Victora, Ashwathi Iyer and Ben Osherson. In particular, I want to thank Akshan Singh and Harsh Banwait for their friendship over the past decade. I could not have asked for better people to have my back.

Last but certainly not least, I have to thank my parents and my brother. None of this would have been possible without them cheering me on and supporting me all my life. Their unconditional love and unyielding support has been a crucial part of shaping me into the person I am, and this is for them.

If I have seen further it is by standing on the shoulders of Giants

Sir Isaac Newton

Table of Contents

Chapter 1 INTRODUCTION **1**
1.1 Quantum Chromodynamics 1
1.2 Quark-Gluon Plasma in Heavy Ion Collisions 4
1.2.1 The Glauber Model 8
1.3 Jets and Jet Quenching 11
1.3.1 Jets in e^+e^- collisions 12
1.3.2 Jets in pp collisions 13
1.3.3 Jets in heavy ion collisions 14
1.3.4 Jet Algorithms 18

Chapter 2 MEASUREMENTS IN HEAVY ION COLLISIONS **21**
2.1 Hadron Suppresion 21
2.2 Dijet Balance: x_J 22
2.3 Modification of jet yields: R_{AA} 24
2.4 Jet Fragmentation 24
2.5 Jet Profile 27

Chapter 3 JET ENERGY LOSS MODELS **30**
3.1 Jet Fluid model 30
3.2 Hybrid Model 34
3.3 Effective Quenching 38

Chapter 4 EXPERIMENTAL SETUP **41**
4.1 The Large Hadron Collider 41
4.2 The ATLAS Detector 43
4.2.1 Inner Detector 43
4.2.2 Calorimeter 45
4.2.3 Muon Spectrometer 46
4.2.4 Other subsystems 47
4.3 Pileup and Centrality in ATLAS 48
4.4 Jet Reconstruction for Heavy Ion Collisions in ATLAS 49
4.5 Jet Calibration for Heavy Ion Collisions in ATLAS 51

Chapter 5 ANGULAR CORRELATIONS BETWEEN TRACKS AND JETS **55**
5.1 Overview 55
5.2 Datasets and Event Selection 57
5.3 Basic Cuts and Corrections 59
5.3.1 Jet Selection and final energy calibration 60
5.3.2 Track selection 62
5.3.3 Track momentum correction 66
5.3.4 Track reconstruction efficiency 68
5.3.5 Fake rates 70

5.3.6 Underlying event subtraction of tracks . . . 72
5.3.7 Unfolding . . . 84
5.4 Systematic Uncertainties . . . 92
5.4.1 Jet energy scale uncertainty . . . 94
5.4.2 Jet energy resolution . . . 97
5.4.3 Tracking selections . . . 97
5.4.4 Systematic uncertainty due to unfolding . . . 98
5.4.5 Systematic uncertainty due to the UE event subtraction . . . 99
5.4.6 MC non-closure . . . 100
5.4.7 Correlations between the systematic uncertainties in Pb+Pb and *pp* collisions . . . 103
5.5 Results . . . 103
5.5.1 $D(p_{\mathrm{T}}, r)$ distributions . . . 104
5.5.2 $R_{D(p_{\mathrm{T}},r)}$ distributions . . . 104
5.5.3 $\Delta D(p_{\mathrm{T}}, r)$ distributions . . . 107
5.5.4 p_{T} integrated distributions . . . 107

Chapter 6 SUMMARY . . . 113

REFERENCES . . . 115

Chapter 1

INTRODUCTION

This section shall discuss the theoretical background necessary to understand jet measurements. It will discuss the fundamentals of quantum chromodynamics (QCD), the quark gluon plasma and the heavy ion collision system it is formed in, and finally jets and jet energy loss.

1.1 Quantum Chromodynamics

Quantum Chromodynamics is a gauge theory with SU(3) symmetry that describes the dynamics of the strong interactions between quarks and gluons. It is part of the Standard Model [1], the building blocks of which are shown in Figure 1.1.

Quarks are fermions with a spin of 1/2, and carry a fractional electric charge as well as a color charge. They all have mass and come in six flavors: up, down, strange, charm, top, bottom. The lightest quarks (u and d) combine and form stable particles, while the heavier quarks can only be produced in energetic environments and decay rapidly. Gluons are gauge bosons (force carriers) with a spin of 1, and are what hold quarks together. The dynamics of the quarks and gluons, collectively referred to as partons, are described by the QCD Lagrangian given by [3]:

$$\mathcal{L}_{\mathrm{QCD}} = \sum_{q} \bar{\psi}_{q,a}(i\gamma^{\mu}\partial_{\mu}\delta_{ab} - g_s\gamma^{\mu}t^{C}_{ab}\mathcal{A}^{C}_{\mu} - m_q\delta_{ab})\psi_{q,b} - \frac{1}{4}F^{A}_{\mu\nu}F^{A\mu\nu} \tag{1.1}$$

where $\psi_{q,a}$ and $\psi_{q,b}$ are quark-field spinors for a quarks with flavor q, mass m_q, and color a and b respectively, with the values for a and b ranging from 1 to 3 (for the three colors). The $\mathcal{A}^{\mathcal{C}}_{\mu}$ corresponds to the gluon field

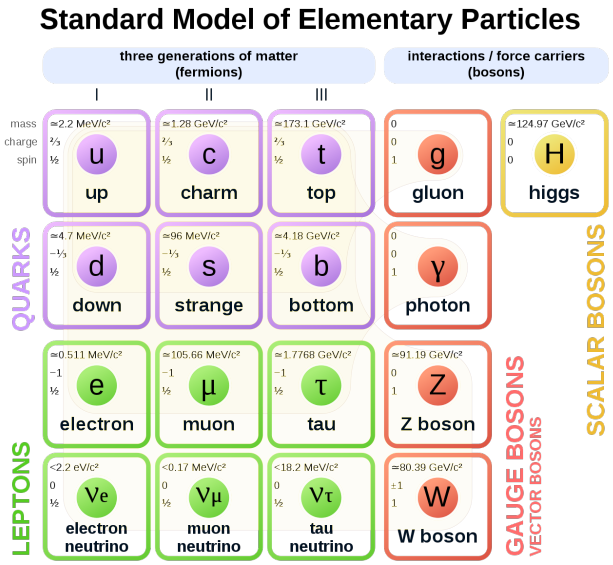

Figure 1.1: The elementary particles of the standard model. Figure from Ref. [2].

with C taking values from 1 through 8 (for the 8 types of gluons). The t^C_{ab} corresponds to the Gell-Mann matrices that are the generators of the SU(3) group, and dictate the rotation of the quarks color in SU(3) space when it interacts with a gluon. The coupling constant is encoded within g_s, which is defined by $g_s \equiv \sqrt{4\pi\alpha_s}$. The field tensor $F^A_{\mu\nu}$ can be written in terms of the structure constants of the SU(3) group f_{ABC}, and is given by:

$$F^A_{\mu\nu} = \partial_\mu \mathcal{A}^A_\nu - \partial_\nu \mathcal{A}^A_\mu - g_s f_{ABC} \mathcal{A}^B \mathcal{A}^C \tag{1.2}$$

While many parallels can be drawn between Quantum Electrodynamics (QED, the theory that describes photons and electrons) and QCD, the main difference between the two comes from the gluon-gluon interactions allowed in QCD, making it non-Abelian. These interactions can be summarized as shown in Figure 1.2.

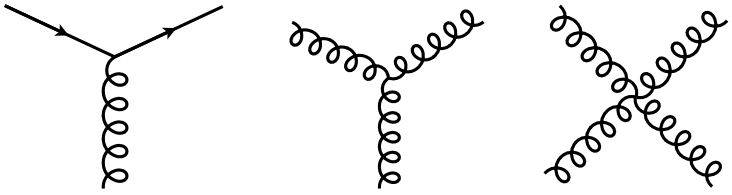

Figure 1.2: The allowed vertices in QCD. The vertices involving three or four gluons are unique to QCD and do not have a QED analog.

A core feature of QCD is that the coupling constant α_s has an energy dependence shown in Figure 1.3. This dependence can be expressed in terms of the β function as

$$Q^2 \frac{\partial \alpha_s(Q^2)}{\partial Q^2} = \beta(\alpha_s(Q^2)) \tag{1.3}$$

where Q is the momentum transfer in the particle reaction [1]. The beta function can be expressed using perturbative QCD (pQCD) as:

$$\beta(\alpha_s) = -(b_0\alpha_s^2 + b_1\alpha_s^3 + b_2\alpha_s^4 ...) \tag{1.4}$$

where the coefficients b_i depend on the number of colors and flavors. This running coupling constant is small and asymptotically tends to zero at large energy scales (or at small distances) and is large at small energy scales (large distances). This running coupling phenomenon leads to two key behaviors: asymptotic freedom and color confinement.

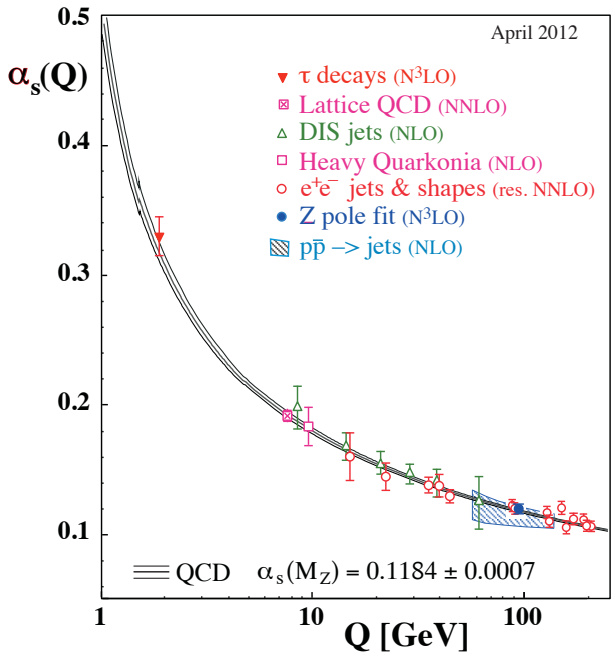

Figure 1.3: The running coupling constant α_s as a function of the momentum transfer Q. Figure from Ref. [3].

[1] The momentum transfer Q is the amount of momentum transferred in a scattering process.

Asymptotic Freedom: At high energy scales (small distances), the QCD coupling constant α_s is small and tends to zero, implying a free particle behavior of quarks and gluons [4, 5]. This has been observed by a variety of deep inelastic scattering (DIS) experiments [6–19]. These scattering experiments shown in Figure 1.4, probe the interior of a nucleon using highly energetic leptons like electrons. The electron scatters off of the target proton, producing a lepton and a hadron shower. First done by MIT-SLAC [20, 21], these DIS experiments showed the weak Q^2 dependence on the inelastic scattering cross-sections, as well as Bjorken scaling [22], where the proton structure functions are independent of the momentum transfer. These experiments revealed the point-like constituents of the proton and paved the road to an asymptotically free theory.

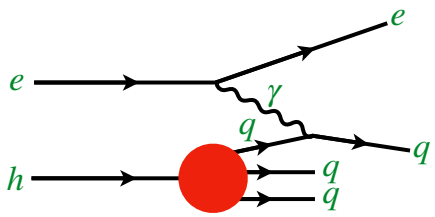

Figure 1.4: Schematic of the deep inelastic scattering experiment.

Color Confinement The opposite end of the running coupling constant phenomenon is color confinement. Proved to be a consequence of asymptotic freedom in Ref. [23], this property of QCD described in Ref. [24] forbids the direct observation of free quarks and gluons, allowing only for composite particles that are color singlets. While there have been numerous efforts to understand the source of this phenomenon like in Refs. [25–31], these are based on numerical calculations. An analytic proof of color confinement still escapes description and in fact, is one of the Millennium Problems [32].

1.2 Quark-Gluon Plasma in Heavy Ion Collisions

The quark-gluon plasma is a state of matter that is comprised of free partons and is formed in extreme conditions of temperature and pressure [33]. First discovered in heavy ion collisions at the Relativistic Heavy Ion Collider (RHIC) [34–37], its study is motivated by the fact that is the only way to access the dynamics of partons that are otherwise confined within hadrons.

A schematic of a heavy ion collision is shown in Figure 1.5. The colliding nuclei have a relativistic γ factor of approximately 3000 and form discs. As they collide, color fields from the partons within the colliding nuclei interact and fill the space between them. The energy density in the collision depends on the

number of colliding nucleons and the collision energy, and can range from 1 GeV/fm^3 for $\sqrt{s_{\rm NN}} = 7.7$ GeV at the lower limit of RHIC energies [38] to 15 GeV/fm^3 for $\sqrt{s_{\rm NN}} = 5.02$ TeV at the Large Hadron Collider (LHC) [39–41]. This is well above the $0.2 - 1$GeV/fm^3 energy density range required to form the QGP [42, 43]. After the collision the QGP cools and expands and the energy density between the receding nuclei starts to decrease. At a certain critical temperature about 1-10 fm/c after the collision, the energy density decreases to lower than what is within a hadron, and the plasma forms a hadron gas [44]. This process, referred to as a chemical freeze-out, occurs at about 160 MeV [36, 45–47]. The hadrons within the gas have energies below the threshold for inelastic particle production but briefly scatter off of each other resulting in modifications to their momentum spectra. This continues till the medium cools further and reaches what is called a thermal freeze-out at 100–150 MeV, at which point the hadrons fly freely towards the detector [48–51].

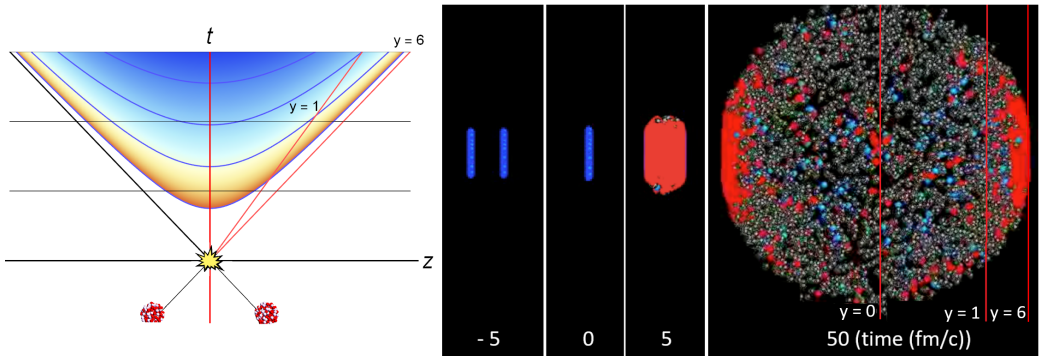

Figure 1.5: (left) Space-time diagram for a heavy ion collision. The color is indicative of the temperature of the QGP formed. (right) Snapshots of a heavy ion collision at $\sqrt{s_{\rm NN}} = 2.76$ TeV at different times. The Lorentz contracted nuclei are in blue while the QGP is in red. Figure from Ref. [52].

It is important to note that the impact parameter of the colliding nuclei plays a significant role in the dynamics of the QGP that is formed. This can be seen in Figure 1.6, where the shape and size of the QGP produced for head-on ("central") collisions is different from that in more glancing ("peripheral") collisions.

The QGP was initially thought to be a weakly coupled parton gas because of asymptotic freedom from QCD. The highly energetic collisions such as those at the LHC would imply weak interactions between the partons that make up the plasma [53–55]. This would result in rare scatterings between the constituents of the hadron gas formed in such a collision, washing out any spatial anisotropies from the "'lumpy"-ness of the colliding nuclei. A strong coupling within the QGP however, would result in the pressure gradients in the medium and spatial anisotropies would be transformed to momentum anisotropies in the particles produced as shown in Figure 1.7 [52]. In this picture, the non-uniform structure of the colliding nuclei would

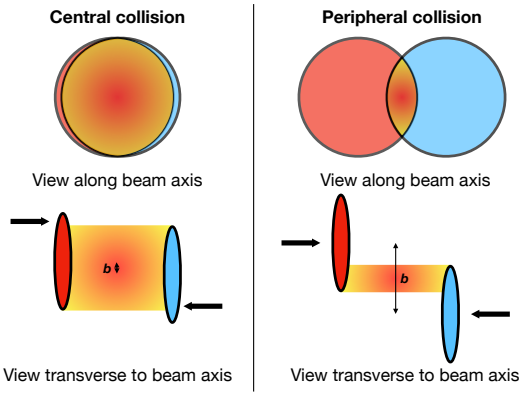

Figure 1.6: A schematic of central (left) and peripheral (right) heavy ion collisions. The impact parameter is given by b.

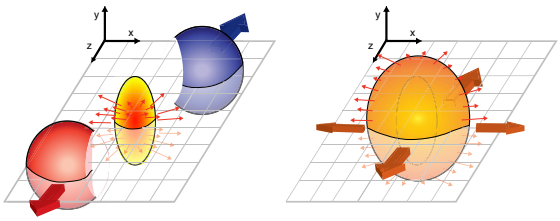

Figure 1.7: A schematic of the initial overlap region (left) and final spatial anisotropy generated (right). Figure from Ref. [63].

cause a momentum anisotropy [56] that would be further enhanced when looking at collisions that are less central and do not have perfect overlap between the colliding nuclei [57, 58]. These observations were seen in azimuthal correlation measurements implying that the medium is indeed strongly coupled [59–62].

Properties of the QGP have been successfully described by relativistic hydrodynamic models. In fact, such models describing photon emission have been used to explain the data measured at both RHIC [64] and LHC [65] energies and have suggested that the initial temperature of the QGP is 300–600 MeV [66]. The hydrodynamic nature of the QGP can be further quantified by studying the azimuthal angular distribution of particles produced in a heavy ion collision [67–69]. These distributions can be expanded in a Fourier series as:

$$\frac{d\bar{N}}{d\phi} = \frac{N}{2\pi}\left(1 + 2\sum_{n=1}^{\infty} v_n \cos(n(\phi - \Psi_n))\right). \tag{1.5}$$

where N is the particle yield, ϕ is the azimuthal angle in the transverse plane and Ψ_n is the orientation of the n^{th} order symmetry plane and is called the reaction plane. The reaction plane, along with the participant plane, are shown in Figure 1.8. The coefficient $v_n = \langle\cos[n(\phi_i - \Psi_n)]\rangle$ is the magnitude of the n^{th} order azimuthal anisotropy, and is referred to as the flow harmonic. The first harmonic v_1 is called directed flow because it indicates a particular direction, while the second harmonic v_2 is called elliptic flow since the azimuthal distribution in polar coordinates for $v_2 \neq 0$ is an ellipse. These are shown in Figure 1.9. The azimuthal correlations that are a result of flow can be described by relativistic hydrodynamics. A comparison of anisotropies measured in terms of v_n in Ref. [70] and a hydrodynamic model described in Ref. [71] is shown

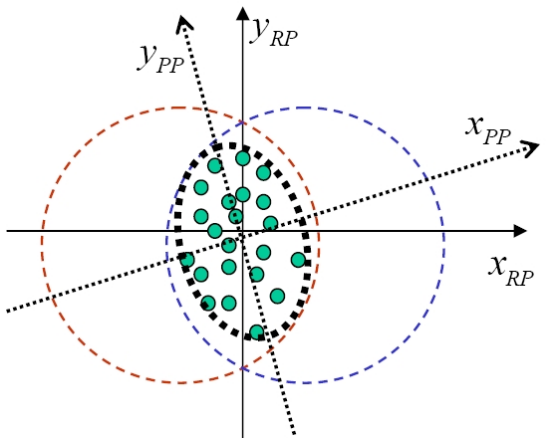

Figure 1.8: Definitions of the Reaction and Participant Plan coordinate systems. Figure from Ref. [72].

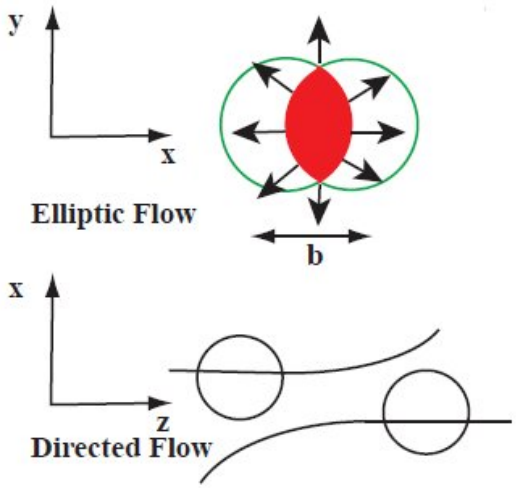

Figure 1.9: Schematics of elliptic and directed flow. Figure from Ref. [72].

in Figure 1.10.

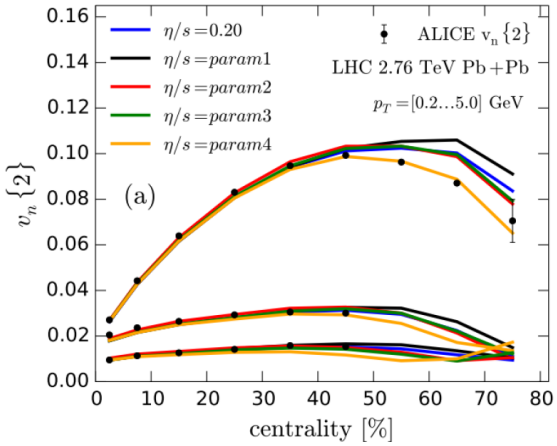

Figure 1.10: Comparison of a hydrodynamic model from Ref. [71] to anisotropy measurements by ALICE [70] for different parameterizations of η/s and for different v_n, $n = 2$, 3, 4 from top to bottom, as a function of collision centrality. Figure from Ref. [52].

The measured anisotropies can be used to constrain the specific viscosity given by the ratio of viscosity to entropy density, η/s, and have shown that the QGP is a near perfect liquid with an η/s of near the theoretical minimum of $1/4\pi$ [34, 73]. In fact, this low shear viscosity is what allows the initial fluctuations in the energy density to survive the chemical freeze-out.

The thermodynamic properties of the QGP form an important field of study. They are of particular interest since the QGP filled the early universe a few microseconds after the Big Bang [53]. The QGP is also

present in the core of neutron-stars [74] and the recent detection of gravitational waves from a neutron-star merger [75] has opened new avenues of investigation [76–78]. These studies have the potential to provide information into the nuclear equation of state since the dynamics of the merger are sensitive to the behavior of extremely dense nuclear matter [79]. The increase in temperatures and densities in merging neutron stars allows for probing different regions of the QCD phase diagram. This is shown in Figure 1.11 as a function of temperature T and baryon chemical potential μ. In particular, differences in gravitational-waves from these systems before and after the merger can be used to provide an observable signature of a first order phase transition [80]. Colliders like RHIC and the LHC on the other hand probe regions that have near zero low baryon densities, where the transition is a smooth crossover that spans a 20–30 MeV temperature range.

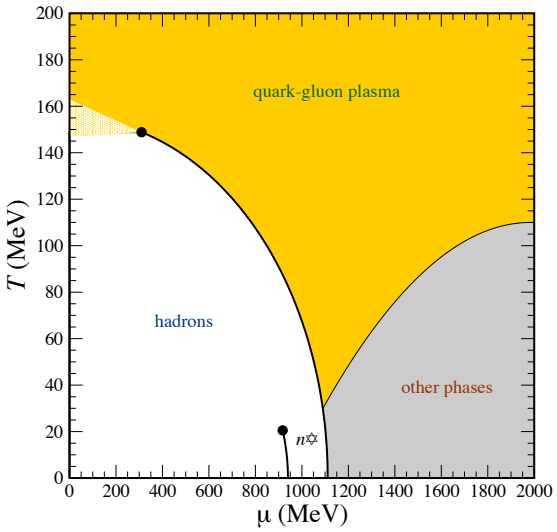

Figure 1.11: The QCD phase diagram of nuclear matter as a function of temperature T and baryon chemical potential μ. The $n\star$ denotes a neutron star. Figure from Ref. [81].

1.2.1 The Glauber Model

The basic parameters of a heavy ion collision such as the number of participants N_{part} and number of binary collisions N_{coll} can be determined using the Glauber Monte Carlo simulations [82]. This technique considers a nucleus-nucleus collision as a collection of independent binary nucleon-nucleon collisions; the colliding nuclei are modeled as a set of uncorrelated nucleons being positioned within the nucleus based on a the nuclear density function uniform in azimuthal and in polar angles. The nuclear density function in this model is a Woods-Saxon distribution given by:

$$\rho(r) = \rho_0 \frac{1 + w(r/R)^2}{1 + e^{\frac{r-R}{a}}} \tag{1.6}$$

where ρ_0 is the nucleon density, R is the nuclear radius, a is the skin depth, w corresponds to deviations from a circular shape and is typically zero for larger nuclei like Cu, W, Au, Pb, and U. For the Pb nuclei used at the LHC, $w = 0$, $R = 6.62$ fm and $a = 0.55$ fm [83]. The nuclear density distribution for Au and Cu is shown in Figure 1.12.

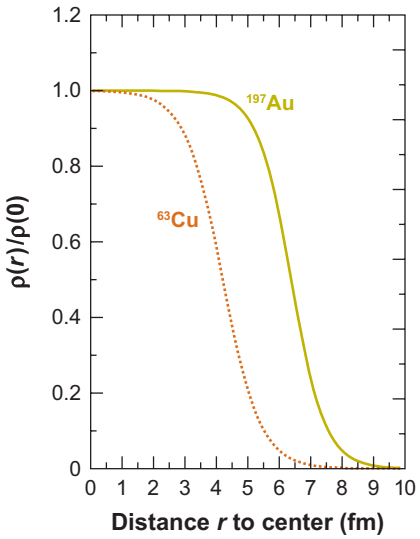

Figure 1.12: The nuclear density distributions for nuclei used at RHIC: Cu ($w = 0$, $R = 4.2$ fm and $a = 0.48$ fm) and Au ($w = 0$, $R = 6.38$ fm and $a = 0.535$ fm) [83]. Figure from Ref. [84].

They are then arranged with a random impact parameter b based on the distribution $d\sigma/db = 2\pi b$ and projected onto the $x-y$ plane as shown in Figure 1.13. They are then made to travel on straight trajectories, colliding if $d \leq \sqrt{\sigma_{\text{inel}}^{\text{NN}}/\pi}$, where d is the distance between the nucleons in a plane transverse to the beam axis and $\sigma_{\text{inel}}^{\text{NN}}$ is the inelastic scattering cross section [84, 85].

An important parameter for colliding nuclei A and B with A and B nucleons is the thickness function T_{AB}. It describes the effective overlap area in which specific nucleons in the two colliding nuclei can interact. It can be defined in terms of the probability per unit area of a given nucleon being located at a particular distance s within the nucleus. For the colliding nuclei A and B, this is given by $T_A(\mathbf{s}) = \int \rho_A(\mathbf{s}, z_A) dz_A$ and $T_B(\mathbf{s}) = \int \rho_B(\mathbf{s}, z_B) dz_B$. Then, T_{AB} is given by

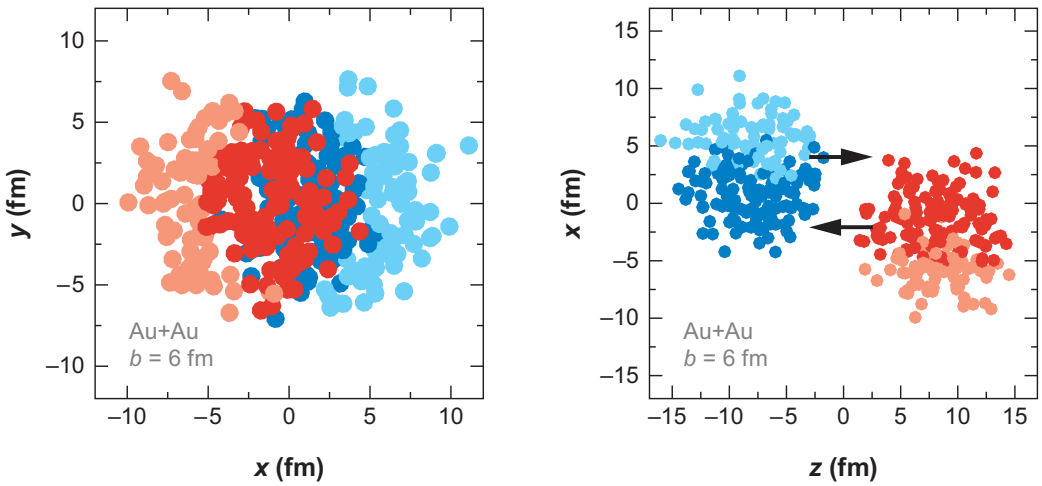

Figure 1.13: A Glauber Monte Carlo event for $Au + Au$ at $\sqrt{s_{\rm NN}}$= 200 geV with impact parameter of 6 fm viewed in the (left) transverse plane and (right) along the beam axis. Darker circles represent the participating nucleons. Figure from Ref. [84].

$$T_{AB}(\mathbf{b}) = \int T_A(\mathbf{s}) T_B(\mathbf{s}-\mathbf{b}) d^2s \tag{1.7}$$

The probability of then having n interactions between nuclei A and B is given by the binomial distribution:

$$P(n,\mathbf{b}) = \binom{AB}{n} \left[T_{AB}(\mathbf{b})\sigma_{\rm inel}^{\rm NN}\right]^n \left[1 - T_{AB}(\mathbf{b})\sigma_{\rm inel}^{\rm NN}\right]^{AB-n} \tag{1.8}$$

where the first term is the number of combinations for finding n collisions from AB possibilities, the second term is the probability for having exactly n collisions, and the last term the probability of $AB - n$ misses. Then the total probability of an interaction between A and B is:

$$\frac{d^2\sigma_{\rm inel}^{\rm AB}}{db^2} \equiv p_{\rm inel}^{\rm AB}(b) = \sum_{n=1}^{AB} P(n,\mathbf{b}) = 1 - \left[1 - T_{AB}(\mathbf{b})\sigma_{\rm inel}^{\rm NN}\right]^{AB} \tag{1.9}$$

and the total cross section is given by

$$\sigma_{\rm inel}^{\rm AB} = \int_0^\infty 2\pi b db \left[1 - \left(1 - T_{AB}(\mathbf{b})\sigma_{\rm inel}^{\rm NN}\right)^{AB}\right] \tag{1.10}$$

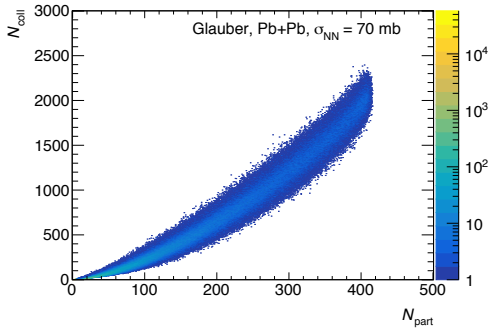

Figure 1.14: The $N_{\text{coll}} - N_{\text{part}}$ correlation for Pb+Pb collisions at $\sqrt{s_{\text{NN}}} = 5.02$ TeV. Figure from Ref. [88].

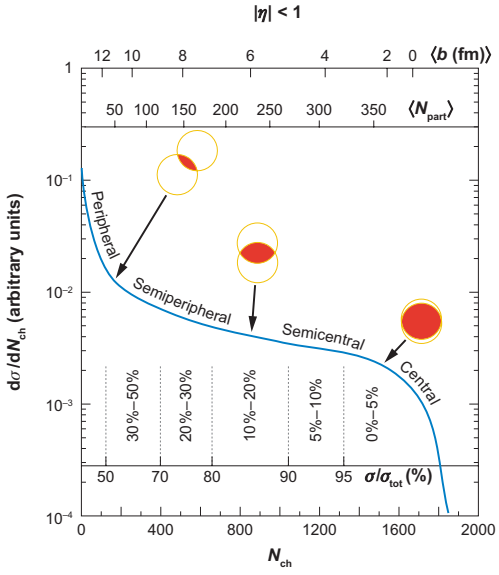

Figure 1.15: The correlation between the observable N_{ch} and N_{part} to determine the centrality distribution. Figure from Ref. [84].

and N_{coll} and $N_{\text{part}}$are given by [86, 87]:

$$N_{\text{coll}}(b) = \sum_{n=1}^{AB} nP(n,b) = AB \times T_{AB}(b)\sigma_{\text{inel}}^{\text{NN}} \tag{1.11}$$

$$\begin{aligned} N_{\text{part}}(b) =& A \int T_A(\mathbf{s})\Big[1 - \big(1 - T_B(\mathbf{s}-\mathbf{b})\sigma_{\text{inel}}^{\text{NN}}\big)^B\Big] d^2s \\ &+ B \int T_B(\mathbf{s}-\mathbf{b})\Big[1 - \big(1 - T_A(\mathbf{s})\sigma_{\text{inel}}^{\text{NN}}\big)^A\Big] d^2s \end{aligned} \tag{1.12}$$

The correlation between N_{coll} and N_{part} can be seen in Figure 1.14. The charged particle multiplicity N_{ch} along with the combination of N_{part} and impact parameter b can be used to determine the centrality of a heavy ion event. An example of this is shown in Figure 1.15.

1.3 Jets and Jet Quenching

The energy required to dissociate partons increases the further apart they are as a consequence of color confinement. If the energy with which they are flying apart is greater than the energy required to separate them, it becomes more favorable to produce a quark-antiquark ($q\bar{q}$) pair. This process of $q\bar{q}$ production

continues recursively until it is not energetically favorable to do so, with the end result being conical sprays of hadrons called jets. This picture is qualitatively supported by Lattice QCD [89]. A schematic of this process is shown in Figure 1.16. Because of their color charge, gluon led jets have a softer fragmentation and result in more particles carrying lesser energy as compared to quark led jets [90].

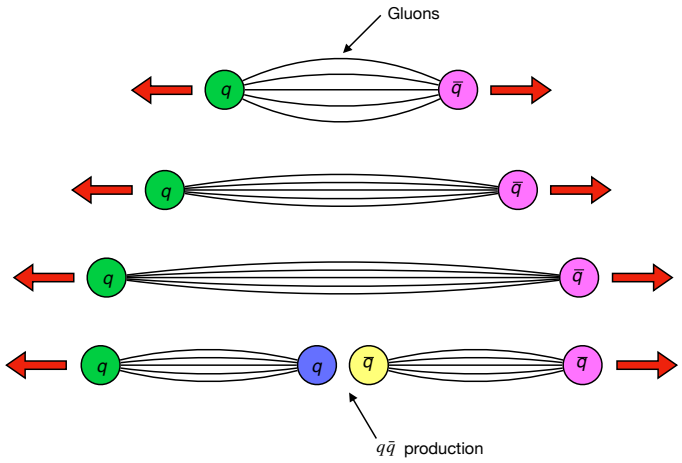

Figure 1.16: A schematic of how jets are produced from a hard process involving $q\bar{q}$. The gluonic flux tubes build up and break as the quarks gain energy, and result in the formation of new $q\bar{q}$ pairs.

1.3.1 Jets in e^+e^- collisions

The simplest process that can be used to study jets is the process $e^+e^- \to q\bar{q} \to 2$ jets. The electron and positron annihilates to produce a photon that can decay into a $q\bar{q}$ pair, that hadronize and form jets. In fact, this was the process that provided experiment evidence of jets at SPEAR (Stanford Positron Electron Accelerating Ring) at SLAC in 1975, where it was observed that the distribution of final state hadrons was not isotropic [91, 92]. Analyses of these distributions showed that they were associated with spin 1/2 quarks. Jets in e^+e^- collisions further provided the first indirect evidence of gluons when three jet events were observed in the $\Upsilon \to ggg$ decay [93, 94]. At the Large Electron-Positron Collider (LEP), higher collision energies allowed the $e^+e^- \to Z^0 \to q\bar{q}$ process. In these processes, to leading order, the $q\bar{q}$ pair evolved via gluon radiation before converting to hadrons [95], allowing for events with more than two jets. Jet production in e^+e^- collisions is also one of the best ways to test the validity of perturbative QCD [96].

1.3.2 Jets in pp collisions

Jet production in a vacuum is well described in context of perturbative QCD [97]. Processes involving large momentum transfers like high p_{T} hadron production are shown in Figure 1.17 [2].

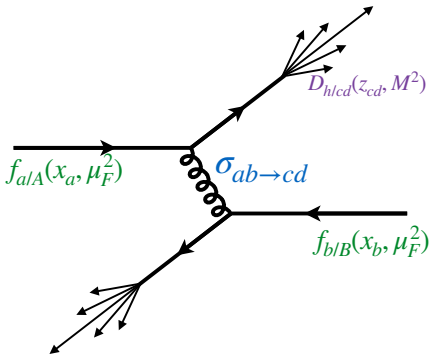

Figure 1.17: Jet production from the process $pp \to hX$, factorizing in terms of the parton distribution functions, scattering cross sections, and jet fragmentation functions.

These processes can be described to leading order by perturbative QCD in terms of the parton distribution functions, scattering cross sections, and final state fragmentation functions as [98]:

$$d\sigma_{pp\to hX} \approx \sum_{abjd} \int dx_a \int dx_b \int dz_j f_{a/p}(x_a, \mu_f) \otimes f_{b/p}(x_b, \mu_f) \otimes d\sigma_{ab\to jd}(\mu_f, \mu_F, \mu_R) \otimes D_{j\to h}(z_j, \mu_f) \tag{1.13}$$

where $x_a = p_a/P_A, x_b = p_b/P_b$ are the initial momentum fractions carried by the interacting partons, $z_j = p_h/p_j$ is the momentum fraction carried by the final observed hadron. $f_{a/p}(x_a, \mu_f)$ and $f_{b/p}(x_b, \mu_f)$ are the two parton distribution functions (PDFs), $d\sigma_{ab\to jd}(\mu_f, \mu_F, \mu_R)$ is the differential cross section for parton scattering and $D_{j\to}(z_j, \mu_F)$ is the fragmentation function (FFs) for parton j to hadron h. μ_f and μ_F are the factorization scales and μ_R is the renormalization scale. These are typically taken to be the same hard scale Q, given by the hadron p_{T}. The PDFs, measured via DIS experiments, characterize the initial state and represent the probability of finding a parton with longitudinal momentum fraction x (shown in Figure 1.18) in the initial hadron, while the FFs describe the probability of fragmenting to a hadron h with

[2] In the context of a particle collision, the p_{T} of a particle is the momentum it carries in a direction perpendicular to the beam axis. It is given by $p_{\mathrm{T}} = |p| \sin\theta$ where θ is the angle of the particle with respect to the beam axis. The rapidity y is related to an outgoing particles momentum along the beam axis, and is given by $y = 1/2 \ln[(E + p_z)/(E - p_z)]$

given kinematic properties.

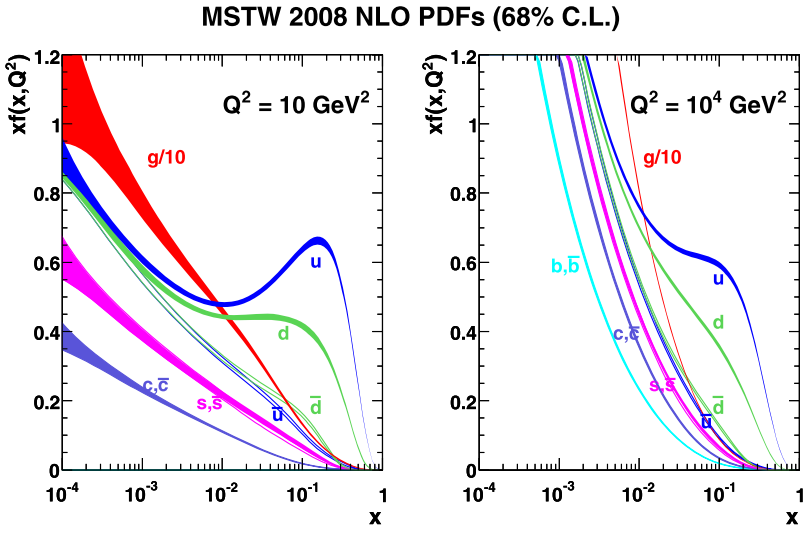

Figure 1.18: The next to leading order (NLO) PDFs at (left) $Q^2 = 10\text{GeV}^2$ and (right) $Q^2 = 10^4\text{GeV}^2$. The band is the associated one-sigma (68%) confidence level uncertainty. Figure from Ref. [99].

The factorization of the jet production process is crucial because it allows for independently measuring and calculating the different components of the cross sections [100]. Jet cross sections in pp and $p\bar{p}$ collisions measured by a variety of different experiments, and their comparison to theory calculations are shown in Figure 1.19. This in particular enables direct comparisons of jet observables in pp collisions to those in heavy ion collisions and determine their modifications. The fragmentation functions in e^+e^- collisions in terms of collision energy $\sqrt{s}$, and the scaled energy of the hadron x, are shown in Figure 1.20.

1.3.3 Jets in heavy ion collisions

In the case of heavy ion collisions, after accounting for geometric scaling effects by the nuclear thickness function as mentioned in Section 1.2, jet observables can be modified due to two sources: the nuclear PDF being distinct from a proton PDF, and the formation of the quark gluon plasma. The former is collectively referred to as cold nuclear matter (CNM) effect, and can be quantified by defining a nuclear modification factor for the PDF:

$$R_a^A(x, Q^2) = \frac{f_{a/A}(x, Q^2)}{f_{a/p}(x, Q^2)} \tag{1.14}$$

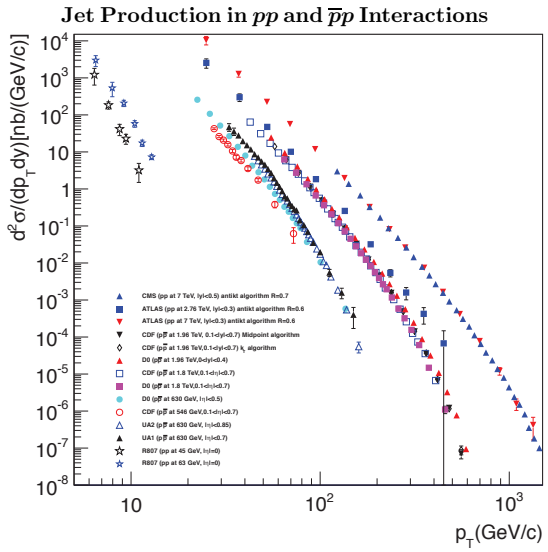

(a) Inclusive differential jet cross sections shown as a function of jet transverse momentum from different experiments. Figure from Ref. [101].

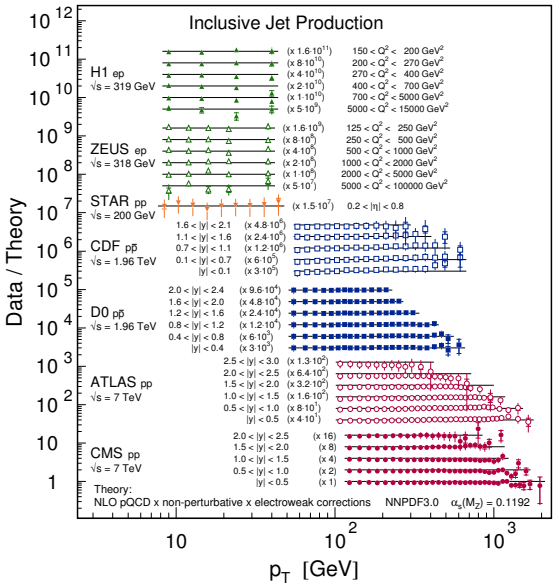

(b) Ratios of data over theory for some jet cross sections measured by different experiments. The next to leading order predictions are derived using the NNPDF3.0 PDF set. Figure from Ref. [102].

Figure 1.19: (Left) Some inclusive jet cross sections in data (left) and their comparison to theory (right).

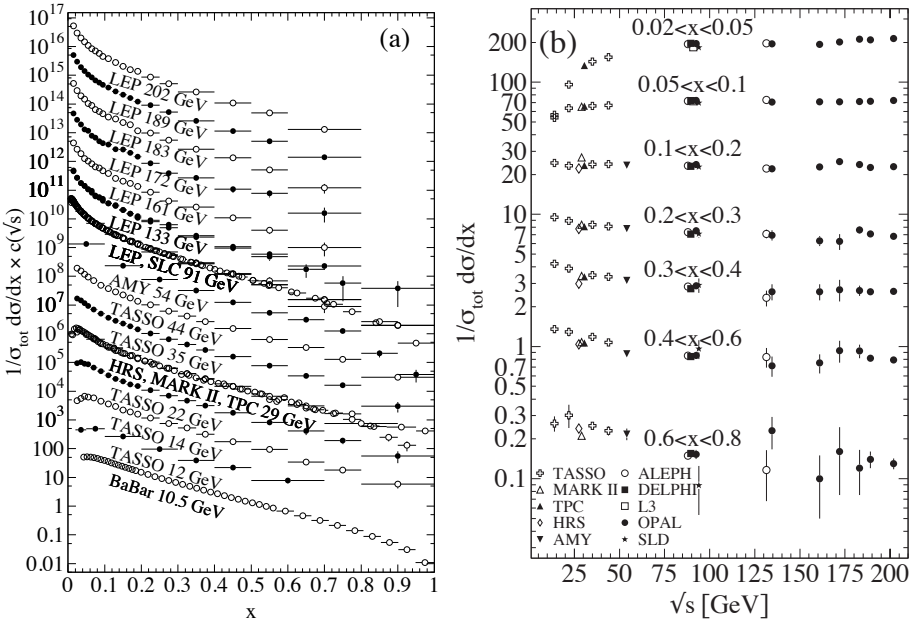

Figure 1.20: Measurements of the e^+e^- fragmentation functions for (left) different center-of-mass energies as a function of x, and (right) for different ranges of x as a function of $\sqrt{s}$. The curves on the left are scaled for visibility. Figure from Ref. [103].

where $f_{a/A}$ and $f_{a/p}$ are the nuclear and proton PDFs respectively. This R_a^A factor is determined by global fits to data from DIS measurements [104–106]. CNM effects include the following contributions:

- Shadowing: This is a destructive interference effect that reduces the interactions of a nucleon incident on a nucleus within its interior and on its back face. This effect reduces the effective number of nucleons in an inelastic interaction to $A^{2/3}$. For Q^2 of the order of a few GeV^2, this effect dominates for $x < 0.05$ and implies $R_a^A(x, Q^2) < 1$ [107].

- Anti-shadowing: This compensates for the shadowing effect based on the momentum sum rule, and for Q^2 of the order of a few GeV^2 implies $R_a^A(x, Q^2) > 1$ over the region $0.05 < x < 0.20$.

- EMC: The modification of the nuclear structure function was first observed by the European Muon Collaboration [108]. Recent observations have suggested that the effect is caused by short-range correlated nucleon pairs within nuclei [109]. For Q^2 of the order of a few GeV^2, this effect dominates for $0.2 < x < 0.80$ and implies $R_a^A(x, Q^2) < 1$.

- Fermi Motion: This effect considers the motion of the nucleons within the nucleus. It results in $R_a^A(x, Q^2) > 1$ over the $x > 0.8$ region for Q^2 of the order of a few GeV^2 [110].

CNM effects are experimentally measured using $p + A$ systems where the size and shape of the plasma, and hence any effects thereof, are smaller. Measurements of the jet nuclear modification factor in p+Pb collisions, $R_{p\mathrm{Pb}}$, indicate that CNM effects are small for jets at all transverse momentum and pseudorapidity measured at the LHC [111–113]. This is shown in Figure 1.21. Energy densities in the Pb+Pb, p+Pb, and pp collision systems are shown in Figure 1.22.

The second source of modification is the formation of the hot and dense quark gluon plasma. The hot nuclear matter effects further serve as an independent confirmation that the medium formed is strongly interacting. Jets are formed early enough that they traverse the Quark Gluon Plasma and as strongly interacting particles, are both affected by, and affect the QGP. This interaction typically results in the jet losing energy and forward momentum [115, 116], with the lost energy being deposited in the medium [117]. Jets can also pick up momentum transverse to the parton direction. The hot nuclear matter effects can be considered to be a combination of collisional and radiative energy losses summarized in Figure 1.23.

- Collisional energy loss: This is a combination of elastic and inelastic collisions of the hard parton with the constituents of the quark gluon plasma.

- Radiative energy loss: This is the larger source of parton energy loss and jet quenching. These are modified by the presence of the plasma due to scatterings off of the plasma constituents. A vari-

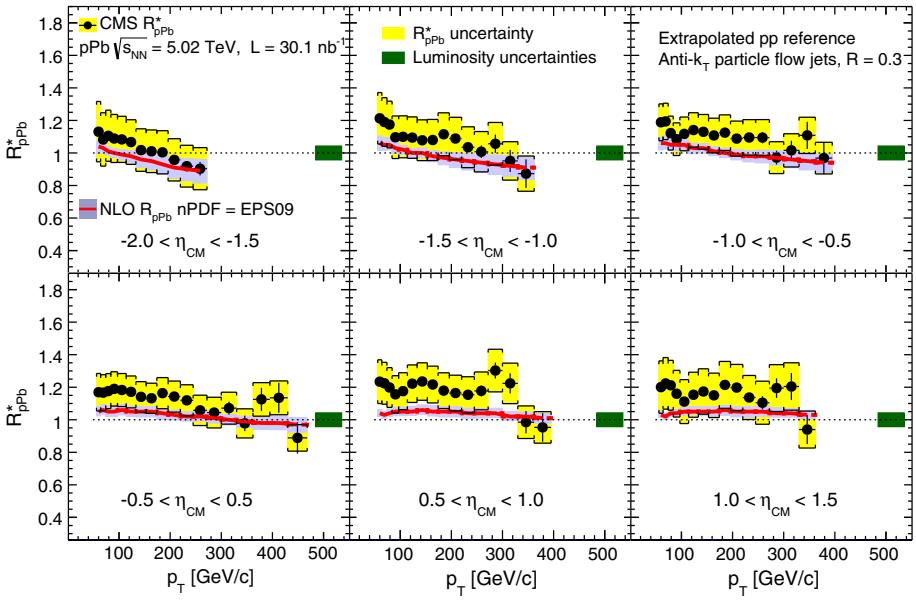

Figure 1.21: The nuclear modification factor for jets in p+Pb collisions as measured by CMS in different rapidity intervals. Figure from Ref. [113].

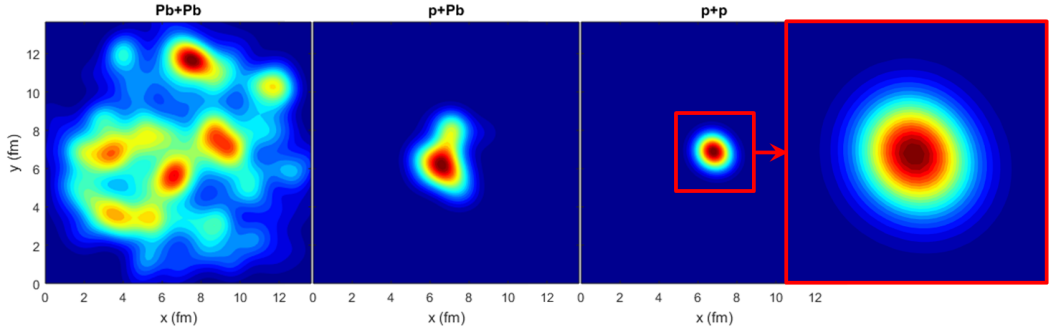

Figure 1.22: Snapshots of typical energy density profiles in (left) Pb+Pb, (middle) p+Pb, and (right+far right) pp collisions. Figure from Ref. [114].

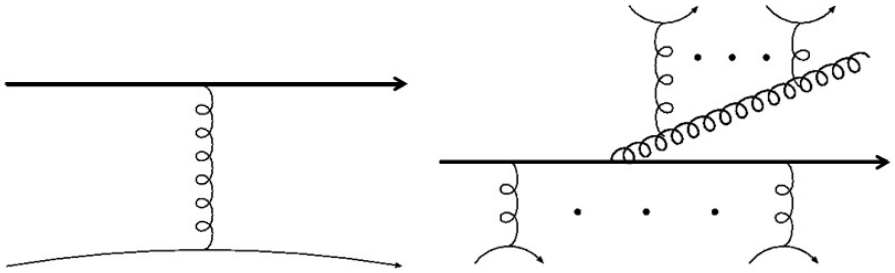

Figure 1.23: The typical diagrams for (left) collisional and (right) radiative energy losses for a parton in a hard scattering as it propagates through the QGP. Figure from Ref. [98].

ety of radiative energy loss frameworks that have been developed include: Baier-Dokshitzer-Mueller-Peigne-Schiff-Zakharov (BDMPS-Z) [118], Gyulassy, Levai and Vitev (GLV) [119], Amesto-Salgado-Wiedemann (ASW) [120], Arnold-Moore-Yaffe (AMY) [121] and higher twist (HT) [122].

Both hot and cold nuclear matter effects can be described by modifying Equation 1.13 as:

$$\begin{aligned} d\sigma_{AB\to hX} \approx \sum_{abjj'd} & f_{a/A}(x_a) \otimes f_{b/B}(x_b) \\ & \otimes d\sigma_{ab\to jd}(\mu_f, \mu_F, \mu_R) \\ & \otimes P_{j\to j'} \\ & \otimes D_{h\to j'}(z_j, \mu_f) \end{aligned} \tag{1.15}$$

where the additional $P_{j\to j'}$ describes the interaction of the hard parton with the colored medium. This is typically taken as part of the fragmentation modification as:

$$\widetilde{D}_{h\to j'}(z_j, \mu_f) \approx \sum_{j'} P_{j\to j'}(p_{j'}|p_j) \otimes D_{h\to j'}(_{j'}) \tag{1.16}$$

1.3.4 Jet Algorithms

Jet algorithms map the momenta of final state particles into the momenta of jets, and form a core component of any jet measurement. They can be broadly categorized as sequential recombination and cone algorithms [123].

Cone algorithms cluster particles in the $\eta - \phi$ space[3] assuming that the particles of a jet will be located in a conical region of the detector. Some examples of cone algorithms are: iterative cone - progressive removal (IC-PR) [124], iterative cone - split merge (IC-SM) [125], and SISCone [126].

Sequential recombination algorithms on the other hand work by grouping particles in momentum space, with the result that they have fluctuating areas in $\eta - \phi$ space. Some examples of these algorithms are: k_t [127], anti-k_t [128], and Cambridge/Aachen (C/A) [129].

Recombination algorithms have an advantage over the cone algorithms in that they are infrared and collinear safe (IRC). This is related to instabilities in the cones that are found due to soft radiation. In a

[3]The pseudorapidity $\eta = -\ln[\tan(\theta/2)]$ is related to the rapidity and is a spatial coordinate that describes the angle θ of a particle with respect to the beam axis. ϕ is the azimuthal angle around the beam axis. The coordinate system of detectors is typically based on the $\eta - \phi$ plane.

collinear safe jet algorithm, the presence of a virtual loop or a collinear splitting of a central particle would not change the number of jets being reconstructed. On the other hand, while a collinear unsafe jet algorithm would not change its output with the presence of a virtual loop, a splitting in the central particle would lead to the left and right most particles forming individual seeds, implying two reconstructed jets [130]. Figure 1.24 describes the collinear safety problem.

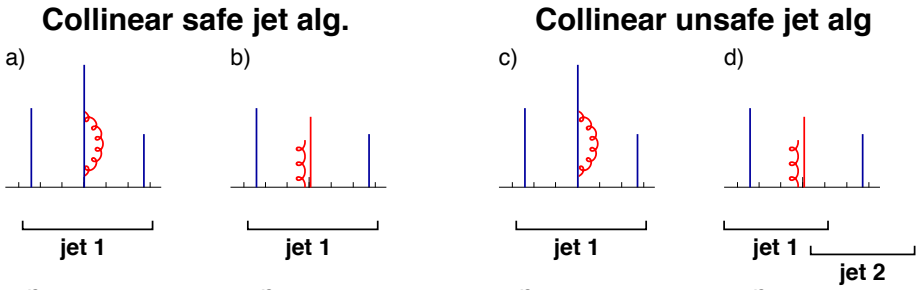

Figure 1.24: An illustration of collinear unsafe behavior. The particle p_{T} is proportional to the height and the horizontal axis indicates rapidity. Figure from Ref. [130].

A schematic describing the infrared safety problem is shown in Figure 1.25. Here an infrared safe algorithm would use the three particles as seeds iteratively find two stable cones. An unsafe algorithm however would find three overlapping cones based on the addition of a soft seed.

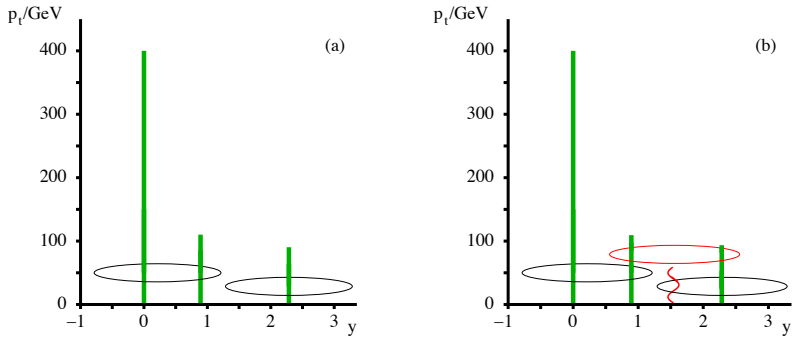

Figure 1.25: An illustration of infrared unsafe behavior. The particle p_{T} is proportional to the height and the horizontal axis indicates rapidity. Figure from Ref. [126].

Sequential recombination algorithms are more popular because they are IRC safe and are discussed in further detail below. The general procedure for sequential recombination algorithms is as follows:

- Calculate all distances d_{ij} between entities i and j, and distance d_{iB} between entity i and beam B
- Find the minimum of d_{ij} and d_{iB}:
  - If d_{ij} is the minimum, combine i and j by summing their four-vectors, remove them from the list of particles and return to beginning.

- If the smallest distance is d_{iB}, then take i as the jet and remove it from the list of particles and return to beginning.

- Continue the procedure till the list of items is empty.

In general the distance d_{ij} between the objects is found the via the prescription

$$d_{ij} = \min(k_{Ti}^{2p}, k_{Tj}^{2p}) \frac{\Delta_{ij}^2}{R^2} \tag{1.17}$$

$$d_{iB} = k_{Ti}^{2p} \tag{1.18}$$

where k_{Ti} is the transverse momentum of particle i and $\Delta_{ij} = \sqrt{\Delta\eta_{ij}^2 + \Delta\phi_{ij}^2}$ is the distance between particles i and j in $\eta - \phi$ space. R the distance parameter and reflects the size of the jet being considered.

Different recombination algorithms use different values of p. The k_t algorithm has $p = 2$. This results in clustering soft particles first, with the final jet having a fluctuating area. This algorithm is susceptible to processes that contribute particles that do not belong to a jet. The C/A algorithm uses $p = 0$. This results in the distances between particles being completely independent of momentum. The anti-k_t algorithm uses $p = -1$. Hence, the algorithm clusters hard particles first, making it the least susceptible to background. The behavior of the different clustering algorithms is shown in Figure 1.26. The anti-k_t algorithm is the default used in all LHC collaborations.

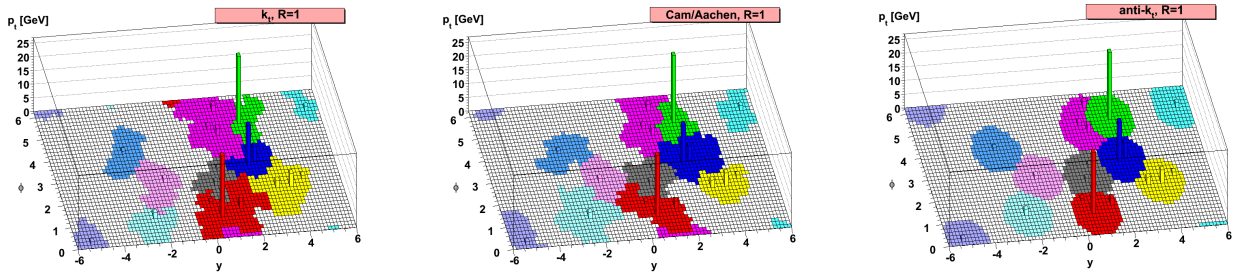

Figure 1.26: Different clustering algorithms applied to the sample parton-level event. Figures from Ref. [128].

Chapter 2

MEASUREMENTS IN HEAVY ION COLLISIONS

This chapter shall discuss some important experimental jet measurements that contextualize and motivate the study of the main analysis in this thesis. These include the study of the hadron yields, dijet balance, jet yields, jet fragmentation, and jet profiles.

2.1 Hadron Suppresion

This discussion is based on Ref. [131]. Done at RHIC by the PHENIX collaboration, this was one of the first experimental measurements of jet quenching that showed the presence of the QGP. This measurement analyzed high p_{T} charged hadrons and neutral π^0s ($p_{\mathrm{T}} > 2$ GeV) from jets produced in Au+Au collisions, collided at $\sqrt{s_{\mathrm{NN}}} = 130$ GeV. Since jets form early in the collision and experience the evolution of the QGP, they are expected to lose energy due to collisional and radiative losses as discussed in Section 1.3. The modifications between the pp and Au+Au system was quantified by constructing the nuclear modification factor R_{AA}, given as:

$$R_{\mathrm{AA}} p_{\mathrm{T}} = \frac{(1/N_{\mathrm{evt}}) d^2 N^{\mathrm{A+A}}/dp_{\mathrm{T}} d\eta}{(\langle N_{\mathrm{binary}} \rangle / \sigma_{\mathrm{inel}}^{\mathrm{N+N}} d^2\sigma^{\mathrm{N+N}}/dp_{\mathrm{T}} d\eta} \tag{2.1}$$

where N_{evt} is the number of Au+Au events, $\langle N_{\mathrm{binary}} \rangle$ is the average number of binary collisions per event, σ is the scattering cross section, and p_{T} and η are the kinematics of the charged particle.

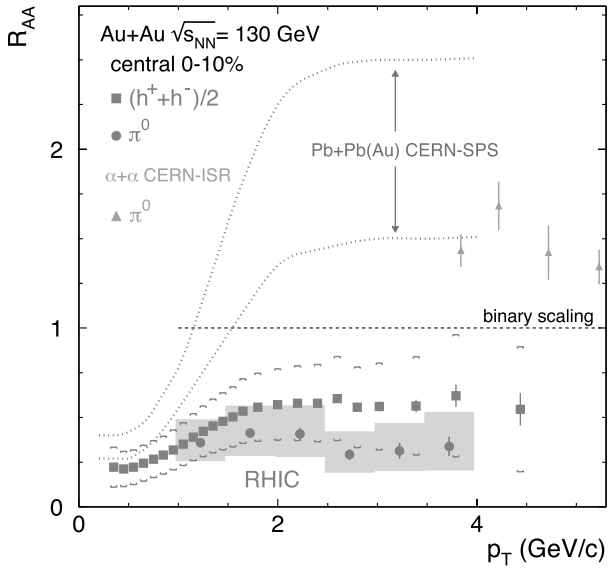

(a) The R_{AA} for charged hadrons and neutral pions in Au+Au collisions at $\sqrt{s_{\mathrm{NN}}} = 130$ GeV. Also shown is the R_{AA} for inclusive cross sections in $\alpha + \alpha$ compared to pp at $\sqrt{s_{\mathrm{NN}}} = 31$ GeV [139] and spectra from Pb+Pband Pb + AU compared to pp at $\sqrt{s_{\mathrm{NN}}} = 17$ GeV [140]. Figure from Ref. [131].

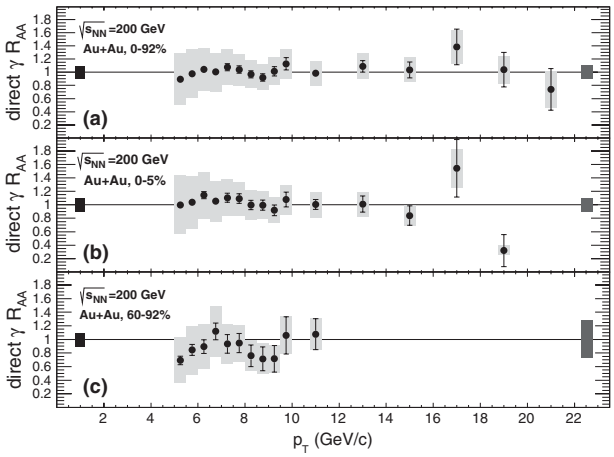

(b) The R_{AA} for photons as a function of p_{T} for three centrality selections in Au+Au collisions at $\sqrt{s_{\mathrm{NN}}} = 200$ GeV. Figure from Ref. [141].

Figure 2.1: R_{AA} evaluated for (left) charged hadrons and pions and (right) photons.

The R_{AA} for charged hadrons and neutral pions is shown in Figure 2.1a. A significant depletion is seen, with the R_{AA} rising for $p_{\mathrm{T}} < 2$ GeV and remaining fairly constant thereafter. Electroweak probes like photons and Z bosons do not lose energy is the QGP since they do not interact strongly, and their R_{AA} is expected to be closer to unity. This can be seen in Figure 2.1b Some other R_{AA} measurements from RHIC and the LHC include [132–138].

2.2 Dijet Balance: x_J

This section will discuss the dijet balance as measured by the ATLAS detector for Pb+Pb collisions at $\sqrt{s_{\mathrm{NN}}} = 2.76$ TeV [142]. The dijet imbalance can be expressed in terms of x_J defined as:

$$x_J = \frac{p_{\mathrm{T}2}}{p_{\mathrm{T}1}} \tag{2.2}$$

where $p_{\mathrm{T}2}$ and $p_{\mathrm{T}1}$ are the transverse momenta of the two highest-p_{T} jets in the event respectively. The minimum $p_{\mathrm{T}2}$ considered is 25 GeV and the pair of jets are separated by $|\Delta\phi| > 7\pi/8$. The dijet yields

normalized by the number of jets and determined as $1/N_{\text{jets}}dN/dx_J$ are presented as a function of x_J for different centrality intervals, as well as different ranges for $p_{\text{T}1}$.

Figure 2.2 shows the x_J distribution for dijet pairs in pp and Pb+Pb collisions in two different centrality bins and two $p_{\text{T}1}$ ranges. It can be seen that the dijet yields in pp are peaked at unity and become narrower for larger $p_{\text{T}1}$ ranges. This reflects the fact that the effects of jet quenching are minimal and the higher-p_{T} jets are better balanced. The dijet yields in peripheral Pb+Pb collisions are similar to the distributions from the pp data, showing that the effects of quenching are smaller. On the other hand, dijet yields in central Pb+Pb collisions are significantly broadened, reflecting the maximal of jet quenching. This is consistent with the picture of the individual jets in the dijet pair traversing different lengths in the QGP and hence losing different amounts of energy. In fact, the distribution for Pb+Pb data is peaked at $x_J = 0.5$, implying that the jets are highly unbalanced. It is further seen that higher p_{T} jets have a narrower x_J distribution. This suggests that the fractional energy loss decreases with increasing jet p_{T}. Similar jet asymmetry has been observed at both RHIC and the LHC [143–146].

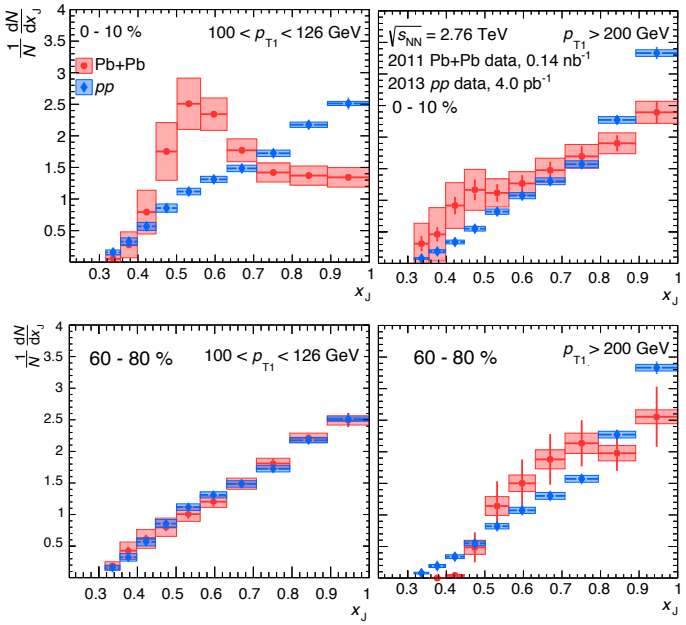

Figure 2.2: The $1/N_{\text{jets}}dN/dx_J$ distributions for $R = 0.4$ jets as a function of x_J for pp (blue) and Pb+Pb (red) collisions. The different panels are for (top) central and (bottom) peripheral collisions in (left) $100 < p_{\text{T}1} < 126$ GeV and (right) $p_{\text{T}1} > 200$ GeV. The pp data is the same in all panels. The statistical uncertainties are indicated by the bars while the boxes indicate the systematic uncertainties. Figures from Ref. [142].

2.3 Modification of jet yields: R_{AA}

This section discusses the measurement of the inclusive jet R_{AA} as measured by the ALICE detector for jets in $\sqrt{s_{\mathrm{NN}}} = 2.76$ TeV Pb+Pb and pp collisions [147].

While measurements that compare jets in a dijet system to each other as discussed in Section 2.2 can provide valuable information about how jets lose energy, they have the following limitation: If both jets lose equal amounts of energy, the dijet yield will still be peaked at unity and no new information will be obtained. Thus, it is useful to compare the jet yields directly between the pp and Pb+Pb systems and construct the jet R_{AA} observable. This is defined as:

$$R_{\mathrm{AA}} = \frac{\frac{1}{N_{\mathrm{evt}}} \left.\frac{d^2 N_{\mathrm{jet}}}{dp_{\mathrm{T}} dy}\right|_{\mathrm{cent}}}{\langle T_{\mathrm{AA}} \rangle \left.\frac{d^2 \sigma_{\mathrm{jet}}}{dp_{\mathrm{T}} dy}\right|_{\mathrm{pp}}} \tag{2.3}$$

where T_{AA} is the nuclear thickness function and accounts for the geometric enhancement between pp and Pb+Pb as discussed in Section 1.2 and [84].

This measurement includes considers jets from both charged particles and neutral π^0s. The jet spectrum in Pb+Pb events, as well as the jet R_{AA} for central Pb+Pb is shown in Figure 2.3. It can be seen that the most central collisions show a clear suppression with an $R_{\mathrm{AA}} \approx 0.25$ at jet p_{T} 30 GeV. The R_{AA} value slowly evolves with jet p_{T} and rises to 0.5 at jet $p_{\mathrm{T}} = 100$ GeV. This modification becomes smaller for more peripheral collisions.

These observations are consistent with results from ATLAS and CMS [116, 148–150]. The ATLAS results at $\sqrt{s_{\mathrm{NN}}} = 5.02$ TeV are shown in Figure 2.4a. The higher collision energy allows access to higher p_{T} jets. The smooth centrality dependence can be more clearly seen in Figure 2.4b, where R_{AA} is shown as a function of $\langle N_{\mathrm{part}} \rangle$ for jets the 100–126 GeV and 200–251 GeV ranges. The magnitude of the suppression is also seen to significantly depend on jet p_{T} for $\langle N_{\mathrm{part}} \rangle \geq 50$.

2.4 Jet Fragmentation

This section will discuss the jet fragmentation as measured by the ATLAS detector for Pb+Pb collisions at $\sqrt{s_{\mathrm{NN}}} = 5.02$ TeV [151]. While measurements of R_{AA}[148, 149, 152] and asymmetry [142, 143, 146] describe how much energy is lost by the jet, fragmentation measurements describe the momentum distribution of particles associated to the jet. These can be described as:

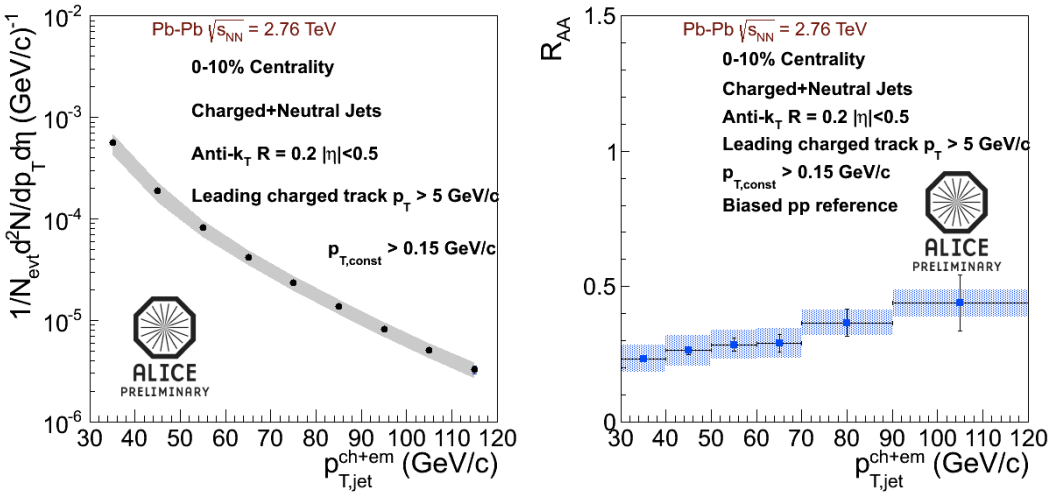

Figure 2.3: (Left) The inclusive jet cross section as a function of jet p_{T} in 0–10% central Pb+Pb collisions at $\sqrt{s_{\mathrm{NN}}} = 2.76$ TeV. The band around the data points represents the systematic uncertainty. (Right) The R_{AA} for 0–10% central Pb+Pb collisions. Figure from Ref. [147].

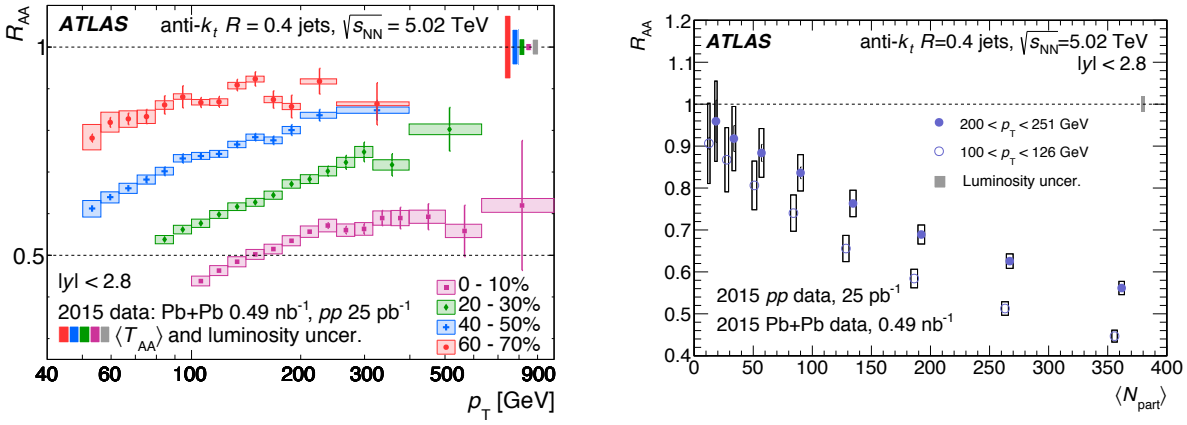

(a) (b)

Figure 2.4: The R_{AA} distributions as a function of (left) jet p_{T} for different centrality bins and (right) $\langle N_{\mathrm{part}} \rangle$ for different jet p_{T} bins, for jet rapidity $|y| < 2.8$. Figures from Ref. [116].

$$D(z) = \frac{1}{N_{\text{jet}}} \frac{dn_{\text{ch}}}{dz} \tag{2.4}$$

$$D(p_{\text{T}}) = \frac{1}{N_{\text{jet}}} \frac{dn_{\text{ch}}}{dp_{\text{T}}} \tag{2.5}$$

where $z = p_{\text{T}} \cos(\Delta R / p_{\text{T}}^{\text{jet}})$ and gives the charged-particle longitudinal momentum fraction relative to the jet. Modifications to the fragmentation functions in Pb+Pb collisions can be evaluated by constructing the ratios $R_{D(z)} = D(z)_{\text{Pb+Pb}}/D(z)_{pp}$ and $R_{D(p_{\text{T}})} = D(p_{\text{T}})_{\text{Pb+Pb}}/D(p_{\text{T}})_{pp}$. The $D(p_{\text{T}})$ distribution is shown in Figure 2.5.

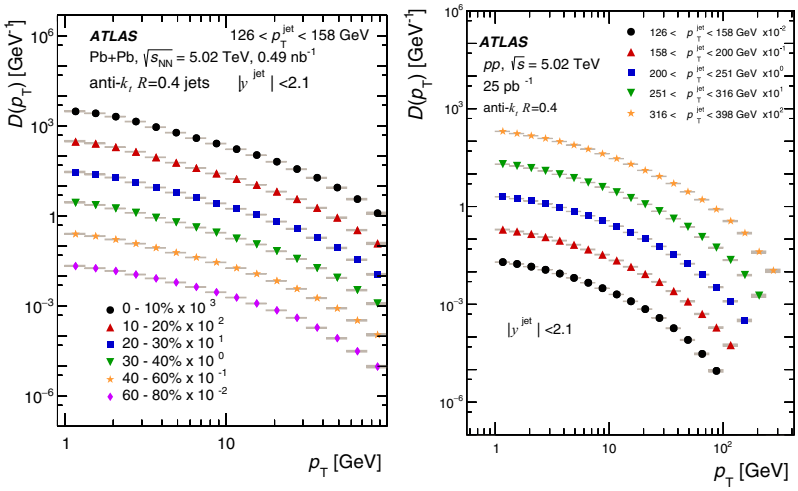

Figure 2.5: (Left) The $D(p_{\text{T}})$ distributions in pp as a function of charged-particle p_{T} for different $p_{\text{T}}^{\text{jet}}$ selections and for jet rapidity $|y| < 2.1$. (Right) The $D(p_{\text{T}})$ distributions in Pb+Pb as a function of charged-particle p_{T} for different centrality selections and for jet rapidity $|y| < 2.1$. The error bars represent statistical uncertainties while the shaded boxes represent systematic uncertainties. Figures from Ref. [151].

The modifications to the $D(z)$ and $D(p_{\text{T}})$ distributions in central (top) and peripheral (bottom) collisions are shown in Figure 2.6. The shape of these modifications is very similar for both $D(z)$ and $D(p_{\text{T}})$. There is an enhancement of particles with low z and p_{T}, followed by a suppression at intermediate z and p_{T}, and finally an enhancement at high z and p_{T}. These modifications become smaller for more peripheral collisions. The low momentum excess can be further investigated by calculating the extra number of particles N_{ch} in Pb+Pb compared to pp as given below:

$$N_{\text{ch}} = \int_{p_{\text{T}_{\text{min}}}}^{p_{\text{T}_{\text{max}}}} \left(D(p_{\text{T}})_{\text{Pb+Pb}} - D(p_{\text{T}})_{pp} \right) dp_{\text{T}} \tag{2.6}$$

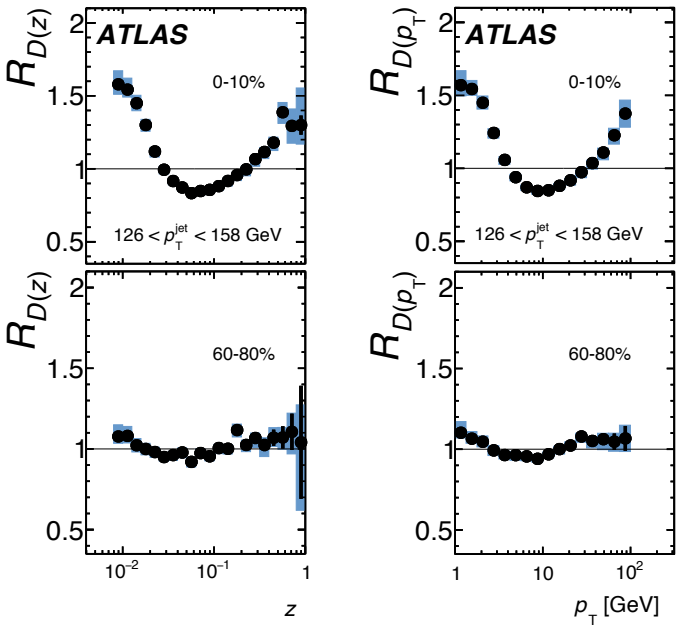

Figure 2.6: The modifications to the (left) $D(z)$ and (right) $D(p_{\mathrm{T}})$ distributions in (top) 0–10% central and (bottom) peripheral Pb+Pb compared to pp as a function of charged-particle z and p_{T} respectively. The error bars represent statistical uncertainties while the shaded boxes represent systematic uncertainties. Figures taken from Ref. [151].

where $p_{\mathrm{T}\,\mathrm{min}} = 1$ GeV and $p_{\mathrm{T}\,\mathrm{max}} = 4.2$ GeV.

The N_{ch} distributions can be seen in Figure 2.7. It can be clearly seen that the size of the enhancement in pp compared to pp at low p_{T} increases as a function of $p_{\mathrm{T}}^{\mathrm{jet}}$, growing from about 1.5 to 2.5 extra particles in the most central Pb+Pb collisions. This excess is even seen in the peripheral Pb+Pb collisions, though it is a lot smaller and ranges from 0.2 to 0.5 extra particles.

The modifications to the $D(z)$ distributions have also been compared to a variety of models, including the Effective Quenching model [153], the Soft Collinear Effective Theory [154, 155], and the Hybrid Model [156]. These comparisons are shown in Figure 2.8, and are discussed in detail in Chapter 3.

2.5 Jet Profile

This section will discuss the momentum profile of the jet as measured by the CMS detector for Pb+Pb collisions at $\sqrt{s_{\mathrm{NN}}} = 5.02$ TeV [157]. This can be considered to be an extension to a fragmentation function measurement in that it provides information about the momentum distribution of charged particles not only within the jet boundary, but also outside. The jet profile is defined as the distribution of particle yields in an annulus of width Δr and is given as:

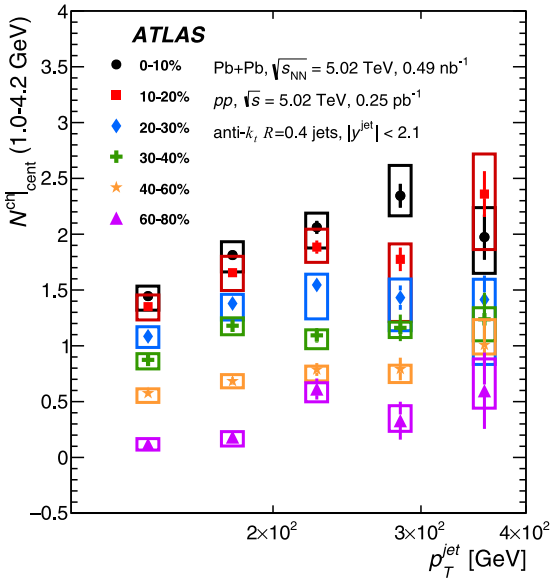

Figure 2.7: The number of extra particles that carry $1 < p_{\mathrm{T}} < 4$ GeV in Pb+Pb compared to pp. The different colors represent different centrality selections. The error bars represent statistical uncertainties while the shaded boxes represent systematic uncertainties. Figure from Ref. [151].

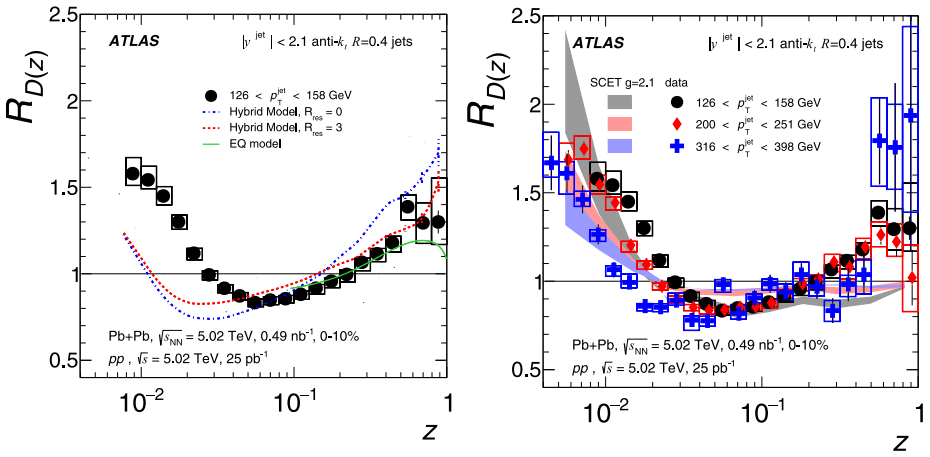

Figure 2.8: The $R_{D(z)}$ distributions compared to the EQ and Hybrid models (left) and SCET (right). The error bars represent statistical uncertainties while the shaded boxes represent systematic uncertainties. Figure taken from Ref. [151].

$$P(\Delta r) = \frac{1}{\delta r}\frac{1}{N_{\text{jet}}}\sum_{\text{jets}}\sum_{\text{tracks}\in(\Delta r_a,\Delta r_b)} p_{\text{T}}^{\text{trk}} \tag{2.7}$$

where Δr_a and Δr_b are the edges of the annulus at ΔR, and $\delta r = \Delta r_b - \Delta r_a$.

The jet profile for pp, Pb+Pb, and the modification to the jet shape variable are shown in Figure 2.9. It can be seen from the bottom panels that there is an excess of low p_{T} particles in Pb+Pb compared to pp at intermediate and large distances from the jet axis. This enhancement is compensated by a depletion of high p_{T} particles ($p_{\text{T}} > 4$ GeV) at all angles. In particular, the depletion in particle yields in 0–10% central Pb+Pb is up to almost half the particle yields in pp for $\Delta r > 0.4$. The modifications be described in terms of jet quenching, coupled with effects from the wake the jet as it propagates through the QGP. This wake can cause an enhancement in the low p_{T} yield of particles that is most easily seen at large angles.

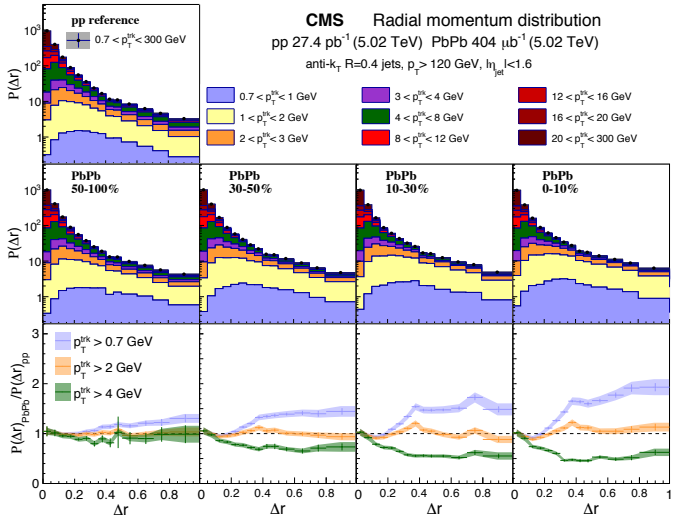

Figure 2.9: The jet profile in pp (top) and Pb+Pb (middle) as a function of distance from the jet axis. The different panels in the middle give the jet shape distribution for different centrality intervals. The modifications to the jet shape are shown at the bottom, with each panel corresponding to a different centrality. Figure from Ref. [157].

Chapter 3

JET ENERGY LOSS MODELS

While there are a number of different observables that can be measured in heavy ion collisions, the underlying goal of these measurements is to characterize the QGP. This makes jet energy loss models that combine dynamics of the jet as well as the QGP invaluable. Since different jet measurements come with their own set of measurement biases and have different sensitivities, it is vital that any viable model be able to describe a variety of observables. Models can also help guide experimentalists in their searches and suggest new directions of exploration. Measurements can then be done to constrain such models, helping further describe the jet-QGP interaction.

This chapter specifically discusses three different models: the Jet Fluid model, the Hybrid Model, and the Effective Quenching model. These were chosen because they have been used to describe a wide variety of observables including the jet R_{AA}, jet fragmentation, and the jet shape. In particular, the Jet Fluid model and Hybrid model incorporate a rigorous description of the interactions between the jet and the QGP and describe the radial dependence of the modification of charged particles in a jet, the central topic of this thesis. The Effective Quenching model is more phenomenological and shows agreement with measured data using only an intuitive functional form for energy loss.

3.1 Jet Fluid model

This discussion is based on the model introduced in Ref. [158]. This model considers the evolution of the jet and QGP in a coupled manner, considering the energy and transverse momentum exchange between them. In this picture, both the jet and medium are allowed to modify each other; the jet is modified via collisional and radiative processes while the medium evolves hydrodynamically and is modified because it picks up the

energy lost by the jet.

The time evolution of the jet is given by a set of coupled transport equations that describe the energy and transverse momentum distributions of the partons within the jet. These are given as

$$f_i(\omega_i, k^2_{\mathrm{T}i}, t) = \frac{dN_i(\omega_i k^2_{\mathrm{T}i}, t)}{d\omega_i dk^2_{\mathrm{T}i}} \tag{3.1}$$

$$\frac{df_j}{dt} = \hat{e_j}\frac{\partial f_j}{\partial \omega_j} + \frac{1}{4}\hat{q}_j \nabla^2_{k_{\mathrm{T}}} f_j + \sum_i \int d\omega_i dk^2_{\mathrm{T}i} \frac{d\widetilde{\Gamma}_{i\to j}}{d\omega_j dk^2_{\mathrm{T}j} dt} f_i - \sum_i \int d\omega_i dk^2_{\mathrm{T}i} \frac{d\widetilde{\Gamma}_{j\to i}}{d\omega_i j dk^2_{\mathrm{T}i} dt} f_i \tag{3.2}$$

where i is the type of parton, ω_i is its energy, and k^2_{T} is its transverse momentum with respect to the jet axis. The first term in Equation 3.2 is the collisional energy loss, the second term is the transverse momentum broadening, and the last two terms are the medium induced gain and loss radiative processes respectively. The splitting processes are are given by:

$$\frac{d\Gamma_{i\to j}}{d\omega_j dk^2_{\mathrm{T}j} dt} = \frac{2\alpha_S}{\pi}\hat{q}_g \frac{xP_{i\to j}(x)}{\omega_j k^4_{\mathrm{T}j}} \sin^2\left(\frac{t-t_i}{2\tau_f}\right) \tag{3.3}$$

where $P_{i\to j}$ is the vacuum splitting function for $i \to j$ with ω_j being the energy of the radiated parton, τ_f is the formation time of the radiated parton, and $k_{\mathrm{T}j}$ is the transverse momentum of the radiated parton with respect to the parent parton. These transport Equations 3.2 can be solved numerically and agree with R_{AA} measurements [148, 149, 159]. The effects of the medium are included by considering the energy-momentum conservation of the jet-QGP system $\partial_\mu[T^{\mu\nu}_{\mathrm{QGP}} + T^{\mu\nu}_{\mathrm{jet}}] = 0$. Then the source term $J^\nu(x)$ that describes the energy transfer between the jet and the medium can be defined as $J^\nu(x) \equiv -\partial_\mu T^{\mu\nu}_{\mathrm{jet}}$, making the QGP evolution being given by

$$\partial_\mu T^{\mu\nu}_{\mathrm{QGP}} = j^\nu \tag{3.4}$$

which characterizes the energy-momentum transfer between the jet and the QGP.

An important component of this model is the flow induced by jets. This can be seen in Figure 3.1, where the evolution of the energy density of the medium can be seen in a sample event. A single jet travels through the QGP, and can be clearly seen in the lower panels after the energy of the medium has been subtracted

out. The "V" shaped feature seen is the mach cone that is induced by the parton as it moves faster than the medium sound velocity.

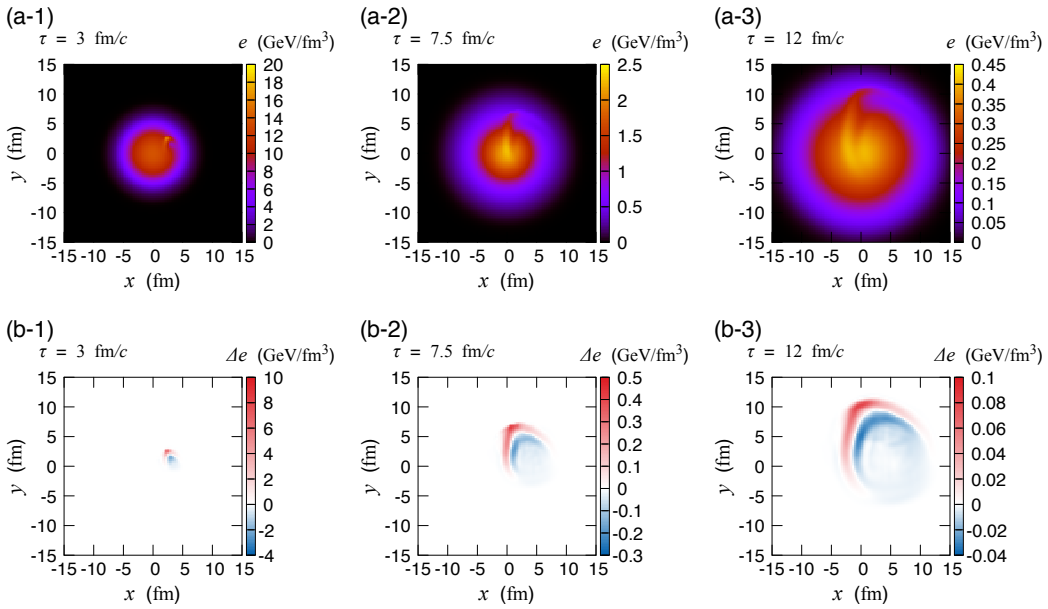

Figure 3.1: (Top) The time evolution of the energy density of the quark gluon plasma with a jet propagating through it. (Bottom) The time evolution of the energy density in the event after the energy density of the QGP has been subtracted out. Figure from Ref. [158].

The final jet energy has two components: the jet shower, and the hydrodynamic response. The former as discussed above comprises of the collisional energy loss, momentum broadening, and medium induced radiation. The latter includes the energy lost from the jet shower that thermalizes into the medium and induces conical flow, some of which is still in the jet cone. This compensates some of the energy lost in the shower and can be seen in Figure 3.2. While the absolute amount of energy lost increases as a function of initial jet energy, the fractional energy loss decreases. Furthermore there is a cone size dependence once the hydrodynamic contributions are included. This is a result of the jet being highly collimated, such that while an increase in the size does not change the energy much, it does affect the hydrodynamic contribution from the medium.

The R_{AA} distributions constructed with this model and compared to data from CMS [149] are shown in Figure 3.3. Including the hydrodynamic contribution decreases the energy loss, hence increasing the R_{AA} value and inducing a cone size dependence to the R_{AA}.

The internal structure of the jet can be described using the jet shape variable, defined as a per-jet quantity as:

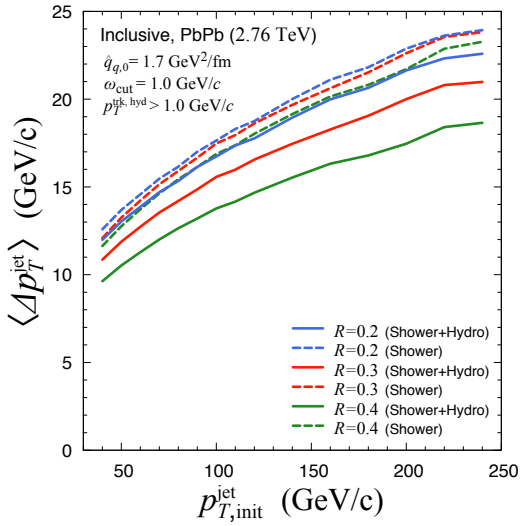

Figure 3.2: (Top) The energy lost by a jets of different radii as a function of their initial energy in central Pb+Pb collisions at $\sqrt{s_{NN}}$= 2.76 TeV. Figure from Ref. [158].

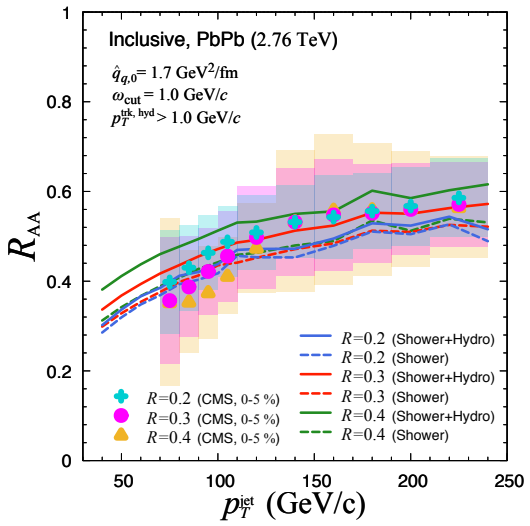

Figure 3.3: The jet R_{AA} measured by CMS [149] and compared to the Jet-Fluid model with and without the hydro dynamic contribution. Figure from Ref. [158].

$$\rho_{\text{jet}} = \frac{1}{N_{\text{jet}}} \sum_{\text{jet}} \left[\frac{1}{p_{\text{T}}^{\text{jet}}} \frac{\sum_{\text{trk}} p_{\text{T}}^{\text{ch}}}{\delta r} \right] \tag{3.5}$$

where the sum is over all jets and for all tracks around a jet in an annulus with mean radius r from the jet axis. The modification in the jet structure then can be defined as $R_{\text{AA}}^{\rho} = \rho_{\text{AA}}(r)/\rho_{\text{pp}}(r)$. A comparison of the jet shape variable ρ and its modification R_{AA}^{ρ} to data measured by CMS is seen in Figure 3.4. The shower and hydro contributions are shown individually. These indicate that the shower contribution to the jet shape variable is falls steeply as a function of distance from the jet axis while the hydro contribution is fairly constant at large distances. This is because the energy loss from the shower is carried away by the jet induced flow to large angles. The R_{AA}^{ρ} distribution further shows that the core is largely unmodified while the outer part of the jet is broadened. The hydro-contribution mainly has an effect at larger distances from the jet axis. This is consistent with the cone-size dependence seen in Figure 3.2.

This model is particularly useful because it identifies both the effect of the medium on the jet, as well as the effect of the jet on the medium.

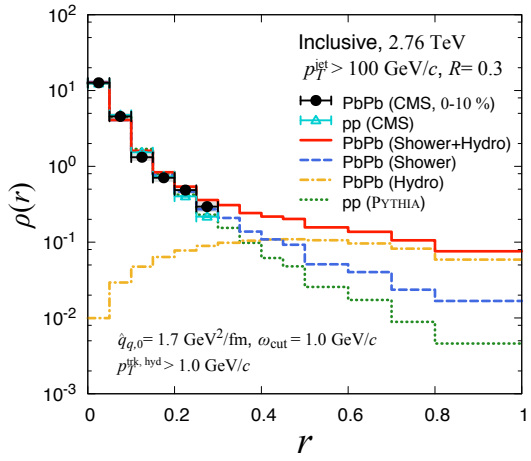

(a) The jet shape as measured by CMS for pp and central Pb+Pb collisions [160] compared to the Jet Fluid model. The shower (blue) and hydro (orange) contributions to the jet shape are highlighted.

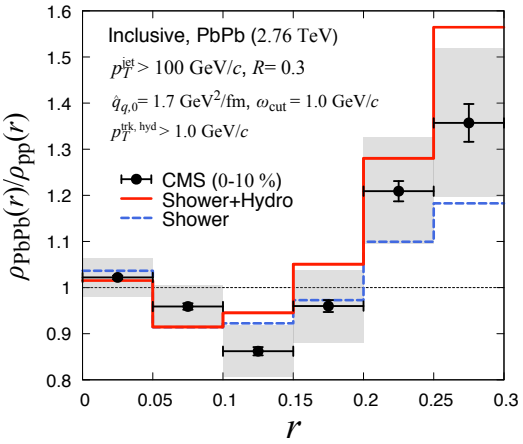

(b) The modification of the jet shape between pp and Pb+Pb as measured by CMS [160] and compared to the Jet Fluid model. The dashed line shows the modeled modification without the hydro-contribution.

Figure 3.4: CMS data fit to calculations from the Jet Fluid model. Figures from Ref. [158].

3.2 Hybrid Model

This discussion is based on the work in Refs. [156, 161, 162] and describes jet quenching using a hybrid strong/weak model. It uses perturbative QCD to describe the weakly coupled hard process of jet production and holographic calculations of the energy loss of energetic probes to model the strong coupling between the probe and the plasma [163, 164]. In this model, the jet evolves in space time with the lifetime of the parton in the shower being given by [165].

$$\tau = 2\frac{E}{Q^2} \tag{3.6}$$

where Q is its virtuality and E its energy. This evolution is unaffected before the proper time at which the plasma hydrodynamizes, $\tau_{\text{hydro}} = 0.6$ fm. After this time, the jet-plasma interaction comes into play and the fragments evolve with the energy loss as:

$$\frac{1}{E_{\text{in}}}\frac{dE}{dx} = -\frac{4}{\pi}\frac{x^2}{x_{\text{stop}}^2}\frac{1}{\sqrt{x_{\text{stop}}^2 - x^2}} \tag{3.7}$$

where E_{in} is the initial energy of the parton prior to any quenching and x_{stop} is its stopping distance (jet thermalization distance). The stopping distance can be written as:

$$x_{\text{stop}} = \frac{1}{2\kappa_{\text{sc}}} \frac{E_{\text{in}}^{1/3}}{T^{4/3}} \tag{3.8}$$

where κ_{sc} is a dimensionless free parameter associated to the strong coupling and is used to fit to the data.

The energy loss is characterized by the strong x^2 dependence for $x \ll x_{\text{stop}}$. Furthermore, when x is comparable to x_{stop}, dE/dx depends nontrivially on E_{in} and x, diverging for $x \to x_{\text{stop}}$ and $E \to 0$. The shower is then embedded into a hydrodynamic description of the QGP from Ref. [166], and the energy loss expressions are integrated for each parton, from the time it is produced to the time that it splits. The splitting probabilities are taken to be independent of the medium, depending only on the initial energy of the daughter partons. These further lose energy as they propagate through the QGP and split. Then the total energy lost by a parton is dependent on the history of splitting and propagation of its parents, grandparents and so on and so forth. The partons further experience kicks transverse to their direction of motion, a phenomena called transverse momentum broadening. This effect is mainly experienced by softer partons that are much more affected by the angular narrowing effects of energy loss, making most measured observables insensitive to the size of this kick. This is directly related to wider jets losing more energy than narrower ones. The wake left in the medium from the partons depositing momentum in the QGP as they propagate through it lends a non-trivial impact to the model predictions. It is a vital part of any model since the contribution from the wake is impossible to separate experimentally. This wake results in a perturbation to the hydrodynamic background resulting in corrections to the final state hadron spectra, making it particularly important for jet substructure observables like jet fragmentation and jet shapes [162].

A screening effect recently included in the hybrid model is based considering the resolving power of the QGP [161]. As depicted in Figure 3.5, the QGP will only resolve daughter partons of a splitting after they are separated by a certain distance L_{res}. It is only after they are resolved that they will be allowed them to lose energy independent of each other. This delayed quenching results in an enhancement of softer partons at larger angles from the jet axis compared to the case where the daughter partons are resolved immediately after they split from the parent parton. The L_{res} parameter has the constraint $1/(\pi T) < L_{\text{res}} < 2/(p_{\text{T}} T$ based on the Debye screening length for the plasma.

The free parameter κ_{sc} is determined by fitting to jet R_{AA} data from CMS [149] as shown in Figure 3.6. It can be seen that including the L_{res} parameter does not really affect the jet R_{AA} prediction. The dependence

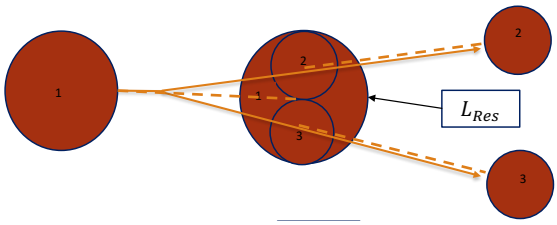

Figure 3.5: A schematic illustrating the resolving power of the QGP. The daughter partons 2 and 3 that come from 1 need to be separated by L_{res} before they are treated individually by the plasma. Prior to that separation, they are treated as one effective parton. Figure from Ref. [161].

of the R_{AA} on the size of the jet radius can be seen. This is consistent with the expectation that wider jets lose more energy.

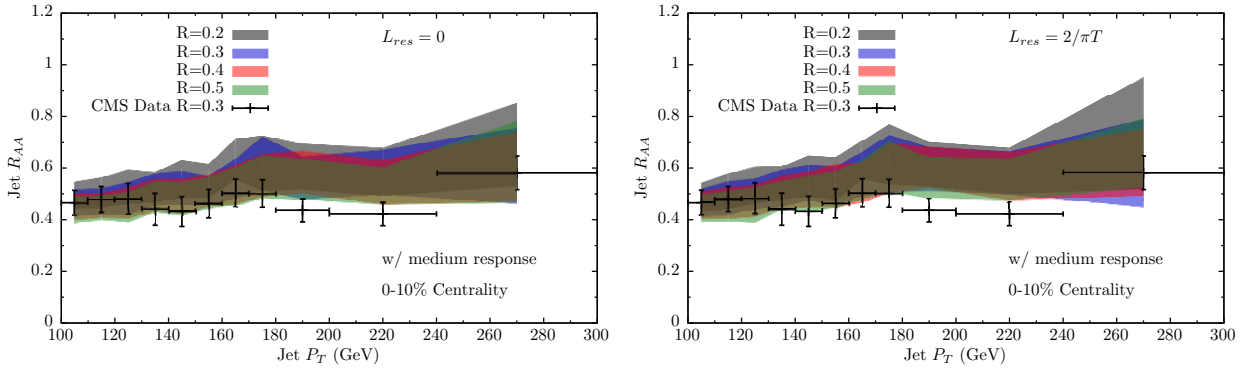

Figure 3.6: The hybrid model without (left) and with (right) the L_{res} parameter, compared to the jet R_{AA} as a function of jet p_{T} in two centrality intervals as measured in Ref. [149]. The different colors correspond to different jet radii. The Hybrid Model is fit to the 100–110 GeV point from the data, giving rise to the colored bands. Figures from Ref. [161].

Fixing the κ_{sc} parameter allows for predictions of other jet measurements like jet fragmentation and jet shape. Figures 3.7a and 3.7b show a comparison of the measured and modeled values of the modifications to the jet fragmentation and jet shape respectively. The model has also been compared to measurements done by ATLAS, ALICE, and STAR [159, 167, 168]

Here it can be seen that adding a medium response and a non-zero L_{res} parameter affects the prediction. While the hard fragments (see Figure 3.7a) are unaffected by the medium response, including the soft particles from the wake compensates some of the suppression of soft fragments in Pb+Pb compared to *pp* collisions. Moreover, including the L_{res} parameter further compensates the suppression for soft fragments, while reducing the enhancement of the hard fragments. This is a result of allowing more hadrons carrying a smaller fraction of the jet energy (low z, high $(\ln(1/z))$ to survive into the final state. The jet shape observable (see Figure 3.7b) quantifies the radial distribution of energy in terms of annuli around the jet

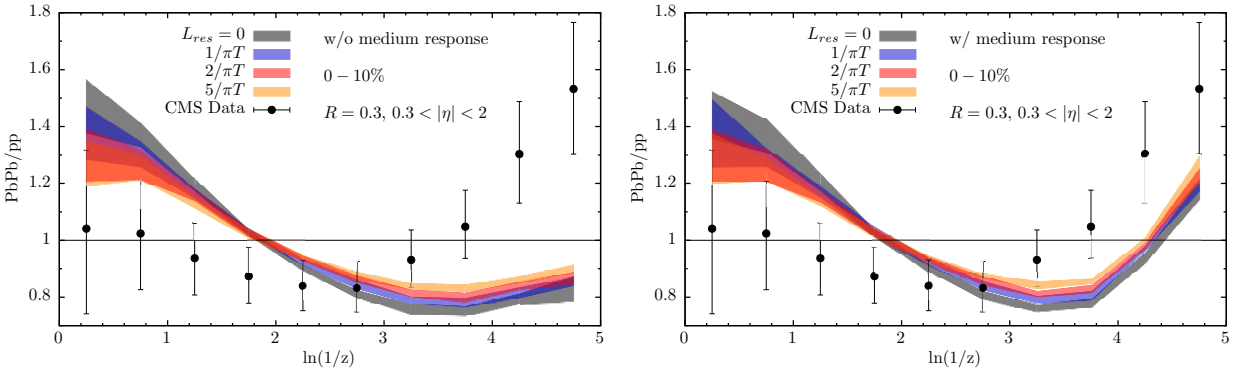

(a) The modification to the jet fragmentation from *pp* to Pb+Pb as a function of $\ln(1/z)$ as measured in Ref. [169] compared to the predictions of the hybrid model. The predictions are shown without (left) and with (right) the effect of the wake from the QGP responding to the jet. The different colors correspond to different L_{res} parameters. Figure taken from Ref. [161].

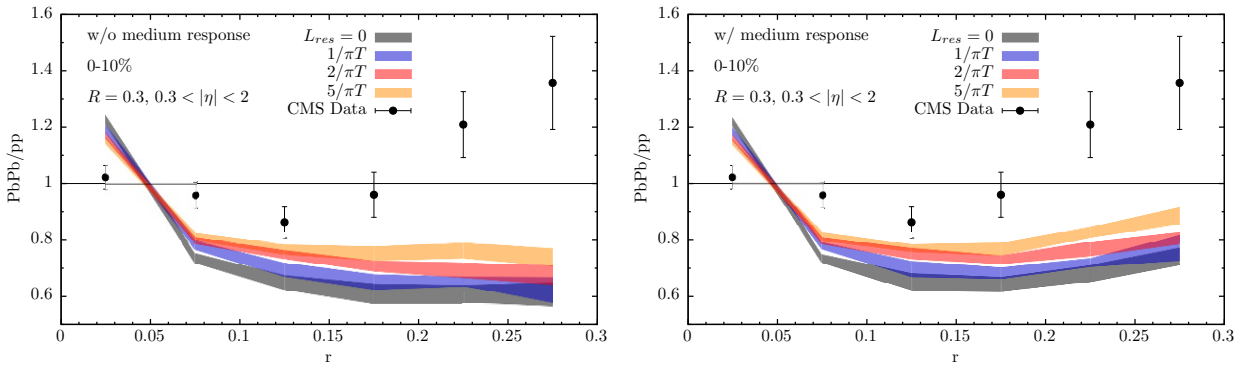

(b) The modification to the jet shape from *pp* to Pb+Pb as a function of r as measured in Ref. [160] compared to the predictions of the hybrid model. The predictions are shown without (left) and with (right) the effect of the wake from the QGP responding to the jet. The different colors correspond to different L_{res} parameters. Figure taken from Ref. [161].

Figure 3.7: A comparison of measured data, MC, and the analytic calculation of the EQ model. Figures from Ref. [153].

axis. It can be seen that introducing the L_{res} parameter enhances the probability to find final state hadrons at larger distances from the jet axis. The jet core ($r < 0.05$) is also affected, with the depletion only slowly evolving with an increasing L_{res}. One must be careful before making conclusions though, since these modifications are made between jets that are quenched (in Pb+Pb) and unquenched (in pp). Taking into account the fact that wider jets lose more energy and that the jet spectrum rapidly falls off, there is a bias for finding narrower quenched jets than unquenched jets. This makes the jet shape after quenching narrower in Pb+Pb compared to pp. While the model is not fully able to capture the features in the data, including the medium response moves it in the correct direction. It can be suggested that the model is missing a description of the medium induced modification to the hadronization process or that the wakes in the plasma are not equilibrating.

3.3 Effective Quenching

This discussion is based on the model introduced in Ref. [153]. This phenomenological model emphasizes the jet p_{T} dependence of the quark to gluon fraction and the difference between quark-jet and gluon-jet quenching. It uses an "extended" power law parameterization of the high-p_{T} hadron spectra coupled with a quenching that is based on a jet p_{T} dependent fractional energy loss. This model considers the different color charges carried by quarks and gluons and their different splitting functions, and assumes that gluon jets lose energy at a rate 9/4 times higher than quark jets. The key assumption of the model are:

- The energy lost by a jet is radiated at large angles and does not appear within the jet cone. This is backed by [146].
- The fragmentation pattern of the jet is unaffected by the presence of the QGP i.e. they fragment as they would in a vacuum. This is motivated by the idea that the QGP is unable to resolve the internal jet structure and is supported by [170, 171].

The model uses the following extended power-law parameterization to describe the high-p_{T} jet spectra:

$$\frac{dn}{dp_{\text{T}}^{\text{jet}}} = A\left(\frac{p_{\text{T}0}}{p_{\text{T}}^{\text{jet}}}\right)^{n+\beta\log(p_{\text{T}}^{\text{jet}}/p_{\text{T}0})} \tag{3.9}$$

where $p_{\text{T}0}$ is a reference transverse momentum at which $A = dn/dp_{\text{T}}^{\text{jet}}$, β is the logarithmic derivative of $dn/dp_{\text{T}}^{\text{jet}}$ at $p_{\text{T}}^{\text{jet}} = p_{\text{T}0}$. Then the combined spectrum from quarks and gluons can be written in terms of

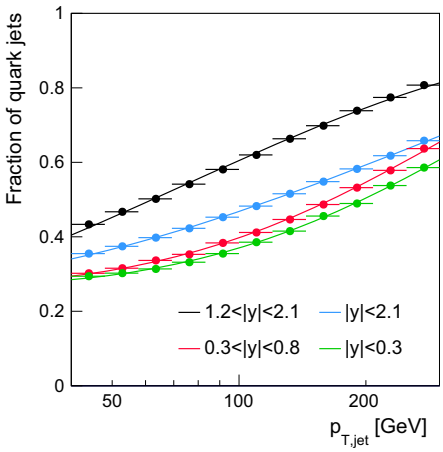

(a) The jet quark fraction as a function of $p_{\mathrm{T}}^{\mathrm{jet}}$ in different rapidity bins. The points are from PYTHIA8 simulations and the lines are fits to the spectra determined using Equation 3.9.

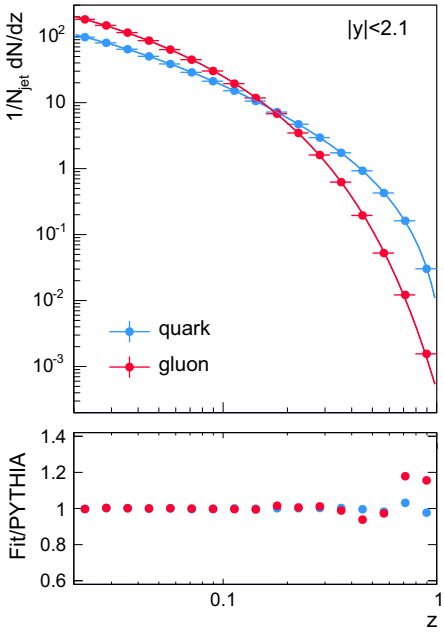

(b) A comparison of the quark and gluon fragmentation. The points are from PYTHIA8 simulations and the lines are fits to those points using Equation 3.10.

Figure 3.8: Fits to quark fractions and fragmentation functions from PYTHIA8. Figures from Ref. [153].

Equation 3.9 with weighted contributions from the different quark and gluon fractions, f_{q0} and $f_{g0} = 1 - f_{q0}$ respectively.

The p_{T} dependence of the quark fraction along with the fit is shown in Figure 3.8a. The fragmentation functions can also be determined using final-state charged hadrons within a $R = 0.4$ jet cone. These are fit to the form $D(z)$, with fits for the quark and gluon fragmentation shown in Figure 3.8b.

$$D(z) = a \times \frac{(1+dz)^b}{(1+ez)^c} \times e^{-fz} \tag{3.10}$$

For the quenched spectra, this model assumes a non-constant fractional shift given below as S. This approach is based on [172] and is used because of the inability of the constant fractional shift to explain the jet p_{T} dependence of measured R_{AA}.

$$S = s' \left(\frac{p_{\mathrm{T}}^{\mathrm{jet}}}{p_{\mathrm{T}0}} \right)^{\alpha} \tag{3.11}$$

where α is an undetermined parameter and s' is the shift for a jet with $p_{\mathrm{T}}^{\mathrm{jet}} = p_{\mathrm{T}0}$. The fractional shift can

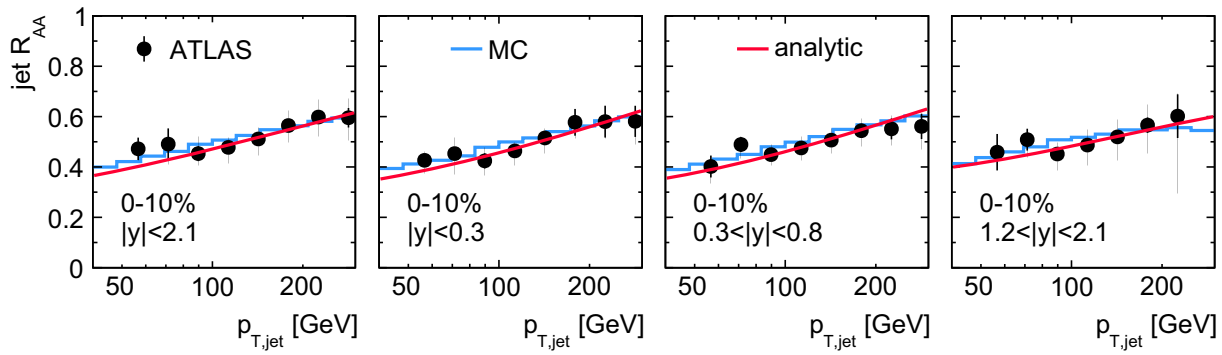

(a) A comparison of the R_{AA} as measured by ATLAS for central Pb+Pb collisions in [148], a MC calculation (blue) and the analytic calculation (red) in the EQ model with the extended power-law parameterization and a non-constant fractional energy loss. The different panels are different rapidity intervals.

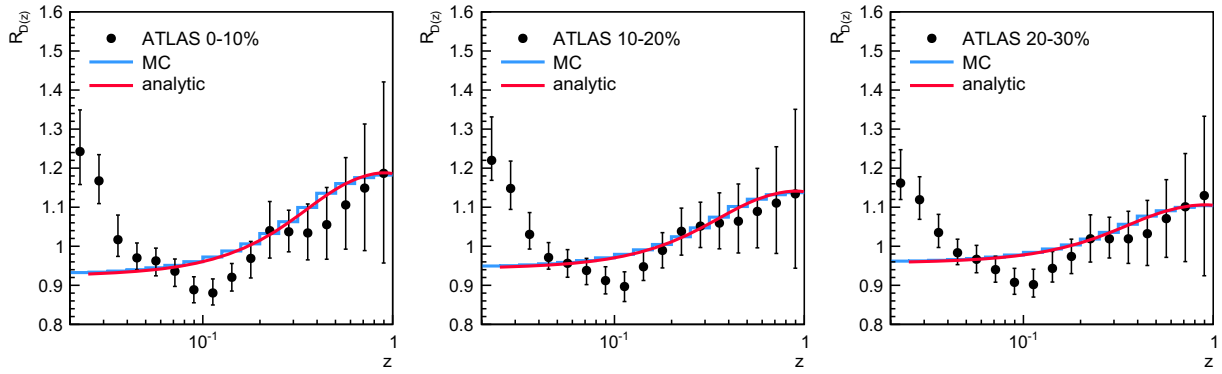

(b) A comparison of the $R_{D(z)}$ as measured by ATLAS in [173], a MC calculation (blue) and the analytic calculation (red) in the EQ model with the extended power-law parameterization and a non-constant fractional energy loss. The different panels are different centrality intervals.

Figure 3.9: A comparison of measured data, MC, and the analytic calculation of the EQ model. Figures from Ref. [153].

be coupled with Equation 3.9 and the quark and gluon fractions to give a functional form of the quenched high-p_{T} hadron spectra for quarks and gluons. This can be further used to construct a jet R_{AA} that is fit to data and is shown in Figure 3.9a. It can be seen that the analytic fits and the MC are in good agreement. While the fits agree with the data by definition, the robustness of the model can be seen in that it describes the data with a single value for α and a simple centrality dependent shift constant s'.

Fits to the $D(z)$ distributions are shown in Figure 3.9b and it can be seen that while the MC and analytic calculation agree well with each other, they are only able to qualitatively capture some features of the data. The enhancement at high z can be explained by an increased quark content of the jet spectrum and subsequent differential quenching for quark and gluon jets. The low z enhancement on the other hand can be considered to be a result of a gluon radiation within the jet or a wake from the medium itself.

Chapter 4

EXPERIMENTAL SETUP

4.1 The Large Hadron Collider

The Large Hadron Collider (LHC) is a part of the European Organization for Nuclear Research (CERN). It has a circumference of 27 kilometers, making it the world's largest particle accelerator, and is housed in a tunnel that is up to 175 meters below the surface of the earth. The LHC ring has eight arcs and eight straight sections, with each straight section being approximately 528 m long. Four of the straight sections are where the major detectors are located, while the other four are used for machine utilities, radio frequency, collimation and beam dumps. The arc sections are built using 1232 dipole superconducting magnets, providing a magnetic field of up to 8.33 T. Another 392 quadrupole magnets are used for focussing the particle beam. Sixteen radio frequency (RF) cavities that provide a voltage of 2 MV and operate at 400 MHz are used to accelerate the proton or ion beams that are kept in their circular path by the dipole magnets. The magnets are cooled down to 1.9 K via liquid Helium.

The LHC beam pipe has two rings with the counter-rotating beams and uses a uses a twin-bore magnet design that optimizes for both cost, as well as space. The counterrotating beams require opposite magnetic dipole fields in both rings, with separate magnetic and vacuum chambers, with the common sections only at the insertion regions and where the major experimental detectors are located. These detectors are: A Toroidal LHC Apparatus (ATLAS), Compact Muon Solenoid (CMS), A Large Ion Collider Experiment (ALICE), and Large Hadron Collider - Beauty (LHCb) [174].

Studying the rare events that the LHC was designed for requires high beam energies and intensities, and the LHC is capable of reaching up to center of mass energies, $\sqrt{s} = 14$ TeV for protons and $\sqrt{s_{\rm NN}} = 5.5$ TeV for lead ions. The LHC delivers up to $10^{34}\text{cm}^2\text{s}^1$ of luminosity to the ATLAS and CMS detectors when

colliding protons. The LHCb detector is a lower luminosity experiment, that receives up to $10^{32}\text{cm}^2\text{s}^1$, and ALICE, a dedicated ion experiment aims at a peak luminosity of $10^{27}\text{cm}^2\text{s}^1$ for nominal lead-lead operation. In 2015, the LHC delivered an integrated luminosity of 0.49 pb^{-1} of Pb+Pb and 25 pb^{-1} of pp data.

A schematic of the entire accelerator complex and the path followed by protons and heavy ions is show in Figure 4.1. The protons in the LHC are obtained by stripping a hydrogen atom of its electrons with an electric field. They are then supplied to the LHC via the Linac2 - Proton Synchrotron Booster - Proton Synchrotron - Super Proton Synchrotron chain. The complete ionization of lead on the other hand is done in multiple stages, with the first stage in Linac3, which provides Pb^{+29} via an ion source. The Pb^{+29} lead ions are further stripped of electrons by passing them through a 0.3 μm foil. The Pb^{+54} ions are selected via mass spectrometer and sent to the Low Energy Ion Ring (LEIR), followed by the Proton Synchrotron and Super Proton Synchrotron, and then finally the LHC. The final stripping of lead ions takes place after the PS, on a 0.8 mm thin aluminum foil.

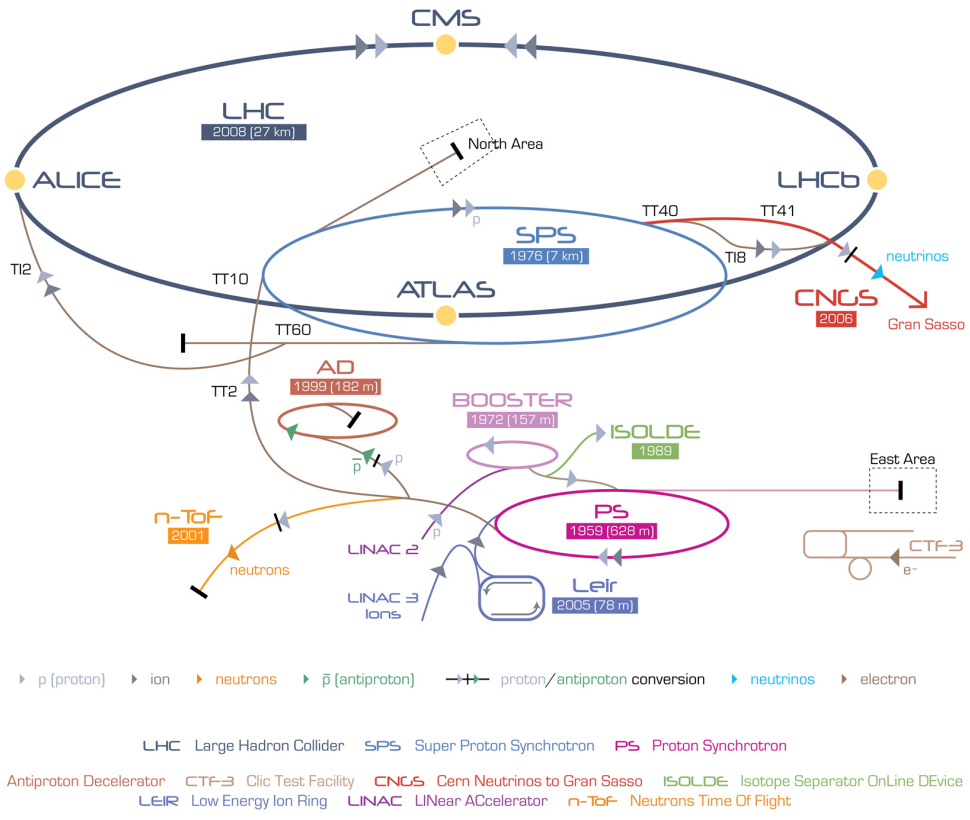

Figure 4.1: The accelerator complex at CERN. ATLAS can be seen inside the SPS on the LHC ring. Figure from Ref. [175].

4.2 The ATLAS Detector

The ATLAS detector (Figure 4.2) is a general purpose detector at the LHC. It uses a right-handed coordinate system with its origin at the nominal interaction point (IP) in the centre of the detector and the z-axis along the beam pipe. The x-axis points from the IP to the centre of the LHC ring, and the y axis points upward. Cylindrical coordinates (r, ϕ) are used in the transverse plane, ϕ being the azimuthal angle around the beam pipe. The pseudorapidity is defined in terms of the polar angle θ as $\eta = -\ln\tan(\theta/2)$. The detector is symmetric in the forward-backward direction, with the positive z direction being the A side, and the negative z direction being the C side. It has full 2π coverage in azimuth. The transverse momentum p_{T}, the transverse energy E_{T}, and the missing transverse energy $E_{\mathrm{T}}^{\mathrm{miss}}$ are defined in the $x-y$ plane unless stated otherwise. The distance ΔR in the pseudorapidity-azimuthal angle space is defined as $\Delta R = \sqrt{\Delta\eta^2 + \Delta\phi^2}$.

The detector was designed keeping in mind the goals of the physics it aimed to explore, and as such has the following characteristics:

- Fast, radiation-hard electronics and sensor
- Fine granularity to be able to manage large particle fluxes
- Large acceptance in pseudorapidity and full azimuthal coverage
- Good electromagnetic calorimetry for photon and electron identification
- Good hadron calorimetry for accurate jet and missing transverse energy measurements
- Good muon identification and momentum resolution
- Highly efficient trigger system

These design goals are achieved with the main subsystems: the inner detector, the calorimeter, the muon spectrometer, and the trigger system. The main analysis discussed in this thesis uses the inner detector, calorimeter, and the trigger system. The muon system is described for completeness.

4.2.1 Inner Detector

The inner detector shown in Figure. 4.3 is designed to reconstruct the charged particle trajectories for particles with momenta down to 0.5 GeV in the interval $|\eta| < 2.5$. It is immersed in a 2T magnetic field from the central solenoid that covers a region of 5.3 m long and has a diameter of 2.5 m. The inner detector has capabilities for pattern recognition, momentum and vertex measurements, and electron identification.

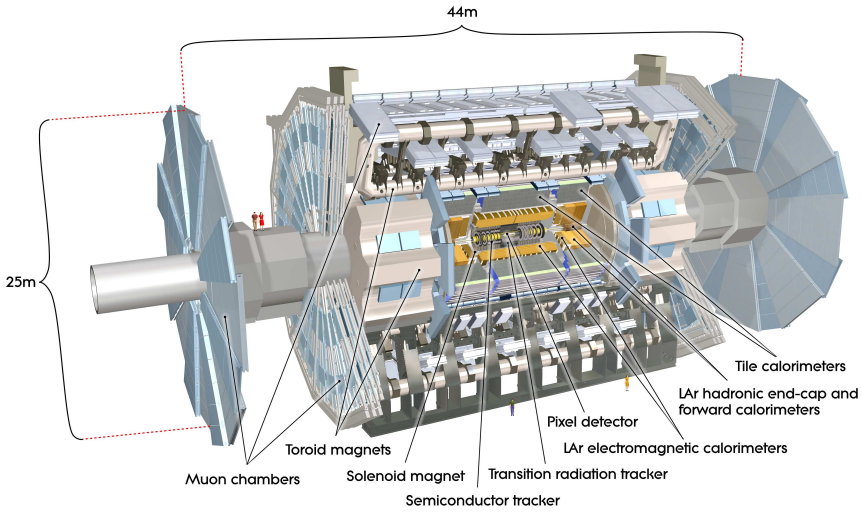

Figure 4.2: The ATLAS detector. Figure from Ref. [176].

These measurements are made using the inner pixel detector, the semi-conductor tracker (SCT), and the transition radiation tracker (TRT).

Pixel system: This system is segmented in $R-\phi$and comprises of four pixel layers : the innermost insertable B layer (IBL) and three identical silicon pixel detectors. The IBL was added to the ATLAS detector during the first long shutdown of the LHC in 2013-2014. It consists of 14 carbon fiber staves, 2 cm wide and 64 cm long, surrounding the beam pipe at a mean radius of 33 mm, and covering a pseudorapidity region of ± 3. Each stave consists of 26880 pixels in a matrix of 80 columns (50 μm pitch), by 336 rows (250 μm pitch) [177, 178]. The other three layers layers have a pixel size in $R-\phi \times z$ of $50 \times 400 \mu\text{m}^2$. The accuracies in the barrel region are $10\mu\text{m}^2$ $(R-\phi)$ and $115\mu\text{m}^2(z)$. The end cap regions have an accuracy of $10\mu\text{m}^2(R-\phi)$ and $115\mu\text{m}^2(R)$. The hit resolution ranges from $\sim$8 $(R-\phi)$ and $\sim$40μm) (z) for the innermost layer, to $\sim$10 μm $(R-\phi)$ and $\sim$115μm (z) for the next three layers [176]. The pixel detector has approximately 80.4 million readout channels.

Semi Conductor Tracker: This subsystem has a coverage that overlaps with the pixel layers, and is arranged in concentric cylinders around the beam axis, with the end caps being disks perpendicular to the beam axis. The SCT has eight strip (80 μm pitch) layers that are crossed by each track. Small angle stereo strips (40 mrad) are used to measure both coordinates, with one set of strips in each layer, parallel to the beam direction. The end cap region has nine layers of double sided modules with strips in the radial direction, with each also having a mean pitch of 80 μm. The intrinsic resolution is $\sim$17μm $(R-\phi)$ and $\sim$580μm (z). There are approximately 6.3 million readout channels from the SCT [176].

Transition Radiation Tracker: The TRT uses a combination of a xenon based gas and 4mm diameter straw tubes and provides for a large number of hits (up to 36) per track. It covers the region $|\eta| < 2.0$, and has a resolution of $\sim$130μm in $r - \phi$, with no information in the z direction. The barrel region of the TRT has straws that are 144 cm long and are parallel to the beam axis, with the wires divided into two halves at $\eta = 0$. The end-caps have 37 cm long straws in a radial configuration. The TRT has approximately 315,000 channels [176].

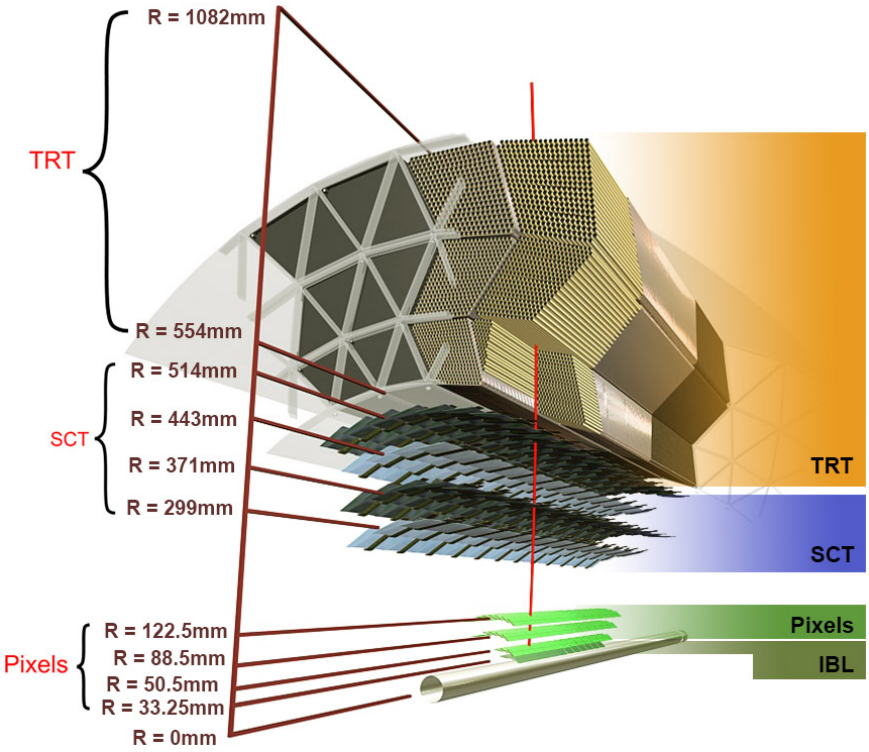

Figure 4.3: ATLAS Inner Detector System. Figure from Ref. [179].

4.2.2 Calorimeter

The calorimeter covers the range of $|\eta| < 4.9$ for using a variety of different techniques. The parameters are summarized in the table below. Over $|\eta| < 2.5$, where there is overlap with the inner detector, the highly granular electromagnetic calorimeter is used for precision measurements of electrons and photons. The rest of calorimeter has coarser granularity that is sufficient for jet reconstruction. The calorimeter contains the electromagnetic and hadronic showers, and limits the punch through to the muon system. The EMCal has a radiation depth greater than 22 radiation lengths in the barrel, and greater than 24 radiation lengths in the end caps. The approximately 10 interaction lengths in the barrel and end cap provide good resolution for high energy jets. The total thickness of the calorimeter is 11 interaction lengths at $\eta = 0$. The calorimeter

is divided into different subsystems, including the Liquid Argon Electromagnetic Calorimeter (LAr EMCal) and the Hadronic calorimeter (HCal).

LAr EMCal: The EMCal covers the region $|\eta| < 1.475$ and has two end caps ($1.375 < |\eta| < 3.2$). It also contains the central solenoid. The barrel calorimeter is divided into two half barrels, separated by 4mm at $z = 0$. Each end cap is divided into two coaxial wheels, with the inner one covering $2.5 < |\eta| < 3.2$ and the outer one covering $1.375 < |\eta| < 2.5$. The EMCal uses accordion shaped kapton electrodes and lead absorber plates that provide full azimuthal symmetry. The EMCal is subdivided into three sections in its depth over $|\eta| < 2.5$, the region used for precision physics. The $|\eta| < 1.8$ region also uses a pre-sampler detector that uses an active LAr layer to correct for energy lost upstream of the calorimeter. A main source of this loss is the central solenoid.

Hadronic Calorimeter: The hadronic calorimeter consists of the tile, LAr Hadronic end cap, and the LAr forward calorimeter. The tile covers the region $|\eta| < 1.0$, with its two barrels covering the range eta $0.8 < |\eta| < 1.7$. It uses steel as the absorber and scintillating tiles for the active material. The tile calorimeter extends radially from an inner radius of 2.28 m to 4.25 m. It has a three layer that are 1.5, 4.1, and 1.8 interaction lengths thick in the barrel region, and 1.5, 2.6, and 3.3 interaction lengths in the extended barrel region. The total detector thickness is 9.7 interaction lengths at $\eta = 0$.

The LAr hadronic end cap calorimeter (HEC) consists of two independent wheels per end cap, and is behind the EMCal end cap. It extends out from $1.5 < |\eta| < 3.2$, and overlaps with the forward calorimeter and the tile calorimeter. The HEC covers the radial region of 0.475 to 2.03 m.

The LAr Forward calorimeter (FCal) provides coverage over the $3.1 < |\eta| < 4.9$. It is approximately 10 interaction lengths deep, and has three modules, one of which is optimized for electromagnetic measurements, while the other two for hadronic measurements. Each module is made of concentric rods and tubes parallel to the beam axis.

A summary of the depth of the calorimeter in terms of the interaction lengths, as a function of pseudo-rapidity is shown in Figure 4.4.

4.2.3 Muon Spectrometer

The muon spectrometer is based on the magnetic deflection of muon tracks in the toroid magnets. The barrel toroid provides bending over the $|\eta| < 1.4$ range, and the end cap magnets provide bending in the $1.6 < |\eta < 2.7$ range. In the transition region ($1.4 < |\eta| < 1.6$), the magnetic deflection is from a combination of the barrel and end-cap fields. The barrel region has tracks that are measured in chambers in a cylindrical

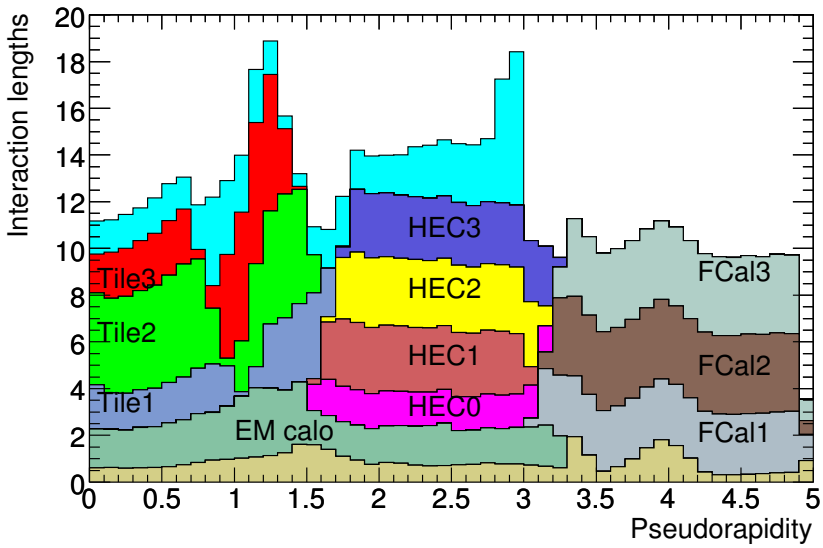

Figure 4.4: Cumulative material in the calorimeter system in units of hadronic interaction length as a function of $|\eta|$. Figure from Ref. [176].

configuration around the beam axis. The transition and end-cap have chambers perpendicular to the beam axis.

4.2.4 Other subsystems

Other major subsystems of the ATLAS detector include the Zero Degree Calorimeter (ZDC), the trigger system

ZDC: The zero degree calorimeter plays a key role in determining the centrality of heavy ion collisions. It consists of quartz rods and tungsten plates, and measures neutral particles at $|\eta| >= 8.2$. It is made of four modules, one electromagnetic, and three hadronic. The Modules are made of 11 tungsten plates that are perpendicular to the beam direction. Photomultiplier tubes are used to detect the Cherenkov radiation from particle showers.

Trigger System: The trigger and data acquisition system (TDAQ) have different subsystems that are associated with sub-detectors. There are three distinct levels: L1, L2, and the event filter. The latter two form the High Level Trigger (HLT) system. The L1 trigger uses custom electronics, while the HLT is software based. Each level uses information from the previous level to select events. The first level uses limited detector information and makes decisions based on muons, electron, photons, jets, and τ-leptons carrying a high transverse momentum. It is also capable of identifying large missing and total transverse

energy. It has a maximum acceptance rate of 75kHz and makes a decision in less that 2.5μs. This event rate is further reduced to 200 Hz by the HLT that uses the full granularity and precision of the inner detector, calorimeter and muon systems to select events.

4.3 Pileup and Centrality in ATLAS

A pileup event is an event in which there are multiple Pb+Pb interactions. The rate of such events is typically minimized in a heavy ion collision by increasing the crossing angle between the colliding beams. Pileup events are further rejected by identifying them using information from the tracking systems and by studying the correlation between the energy deposited in the ZDC and the FCal. In heavy ion collisions, all tracks in the tracking system are fit back to a single primary vertex with the fits that do not converge being rejected. Then events that have a track multiplicity corresponding to a single Pb+Pb interaction and an energy deposition in the calorimeter that is consistent with multiple Pb+Pb interactions are pileup events [180]. Pileup events are also identified using the anti-correlation between the number of participant and spectator nucleons in a heavy ion collision. Figure 4.5 shows the total energy in the ZDC normalized by the energy of a single neutron vs. the sum of transverse energy in the FCal, $\Sigma E_{\mathrm{T}}^{\mathrm{FCal}}$. The former comes from spectators of the collision, while the latter from the participants. Events in which the ZDC measures more neutrons than expected for a given energy in the FCal are then identified as pileup events.

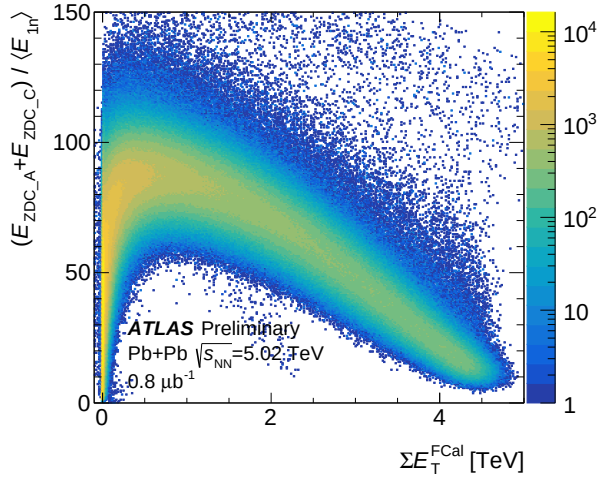

Figure 4.5: The correlation of the sum of energies in the ZDC arms vs. the sum of transverse energies in the FCal. Multiple Pb+Pb interactions in the same beam crossing with at least one of them being a central collision would deposit large amounts of energy in the FCal and the ZCD, and are seen as the grass near the top right of the figure. This is used to identify pileup events. Figure from Ref. [181].

Once pileup events have been identified and removed, the event centrality can be determined. This is

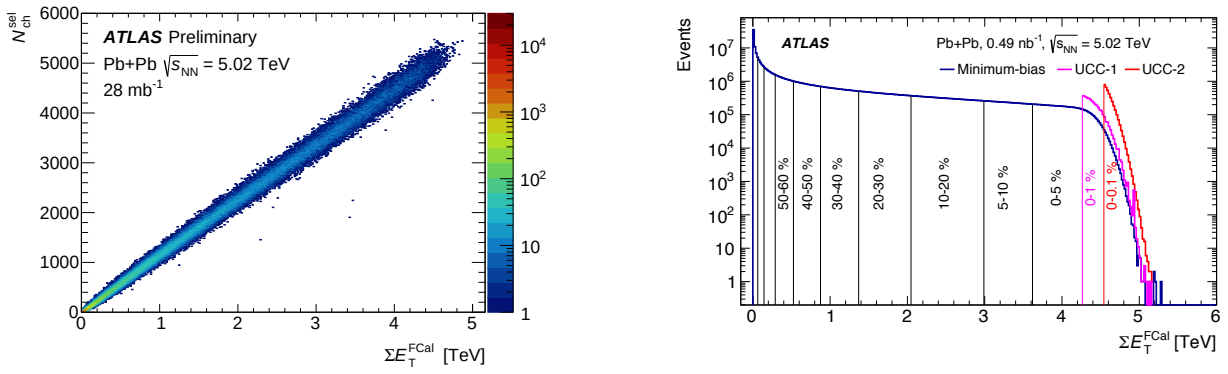

(a) (b)

Figure 4.6: (Left) Charged particle multiplicity $N_{\text{ch}}^{\text{sel}}$ versus the total transverse energy in the FCal, $\Sigma E_{\text{T}}^{\text{FCal}}$. Figure from Ref. [181]. (Right) The $\Sigma E_{\text{T}}^{\text{FCal}}$ distribution for events selected by the minimum bias trigger along with the centrality percentiles. Also shown are the number of events over the 0–1% and 0–0.1% centrality intervals selected by the ultra-central triggers. Figure from Ref. [59]. Both plots are for Pb+Pb collisions with $\sqrt{s_{\text{NN}}} = 5.02$ TeV.

done by coupling information from the Glauber Model with signals from the ZDC and FCal [59, 182]. The centrality of an event can be mapped to the charged particle multiplicity N_{ch} using the Glauber Model as was shown in Figure 1.15. It can also be seen from Figure 4.6a that the charged particle multiplicity is strongly correlated with $\Sigma E_{\text{T}}^{\text{FCal}}$. Then an MC Glauber simulation can be used to describe the distribution of transverse energy in the FCal, $\Sigma E_{\text{T}}^{\text{FCal}}$, shown in Figure 4.6b, and divide it into percentiles [183]. The 0–10% centrality corresponds to most central collisions with the maximum overlap between the colliding nuclei, while the 90–100% corresponds to the most peripheral collisions with the least overlap between the colliding nuclei. Since the energy in the barrel region ($|\eta| < 3.2$) is highly correlated with the energy in the FCal ($3.2 < |\eta| < 4.9$) as shown in Figure 4.7, using different regions of the detector to estimate event centrality and conduct measurements ensures a consistent centrality determination while avoiding autocorrelations in the analysis.

4.4 Jet Reconstruction for Heavy Ion Collisions in ATLAS

Of the jet reconstruction algorithms that were discussed in Section 1.3.4, the LHC collaborations use the anti-k_t algorithm. The ATLAS jet reconstruction procedure in heavy ion collisions is described in Ref. [116], and is summarized in Figure 4.8. It is different from the procedure for pp collisions because of the large underlying event present in the heavy ion collision system.

This procedure uses the anti-k_t algorithm as implemented in FastJet software package [187]. The anti-k_t algorithm is run in four-momentum recombination mode with its inputs being the $\eta \times \phi = 0.1 \times \pi/32$

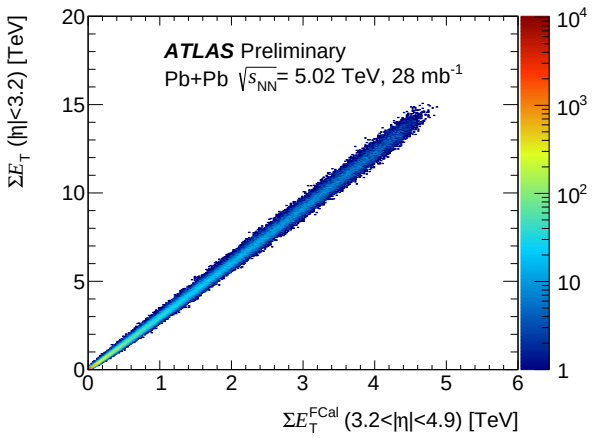

Figure 4.7: Correlation of the total energy in the calorimeter in the interval of $|\eta| < 3.2$ with the total energy measured in the forward calorimeters for Pb+Pb collisions with $\sqrt{s_{\mathrm{NN}}} = 5.02$ TeV. Figure from Ref. [181].

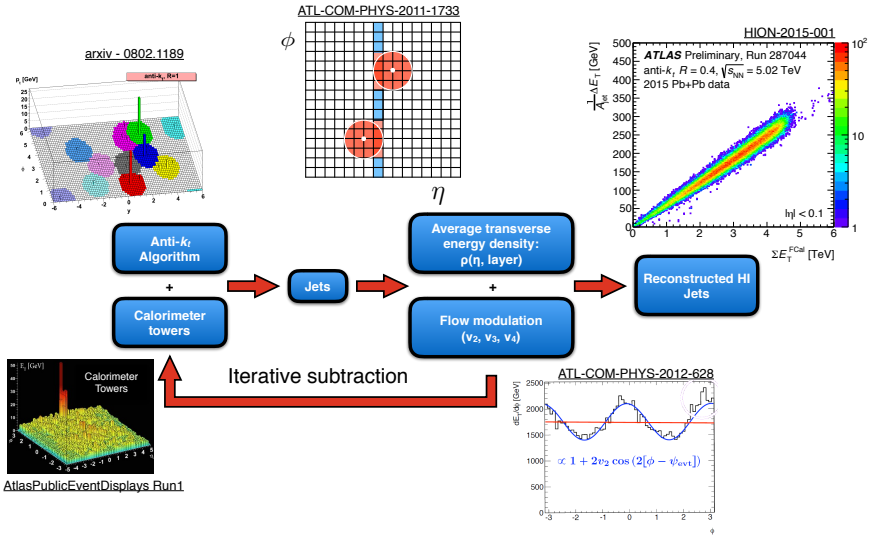

Figure 4.8: A schematic of the ATLAS jet reconstruction procedure. Inset figures from Refs. [128, 181, 184–186].

calorimeter towers. The tower energies are the sum of the energies of all layers in the tower with cells that straddle tower boundaries having their energies fractionally distributed. The anti-k_t algorithm is first run with the distance parameter $R = 0.2$, to give seed jets.

These seed jets contain at least one tower with $E_{\mathrm{T}} > 3$ GeV, and have the ratio of the maximum tower transverse energy to the average tower transverse energy, ${E_{\mathrm{T}}}^{Max}/\langle E_{\mathrm{T}} \rangle > 4$. Then the underlying event subtraction procedure is performed. A first estimate of the average underlying event energy density $\rho_i(\eta)$ is done in 0.1 slices of η in each calorimeter layer i after excluding the regions that overlap with the seed jets. A modulation is applied to account for the flow from the QGP (discussed in Section 1.2) and the underlying

event is subtracted to give E_{Tj}^{sub}:

$$E_{Tj}^{\text{sub}} = E_{Tj} - A_j \rho_i(\eta_j)\Big(1 + 2\sum_{n=2}^{4} v_{ni}\big(\cos[2(\phi_j - \Psi_n)]\big)\Big) \tag{4.1}$$

where E_{Tj}, η_j, ϕ_j and A_j are the cell E_T, η, ϕ and area for cell j in layer i. v_{ni} are the n^{th} order harmonics of the modulation in layer $i$and are given by:

$$v_{ni} = \frac{\sum_{j\in i} E_{\text{T}j}\cos[2(\phi_j - \Psi_n)]}{\sum_{j\in i} E_{\text{T}j}} \tag{4.2}$$

where the sum is over all cells j in layer i. Ψ_n is the event plane angle and is given by [188]:

$$\Psi_n = \frac{1}{n}\tan^{-1}\left[\frac{\langle\sum_k w_k E_{\text{T}k}\sin(n\phi_k)\rangle}{\sum_k E_{\text{T}k}\sin(n\phi_k)}\right] \tag{4.3}$$

where the sum is over all k cells in the FCal and ϕ_k is the azimuthal angle of the cell. The w_k weights are to ensure a uniform Ψ_n distribution. The dominant effect in the modulation is from the second and third harmonic, v_2 and v_3 [188].

Once the background is subtracted, the anti-k_t algorithm is run again with the distance parameter $R = 0.2$. The underlying event is re-estimated after excluding areas that are within $\Delta R = 0.4$ of the seeds. Updated values of ρ'_i and v'_2 are recalculated and used to estimate the background that is subtracted from the original cell energies. This is then subtracted from the original cell energies to give kinematics for the $R = 0.4$ jets. The average subtracted energy normalized by the area of the jet reconstructed jet, as a function of the energy in the forward calorimeter is shown in Fig 4.9. It can be seen that in the barrel region for $|\eta| < 0.1$, $R = 0.4$ jets have a background that is approximately $300/(\pi \times 0.4^2) \approx 150$ GeV. Figure 4.10 shows an ATLAS event display for a heavy ion collision with a reconstructed jet.

4.5 Jet Calibration for Heavy Ion Collisions in ATLAS

The hadronic shower (jet) has both electromagnetic and non-electromagnetic components that interact with the calorimeter material differently. Thus the energy response of the calorimeter for these components is different (this is called a non-compensating calorimeter [189]), and hence, calibrations are required to

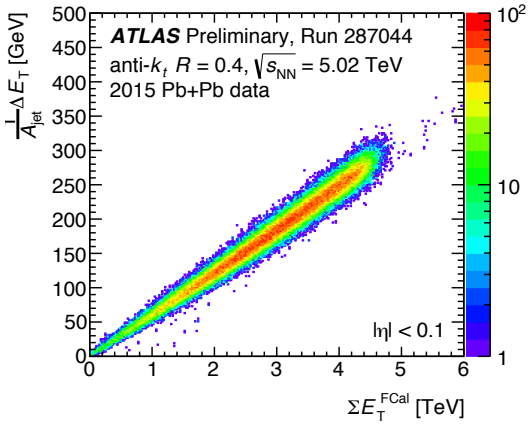

Figure 4.9: The subtracted transverse energy ΔE_{T}, normalized by the jet area A_{jet} as a function of $\Sigma E_{\mathrm{T}}^{\mathrm{FCal}}$ in Pb+Pb collisions at $\sqrt{s_{\mathrm{NN}}} = 5.02$ TeV. Figure from Ref. [181].

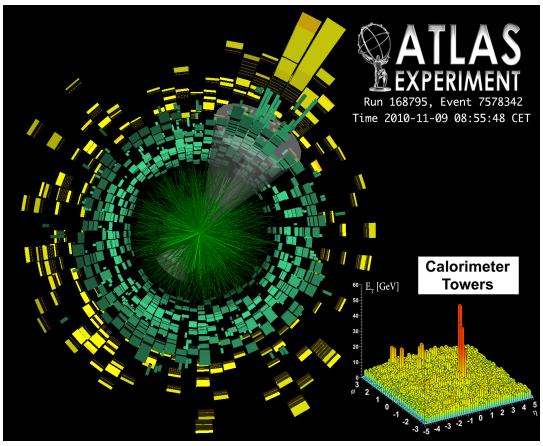

Figure 4.10: An asymmetric dijet event in Pb+Pb collisions at $\sqrt{s_{\mathrm{NN}}}$= 2.76 TeV as measured by the ATLAS detector. Figure from Ref. [184].

correct the reconstructed jet kinematics. These take into account features of the detector, the reconstruction algorithm, and jet fragmentation and include the following [190]:

Origin Correction: This correction ensures that jets point back to the primary vertex and not the nominal center of the detector.

MC based Calibration: This is a MC based correction that depends on the comparison between the energy and pseudorapidity of the reconstructed jet and the corresponding matched truth jet.

***In situ*+Cross Calibration:** This calibration is based on the differences between data and MC as described by a well-measured object like a photon or Z boson [191, 192]. This poses a challenge for heavy ion collisions because unlike in *pp* collisions, there simply aren't enough statistics for these objects. Here the cross-calibration procedure accounts for differences in the jet reconstruction procedure in heavy ion collisions and *pp* collisions, and enables the usage of the *in situ* corrections from *pp* collisions.

The validity of the jet reconstruction and calibration procedure can be tested by evaluating the jet energy scale and jet energy resolution. These are the mean and width respectively of the jet response distribution that is given by $p_{\mathrm{T}}^{\mathrm{reco}}/p_{\mathrm{T}}^{\mathrm{truth}}$ in MC, where $p_{\mathrm{T}}^{\mathrm{reco}}$ is the reconstructed jets transverse momentum, while $p_{\mathrm{T}}^{\mathrm{truth}}$ is the transverse momentum of the corresponding "truth" jet. This is shown in Figure 4.11.

The JES is seen to be almost unity within 1%. across a broad kinematic range. The JER is smaller for jets with higher transverse momentum, and depends on centrality. It is the largest in central collisions and

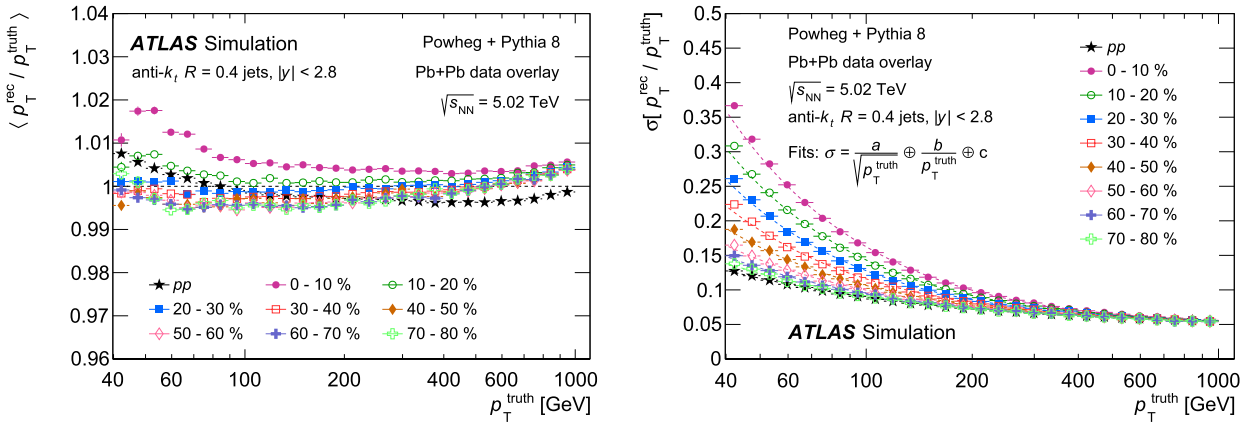

Figure 4.11: The Jet Energy Scale (left) and Jet Energy Resolution (right) as a function of $p_{\mathrm{T}}^{\mathrm{truth}}$. Both are for jets with $|y| < 2.8$. The different curves are for pp and varying Pb+Pb centrality. Figures from Ref. [116].

gets better for more peripheral collisions. The JER can be fit to the form [167]:

$$\frac{\sigma[\Delta E_{\mathrm{T}}]}{E_{\mathrm{T}}^{\mathrm{true}}} = \frac{a}{\sqrt{E_{\mathrm{T}}^{\mathrm{true}}}} \oplus \frac{b}{E_{\mathrm{T}}^{\mathrm{true}}} \oplus c \tag{4.4}$$

where a and c are related to the detector response. The b term describes the underlying event fluctuations and depends on centrality. The large underlying event in central collisions results in the JER being the largest in that centrality interval.

The η and ϕ position resolution of the jet can be derived via a similar procedure and is shown in Figure 4.12 as a function of the $p_{\mathrm{T}}^{\mathrm{truth}}$.

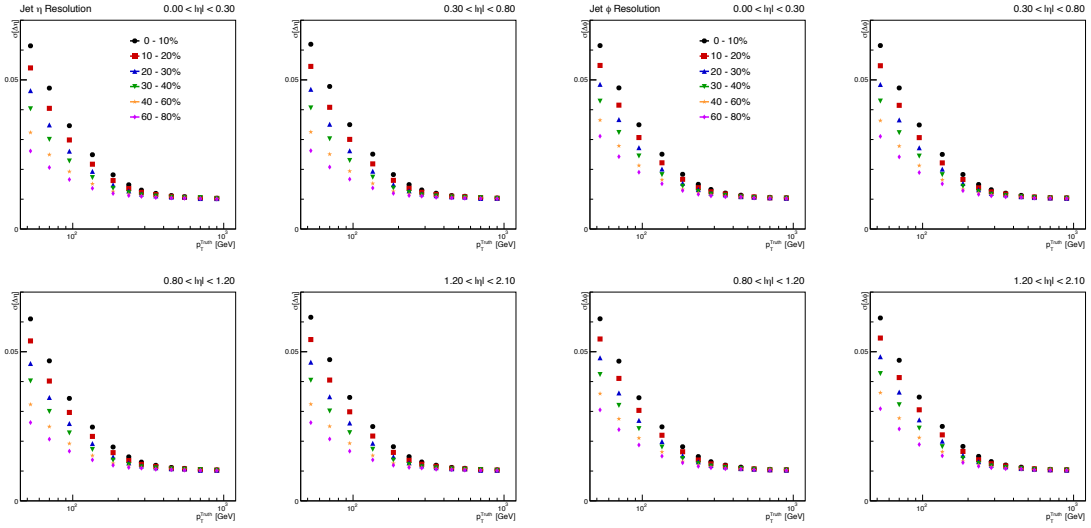

(a) (b)

Figure 4.12: The (left) η and (right) ϕ position resolution of the jet as a function of $p_{\mathrm{T}}^{\mathrm{truth}}$ in Pb+Pb collisions at $\sqrt{s_{\mathrm{NN}}} = 5.02$ TeV for different centrality and η regions.

Chapter 5

ANGULAR CORRELATIONS BETWEEN TRACKS AND JETS

5.1 Overview

Measurements of jets in heavy ion collisions are powerful tools to determine the properties of the quark gluon plasma by measuring the modification of jet production and fragmentation after the jets have traversed the hot QCD matter. As discussed in Section 2, jets with large transverse momenta in central lead-lead (Pb+Pb) collisions at the LHC are measured at approximately half the rates in *pp* collisions when the nuclear overlap function of Pb+Pb collisions is taken into account [116, 137, 148, 149, 159, 193]. Back-to-back dijet [142, 144, 146] and photon-jet pairs [145, 194] are observed to have less balanced transverse momenta in Pb+Pb collisions compared to *pp* collisions. Jet shape measurements in the *pp* and Pb+Pb collision systems have shown a broadening of the jets due to the QGP [160, 195–197], and jet fragmentation functions in Pb+Pb collisions are modified with an excess for low and high momentum particles and depletion of intermediate momentum particles inside the jet compared to pp collisions [151, 169, 173, 198]. Particles carrying a large fraction of the jet momentum are generally closely aligned with the jet axis, whereas low momentum particles are observed to have a much broader angular distribution extending outside the jet [117, 146, 157, 199]. All these studies have suggested that the energy lost via jet-quenching is being transferred to soft particles around the jet axis via soft gluon emission [98, 158, 162, 200–203] and investigating the radial distribution of particles as a function of transverse momentum has the potential to provide further insight into the structure of jets in the QGP. This can help provide information on not only how the jet is affected by the plasma, but

also how the plasma is affected by the jet.

This thesis presents charged-particle p_{T} distributions around the jet axis as shown in Figure 5.1. The measured yields are defined as:

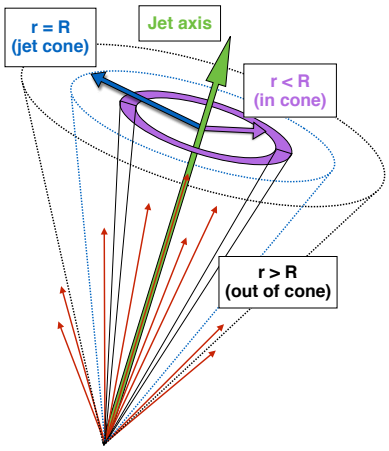

Figure 5.1: A schematic showing the distribution of tracks inside and outside a jet cone of radius R.

$$D(p_{\mathrm{T}}, r) = \frac{1}{N_{\mathrm{jet}}} \frac{1}{A} \frac{\mathrm{d}n_{\mathrm{ch}}(p_{\mathrm{T}}, r)}{\mathrm{d}p_{\mathrm{T}}}, \tag{5.1}$$

where $r = \sqrt{\Delta\eta^2 + \Delta\phi^2}$ is the angular distance from the jet axis and N_{jet} is the number of jets in consideration. $A = \pi(r_{\mathrm{max}}^2 - r_{\mathrm{min}}^2)$ is the area of an annulus around the jet axis with its inner and outer radii r_{min} and r_{max} respectively and $n_{\mathrm{ch}}(p_{\mathrm{T}}, r)$ is the number of charged particles with a given p_{T} within the annulus. The boundaries of the annuli are given by: 0.0, 0.05, 0.1, 0.15, 0.2, 0.25, 0.3, 0.4, 0.5, 0.6, 0.7, 0.8. The ratios of the charged-particle yields measured in Pb+Pb and pp collisions,

$$R_{D(p_{\mathrm{T}},r)} = \frac{D(p_{\mathrm{T}}, r)_{\mathrm{Pb+Pb}}}{D(p_{\mathrm{T}}, r)_{pp}}, \tag{5.2}$$

quantify the modifications of the yields due to the QGP medium. Furthermore, the differences between the $D(p_{\mathrm{T}}, r)$ distributions in Pb+Pb and pp collisions,

$$\Delta D(p_{\mathrm{T}}, r) = D(p_{\mathrm{T}}, r)_{\mathrm{Pb+Pb}} - D(p_{\mathrm{T}}, r)_{pp}, \tag{5.3}$$

allow for measuring the absolute differences in charged-particle yields between the two collision systems.

The following sections describe all details of this analysis as follows:

- The datasets and event selection criteria used for this analysis are discussed in Section 5.2
- The cuts and corrections applied in the analysis procedure are discussed in 5.3
- The various sources of systematic uncertainties and their sizes are discussed in 5.4
- The results of this analysis are described and interpreted in 5.5

5.2 Datasets and Event Selection

The Pb+Pb and *pp* data used in this analysis were recorded in 2015. The data samples consisted of 25 pb^{-1} of $\sqrt{s} = 5.02$ TeV *pp* and 0.49 nb^{-1} of $\sqrt{s_{\mathrm{NN}}} = 5.02$ TeV Pb+Pb data.

Events in both the *pp* and Pb+Pb samples were selected by the ATLAS Trigger system discussed in Chapter 4. The general scheme is to identify events using the Level 1 (L1) triggers, and pass them as "seeds" to the High Level Trigger (HLT). In Pb+Pb, the selection was based on the L1 Total Energy trigger, `L1_TE50` that identified events with at least 50 GeV in the calorimeter system. These events were passed to the HLT, where the `HLT_j75_ion_L1TE50` used an online jet reconstruction algorithm to select on jets above 75 GeV. In *pp*, the event selection was done using a L1 jet trigger, `L1_j20`, that used a simple sliding window algorithm to find jet candidates with a $p_{\mathrm{T}}^{\mathrm{jet}} > 20$ GeV. These were then used as seeds to the HLT, where the `HLT_j85` trigger further selection on jets with $p_{\mathrm{T}}^{\mathrm{jet}} > 85$ GeV. The performance of the jet triggers in 2015 is described in Refs. [204, 205] and the trigger efficiency is shown in Figure 5.2. This analysis then further selected jets with $p_{\mathrm{T}}^{\mathrm{jet}} > 100$ GeV, thus ensuring a fully efficient trigger selection.

In addition to the jet triggered samples described above, a Minimum Bias Pb+Pb data sample was also recorded. This was triggered based on a logical OR of the total energy trigger with a threshold of 50 GeV and the ZDC coincidence trigger was used as part of the MC overlay procedure

In both samples, events were required to have a reconstructed vertex within 150 mm of the nominal IP along the beam axis. The pileup was negligible in the Pb+Pb while the *pp* data was collected in low pileup mode, where the average number of interactions per bunch crossing in *pp* collisions ranged from 0.6 to 1.3.

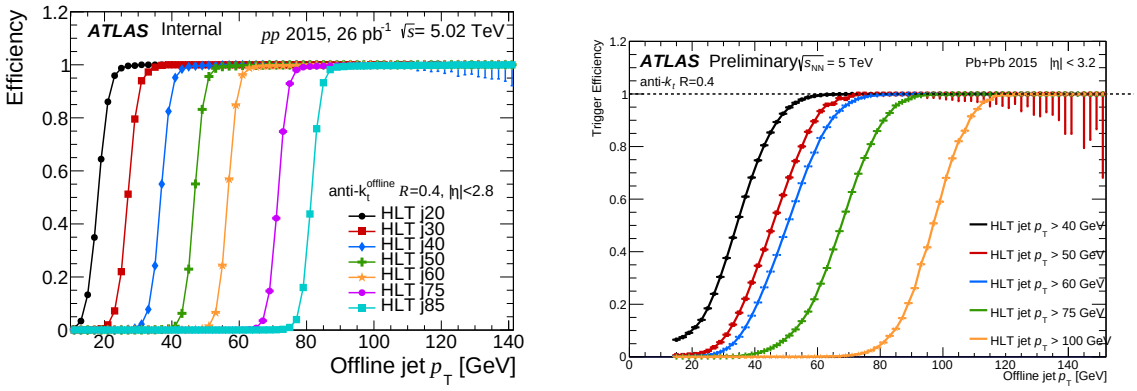

Figure 5.2: Jet trigger efficiencies for (left) *pp* and (right) 0–80% central Pb+Pb collisions at 5.02 TeV for R=0.4 offline jets. The broader turn-on of the jet trigger in Pb+Pb compared to *pp* collisions is caused by significant differences between the HI jet trigger reconstruction algorithm used at the time of the data taking and the current version of the offline reconstruction software. Figure from Ref. [206]

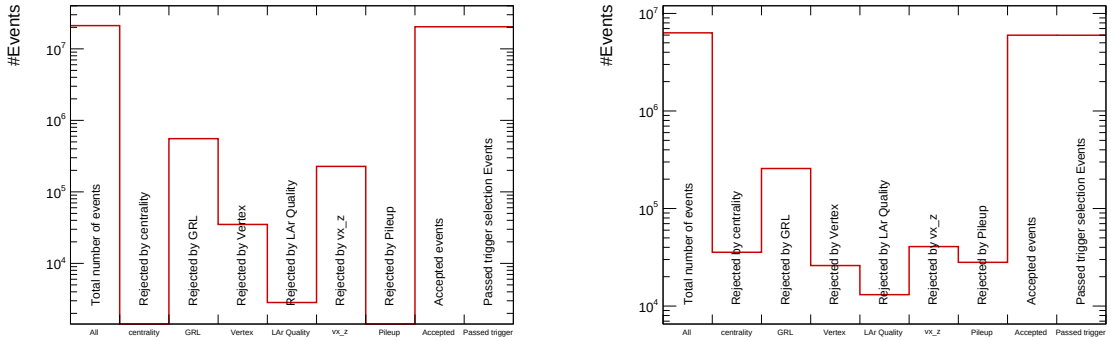

Figure 5.3: The number of 2015 *pp* (left) and Pb+Pb (right) events used and rejected by various event quality cuts.

Only events taken during stable beam conditions and satisfying detector and data-quality requirements that include the detector subsystems being in nominal operating conditions were considered. The total number of *pp* and Pb+Pb events entering the analysis, along with the with rejection power of various event quality cuts is shown in Figure 5.3. Some of these events are rejected by multiple cuts. "Rejection by centrality" indicates the number of events outside the 0-80% centrality bin.

The centrality intervals used in this analysis were defined according to successive percentiles of the $\Sigma E_{\mathrm{T}}^{\mathrm{FCal}}$ distribution obtained in minimum bias (MB) collisions, ordered from the most central (highest $\Sigma E_{\mathrm{T}}^{\mathrm{FCal}}$) to the most peripheral (lowest $\Sigma E_{\mathrm{T}}^{\mathrm{FCal}}$) collisions: 0–10%, 10–20%, 20–30%, 30–40%, 40–60%, 60–80%.

The *pp* Monte Carlo (MC) used a set of 1.8×10^7 5.02 TeV hard-scattering dijet *pp* events generated with Powheg+Pythia8 [207, 208] using the A14 tune of parameters [209] and the NNPDF23LO PDF set

[210]. The Pb+Pb MC was generated by overlaying the additional sample of MB Pb+Pb data events on a separate set of 1.8×10^7 5.02 TeV hard-scattering dijet pp events generated with the same tune and PDFs as the pp MC. This "MC overlay" sample was reweighted on an event-by-event basis such that it had the same centrality distribution as the jet triggered sample. Another sample of MB Pb+Pb events was generated using HIJING (version 1.38b) [211] and was only used to evaluate the track reconstruction performance. The detector response in all MC samples was simulated using GEANT4 [212, 213]. These MC samples were used to evaluate the performance of the detector and analysis procedure and correct the measured distributions for detector effects.

The time dependence of the underlying event (a core part of this measurement) was tested by dividing the data and MC into three data taking periods with approximately equal number of events in each period. The underlying event determined for each period compared to the nominal underlying event evaluated for the entire dataset is shown in Figure 5.4, and it can be seen that it is stable throughout the data taking period.

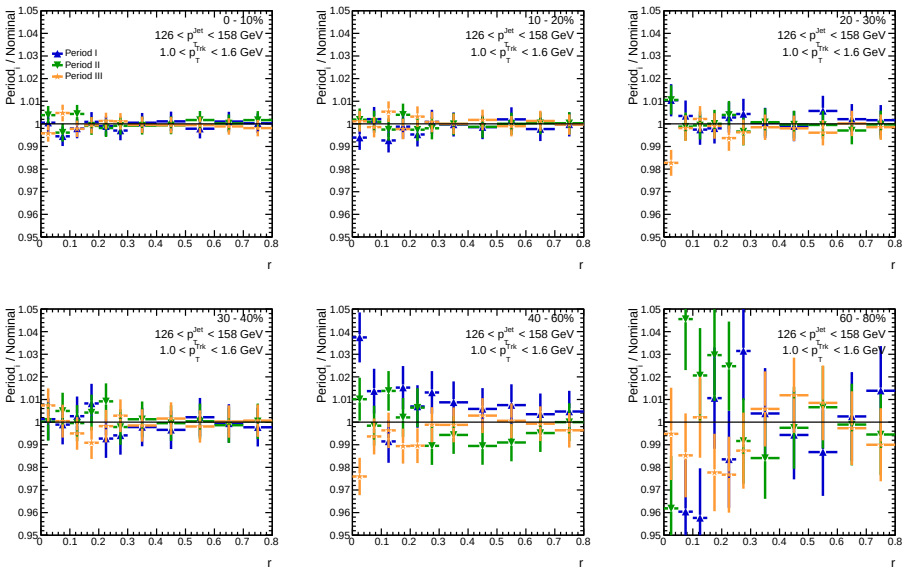

Figure 5.4: Stability of the underlying event for three different periods of the data taking. The different curves indicate the ratio of the underlying event in each period of data taking to the underlying event determined in the entire dataset.

5.3 Basic Cuts and Corrections

A description of the analysis procedure to reconstruct the $D(p_{\mathrm{T}}, r)$ distribution, along with the derivation and application of the various corrections is presented in the following sections. The analysis structure is

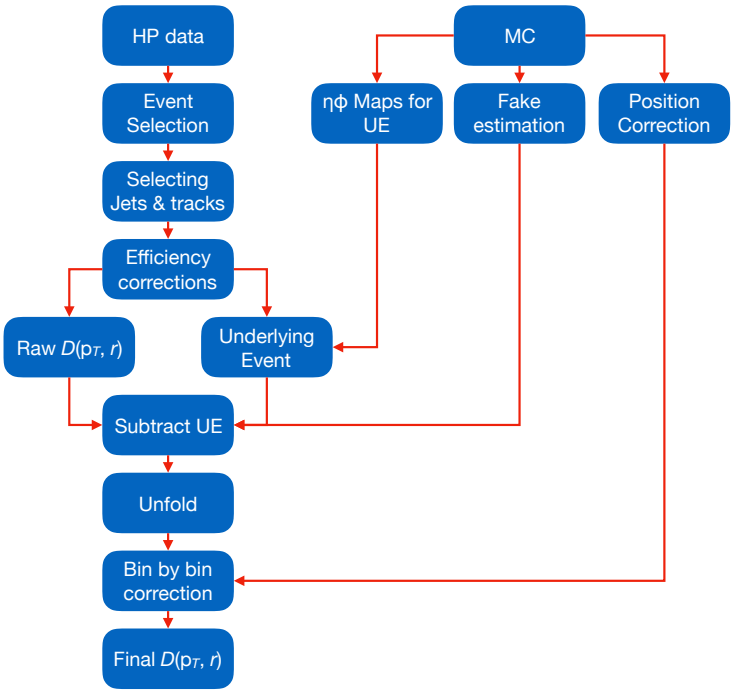

Figure 5.5: The diagram presents various corrections and cuts that are applied during the analysis.

illustrated by the diagram in Figure 5.5 where each part of the analyses is described in a separate subsection and can be summarized as follows:

- Jet selection
- Track selection
- Track momentum correction
- Fake rates
- Tracking efficiency
- Underlying event subtraction of tracks
- Unfolding

5.3.1 Jet Selection and final energy calibration

Since the Inner Detector (ID) covers the $|\eta| < 2.5$, the analysis can only be performed for jets within the pseudorapidity interval of $|\eta| < 1.7$ to have the entire $r = 0.8$ cone under investigation fully covered by the tracking detector. In both collision systems, jets are measured with $p_{\mathrm{T}}^{\mathrm{jet}}$ between 126 GeV and 316 GeV in

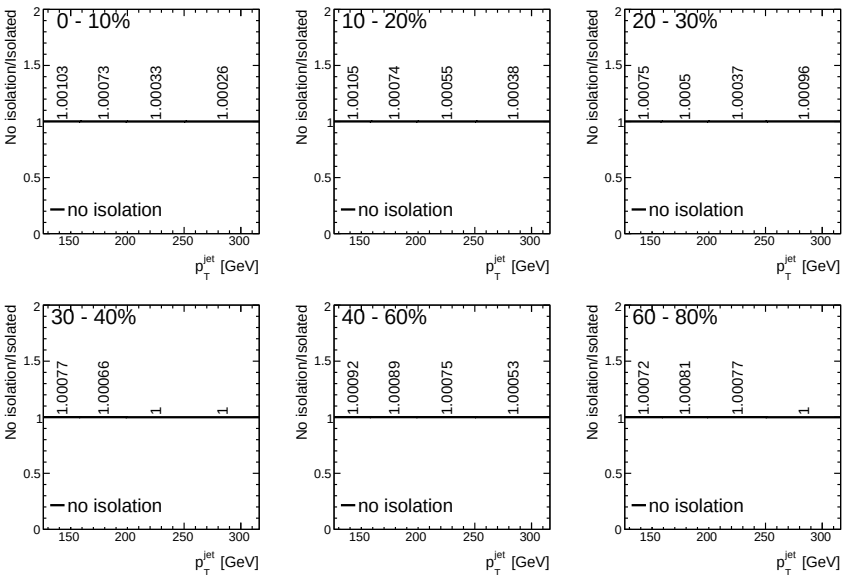

Figure 5.6: The ratios of the jet spectra with no isolation to that with isolation in the kinematic range of interest for Pb+Pb collisions, in all centralities. The isolation requirement rejects less that 0.1% of jets, and has almost no impact on the final measurement.

following four successive intervals: 126–158, 158–200, 200–251, and 251–316 GeV. The $p_{\mathrm{T}}^{\mathrm{jet}}$ cut is chosen so as to exclude the contribution of "UE jets" generated by fluctuations in the underlying event. This binning is also used in previous heavy ion jet measurements such as Ref. [151].

Truth jets were associated with the nearest reconstructed jet using the matching of $\Delta R < 0.2$ for the performance study and to build response matrices for the unfolding procedure. The same ΔR matching criteria were employed in previous ATLAS HI jet analyses and are justified by a detailed performance study [185]. To prevent nearby jets from distorting the measurement of $D(p_{\mathrm{T}}, r)$ distributions, jets are rejected if there is a neighboring jet with higher $p_{\mathrm{T}}^{\mathrm{jet}}$ within an angular distance of $\Delta R < 1.0$. The isolation cut removes approximately 0.01% of jets (see Figure 5.6), and has almost no impact on the final measurement.

No correction for the jet reconstruction efficiency is necessary, as the analysis is performed in the jet p_{T} region where the jet reconstruction is fully efficient [111]. The jet energy measured in the calorimeter can be affected by the presence of dead cells or cells with a bad response, by noise spikes in the hadronic end-cap or the EM calorimeter, and by out-of-time energy deposits from cosmic rays and beam backgrounds. In the *pp* analysis, these bad jets are removed via a set of standard recommended cuts. The rate of these jets in the kinematic region of interest (100–316 GeV) is less than 0.5%. This cleaning procedure is not applied in Pb+Pb collisions because it is incompatible with the heavy ion jet reconstruction procedure, and also because the low luminosity ensures noise bursts are negligible. This is standard procedure for all heavy ion jet analyses.

5.3.2 Track selection

The track selection cuts used here follow the cuts used in [151]. These provide a low level of fake tracks and a track reconstruction efficiency that is independent of the p_{T} of the jet the track is associated with.

The cuts used here are the "tight" cuts as described in Ref. [214] and were utilized in previous HI jet fragmentation measurements. The default tracking cuts used both in pp and Pb+Pb analysis are:

- track $p_{\mathrm{T}} > 1$ GeV
- track $|\eta| < 2.5$
- tracks should have at least 9 silicon hits in $|\eta| \leq 1.65$
- tracks should have at least 11 silicon hits in $|\eta| > 1.65$
- tracks should have at least 1 hit in IB-layer + B-layer.
- tracks should have a IB-layer hit if it is expected, that is, if the track passed an active module.
- tracks should have a B-layer hit if it is expected and IB-layer hit is not expected.
- tracks should have less than 3 holes in silicon detectors.
- tracks should have 0 holes in pixel detector.
- impact parameters of track with respect to primary vertex: $|d_0| < 0.47e^{(-0.15p_{\mathrm{T}})}+0.19e^{(3.4\mathrm{E}-4p_{\mathrm{T}})}$ mm, $|z_0 * \sin\theta|$ <1.0 mm. The recommended values are $|d_0| < 1.5$ mm for tracks with $p_{\mathrm{T}} < 10$ GeV and $|d_0| < 0.2$ mm for tracks with $p_{\mathrm{T}} > 10$ GeV. This was chosen to guarantee a smooth behavior of the d_0 parameter as a function of track momentum.
- All tracks with $p_{\mathrm{T}}^{\mathrm{ch}} > p_{\mathrm{T}}^{\mathrm{jet}} + \sqrt{(3 \times \sigma_{\mathrm{JER}}(p_{\mathrm{T}}^{\mathrm{jet}}))^2 + (3 \times \sigma_{\mathrm{TMR}}(p_{\mathrm{T}}^{\mathrm{ch}}))^2}$ are rejected from the analysis, where the TMR stands for track momentum resolution. The purpose of this cut is to be consistent with previous fragmentation measurements [151]. It has minimal impact on this analysis because the analysis is restricted to tracks below 63 GeV and jets above 100 GeV.

A tighter tracking selection is used for systematic studies ("tight+" cuts). These cuts include all of the default cuts plus a 3σ cut on the significance of the d_0 and $z_0 \sin\theta$. Figures 5.7-5.9 shows comparisons of the data and MC tracking quantities in pp and Pb+Pb collisions, respectively, for different track p_{T} intervals. It can be seen that the MC describes the data well. A 20% discrepancy is observed for low impact parameters. The discrepancy is present far from the values of corresponding tracking cuts. There is a small shift in

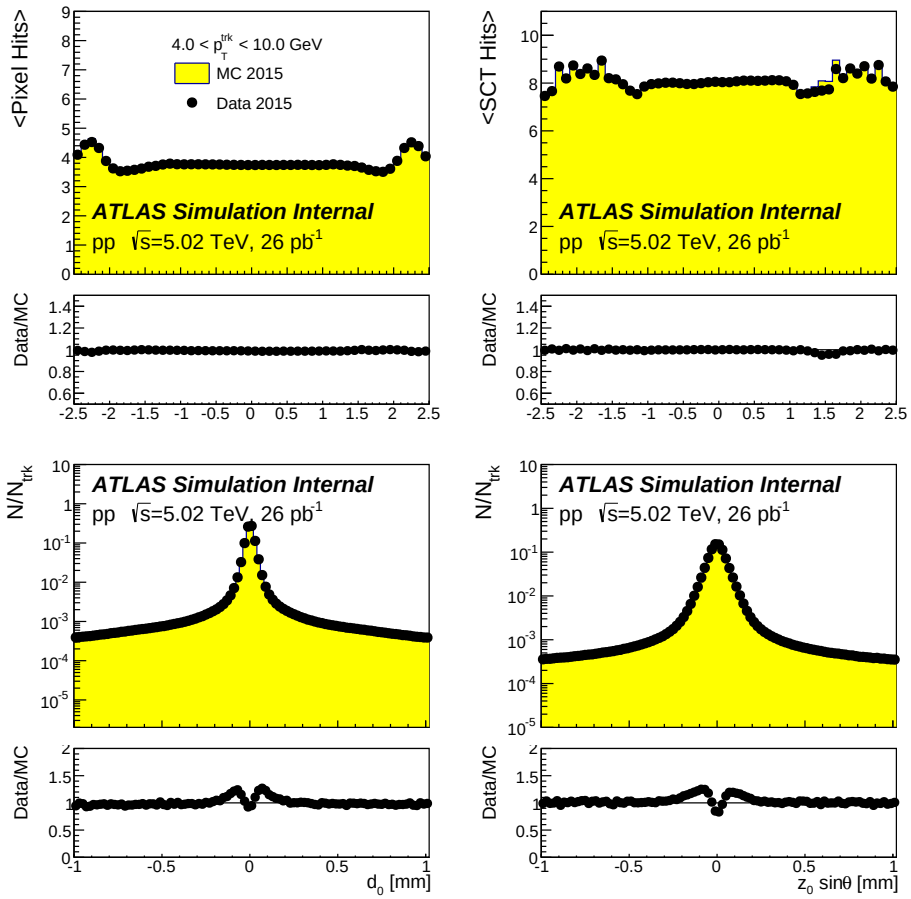

Figure 5.7: Track quantity comparison between data (points) and MC (yellow histogram) in pp collisions. Tracks are selected to have $4.2 < p_{\mathrm{T}}^{\mathrm{ch}} < 10$ GeV. Below each direct data and MC overlay is the corresponding data to MC ratio. The quantities compared are: average number of pixel hits as a function of η^{ch} (top left), average number of SCT hits as a function of η^{ch} (top right), and number of tracks, N_{trk}, normalized d_0 (bottom left), and $z_0 \sin\theta$ distributions (bottom right). Figure from Ref. [206].

the $z0$ distribution in the MC samples. This difference is caused by the allowance of a small difference in the z position of the primary vertex in the MC overlay procedure. However this has negligible impact on the analysis as the overall quality requirement on the pointing parameter in the $z0$ is 1 mm. Furthermore, Figure 5.9 shows the same comparison for high p_{T} tracks. All the comparisons of distributions show the same qualitative features as seen at lower p_{T} with improving pointing with increasing track p_{T}. The comparison of the reconstructed $p_{\mathrm{T}}^{\mathrm{ch}}$ with the generated kinematics for tracks passing these cuts is shown in Figure 5.10.

Figure 5.11 presents the impact of individual tracking requirements in terms of the ratio of the number of tracks that pass given cut and the total number of reconstructed tracks in pp MC. This is shown as a function of track pseudorapidity in two different track p_{T} intervals and as a function of track p_{T} in two different pseudorapidity intervals. The highest rejection for low p_{T} tracks is provided by the cut on d_0 pointing. At high p_{T} the dominant effect is seen from the requirement on the number of silicon hits.

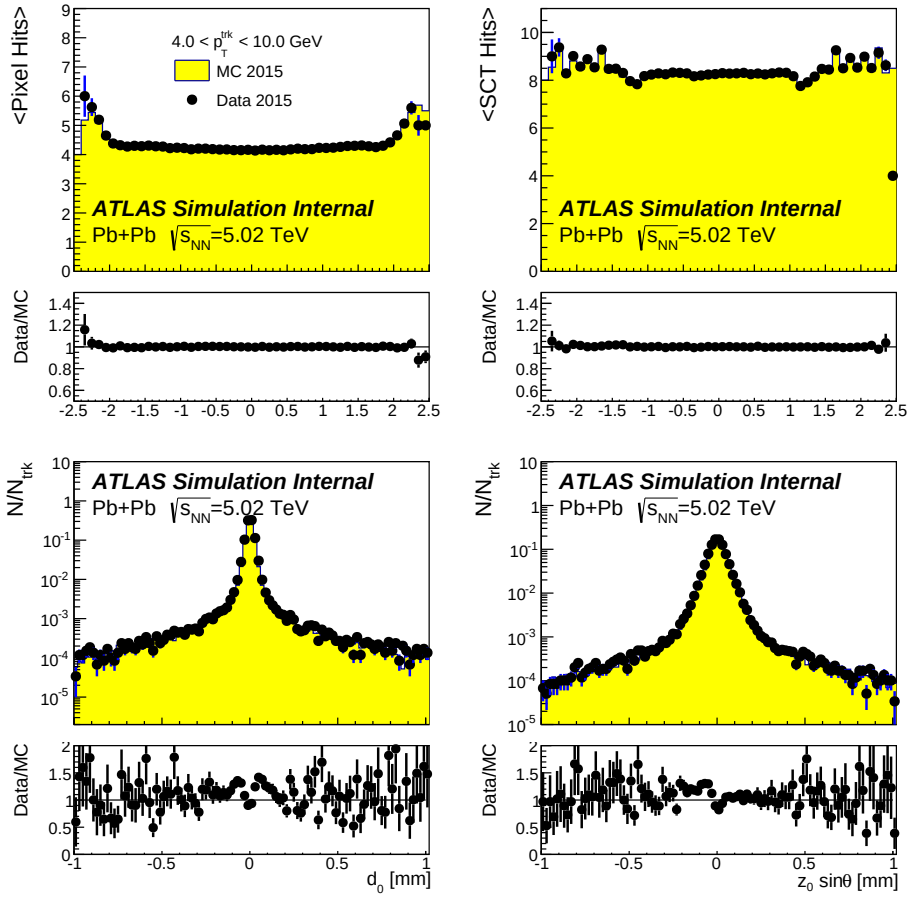

Figure 5.8: Track quantity comparison between data (points) and MC (yellow histogram) in 0-10% central Pb+Pb collisions. Tracks are selected to have $4.2 < p_{\mathrm{T}}^{\mathrm{ch}} < 10$ GeV. Below each direct data and MC overlay is the corresponding data to MC ratio. The quantities compared are: average number of pixel hits as a function of η^{ch} (top left), average number of SCT hits as a function of η^{ch} (top right), track d_0 (bottom left), and track $z_0 \sin\theta$ (bottom right). Figure from Ref. [206].

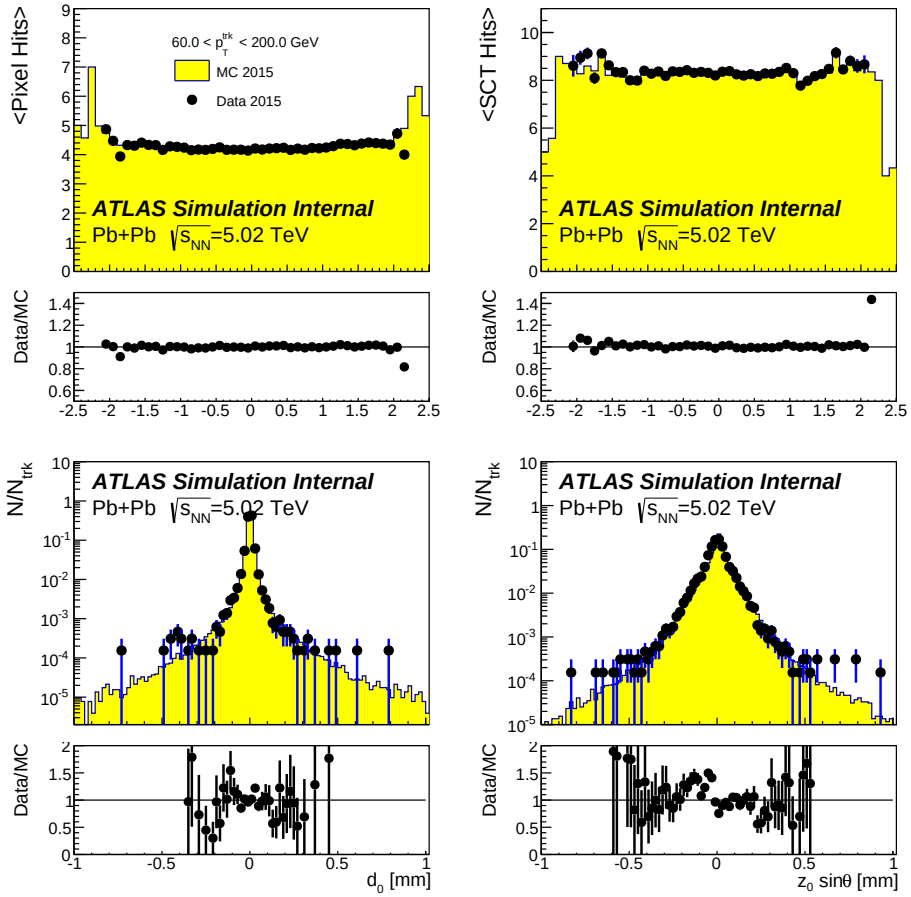

Figure 5.9: Track quantity comparison between data (points) and MC (yellow histogram) in Pb+Pb collisions inclusive in collisions centrality. Tracks are selected to have $60 < p_{\mathrm{T}}^{\mathrm{ch}} < 200$ GeV and to originate from jet with p_{T} in the interval from 251 to 316 GeV. Below each direct data and MC overlay is the corresponding data to MC ratio. The quantities compared are: average number of pixel hits as a function of η^{ch} (top left), average number of SCT hits as a function of η^{ch} (top right), track d_0 (bottom left), and track $z_0 \sin\theta$ (bottom right). Figure from Ref. [206].

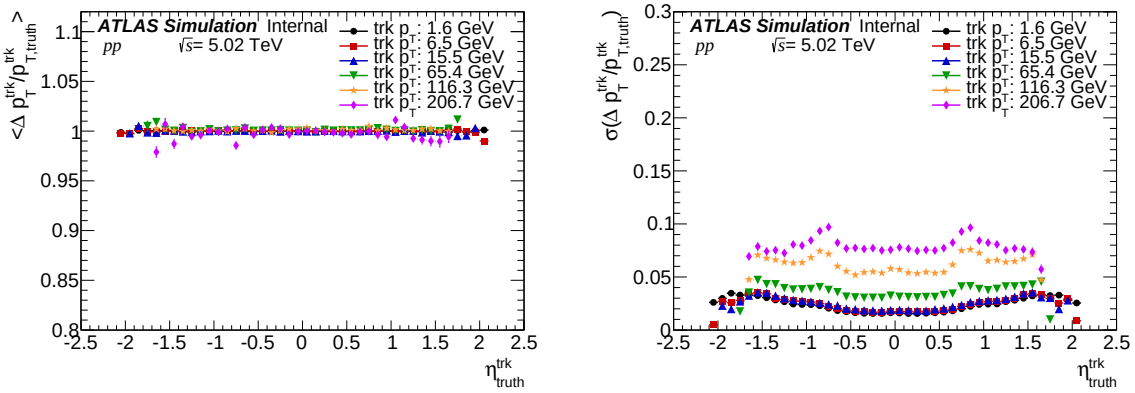

Figure 5.10: (left) Comparison of the generated and reconstructed track p_{T} as a function of $\eta^{\mathrm{trk}}_{\mathrm{truth}}$ for five track $p_{\mathrm{T}}^{\mathrm{trk,Truth}}$ selections. (right) Track momentum resolution as a function of $\eta^{\mathrm{trk}}_{\mathrm{truth}}$ for five $p_{\mathrm{T}}^{\mathrm{trk,Truth}}$ selections. Both plots are for *pp* MC. All tracks shown in this plot have passed the 2015 default tracking cuts defined in this section. The p_{T} in the legend corresponds to the bin centers in the following track p_{T} bins: 1.3 – 1.8 GeV, 5.6 – 7.5 GeV, 13.3 – 17.7 GeV, 56.1 – 74.8 GeV, 99.7 – 132.9 GeV, 177.2 – 236.2 GeV. Figure from Ref. [206].

Similarly, Figure 5.12 presents the impact of individual tracking requirements in Pb+Pb MC. The difference between the impact of individual cuts can be attributed to a different setting of the tracking algorithm and to the overall increase of the track multiplicity as the number of rejected tracks does not linearly scale with the multiplicity that enters the denominator.

The primary particles[1] used in this analysis have a mean lifetime $\tau > 0.3 \times 10^{-10}$ s and are either directly produced in *pp* interactions or from subsequent decays of particles with a shorter lifetime. They are required to have their barcode in the range $0 - 200000$. Of these, particles with barcode < 10000 are coming from Pythia, while the remaining are from HIJING. Particles with barcodes above 200000 are secondaries, and come from weak decays of Λ, K_S, Ξ, Σ, Ω and from particles created in interactions with the material. Strange baryons are included: $\Sigma-$ (PDG ID 3112), $\Sigma+$ (PDG ID 3222), $\Xi-$ (PDG ID 3312), $\Omega-$ (PDG ID 3334).

5.3.3 Track momentum correction

Specific corrections are needed for track momentum in 5.02 TeV *pp* and Pb+Pb data to account for a miss-alignment introduced in the track reconstruction. The sign charge dependent momentum scale shift was observed in *pp* data when the transverse momentum of muons reconstructed using muon spectrometer was compared to the transverse momentum of muons from the inner detector. The difference as a function of muon momentum in Pb+Pb data can be seen in Figure 5.13. The correction to track p_{T} as a function of

[1]Primary particles are defined as particles with a mean lifetime $\tau > 0.3 \times 10^{-10}$ s either directly produced in *pp* interactions or from subsequent decays of particles with a shorter lifetime.All other particles are considered to be secondary.

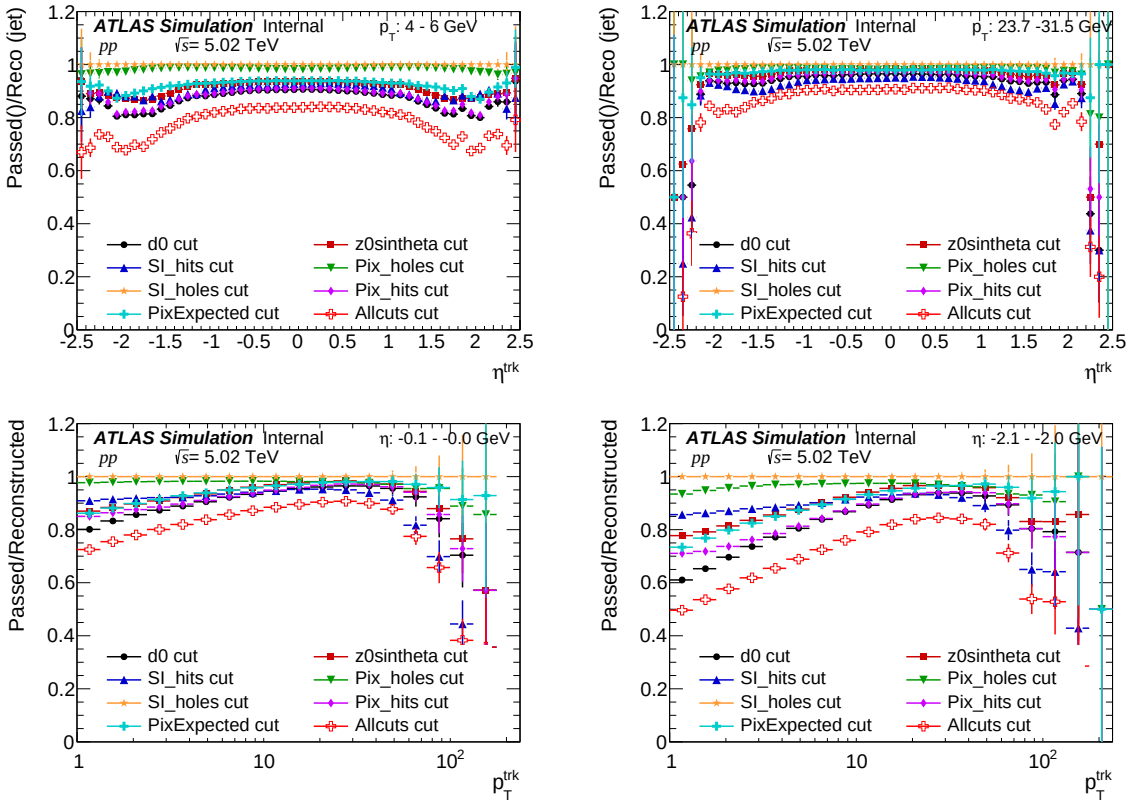

Figure 5.11: The impact of each cut applied individually in the pp MC to the starting collection of tracks, as a function of η^{ch}(top) for $1.3 < p_{\mathrm{T}}^{\mathrm{ch}} < 4.6$ GeV (left) and for $23.7 < p_{\mathrm{T}}^{\mathrm{ch}} < 31.5$ GeV and as a function of track p_{T} for two different pseudorapidity intervals (bottom). The final combination of all cuts is shown as well. Figure from Ref. [206].

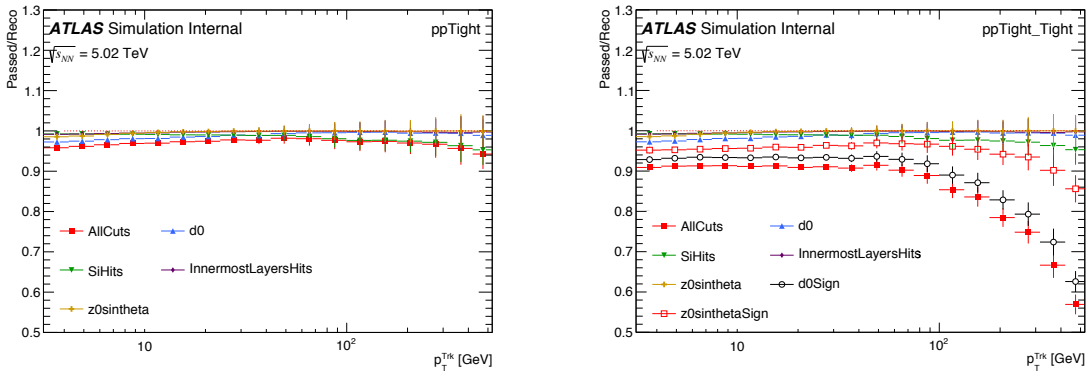

Figure 5.12: The impact of each cut applied individually in the Pb+Pb MC to the starting collection of tracks, as a function of the track p_{T} inclusive in collision centrality for the default and the tight set of tracking requirements. The final combination of all cuts is shown as well.

track η and track ϕ is applied through sagitta bias maps introduced in Ref. [215].

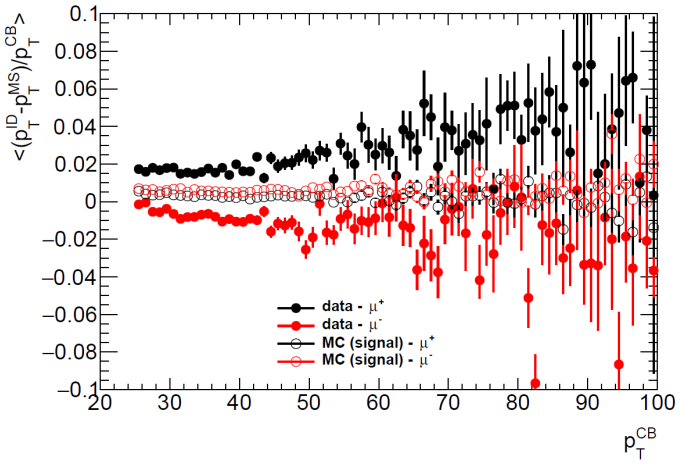

Figure 5.13: Comparisons of track momentum scale of positive and negative muons reconstructed using muon spectrometer and inner detector. The muon traverse momentum evaluated from muon spectrometer (MC) is compared by that evaluated using the inner detector (ID) and the relative scale is normalized by the momentum that uses both detectors. Figure from Ref. [216].

5.3.4 Track reconstruction efficiency

The tracking reconstruction efficiency is defined as the ratio between the number of primary truth charged particles that are reconstructed and the total number of primary truth charged particles in the given p_{T} and η bin. It is evaluated using MC tracks, where tracks are required to pass all the tracking cuts imposed on the data.

Matching between the reconstructed and the truth track is done via a cut on $\mathrm{mc}_{\mathrm{prob}}$. This is defined as the probability that a reconstructed track matched to a truth track actually was a truth track. It is calculated as:

$$\mathrm{mc}_{\mathrm{prob}} = \frac{10N_{\mathrm{pix}}^{\mathrm{common}} + 5N_{\mathrm{SCT}}^{\mathrm{common}} + N_{\mathrm{TRT}}^{\mathrm{common}}}{10N_{\mathrm{pix}}^{\mathrm{track}} + 5N_{\mathrm{SCT}}^{\mathrm{track}} + N_{\mathrm{TRT}}^{\mathrm{track}}} \tag{5.4}$$

where N_X^{common} are the number of hits in detector X in common between the truth and reconstructed track. N_X^{track} is the number of total hits in the reconstructed track.

Tracks with $\mathrm{mc}_{\mathrm{prob}} > 0.3$ are associated with the truth track and those with a lower value are not and are classified as fake tracks. The choice of $\mathrm{mc}_{\mathrm{prob}} = 0.3$ is based on the recommendation from the ATLAS tracking group and was used in [217]. The sensitivity of the measurement on the value of the $\mathrm{mc}_{\mathrm{prob}}$ cut is included in the systematic uncertainties.

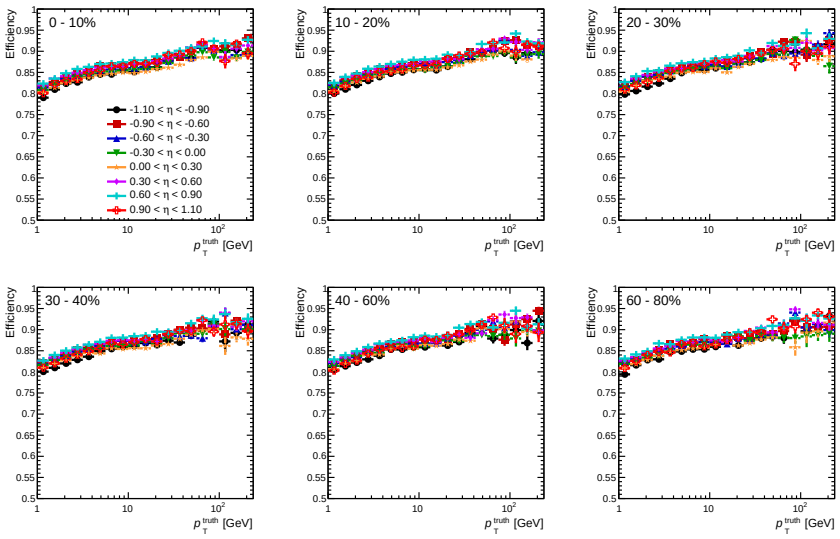

Figure 5.14: Efficiency for reconstructing tracks evaluated using the default tracking selections in different track η bins in the Pb+Pb MC overlay samples. Each panel is a different centrality bin.

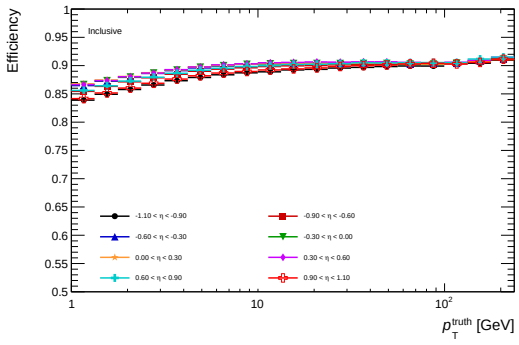

Figure 5.15: Efficiency for reconstructing tracks evaluated using the default tracking selections in different track η bins in the pp MC samples.

In MC samples, the "track barcode" classifies reconstructed tracks to different classes based on the origin (primary, secondary, pileup, beam halo, fake). We require $0 <$ barcode < 200000 in evaluation of the tracking efficiency to remove pileup, beam halo, secondary particles, and fake particles. Reconstructed tracks that do not have a matched truth track with given $\mathrm{mc}_{\mathrm{prob}}$ are labeled all together as fake tracks. The tracking cuts need to provide both good efficiency for generator level tracks and to adequately reject fakes.

The final efficiency corrections applied were determined and applied as a function track p_{T} and track η, and can be seen in Figures 5.14-5.15 for pp and Pb+Pb collisions. No significant dependence on the collision centrality is observed. The efficiency exhibits a small, but monotonic increase with the track p_{T}. Only a small variation with the track η is observed in the region $|\eta| < 1.1$. The efficiency correction is applied on a track-by-track basis, assuming $p_{\mathrm{T}}^{\mathrm{ch}} = p_{\mathrm{T}}^{\mathrm{truth}}$. While that assumption is not strictly valid, the efficiency varies

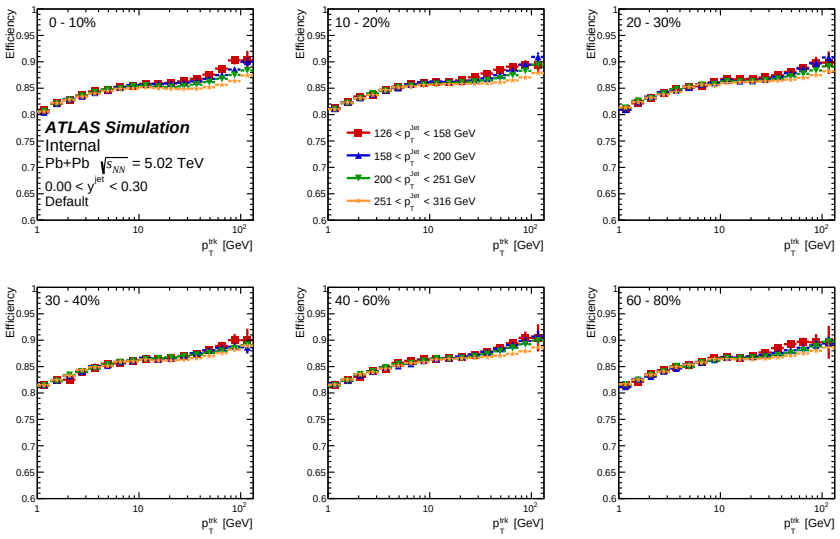

Figure 5.16: Efficiency for reconstructing tracks evaluated using the default tracking selections in different jet p_{T} bins and jet rapidity interval $|y| < 0.3$ in the Pb+Pb MC overlay samples. Each panel is a different centrality bin.

sufficiently slowly with $p_{\mathrm{T}}^{\mathrm{truth}}$ that the error introduced by this assumption is negligible, up to 1%. The tracking efficiency determined in Ref. [151] was not seen to be dependent on $p_{\mathrm{T}}^{\mathrm{jet}}$ for $p_{\mathrm{T}}^{\mathrm{ch}} \lesssim 40$ GeV as can be seen in Figures 5.16-5.18. The small depletion of the efficiency for tracks with $p_{\mathrm{T}} \sim 10 - 40$ GeV was attributed to the convolution of how jet fragments and with the performance of the track reconstruction in the dense core of the jet [151].

5.3.5 Fake rates

Reconstructed tracks that cannot be matched to a primary particle in the MC samples or are matched to a secondary particle are considered to be "fake" tracks. The rate of these tracks was evaluated and extensively studied in Ref. [151] in the pp, Pb+Pb HIJING MC, and in Pb+Pb MC overlay samples. The MC overlay sample is used to crosscheck the fake rate at higher p_{T}, but is not used for any corrections. It was shown that as the $p_{\mathrm{T}}^{\mathrm{ch}}$ approaches the $p_{\mathrm{T}}^{\mathrm{jet}}$ the fraction of fake tracks increases due to the steeply falling spectra of generator level tracks. Figures 5.19 and 5.20 show the fraction of tracks that are identified as fakes, secondaries, or part of UE in case of Pb+Pb collisions as a function of $p_{\mathrm{T}}^{\mathrm{ch}}$ for selections in $p_{\mathrm{T}}^{\mathrm{jet}}$in pp and Pb+Pb collisions, respectively. The rate decreases with $p_{\mathrm{T}}^{\mathrm{ch}}$ up to approximately 10 GeV and then remains constant until $p_{\mathrm{T}}^{\mathrm{ch}}$ approaches $p_{\mathrm{T}}^{\mathrm{jet}}$ where the rate increases again. In Pb+Pb collisions, the "fake" rate also includes tracks which are from the underlying event from the real collisions into which the jet is overlaid. The rate of these underlying event tracks increases with decreasing $p_{\mathrm{T}}^{\mathrm{ch}}$ and increasing collision centrality.

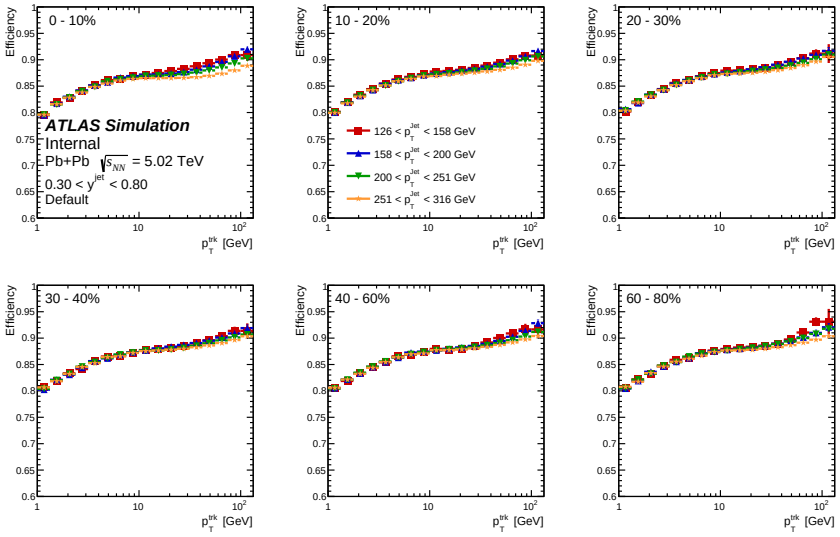

Figure 5.17: Efficiency for reconstructing tracks evaluated using the default tracking selections in different jet p_{T} bins and jet rapidity interval $0.3 < |y| < 0.8$ in the Pb+Pb MC overlay samples. Each panel is a different centrality bin..

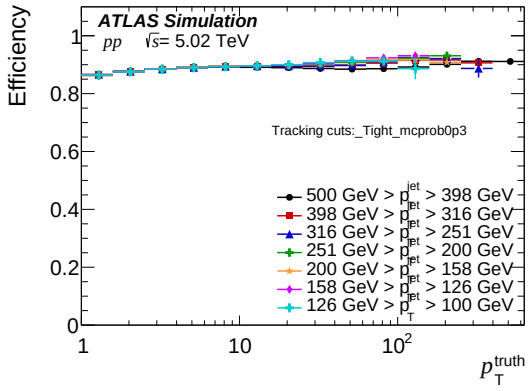

Figure 5.18: Efficiency for reconstructing tracks evaluated using the default tracking selections in different jet p_{T} bins, in the pp MC samples.

The contribution from UE is negligible for tracks with p_{T} above 10 GeV as no centrality dependence is seen. The Figure 5.20 excludes the very low p_{T} region where the distribution would be completely dominated by the UE. The size of the UE is then presented further in Figure 5.29. To separate the contribution of UE tracks (see section 5.3.6) from the fake tracks in Pb+Pb collisions and cross-check the centrality dependence of the fake rate, 200,000 MB Pb+Pb fully reconstructed HIJING MC [211] events were used. The HIJING MC generator is capable of simulating global properties of HI collisions. The estimated fake rate of tracks associated with jets with $p_{\mathrm{T}} > 40$ GeV is at the level of 1% and it exhibits similar behavior as observed in Figure 5.20. No significant dependence of the fake rate on the collision centrality was found [151].

To correct for the contribution from fake and secondary particles, charged particle distributions are estimated using reconstructed tracks that do not have a truth match as defined by criteria described in previous paragraphs. These distributions are then subtracted from the measured distributions both in the data and MC. This procedure is applied for tracks above 10 GeV in Pb+Pb collisions and for tracks above 1 GeV in pp collisions. The correction also removes any residual UE above 10 GeV in case of Pb+Pb. The choice of the 10 GeV cut is based on the centrality dependence of the rate of truth-unmatched tracks in MC overlay samples shown in Figure 5.20. The correction for UE, fake and secondary tracks below 10 GeV in Pb+Pb collisions is discussed in the next section.

5.3.6 Underlying event subtraction of tracks

Charged particles from the nucleon-nucleon scatterings that are not associated with the hard scattering in question constitute a background to the $D(p_{\mathrm{T}}, r)$ distributions that needs to be subtracted from the measured distributions. This background strongly depends on the collisions centrality and on the charged particle p_{T}. In the measurement of the inclusive jet fragmentation functions it was found that the UE contribution is negligible for charged particles with $p_{\mathrm{T}} > 10$ GeV [151]. This can be seen in the centrality dependence of the combined rate of fake and underlying event charged particles shown in Figure 5.20 where no significant centrality dependence is observed for track above 10 GeV.

In pp collisions, the UE is not subtracted. The pileup contribution is negligible and subtracting the intrinsic UE from the hard scattering processes would also necessitate a similar subtraction in the particle level fragmentation functions in Pb+Pb that would be generator dependent and make comparisons between pp and Pb+Pb non-trivial.

In Pb+Pb collisions, the UE from the soft processes is estimated using two independent methods. The "Map method" is nominally used for the analysis while the "Cone method" is used to provide a systematic uncertainty. The former uses charged particle distributions of $\mathrm{d}N_{\mathrm{ch}}/\mathrm{d}\phi\mathrm{d}\eta(\mathrm{cent}, p_{\mathrm{T}}, \mathrm{d}\Psi_{\mathrm{ch}})$ in MC overlay

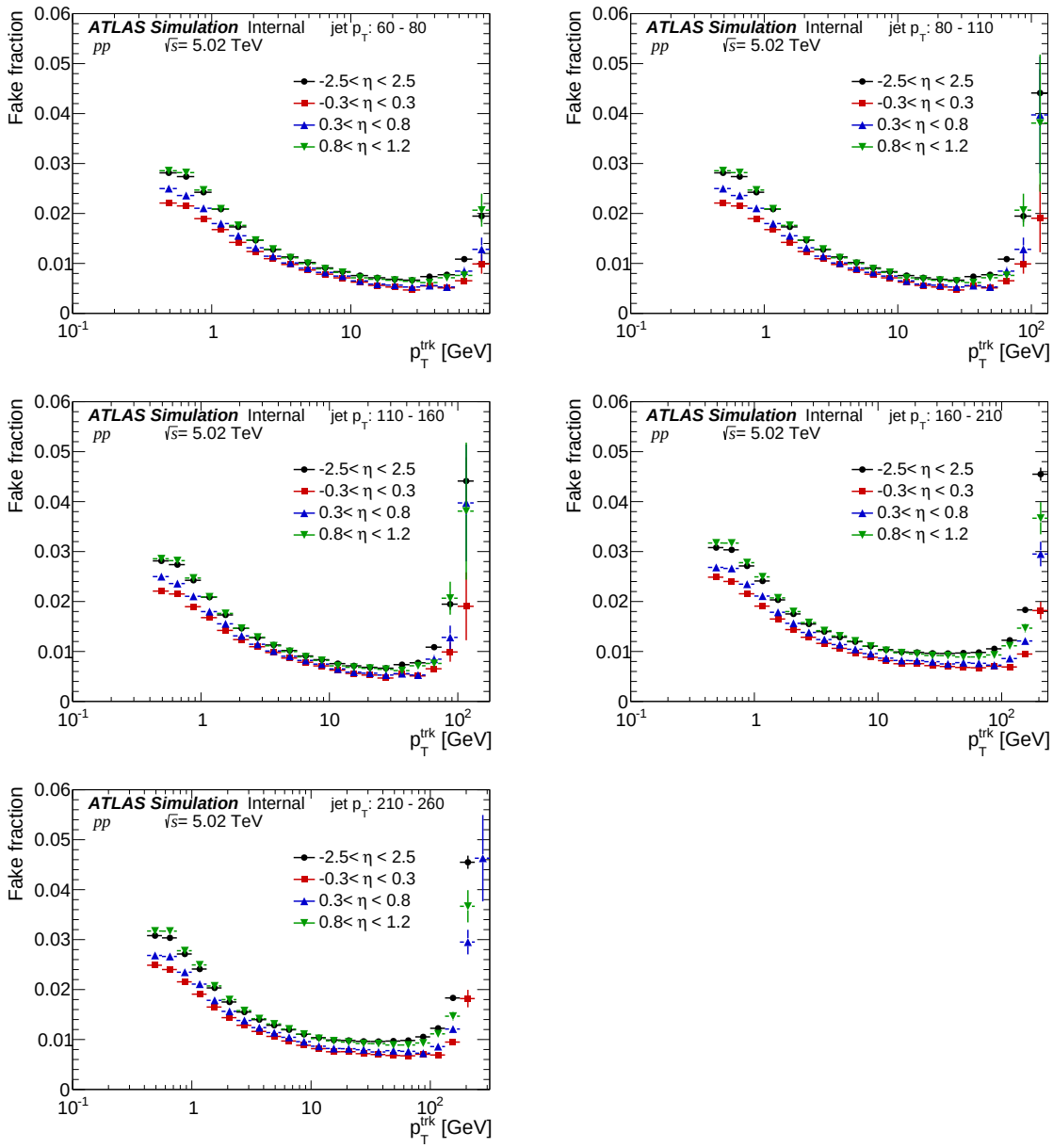

Figure 5.19: Fake rate for five different $p_{\mathrm{T}}^{\mathrm{jet}}$ selections in 5.02 TeV pp collisions and four pseudorapidity intervals. The fake rate is evaluated for default value of $\mathrm{mc}_{\mathrm{prob}}$ cut of 0.3 used in 2015 analysis. Figure from Ref. [206].

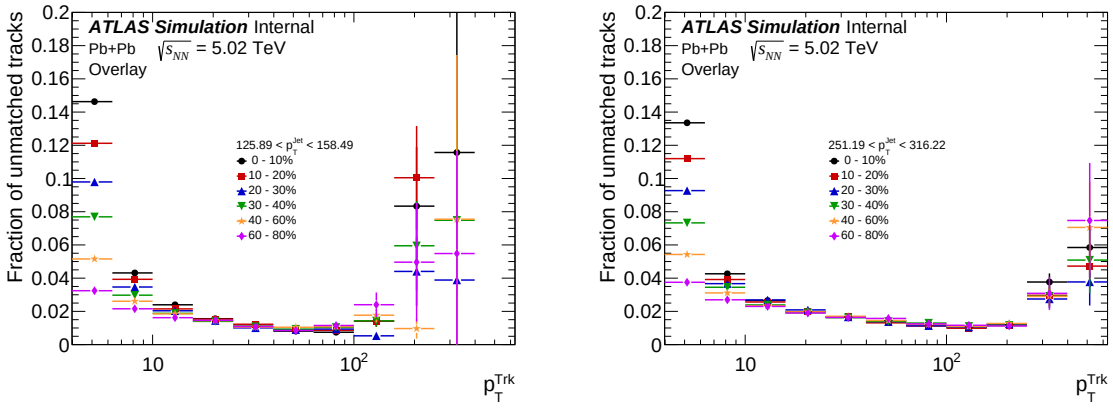

Figure 5.20: Rate of tracks unmatched to truth tracks in Pb+Pb collisions for different centrality selections as indicated on the plot as a function of $p_{\mathrm{T}}^{\mathrm{ch}}$. The unmatched tracks include both fake tracks and tracks from the underlying event. The panels show two $p_{\mathrm{T}}^{\mathrm{jet}}$ selections: 126-158 GeV (left) and 251-316 GeV (right). The low p_{T} part is omitted as it is dominated by the contribution from the UE. Figure from Ref. [206].

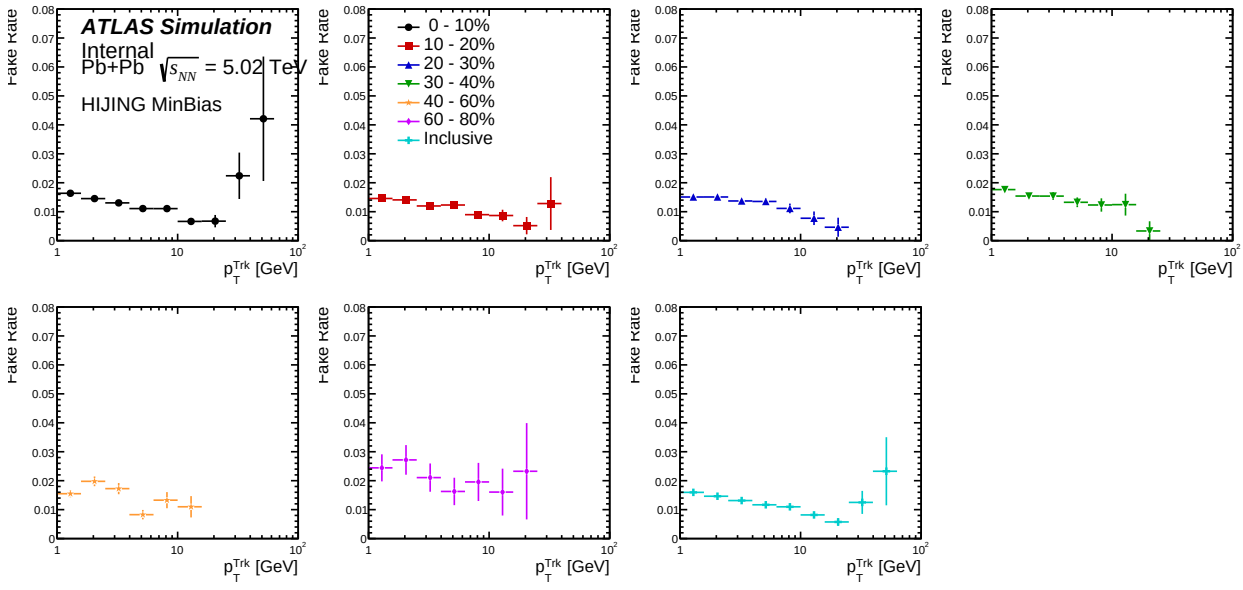

Figure 5.21: Fake rate for six different centrality intervals in 5.02 TeV Pb+Pb HIJING MC collisions. The fake rate is evaluated for default value of $\mathrm{mc}_{\mathrm{prob}} = 0.3$ in 2015 analysis.

events, while the latter evaluates the underlying event on an event-by-event basis using a grid of cones.

Map Method

In the "Map Method", $\eta - \phi$ maps of the average number of UE charged particles in a given annulus around a jet ($n_{\mathrm{ch}}^{\mathrm{UE^{Map}}}$) are determined in MC overlay events using tracks without a truth match. The maps are filled as a function of the distance from the jet, $p_{\mathrm{T}}^{\mathrm{jet}}$, η^{jet}, ϕ^{jet}, angle of the jet to the reaction plane[2] $\mathrm{d}\Psi_{\mathrm{ch}}$, p_{T} and centrality.

Examples of the these distributions for three different annuli (0–0.05, 0.25 – 0.30, 0.60–0.70), in the $\mathrm{d}\Psi$ interval of 0.80 – 1.00, for six collision centrality classes and for 1–1.6 GeV particles in 126 – 158 GeV jets are shown in Figure 5.22. The number of UE particles associated with a jet decreases with size of the annulus, decreasing centrality, increasing track p_{T} and increasing distance to the reaction plane.

The underlying event is then estimated by convoluting the $n_{\mathrm{ch}}^{\mathrm{UE^{Map}}}$ distributions with the η_{jet}, ϕ_{jet}, and $\mathrm{d}\Psi_{\mathrm{jet}}$ distributions of jets. The UE estimated by this method in MC consists of tracks without a truth match, and hence is the "true" underlying event by definition. This $\mathrm{UE^{MC}}$ can then be used to correct any correlations between the underlying event as determined by the cone method and the JER (discussed in later sections). The UE normalized to unit area, as a function of ΔR with respect to the jet axis is shown in Figure 5.23 for the lowest track p_{T} interval where the UE contribution is the largest. The two distributions are the UE with and without secondary particles. The UE strongly decreases for more peripheral collisions and for increasing track p_{T}. Little radial dependence is seen when the secondaries are not included. A small effect is expected because there is an enhancement in the number of jets at mid rapidity, along with a decrease in the UE yield as a function of η. Since the secondaries are generated by primary PYTHIA particles, the enhancement is expected towards the jet core, where there is a higher multiplicity of primary particles.

Cone Method

The cone method uses a regular grid of 9 cones of size $R = 0.8$ covering the full inner detector region (shown in Figure 5.24). The size of the cone corresponds to the radial phase space being investigated (0.8 in this case). Cones within a distance of $dR = 1.6$ to a reconstructed jet are excluded if $p_{\mathrm{T}}^{\mathrm{jet}} > 90$ GeV. They are also excluded if they contain a track with $p_{\mathrm{T}} > 10$ GeV. The 10 GeV was cut was chosen based on the small centrality dependence of the combined rate of fake and underlying event tracks above 10 GeV as shown in Figure 5.21. The fraction of events as a function of number of cones used in each centrality bin is shown in

[2]The reaction plane angle Ψ is determined on an event-by-event basis by a standard method using the ϕ variation of transverse energy in the forward calorimeter

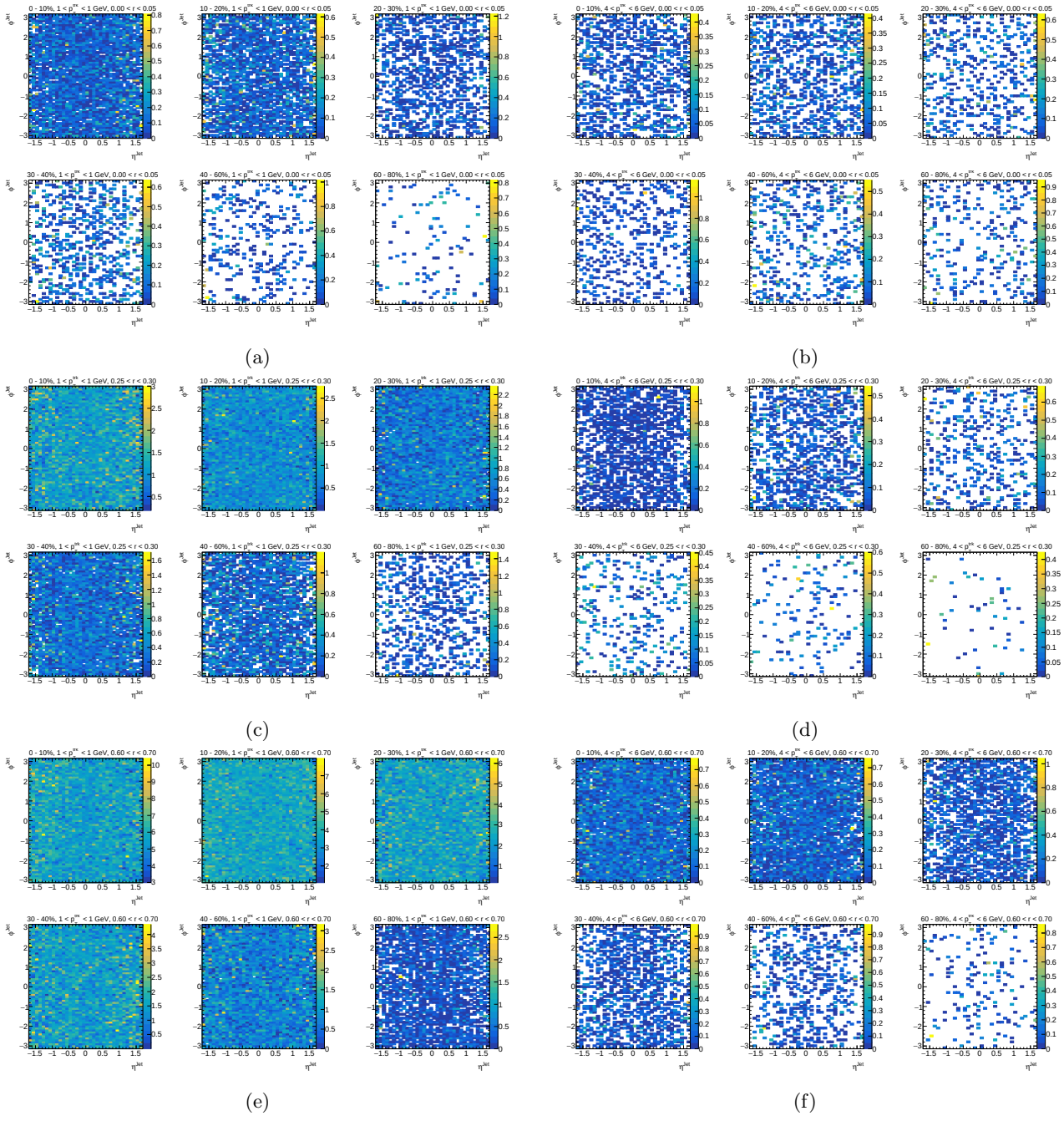

Figure 5.22: Per jet $n_{\mathrm{ch}}^{\mathrm{UE}^{\mathrm{Map}}}$ distributions of charged particles evaluated for 1–1.6 GeV (left) and 4–6 GeV tracks in the jet core (top), near the jet edge (middle), and far from the jet (bottom) for $\mathrm{d}\Psi$ in the interval 0.8–1.00, for six centralities, and 126–158 GeV jets.

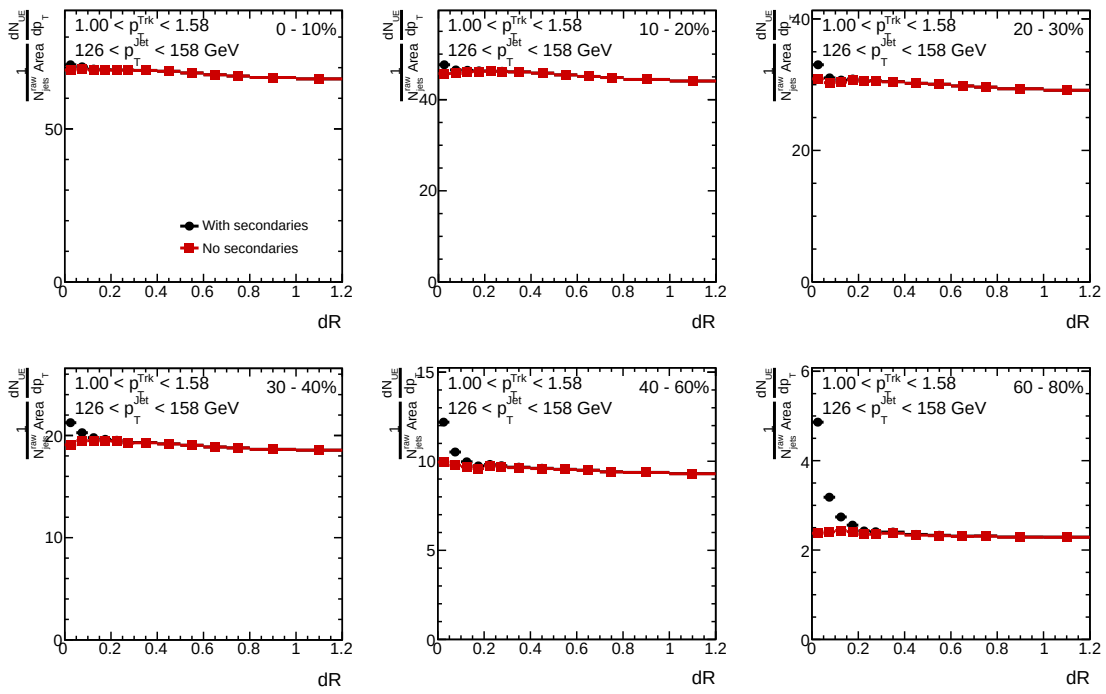

Figure 5.23: UE estimated from tracks which do not have an associated truth particle in jet with p_{T} from 126 to 158 GeV and for the lowest track p_{T} interval (1–1.58 GeV). The two different distribution shows the UE with and without the contribution from the secondary particles.

Figure 5.25. It can be seen that in the MC the number of cones used is consistent with there being no jet quenching. This is as expected since the jets in the Pb+Pb MC overlay are coming from PYTHIA and are unquenched. Moreover, quenching in central Pb+Pb data leads to only one jet causing exclusions, consistent with most events using 7 cones. For more peripheral Pb+Pb collisions, the cone distribution tends to look like the distribution with no quenching.

The resulting UE charged particle yields $\mathrm{d}n_{\mathrm{ch}}^{\mathrm{UECone}}/\mathrm{d}p_{\mathrm{T}}^{\mathrm{ch}}$ are evaluated over the 1 – 10 GeV range as a function of p_{T} $p_{\mathrm{T}}^{\mathrm{jet}}$ centrality, and r, and then averaged over all cones according to.

$$\frac{\mathrm{d}n_{\mathrm{ch}}^{\mathrm{UECone}}}{\mathrm{d}p_{\mathrm{T}}^{\mathrm{ch}}} = \frac{1}{N_{\mathrm{cones}}} \frac{1}{\varepsilon} \frac{\Delta N_{\mathrm{ch}}^{\mathrm{cone}}(p_{\mathrm{T}}^{\mathrm{ch}}, p_{\mathrm{T}}^{\mathrm{jet}}, \eta^{\mathrm{jet}})}{\Delta p_{\mathrm{T}}^{\mathrm{ch}}} \tag{5.5}$$

Here N_{cones} is the number of background cones associated with a given jet with $p_{\mathrm{T}}^{\mathrm{jet}}$. $\Delta N_{\mathrm{ch}}^{\mathrm{cone}}$ is the number of charged particles summed across all background cones associated to the jet in question. The cone method estimates the UE yields only from events containing jets included in the analysis, ensuring that the background automatically had the correct distribution of centralities within a given centrality bin.

The UE contribution as measured using the cone method in data needs to be further corrected for three

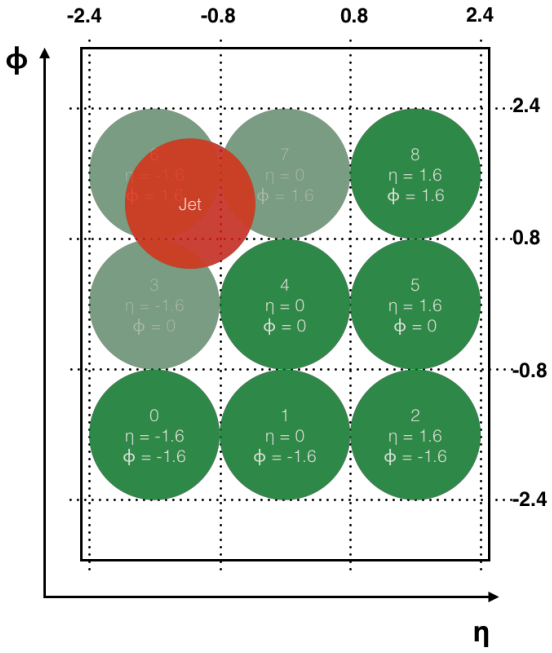

Figure 5.24: Illustration of the cone method to estimate the underlying event. Cones numbered 3, 6, and 7 are excluded based based on the jet shown in red.

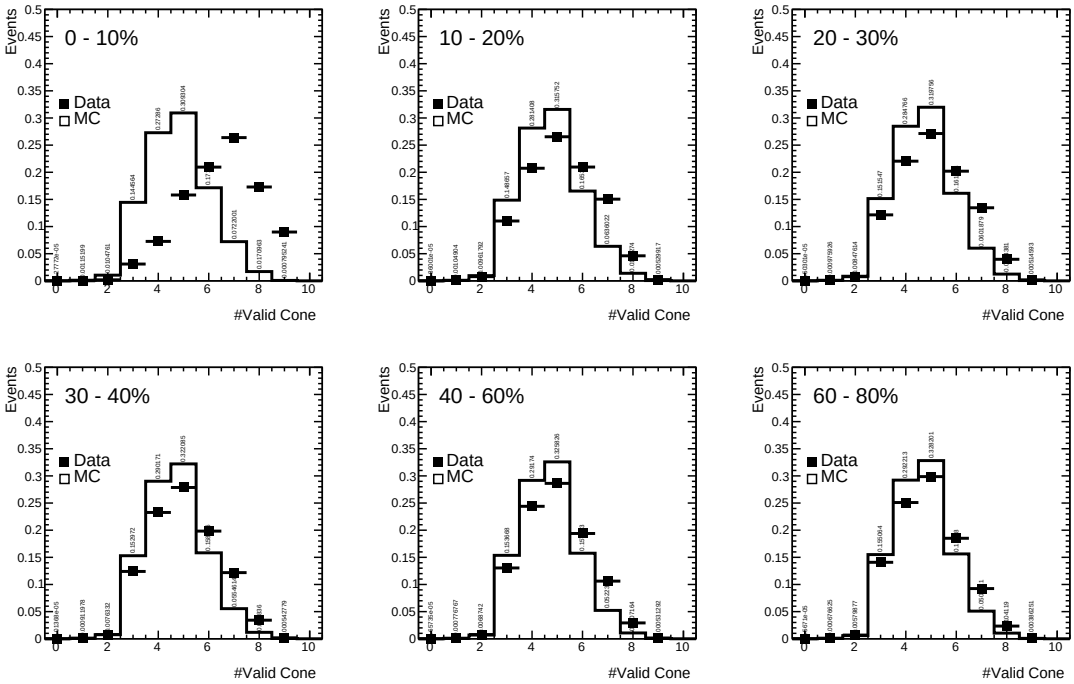

Figure 5.25: Fraction of events as a function of the number of cones used for the estimation of the underlying event.

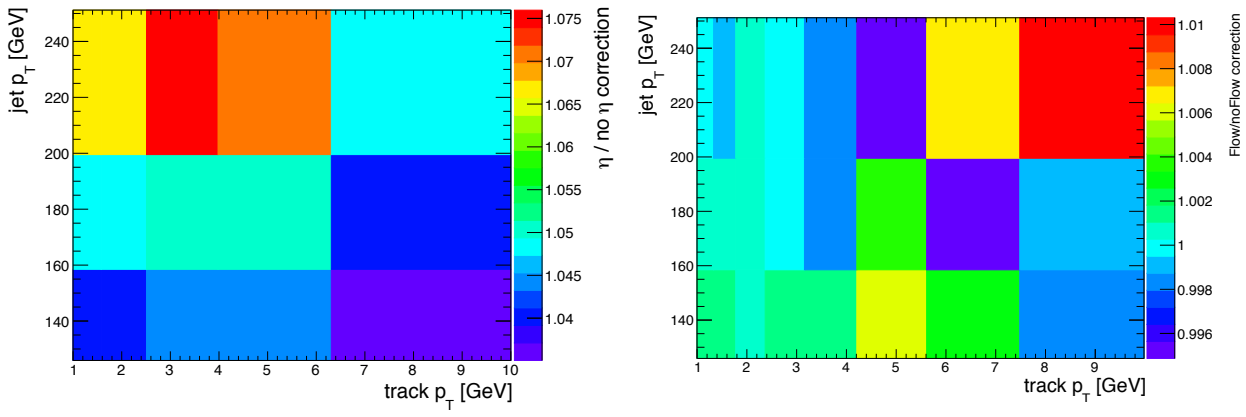

(a) (b)

Figure 5.26: Ratio of the $N_{\mathrm{ch}}^{\mathrm{UE\ cone}}$ distributions with and without the correction for (left) η dependence and (right) elliptic flow in the most central 0-10% Pb+Pb collisions, evaluated with a subset of the data (70k events). Figures from Ref. [206].

effects:

Correction for η-dependence: To account for differences in the yields of UE particles at the position of the jet and at the position of the track for the random cone entering the UE estimate, the η distribution of charged particles from MC overlay events is used to appropriately weigh the UE tracks. The correction is then the ratio of the value of the $\mathrm{d}n_{\mathrm{ch}}/\mathrm{d}\eta$ at the position of the jet and the track. The impact of the correction in 0-10% Pb+Pb collisions is shown in Figure 5.26a

Correction for flow: Elliptic flow is the characteristic sinusoidal modulation of the yields of particles along the azimuth in heavy ion collisions. The maximum amplitude of the modulation determines the reaction plane, with more momenta being measured in plane than out of plane. Ref. [59] provides a basic measurement of the magnitude of the elliptic flow, and its p_{T} dependence. The correction for this effect was based on a parametrization of the $p_{\mathrm{T}}^{\mathrm{ch}}$and centrality dependence of previously measured elliptic flow coefficients, v_2 [59]. The reaction plane angle Ψ is estimated on an event-by-event basis by using the ϕ variation of transverse energy in the forward calorimeter. The correction factor is evaluated as a function of the distance of the jet from the reaction plane $\cos 2(\phi^{\mathrm{jet}} - \Psi)$. The correction is less (greater) than unity for jets in a direction perpendicular (parallel) to the reaction plane. Jets perpendicular (parallel) to the plane typically have a lower (higher) UE, and a cone at a random position in the ID is corrected down (up). The size of the correction is at the level of a few percent, and decreases with increasing track p_{T}, as is shown in Figure 5.26b

UE and JER correlation: The interplay between the UE and the JER will be described here is discussed in further detail in Ref. [218]. Due to the steeply falling nature of the jet p_{T} spectra, the smearing due to jet energy resolution leads to a net migration of jets from lower p_{T} to higher p_{T} values (hereafter referred to as "up-feeding") such that a jet reconstructed with a given $p_{\mathrm{T}}^{\mathrm{rec}}$ will correspond, on average, to a lower truth jet p_{T}, $\langle p_{\mathrm{T}}^{\mathrm{truth}} \rangle$. The up-feeding was observed to induce in the MC a difference between the UE yields determined using the MC overlay events and the actual UE contribution to reconstructed jets. The magnitude of this difference was found to be centrality dependent and exhibited a weak p_{T} dependence. That difference was found to result from intrinsic correlations between the UE contribution to the yield of particles measured inside the jet and the MC p_{T} shift, $\Delta p_{\mathrm{T}}^{\mathrm{jet}} = p_{\mathrm{T}}^{\mathrm{rec}} - p_{\mathrm{T}}^{\mathrm{truth}}$. In particular, jets with positive (negative) $\Delta p_{\mathrm{T}}^{\mathrm{jet}}$ were found to have an UE contribution larger (smaller) than jets with $\Delta p_{\mathrm{T}}^{\mathrm{jet}} \sim 0$.

To correct for this effect, the centrality-, p_{T}-, $r-$ and $p_{\mathrm{T}}^{\mathrm{ch}}$-dependent multiplicative correction factors were applied on $\mathrm{d}n_{\mathrm{ch}}^{\mathrm{UE^{Cone}}}/\mathrm{d}p_{\mathrm{T}}^{\mathrm{ch}}$ distributions. These multiplicative factors, w_{UE}, were estimated as a ratio of UE distributions calculated in MC samples using the "Map method", $D(p_{\mathrm{T}}, r)_f$, and the "Cone Method".

$$w_{\mathrm{UE}}(p_{\mathrm{T}}) = \left. \frac{\mathrm{d}n_{\mathrm{ch}}^{\mathrm{UE^{Map}}}/\mathrm{d}p_{\mathrm{T}}^{\mathrm{ch}}}{\mathrm{d}n_{\mathrm{ch}}^{\mathrm{UE^{Cone}}}/\mathrm{d}p_{\mathrm{T}}^{\mathrm{ch}}} \right|_{\mathrm{MC}} \tag{5.6}$$

Examples of these factors are shown in Figure 5.27. The correction by construction corrects also for fakes and secondary contribution in the track p_{T} region 1-10 GeV in Pb+Pb collisions. The size of these corrections integrated over $r = 0.4$ is comparable to the UE-JER correction done in [151].

The absolute magnitude of the correction increases towards the higher track p_{T} in the jet core where the UE is smaller. This behavior has two contributions: the intrinsic correlations between the UE contribution to the yield of particles measured inside the jet and the MC p_{T} shift as it was discussed earlier, and the correlation of production of secondary particles with the jet. The production of secondary particles is associated with presence of primary particles. Thus, the production of secondary particles is enhanced in the jet due to the higher density of primary particles compared to the regions outside a jet. This was shown in Figure 5.23 where the UE evaluated in term of particles without matching to truth particles in MC with and without the contribution from secondary particles is presented and where the yield of secondary particles is significant only at smaller dR, that is, within a jet. Figure 5.23 also shows that the relative yield of secondary particles to the yield of the UE particles is increasing with decreasing collisions centrality. Furthermore, the relative contribution of secondary particles to the UE increases with the track p_{T} as the fraction of the secondary particles decreases only slowly with the increasing track p_{T} (Figure 5.20), however,

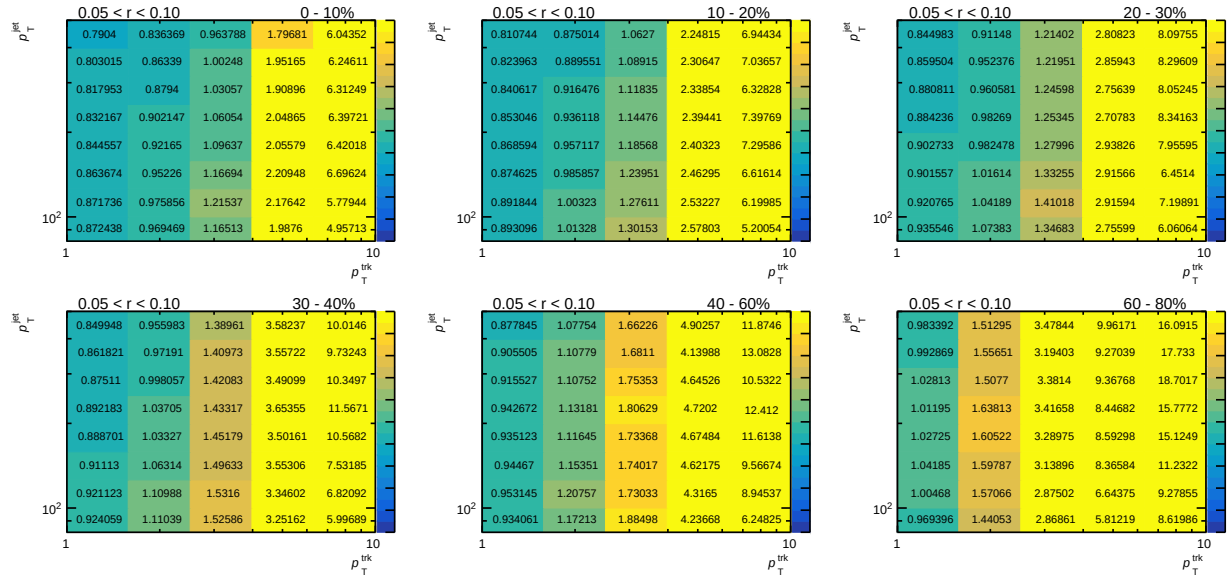

(a)

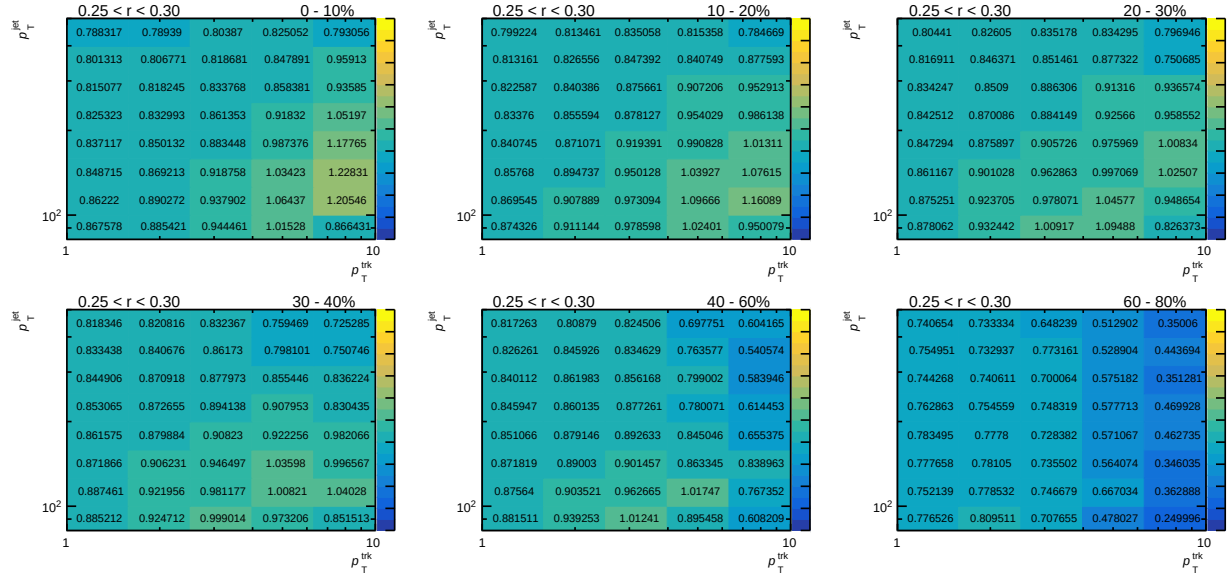

(b)

Figure 5.27: The multiplicative correction factors that correct for the correlation between the UE and the JER, fake and secondary particles in different centrality classes and $0.05 < r < 0.10$ (top) and $0.25 < r < 0.30$ (bottom).

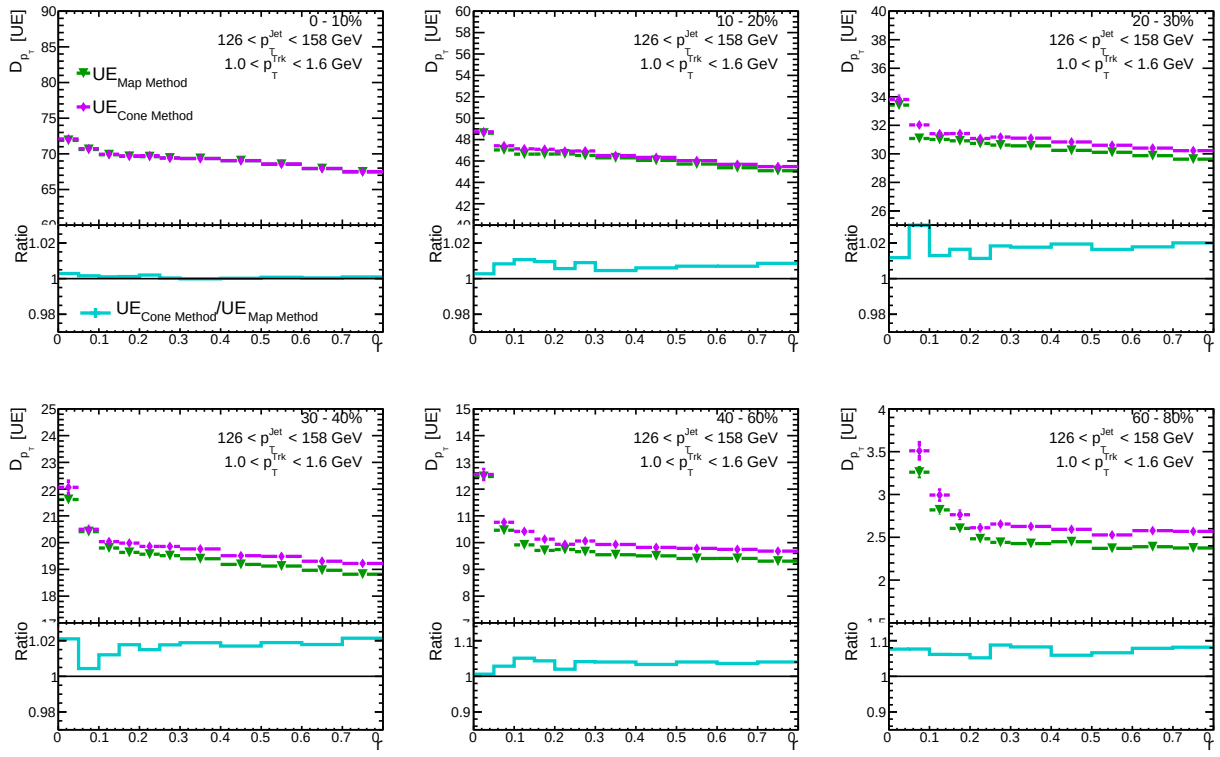

Figure 5.28: The difference between the cone method and the map method as a function for r for 0-10% Pb+Pb collisions, in 126-158 GeV jets, 1-1.6 GeV tracks.

the UE decreases strongly with the increasing track p_{T} (Figure 5.29). This results in lower UE contribution estimated using the MB collisions where tracks are not associated to a jet.

As shown in Figure 5.28, the two UE estimation methods give almost identical UE at angles outside the $R = 0.4$ jet as the role of the two effects discussed here decreases. The difference between the methods varies slowly with $p_{\mathrm{T}}^{\mathrm{jet}}$ and track p_{T}, with a small centrality dependence coming from fact that the underlying event strongly depends on the centrality.

For $p_{\mathrm{T}} > 10$ GeV and in pp system fake contribution is corrected as described at the beginning of Section 5.3.4. The corrected UE distributions, $\mathrm{d}n_{\mathrm{ch}}^{\mathrm{UE+fake}}/\mathrm{d}p_{\mathrm{T}}^{\mathrm{ch}}$ are then subtracted from measured distributions as follows

$$\frac{\mathrm{d}n_{\mathrm{ch}}^{\mathrm{sub}}}{\mathrm{d}p_{\mathrm{T}}^{\mathrm{ch}}} = \frac{\mathrm{d}n_{\mathrm{ch}}^{\mathrm{meas}}}{\mathrm{d}p_{\mathrm{T}}^{\mathrm{ch}}} - w_{\mathrm{UE}}(p_{\mathrm{T}}) \left(\frac{\mathrm{d}n_{\mathrm{ch}}^{\mathrm{UE^{Cone}}}}{\mathrm{d}p_{\mathrm{T}}^{\mathrm{ch}}}\bigg|_{\mathrm{Data}} \right) = \frac{\mathrm{d}n_{\mathrm{ch}}^{\mathrm{meas}}}{\mathrm{d}p_{\mathrm{T}}^{\mathrm{ch}}} - \frac{\mathrm{d}n_{\mathrm{ch}}^{\mathrm{UE+fake}}}{\mathrm{d}p_{\mathrm{T}}^{\mathrm{ch}}} \tag{5.7}$$

The impact of the underlying event and fake track subtraction on the $D(p_{\mathrm{T}}, r)$ distributions is shown in Figure 5.29. The magnitude of this correction is the largest for low track p_{T} in central Pb+Pb collisions

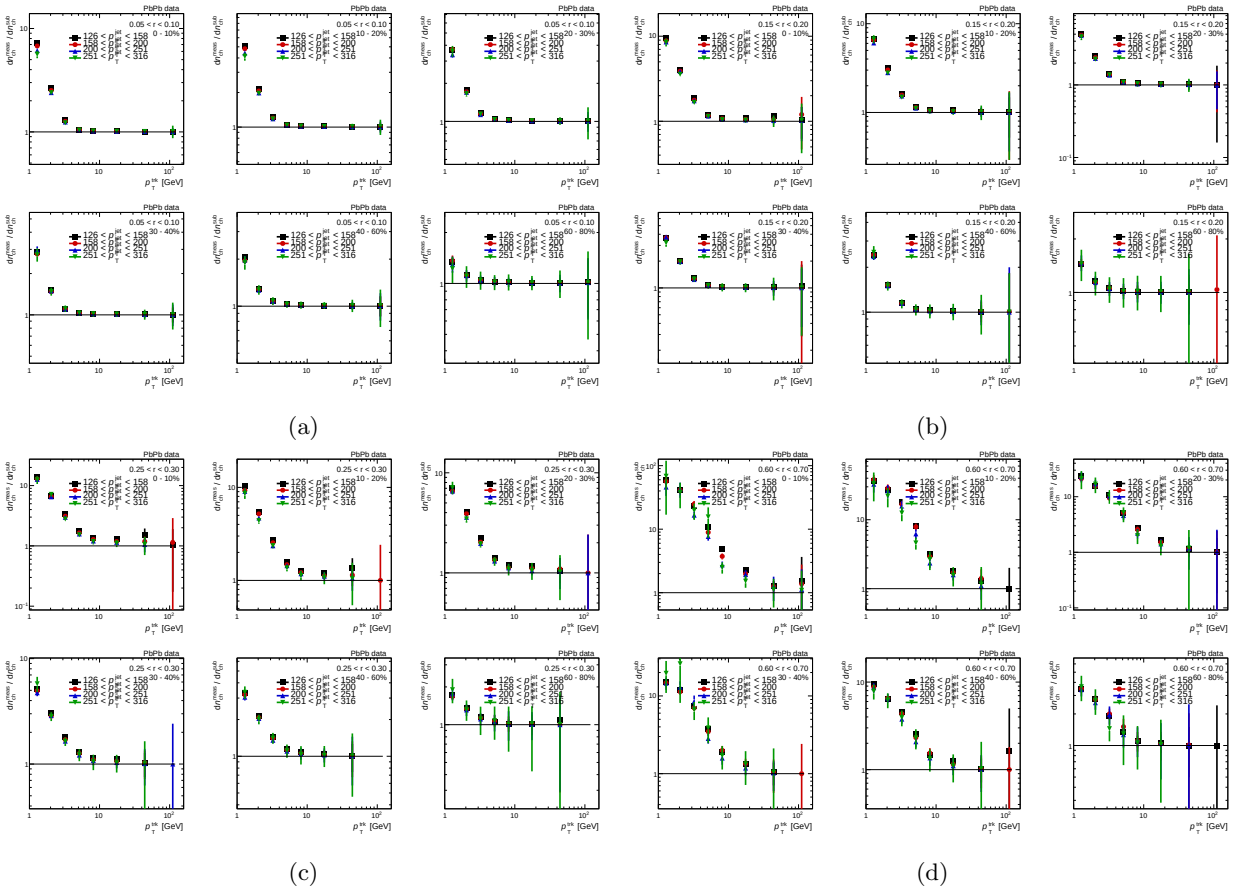

Figure 5.29: Ratio between the raw $D(p_{\mathrm{T}}, r)$ distributions before and after the UE subtraction in different centrality classes and different jet p_{T} intervals for different distances from the jet axis: $0.05 < r < 0.10$, $0.15 < r < 0.20$, $0.25 < r < 0.30$, $0.60 < r < 0.70$.

and the largest annulus. In the most extreme case the S/B ratios can be as low as 1/100. The size of the correction decreases rapidly with increasing track p_{T}, decreasing centrality and towards the core of the jet. In *pp* collisions the magnitude of the fake track subtraction is always much less than 5%.

The basic performance of the UE subtraction was tested in the MC overlay dataset. This closure test was performed using the MC overlay sample that has the same UE as in the data and will be discussed in the next subsection. The truth $R_{D(p_{\mathrm{T}},r)}$ distributions were compared to fully corrected $R_{D(p_{\mathrm{T}},r)}$ distributions where the UE contribution is subtracted by the same method as used in the data (see Figure 5.41a). From the above mentioned tests we concluded that the UE subtraction procedure is correct and works well. The UE estimate is subjected to a variation as part of the systematic uncertainties. For the *pp* data, we have not performed any UE subtraction.

5.3.7 Unfolding

Unfolding procedures are used to remove Instrumental effects like detector resolutions and allow for direct comparisons to theory calculations [219]. This is done via the approach based on Bayes theorem that is implemented in the RooUnfold package and uses "response matrices" [220]. These matrices are multidimensional object that created using the MC and describe the migration between the reconstructed quantities and the corresponding truth quantities that are to be unfolded.

This analysis uses three separate unfolding procedures that are discussed in this section.

- One dimensional unfolding for the $p_{\mathrm{T}}^{\mathrm{jet}}$ spectra for the normalization.
- Two dimensional Bayesian unfolding in $p_{\mathrm{T}}^{\mathrm{ch}}$ and $p_{\mathrm{T}}^{\mathrm{jet}}$ for jet p_{T} dependent yields of charged particles.
- Bin by bin correction for the jet and track position resolution.

To achieve better correspondence with the data, the response matrices for both the one and two dimensional unfolding are reweighted so that the distributions match the shapes in the reconstructed data.

One Dimensional Unfolding for Jet Spectra

The charged particle spectra need to be normalized by the number of jets in given jet p_{T} interval. Thus, the jet spectra needs to be corrected for bin migration due to the finite JER by unfolding procedure. The unfolding is done via a one dimensional Bayesian unfolding procedure with 4 iterations implemented as part of the RooUnfold [220] package. The *pp* and Pb+Pb MC samples are used to construct two dimensional response matrices in terms of $p_{\mathrm{T}}^{\mathrm{jet,truth}}$ and $p_{\mathrm{T}}^{\mathrm{jet,reco}}$. These matrices can be seen in Figure 5.30 and are evaluated separately for *pp* and in different centrality intervals for Pb+Pb collisions. The technical closure of this unfolding procedure (done using un-reweighted response matrices to unfold the reconstructed jet spectra) is shown in Figure 5.31, as a function of $p_{\mathrm{T}}^{\mathrm{jet}}$ for jets in the $|y| < 1.7$ region. A good recovery of the truth distribution is seen for both 1% for Pb+Pb and *pp* MC samples.

Two Dimensional Unfolding for Charged Particle Spectra

The observed correlation between the jet response in the detector and the jet fragmentation necessitates a two dimensional unfolding [151]. For example, gluon jets, which have in general a softer fragmentation function, are observed to have a lower energy response than quark jets [190]. We use the RooUnfold [220] implementation of the two dimensional iterative Bayesian unfolding [221] with 4 iterations. The MC Pb+Pb and *pp* samples are used to construct a 4-dimensional response matrix in $p_{\mathrm{T}}^{\mathrm{trk,Truth}}$, $p_{\mathrm{T}}^{\mathrm{jet,truth}}$, $p_{\mathrm{T}}^{\mathrm{trk,reco}}$, and

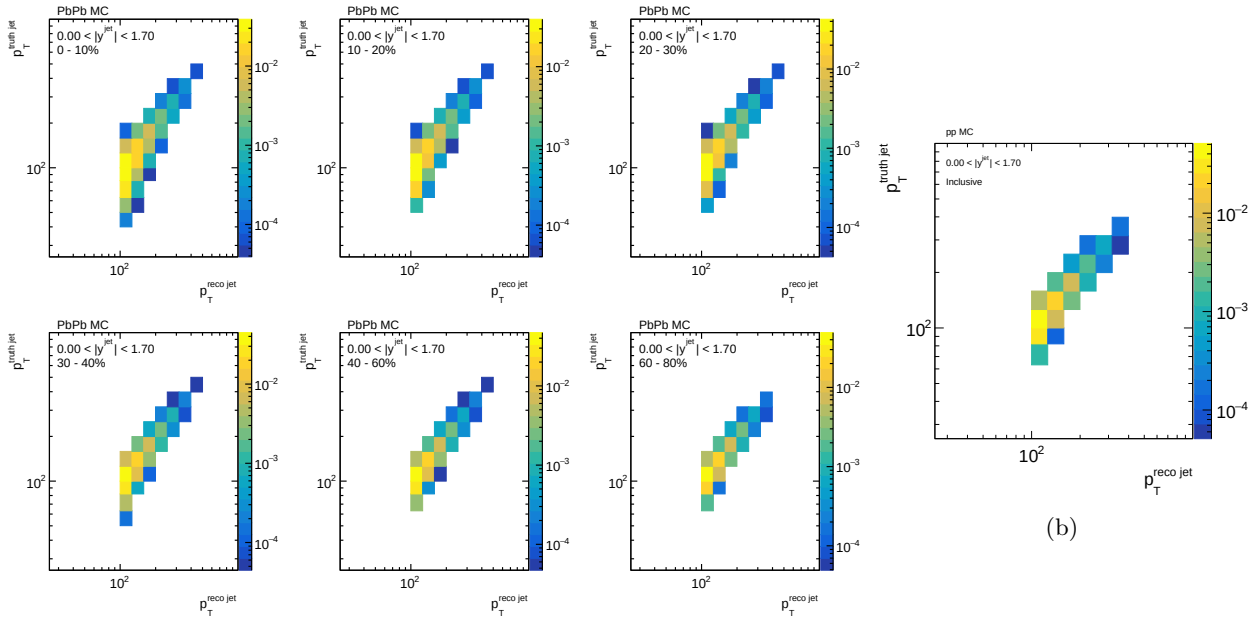

(a) (b)

Figure 5.30: The response matrices in terms of $p_{\mathrm{T}}^{\mathrm{jet,reco}}$ and $p_{\mathrm{T}}^{\mathrm{jet,truth}}$ in the jet $|y|$ <1.7 region, in (left) data overlay Pb+Pb MC samples, with each panel being a different centrality bin and (right) in *pp* MC samples.

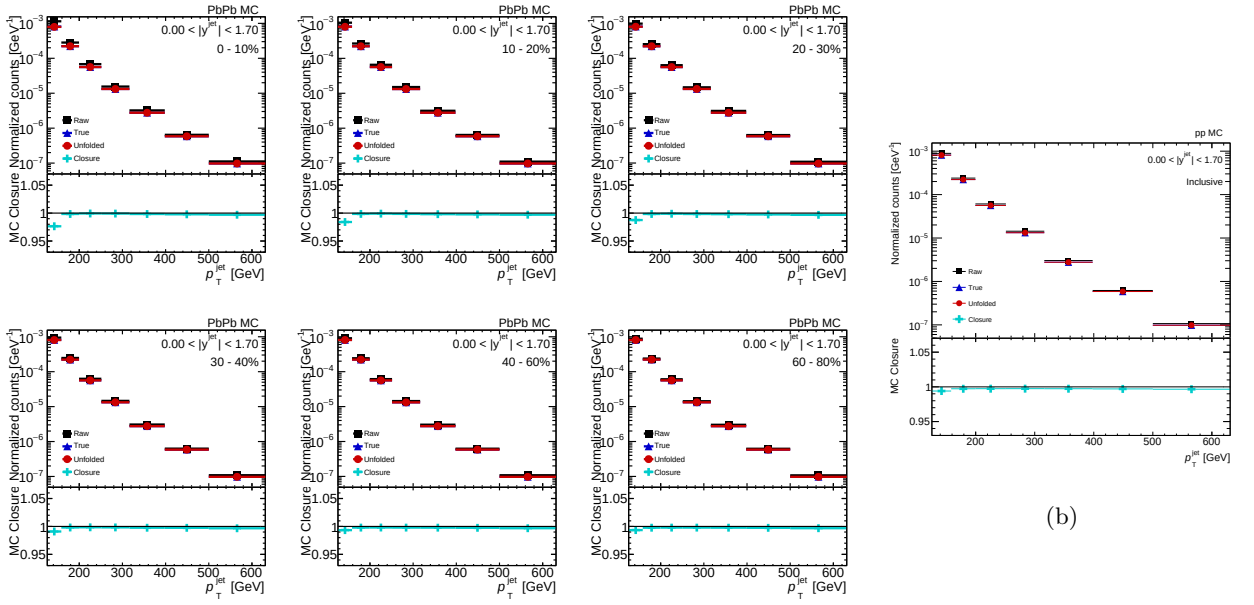

(a) (b)

Figure 5.31: The jet spectra and MC closure as a function of $p_{\mathrm{T}}^{\mathrm{jet}}$ in the jet $|y|$ <1.7 region, in (left) data overlay Pb+Pb MC samples, with each panel being a different centrality bin and (right) in *pp* MC samples. The closure is seen to be well within 1%.

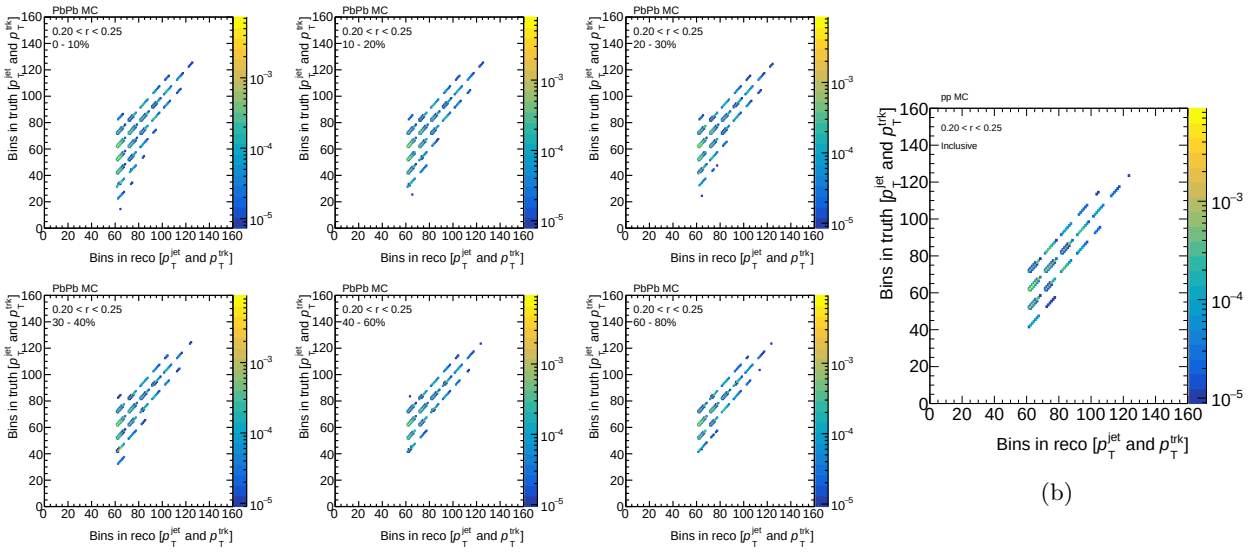

(a) (b)

Figure 5.32: The response matrices in terms of $p_{\mathrm{T}}^{\mathrm{jet,reco}}$, $p_{\mathrm{T}}^{\mathrm{jet,truth}}$, $p_{\mathrm{T}}^{\mathrm{trk,reco}}$, and $p_{\mathrm{T}}^{\mathrm{trk,Truth}}$, for reconstructed track - reconstructed jet pairs, that have $0.20 < r < 0.25$, in (left) data overlay Pb+Pb MC samples, with each panel being a different centrality bin and (right) in pp MC samples.

$p_{\mathrm{T}}^{\mathrm{jet,reco}}$, shown in Figure 5.32. The response matrix A_{ijkl} describes the probability that an event from the truth track p_{T} bin j and truth jet p_{T} bin l is found in reconstructed bin i,k:

$$\mu_{jl} = \sum_{i,k} A_{ijkl} x_{jl}^{\mathrm{truth}}. \tag{5.8}$$

Bin-by-bin correction for Angular resolution

There is an additional unfolding procedure applied in this analysis to correct for the jet and the track position resolution that results in the migration in angular distance r. The migration is dominated by the poor jet angular resolution (shown in Figure 4.12), since the track angular resolution shown in Figure 5.33 is very good.

The correction factors are derived using response matrices that correlate the reconstructed and truth angular distance r. These matrices are evaluated for different jet and track p_{T} in different centrality classes. Examples of the response matrices are shown in Figure 5.34 for Pb+Pb and pp MC samples. The bin-by-bin correction procedure is applied to $D(p_{\mathrm{T}}, r)$ distribution unfolded to the particle level in terms of track and jet p_{T} by the two unfolding procedures discussed above. The correction factors for angular resolution were derived using the the reconstructed jets and tracks where the reconstructed jet and track p_{T} is replaced by the corresponding truth p_{T}. The bin-by-bin factors are then estimated as ratio of projections from the

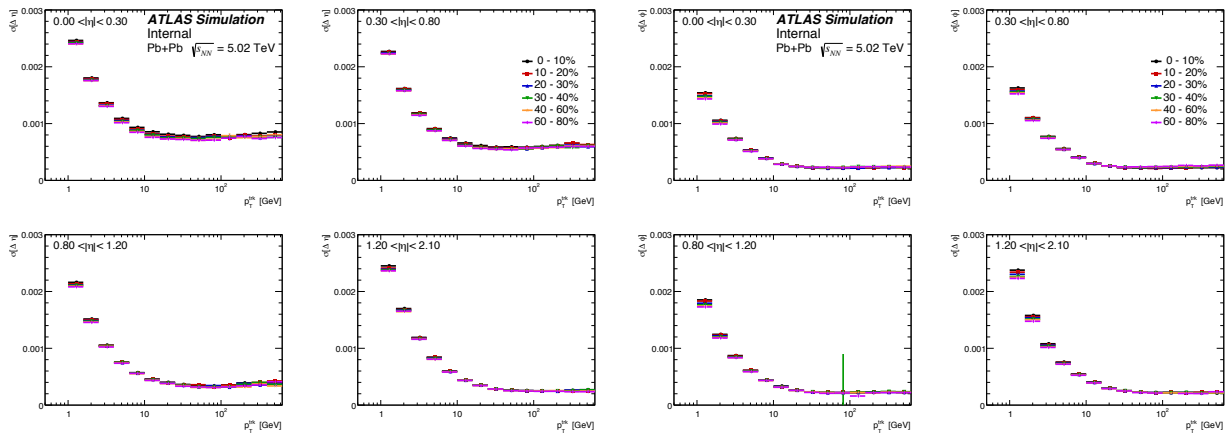

(a) (b)

Figure 5.33: The (left) η and (right) ϕ position resolution of the tracker as a function of $p_{\mathrm{T}}^{\mathrm{truth}}$ for different centrality and η regions in Pb+Pb MC overlay samples. The different curves are different centralities, and it can be seen that there is no centrality dependence.

response matrices on the truth and reconstructed axis. These correction factors are shown in Figure 5.35 for Pb+Pb and pp collisions as a function of r. The efficiency and purity are a measure of what fraction of jets are reconstructed in the same bin as their generator level counterpart. The efficiency is given by the fractional distribution of reconstructed jets at a fixed truth $p_{\mathrm{T}}^{\mathrm{jet}}$ while the purity is given by the fractional distribution of truth jets at a fixed reconstructed $p_{\mathrm{T}}^{\mathrm{jet}}$. These are shown in the Figures 5.36.

The robustness of this correction can be validated by constructing $D(p_{\mathrm{T}}, r)$ distributions using a coarser p_{T} binning (entire analysis chain is re-done) and comparing them to a summation of the individually unfolded narrow bins. This comparison can be seen in Figure 5.37, for $1 < p_{\mathrm{T}} < 4$ GeV, $126 < p_{\mathrm{T}}^{\mathrm{jet}} < 158$ GeV, for 0-10%. central Pb+Pb and pp collisions, and is seen to be unity.

It can be seen that these corrections become large at the edges of the jet cone for tracks that carry a significant fraction of the jet momentum. This is an artifact of the jet reconstruction algorithm, where a truth track near the edge of a truth jet will pull the reconstructed jet towards itself, causing a depletion of high p_{T} particles at the edge of the jet cone. This depletion can be seen in the distribution of truth charged particles in truth jets shown in Figure 5.38 and was also seen in Ref. [222]. These large factors result in a large non-closure near the jet edge for tracks carrying a significant momentum fraction of the jet. To exclude these effects, the results are only shown for tracks that show a closure of less than 5%.

The $D(p_{\mathrm{T}}, r)$ distributions at various stages of the analysis in pp and Pb+Pb MC and data are shown in Figure 5.39 and Figure 5.40.

The MC closure of the charged particle spectra as a function of p_{T} in pp MC and Pb+Pb MC overlay

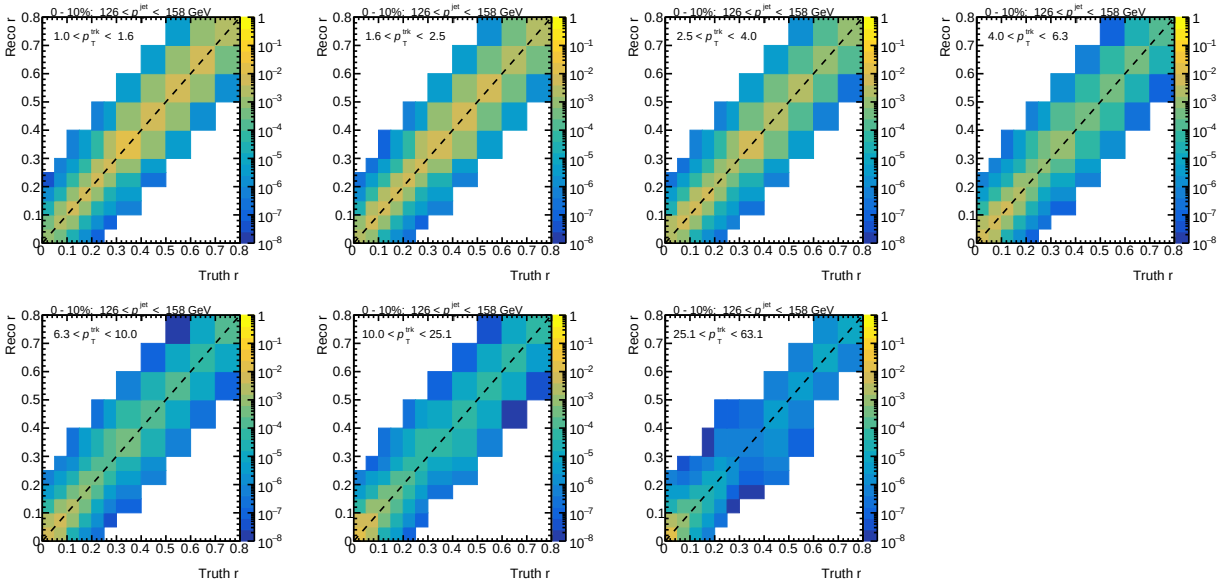

(a)

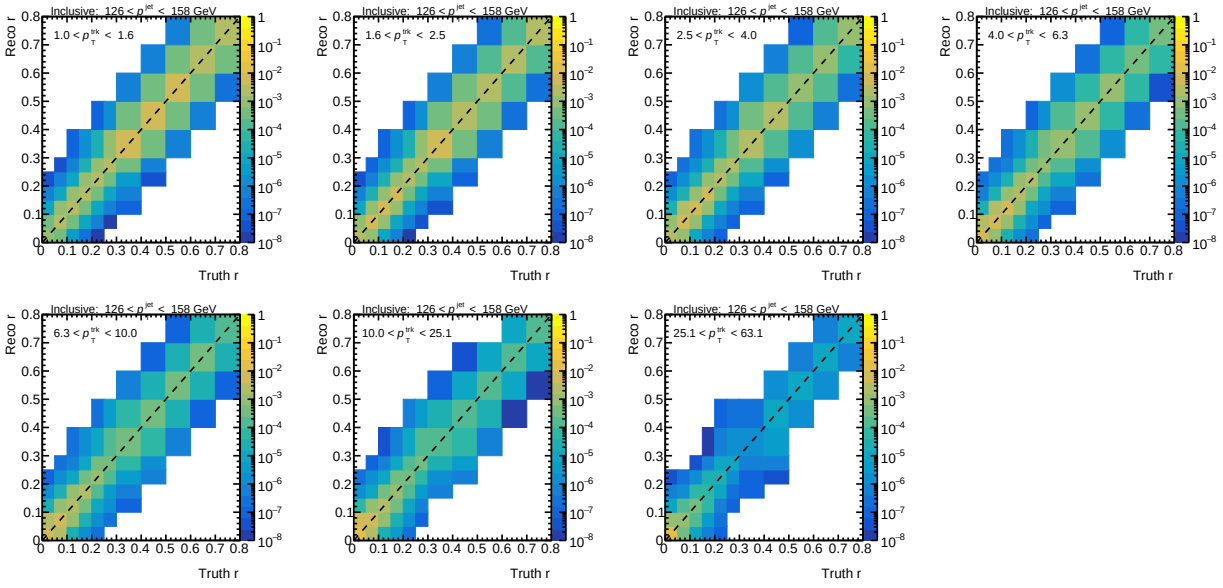

(b)

Figure 5.34: The response matrix for the bin by bin correction applied to the unfolded charged particle spectra. This accounts for the jet position resolution. Each panel is a different $p_{\mathrm{T}}^{\mathrm{ch}}$ bin, for $126 < p_{\mathrm{T}}^{\mathrm{jet}} < 158$ GeV jets, in (top) central collisions from Pb+Pb MC overlay samples and (bottom) *pp* MC samples.

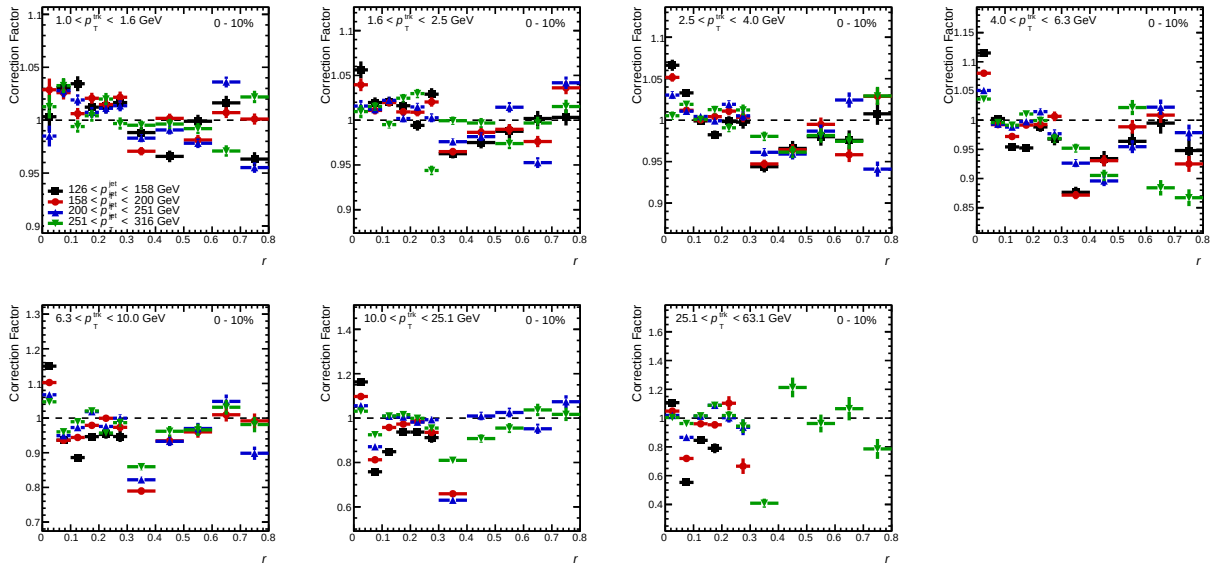

(a)

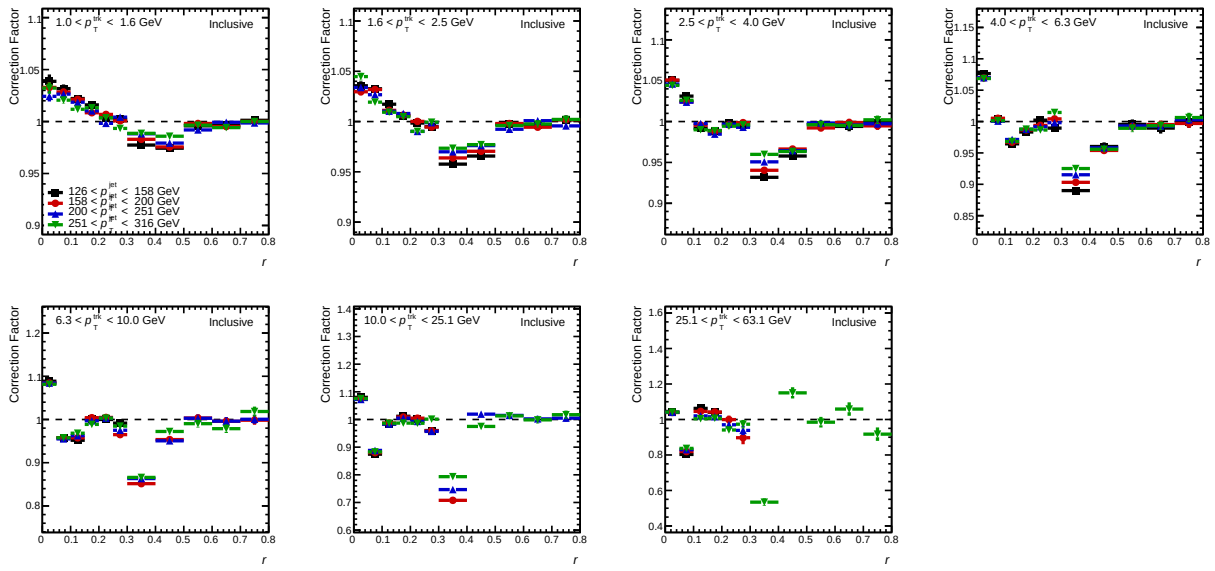

(b)

Figure 5.35: The correction factors applied to the unfolded charged particle spectra, as a function of r, with each panel showing a different track p_{T} bin, and each curve showing a different $p_{\mathrm{T}}^{\mathrm{jet}}$ range, in (top) central collisions from Pb+Pb MC overlay samples and (bottom) pp MC samples.

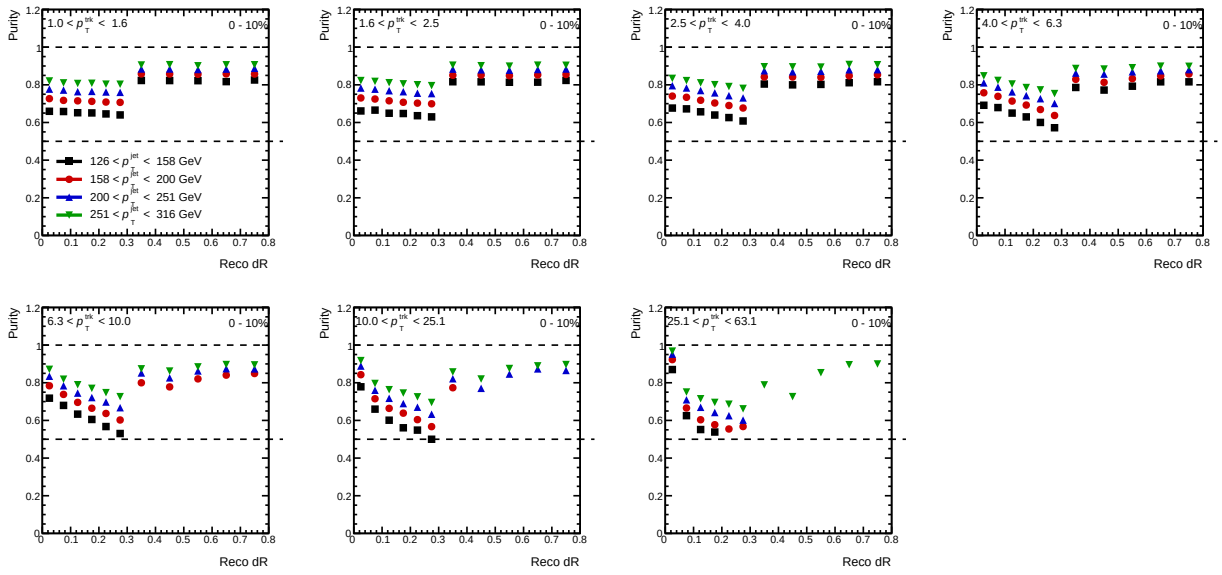

(a)

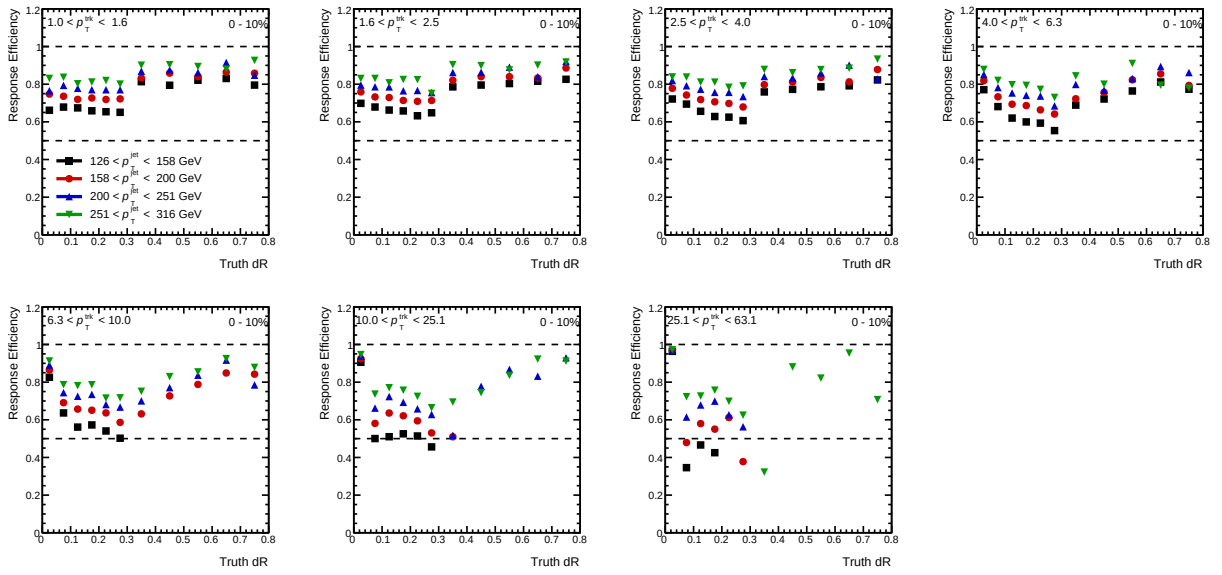

(b)

Figure 5.36: The (top) purity and (bottom) efficiency of the bin-by-bin unfolding factors used to correct for the angular resolution for different $p_{\mathrm{T}}^{\mathrm{ch}}$ ranges tracks (in different panels), shown as a function of r for different $p_{\mathrm{T}}^{\mathrm{jet}}$ ranges, in the most central 0–10% Pb+Pb collisions.

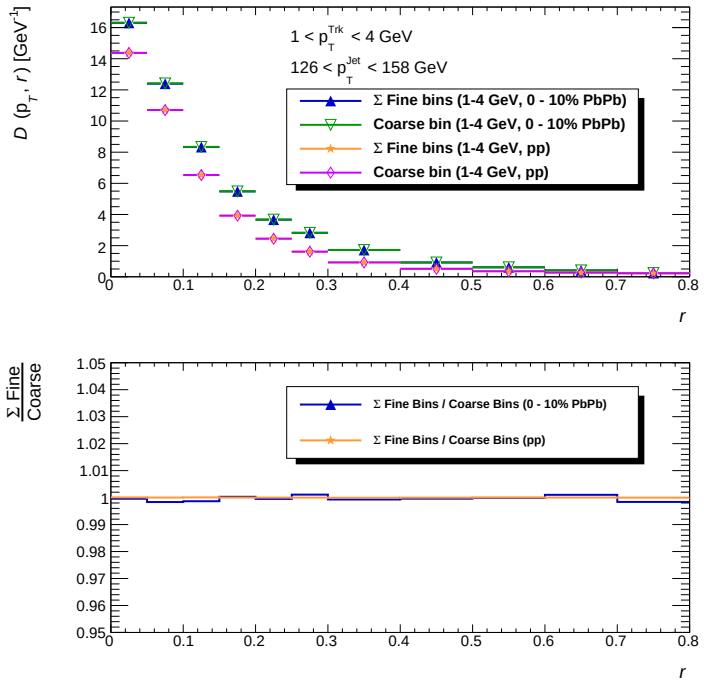

Figure 5.37: The $D(p_{\mathrm{T}}, r)$ distributions in pp and 0–10% central Pb+Pb, constructed using a single bin from 1–4 GeV (merging the first three p_{T} bins in this analysis) compared to the $D(p_{\mathrm{T}}, r)$ distributions constructed by adding up the bins individually: 1–1.6 GeV, 1.6–2.5 GeV and 2.5–4 GeV. This comparison tests the robustness of the angular bin by bin correction and its dependence on the width of the p_{T} bins.

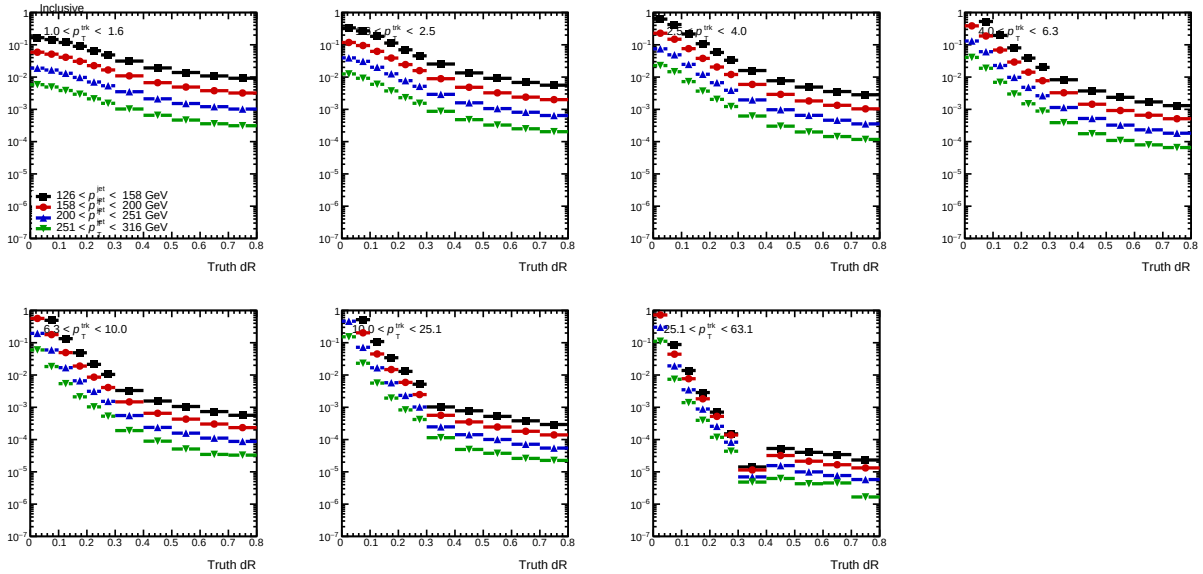

Figure 5.38: The distribution of truth charged particles in truth jets for different track p_{T} ranges and $p_{\mathrm{T}}^{\mathrm{jet}}$ ranges in pp collisions. It can be seen that there is a kink in the distribution at the jet edge for high p_{T} tracks.

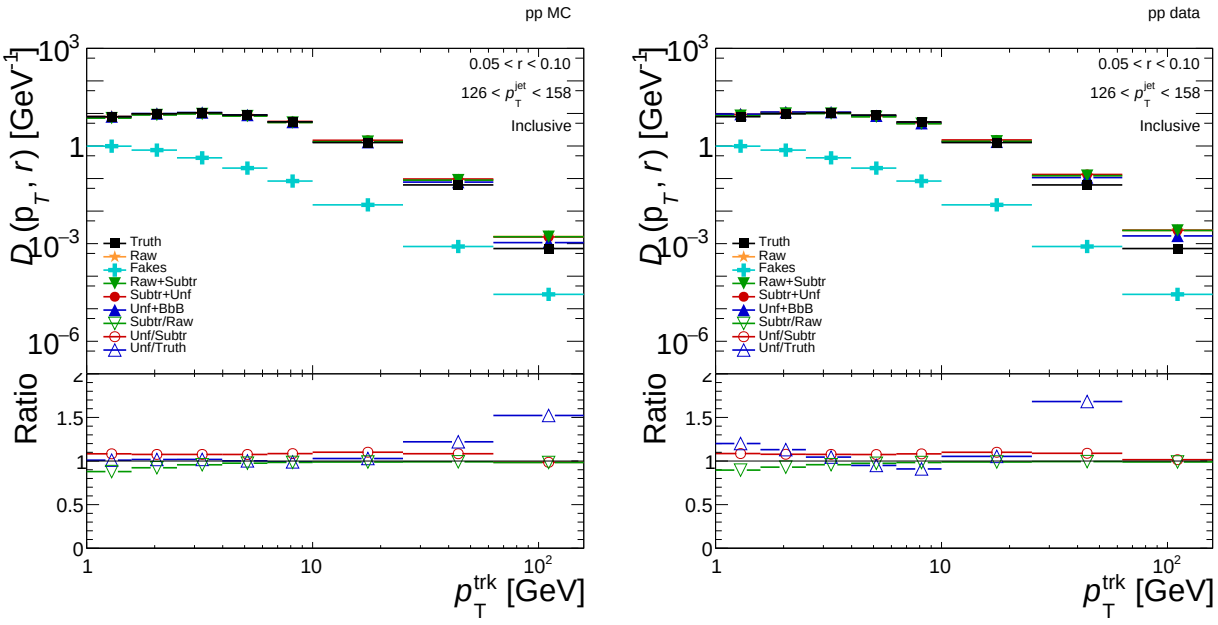

(a) (b)

Figure 5.39: The evolution of the $D(p_{\mathrm{T}}, r)$ distributions for pp MC (left) and data (right) as various corrections are applied. The spectra is shown for tracks with $0.05 < \Delta r < 0.10$ away from the jet axis, for $126 < p_{\mathrm{T}}^{\mathrm{jet}} < 158$ GeV. The ratios showing the effect of the unfolding and bin by bin corrections (left and right), as well as the MC closure (left) are shown in the lower half of the panels.

samples can be seen in Figures 5.41 and is well within 1% for low p_{T} particles.

5.4 Systematic Uncertainties

This section gives an overview of the sources of systematic uncertainties on the pp and Pb+Pb charged particle spectra associated with jet. These include:

- Jet energy scale
- Jet energy resolution
- Tracking selections
- Unfolding
- Underlying event contribution
- MC non-closure

The systematic uncertainties are evaluated separately for $D(p_{\mathrm{T}}, r)$ distributions and for their ratios as a function of jet p_{T} for pp and Pb+Pb collisions. For each systematic variation, the entire analysis

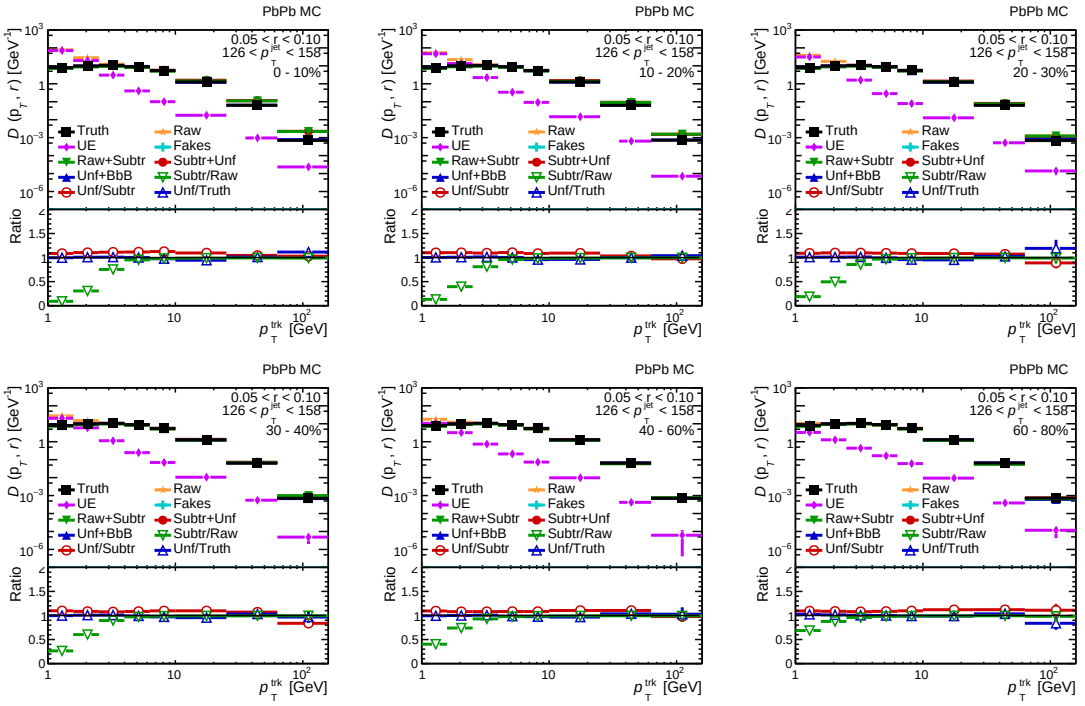

(a)

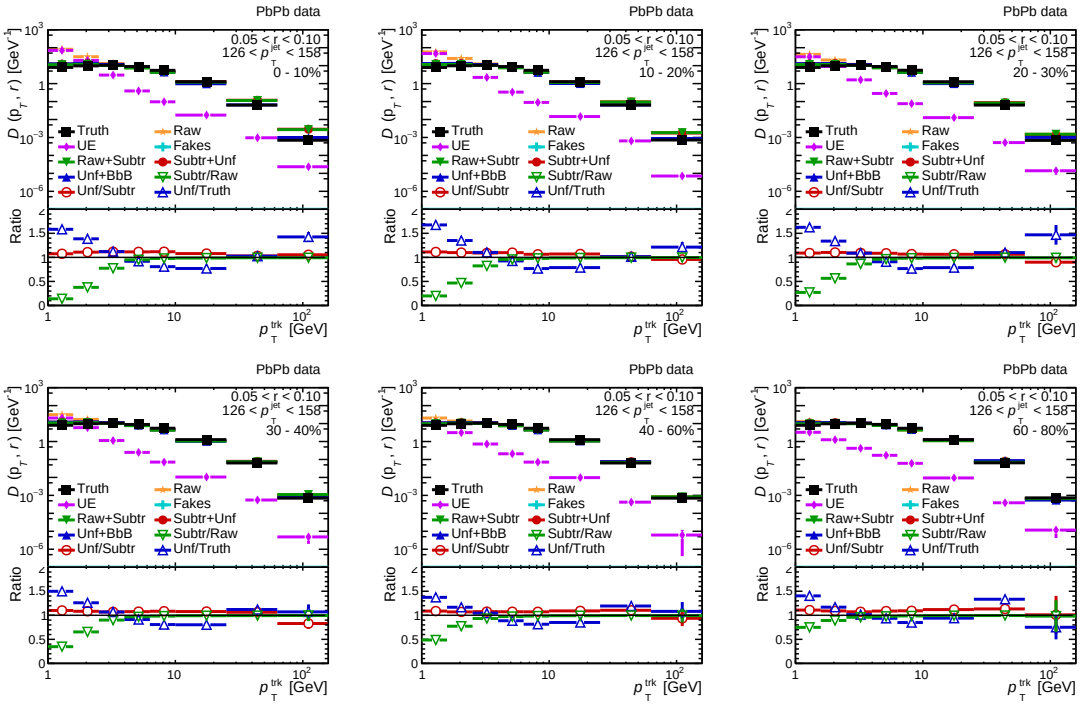

(b)

Figure 5.40: The evolution of the $D(p_{\mathrm{T}}, r)$ distributions for Pb+Pb MC (top) and data (bottom) as various corrections are applied. The spectra is shown for tracks with $0.05 < \Delta r < 0.10$ away from the jet axis, for $126 < p_{\mathrm{T}}^{\mathrm{jet}} < 158$ GeV. The ratios showing the effect of the subtraction, unfolding and bin by bin correction as well as the comparison to truth are shown in the lower half of each panel. The different panels are different centrality selections.

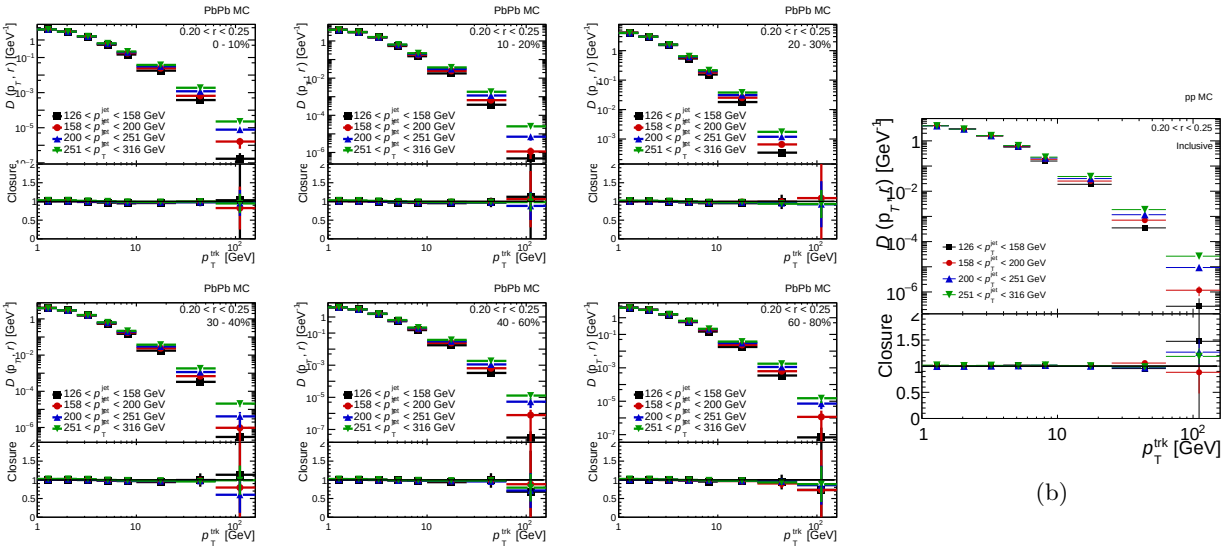

(a) (b)

Figure 5.41: The response matrices in terms of $p_{\mathrm{T}}^{\mathrm{jet,reco}}$ and $p_{\mathrm{T}}^{\mathrm{jet,truth}}$ in the jet $|y|$ <1.7 region, in (left) Pb+Pb MC overlay with each panel being a different centrality bin and (right) in pp MC.

procedure is repeated to ensure that the jets are treated in a consistent manner throughout the analysis. The positive relative shift was used to calculate the upper bound of the systematic uncertainty, whereas the negative relative shift was used to calculate the lower bound. All uncertainties except the unfolding and the MC non-closure are assumed to be correlated and are evaluated by comparing the $R_{D(p_{\mathrm{T}},r)}$ distributions for the various systematic variations to the nominal $R_{D(p_{\mathrm{T}},r)}$ distribution. For uncorrelated systematic uncertainties, the uncertainty on the $R_{D(p_{\mathrm{T}},r)}$ distribution is evaluated by adding the uncertainties on the pp and Pb+Pb $D(p_{\mathrm{T}},r)$ distributions in quadrature. The total systematic uncertainties on the $R_{D(p_{\mathrm{T}},r)}$ distributions for a selection of track p_{T} ranges (1.0–1.6 GeV, 2.5–4.0 GeV, 6.3–10 GeV) in jets with p_{T} in the 126–158 GeV range are shown in Figures 5.42 and 5.43.

5.4.1 Jet energy scale uncertainty

The uncertainty on the JES for heavy ion jets has two parts. The first is taken from pp JES uncertainties for jets in pp collisions while the second is specific to the heavy ion jets. For the pp part we use the strongly reduced set of 4 nuisance parameters using Scenario 1 as described in Ref. [223]. Nuisance parameters that are not applicable for HI jet collections (pileup, b-jets, flavor and MC non closure) are removed or replaced (flavor uncertainties). The heavy ion specific components are from the cross calibration [191] and the jet flavor uncertainties at 5.02 TeV [111]. For each component of the variation the response matrices are regenerated with the shifted $p_{\mathrm{T}}^{\mathrm{jet}}$:

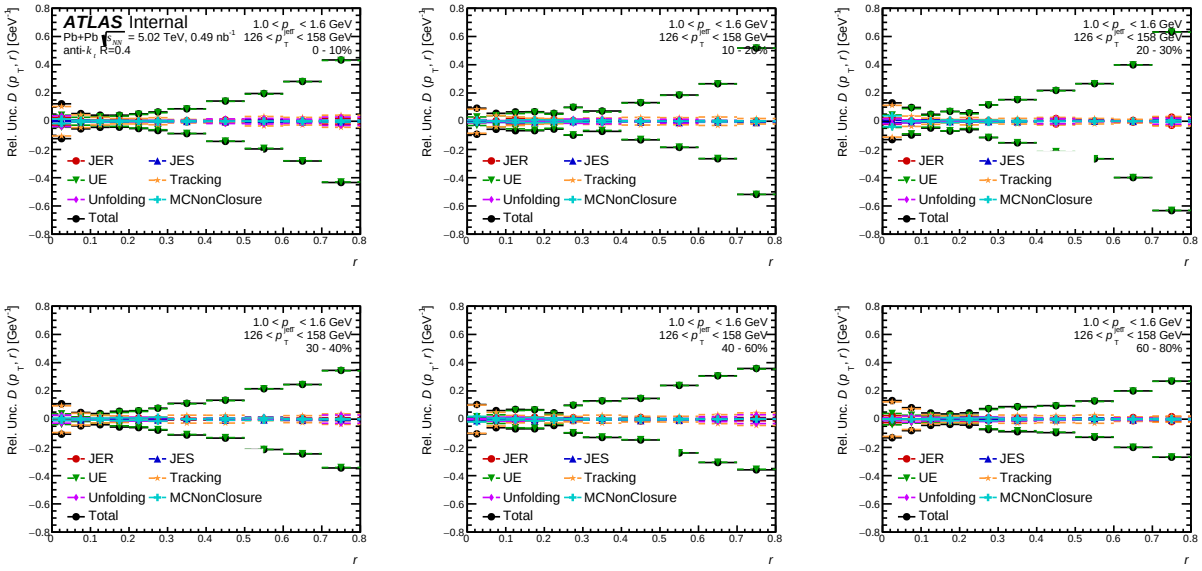

(a)

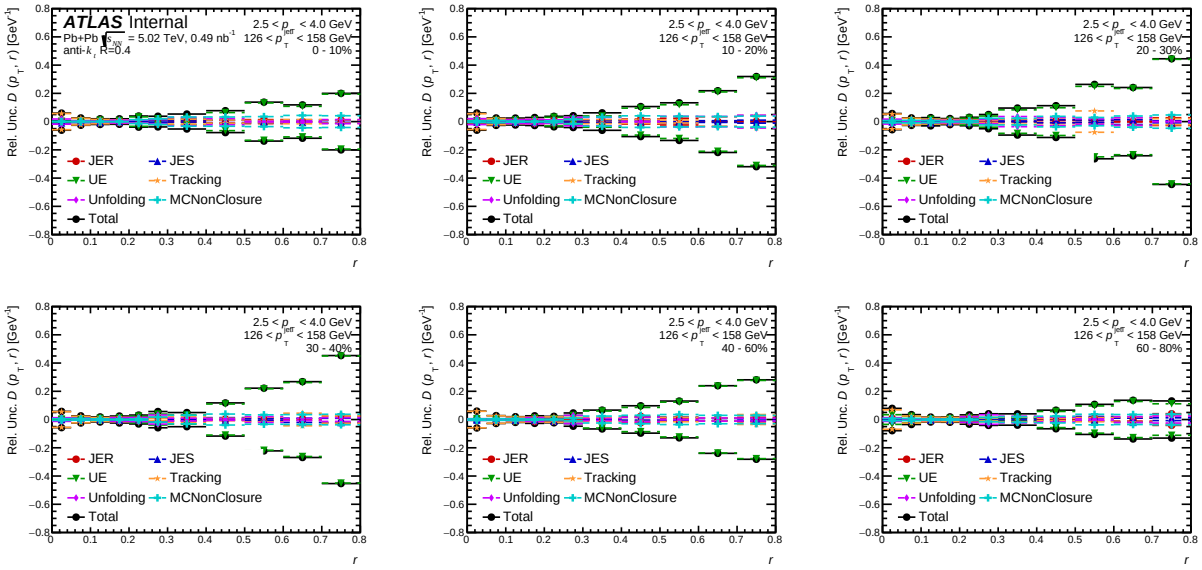

(b)

Figure 5.42: A summary of the systematic uncertainties on $R_{D(p_T,r)}$ distributions for different track $1.0 < p_T < 1.6$ GeV (top) and $2.5 < p_T < 4.0$ GeV (bottom), for jets with p_T 126–158 GeV, as a function of r for different centrality bins. Different panels are different centrality bins. The total systematic uncertainty and its individual contributions are shown.

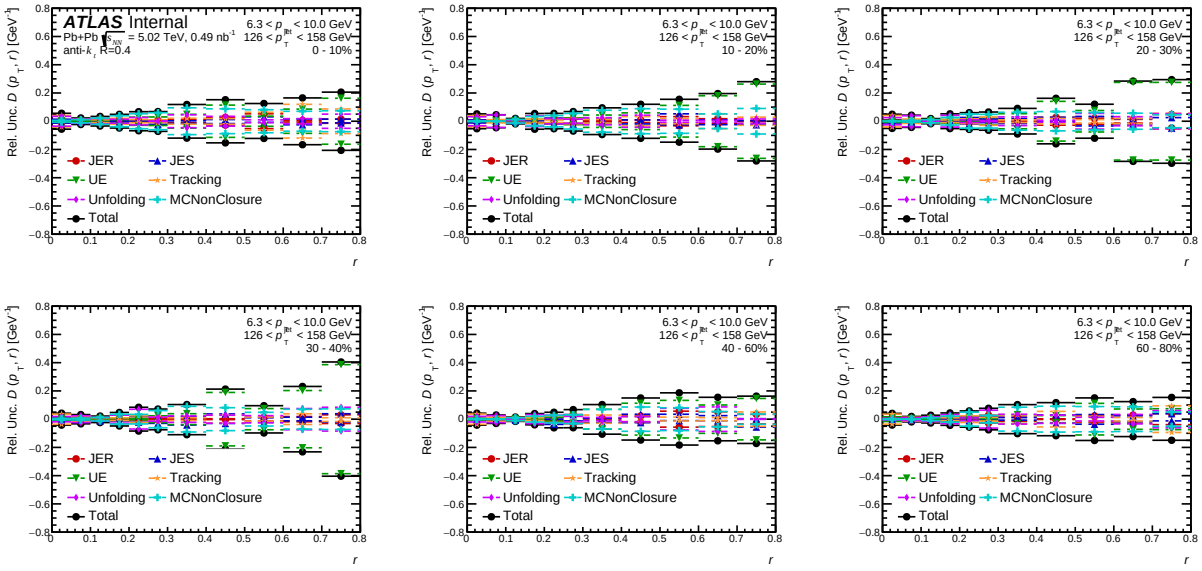

(a)

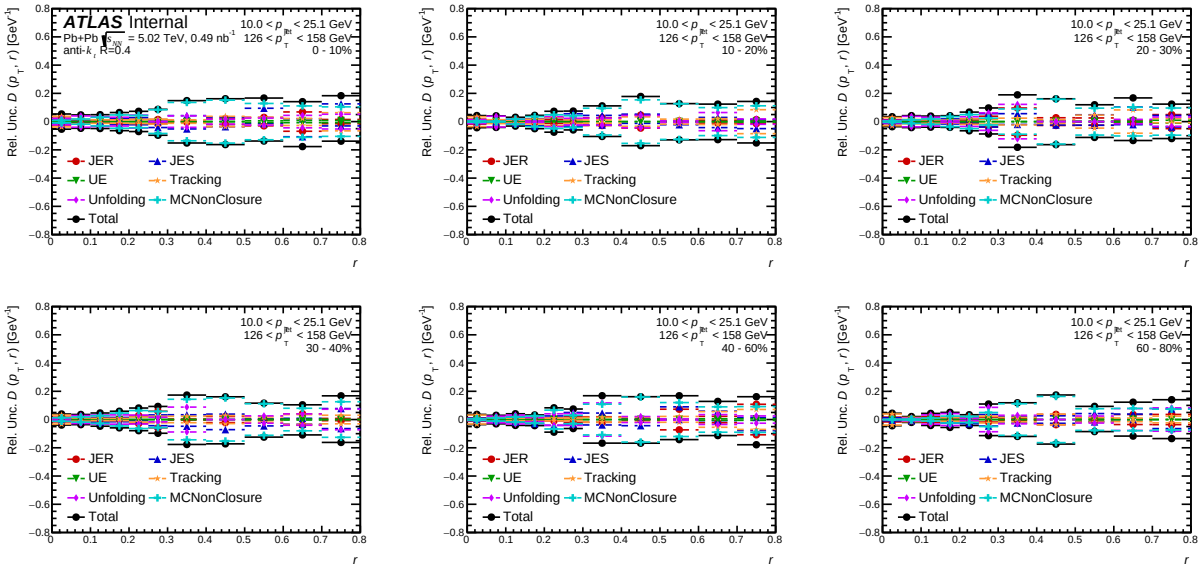

(b)

Figure 5.43: A summary of the systematic uncertainties on $R_{D(p_{\mathrm{T}},r)}$ distributions for different track $6.3 < p_{\mathrm{T}} < 10.0$ GeV (top) and $10.0 < p_{\mathrm{T}} < 25.1$ GeV (bottom), for jets with p_{T} 126–158 GeV, as a function of r for different centrality bins. Different panels are different centrality bins. The total systematic uncertainty and its individual contributions are shown.

$$p_{\mathrm{T}}{}^{\star,\mathrm{reco}} = p_{\mathrm{T}}{}^{\mathrm{reco}}(1 \pm U^{\mathrm{JES}}(p_{\mathrm{T}}, \eta)). \tag{5.9}$$

The data is then re-unfolded with these response matrices and the variation in the fragmentation functions is taken as the systematic uncertainty.

The centrality dependent uncertainty on the JES was evaluated by shifting the jet p_{T} of all measured jets up and down by shift between 0% and 0.5%. The magnitude of the shift depends on the centrality in the way that the uncertainty on the jet p_{T} is 0.5% in 1% most central collisions and than linearly decreases to 0% in 60% peripheral bin. The size of the shift reflects the uncertainty on the JES evaluated as using the $r-$track study where the sum of p_{T} of the tracks associated to a reconstructed jet is compared to the reconstructed jet p_{T} in ratio that is than compared between PbPb data and MC [148, 192].

5.4.2 Jet energy resolution

To account for systematic uncertainties due to disagreement between the jet energy resolution in data and MC, the unfolding procedure was repeated with a modified response matrix. The matrix was generated by repeating the MC study with modifications to the Δp_{T} for each matched truth-reconstructed jet pair. The procedure to generate modified migration matrices follows the standard procedure applied in pp jet measurements and is used for both the pp and Pb+Pb collisions. The `JetEnergyResolutionProvider` tool [224] was used to retrieve uncertainty on the fractional resolution, $\sigma_{\mathrm{JER}}^{\mathrm{syst}}$ as a function of jet p_{T} and η. An additional HI jet specific uncertainty from the cross calibration of the HI jet collections [191] is applied to jets in both pp and Pb+Pb collisions. The full JER uncertainty on 2015 pp data is shown also in Ref. [225] The jet $p_{\mathrm{T}}{}^{\mathrm{reco}}$ was then smeared by

$$p_{\mathrm{T}}{}^{\star,\mathrm{reco}} = p_{\mathrm{T}}{}^{\mathrm{reco}} \times \mathcal{N}(1, \sigma_{\mathrm{JER}}^{\mathrm{eff}}), \tag{5.10}$$

where $\mathcal{N}(1, \sigma_{\mathrm{JER}}^{\mathrm{eff}})$ is the normal distribution with the effective resolution $\sigma_{\mathrm{JER}}^{\mathrm{eff}} = \sqrt{(\sigma_{\mathrm{JER}} + \sigma_{\mathrm{JER}}^{\mathrm{syst}})^2 - \sigma_{\mathrm{JER}}^2}$.

5.4.3 Tracking selections

Track selection This uncertainty was estimated by tightening the tracking cuts by adding the cuts on the significance of d_0 and z_0 as described in the Section 5.3.2. The entire analysis is redone with these track selections (including re-deriving the tracking efficiencies and the $\eta - \phi$ maps for the UE estimation) and the difference from the nominal analysis is taken as the systematic uncertainty.

Truth track definition This uncertainty quantifies the robustness of the matching of reconstructed to truth particles. The uncertainty is taken as a difference in the final results obtained with $\mathrm{mc}_{\mathrm{prob}} > 0.3$ and results obtained with $\mathrm{mc}_{\mathrm{prob}} > 0.5$. This systematic included a re-derivation of the $\eta - \phi$ maps for UE estimation.

Detector material description in simulation The uncertainty on the inner detector material varies with $p_{\mathrm{T}}^{\mathrm{ch}}$ and η^{ch} from 0.5% to 2.0% [214] on the efficiency correction. This systematic also included a re-derivation of the $\eta - \phi$ maps for UE estimation.

Tracking in dense environments There is a 0.4% uncertainty on the efficiency due to tracking in dense environments (the core of the jet) [214]. This systematic also included a re-derivation of the $\eta - \phi$ maps for UE estimation.

Fake rate and secondaries The uncertainty on the rate of fake tracks and secondaries is taken to be 30% independent of $p_{\mathrm{T}}^{\mathrm{ch}}$ and η^{ch} [214, 226]. This uncertainty is conservatively symmetrized.

Uncertainty on the track momentum To account for a possible misalignment in pp and Pb+Pb data, the reconstructed p_{T} of each track (corrected first as described in section 5.3.3) was changed according to [215]:

$$p_{\mathrm{T}} \to p_{\mathrm{T}} \times (1 + q \times p_{\mathrm{T}} \delta_{sagitta}(\eta, \phi))^{-1}, \tag{5.11}$$

where q is charge of the track and $\delta_{sagitta}(\eta, \phi)$ is uncertainty on the track curvature. The uncertainty derived for 5.02 TeV pp and Pb+Pb data is included in InDetTrackSystematicsTools-00-00-19. Due to statistical origin of the uncertainty the resulting systematic uncertainty is symmetrized. This systematic also included a re-derivation of the $\eta - \phi$ maps for UE estimation.

5.4.4 Systematic uncertainty due to unfolding

The systematic uncertainty associated with the unfolding is connected with the sensitivity of the unfolding procedure to the choice of the input distributions. The systematic is evaluated by generating response matrices from the MC distributions without the reweighting factor that is used to match the jet spectrum and $D(p_{\mathrm{T}}, r)$ distributions in data, and then unfolding the data using these response matrices. This has minimal effect on track p_{T} because of the good track momentum resolution in the kinematic region of

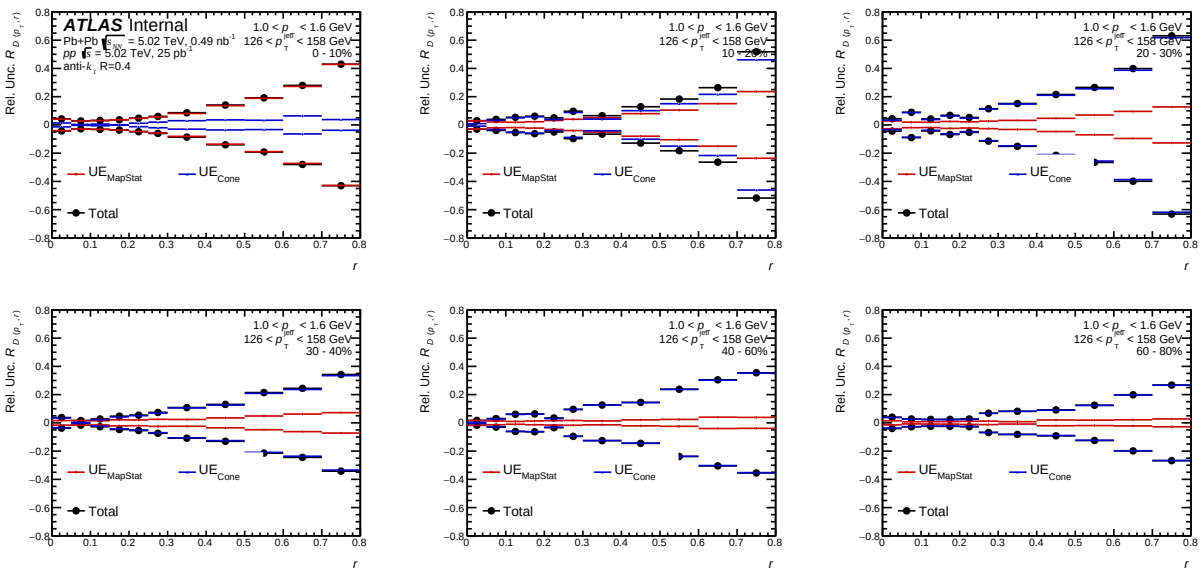

Figure 5.44: Size of the individual contributions to the underlying event systematic uncertainty as a function for r for 0-10% Pb+Pb collisions, in 126-158 GeV jets, 1-1.6 GeV tracks.

interest. The uncertainty is evaluated by comparing the nominal result with the un-reweighed result, and is considered to be uncorrelated between Pb+Pb and pp.

5.4.5 Systematic uncertainty due to the UE event subtraction

The systematic uncertainty associated with the estimation of the UE has two main components: one is the statistical uncertainty on the $\eta - \phi$ maps used in the map method (described in section 5.3.6), and the other is the comparison of the map method to the alternative cone method (discussed in section 5.3.6. More details on the cone method can be found in Ref. [151]. The contributions of both components to the underlying event uncertainty can be seen in Figure 5.44, with the uncertainty from the map statistic dominating in central collisions. The uncertainty on the underlying event convolutes with the signal to background ratio to produce the uncertainty on the charged particle spectra.

Uncertainty from map statistic: The $\eta - \phi$ maps used in the estimation of the underlying event are sparsely populated for high track p_{T} and high $p_{\mathrm{T}}^{\mathrm{jet}}$, and are susceptible to statistical fluctuations. To take this into account, 100 pseudo-experiments are conducted to re-estimate the set of maps, with a bin-by-bin gaussian variation where the mean and standard deviation were taken to be the bin content and bin error from the nominal set of maps. The distribution of the relative difference between each estimation of the shifted underlying event and and the nominal value is fit to a gaussian. The width of this gaussian is taken

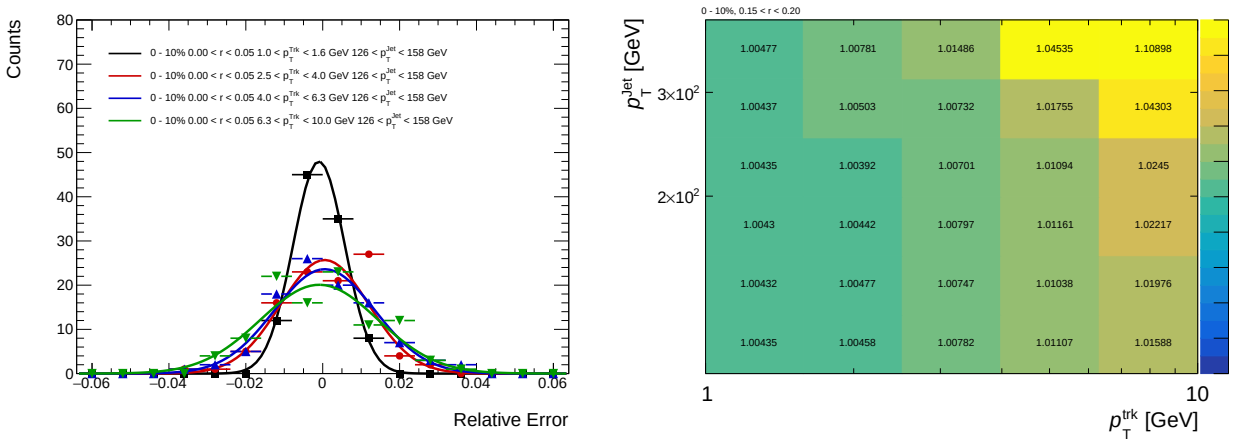

(a) (b)

Figure 5.45: (Left) An example of the relative difference between the nominal and shifted values of the UE, fit to a gaussian. The width is taken as the systematic uncertainty. Wider distributions larger statistical uncertainty on the bin content in the $\eta - \phi$ map used to estimate the UE. (Right) Size of the systematic uncertainty from the map statistic component, as a function for $p_{\mathrm{T}}^{\mathrm{ch}}$ and $p_{\mathrm{T}}^{\mathrm{jet}}$ for 0-10% Pb+Pb collisions, $0.15 < r < 0.20$ away from the jet axis.

to be the systematic uncertainty. This uncertainty is symmetrized to be conservative. A few examples of the distribution of normalized relative differences can be seen in Figure 5.45a. The size of the systematic from this can be seen in Fig.5.45b.

Uncertainty from cone method: The difference between the UE from the two methods is discussed in section 5.3.6 and is shown in Figure 5.28. The effect of the different UE estimation methods on the charged particle spectra is seen in Fig.5.46. This uncertainty is conservatively symmetrized. While the absolute size of the uncertainty on the UE is typically small, the small signal-to-background ratio makes this the dominant systematic uncertainty in central collisions for lowest p_{T} tracks and large r.

5.4.6 MC non-closure

To make sure that all the sources of systematic uncertainties were covered, the systematic uncertainty from the non closure in the MC was also evaluated. It was calculated using the technical closure (done using non-reweighed response matrices) between the fully corrected and reconstructed charged particle distributions in MC to the charged particle distributions evaluated at the truth level. This uncertainty can be considered a measure of unknowns in the analysis, but it also includes fluctuations due to the finite statistics in the MC which are used to evaluate it (especially in high $p_{\mathrm{T}}^{\mathrm{ch}}$ regions of the analysis. The non-closure can be seen in Figure 5.47. The systematic uncertainty is taken to be uncorrelated between Pb+Pb and pp

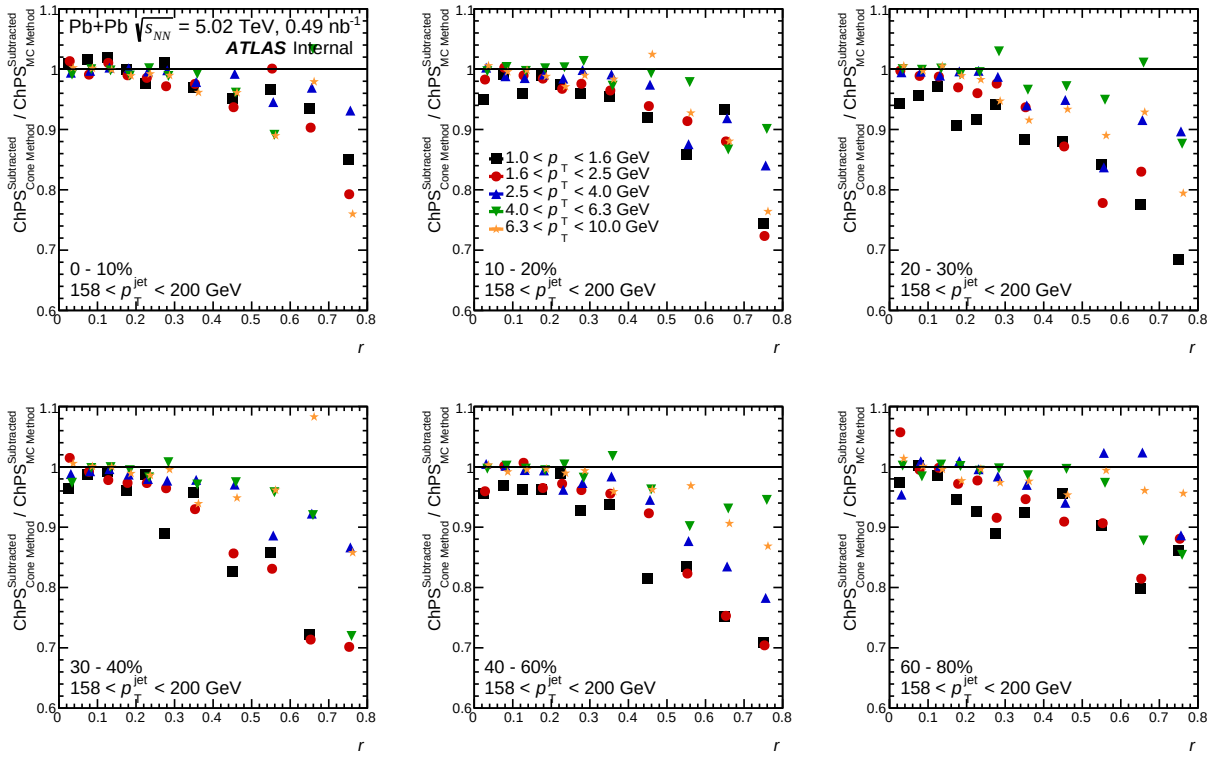

Figure 5.46: Ratio of the charged particle spectra as determined using two different UE estimation methods as a function for r for 0-10% Pb+Pb collisions in 126-158 GeV jets and 1-1.6 GeV tracks. Deviations from unity are a combination of the difference between the two methods and the signal to background ratio. The largest differences between the spectra are seen at large r, where the signal to background is the smallest. Points are offset along the x-axis for ease of viewing.

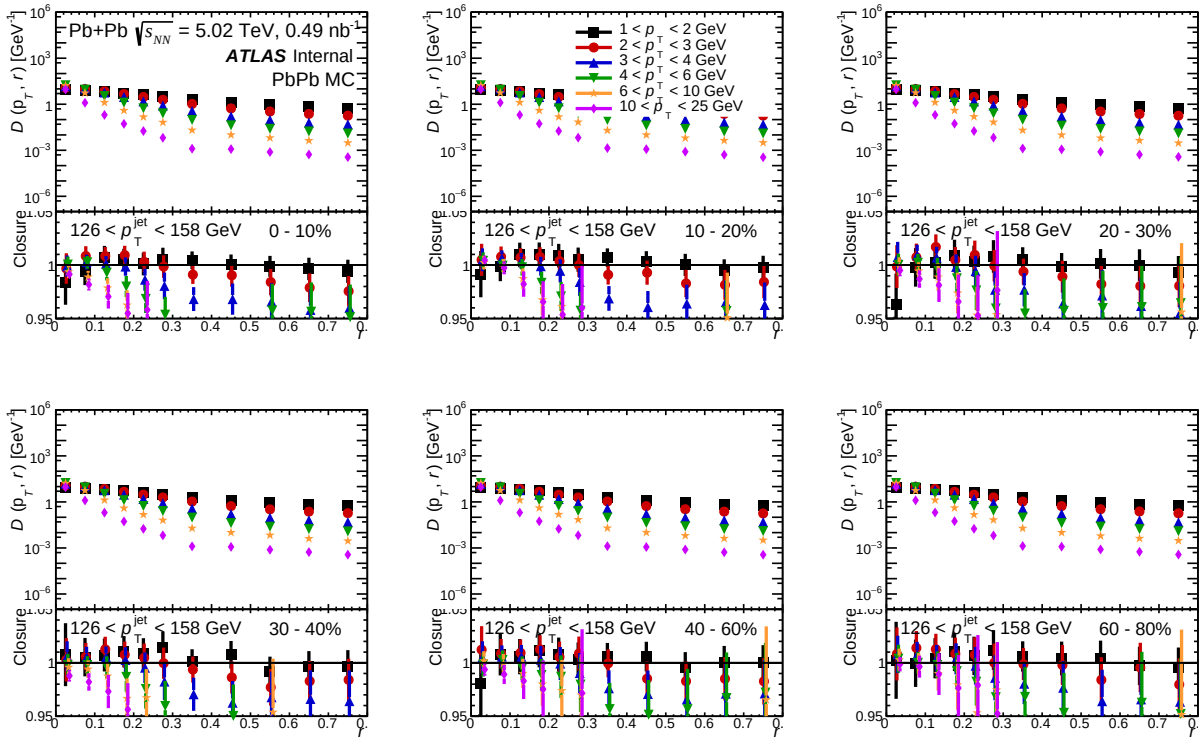

Figure 5.47: Size of the non-closure as a function for r for 0-10% Pb+Pb collisions, in 126-158 GeV jets for different $p_{\mathrm{T}}^{\mathrm{ch}}$ ranges. Points in the bottom panel are offset along the x-axis for ease of viewing.

5.4.7 Correlations between the systematic uncertainties in Pb+Pb and *pp* collisions

Due to the common analysis and reconstruction procedure, and detector conditions, the systematic uncertainties are correlated between the *pp* and Pb+Pb collisions in most cases. Table 5.1 summarizes correlations between *pp* and Pb+Pb and also point-to-point correlations of individual distributions. The unfolding uncertainty is uncorrelated between the two systems because it comes from the sensitivity of the unfolding to the starting MC distribution. In Pb+Pb collisions where the fragmentation is modified by the presence of the QGP, this sensitivity could be different than in *pp* collisions where the fragmentation functions are quite similar to those in PYTHIA8 [217]. The impact of the modification of the fragmentation process in Pb+Pb compared to *pp* and MC simulations is account for in the HI specific data-driven and centrality dependent uncertainty on the JES.

Uncertainty	***pp* and Pb+Pb correlated**	**Point-to-point correlated**	**One/two sided or symmetrized**
JES (*pp*)	yes	yes	two sided
JES (HI)	no	yes	two sided
JER	yes	yes	symmetrized
Track selection	yes	yes	one sided
$\mathrm{mc}_{\mathrm{prob}}$	yes	yes	one sided
Material	yes	yes	one sided
Dense environment	yes	yes	one sided
Fake rate	yes	yes	symmetrized
Track momentum	yes	no	two sided
Unfolding	no	yes	symmetrized
UE subtraction	no	yes	symmetrized
MC non-closure	no	no	symmetrized

Table 5.1: Summary of correlation of different systematic uncertainties.

In the case where the systematic uncertainties are correlated, we evaluate $R_{D(p_{\mathrm{T}},r)}$ ratios using the systematic variation from the nominal distributions in both *pp* and Pb+Pb. The variation in the ratio is used as the systematic uncertainty. The variations in the ratios are summed in quadrature to get the total systematic uncertainty on the ratio.

5.5 Results

The $D(p_{\mathrm{T}}, r)$ distributions are studied as a function of $p_{\mathrm{T}}^{\mathrm{jet}}$ for *pp* data and Pb+Pb collisions with different centralities. The interplay between the hot and dense matter and the parton shower is explored by evaluating the ratios and differences between the $D(p_{\mathrm{T}}, r)$ distributions in Pb+Pb and *pp* collisions. Some selected

moments of these distributions are also investigated.

5.5.1 $D(p_{\mathrm{T}}, r)$ distributions

The $D(p_{\mathrm{T}}, r)$ distributions evaluated in pp and Pb+Pb collisions for $126 < p_{\mathrm{T}}^{\mathrm{jet}} < 158$ GeV are shown in Figure 5.48. These distributions decrease as a function of distance from the jet axis. The rate at which they fall off sharply increases for higher p_{T} particles, with most of these being concentrated near the jet axis. The distributions exhibit a difference in shape between Pb+Pb and pp collisions, with the Pb+Pb distributions being broader at low p_{T} (p_{T} <4 GeV) and narrower at high p_{T} ($p_{\mathrm{T}} > 4$ GeV) in 0–10% central collisions. This modification is centrality dependent and is smaller for peripheral Pb+Pb collisions.

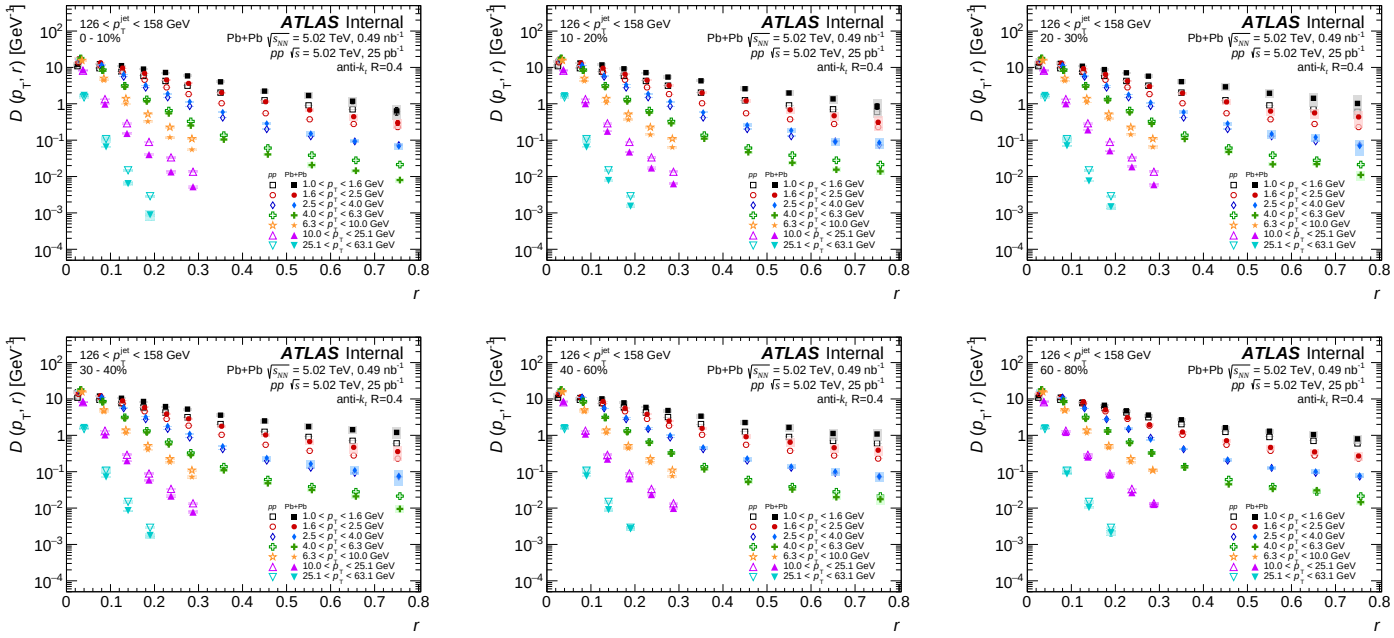

Figure 5.48: The $D(p_{\mathrm{T}}, r)$ distributions in pp (open symbols) and Pb+Pb (closed symbols) as a function of angular distance r for $p_{\mathrm{T}}^{\mathrm{jet}}$ of 126 to 158 GeV. The colors represent different track p_{T} ranges, and each panel is a different centrality selection. The vertical bars on the data points indicate statistical uncertainties while the shaded boxes indicate systematic uncertainties. The widths of the boxes are not indicative of the bin size and the points are shifted horizontally for better visibility. The distributions for $p_{\mathrm{T}} > 6.3$ GeV are restricted to smaller r values as discussed in Section 5.3.

5.5.2 $R_{D(p_{\mathrm{T}},r)}$ distributions

In order to quantify the differences seen in Figure 5.48, ratios of the $D(p_{\mathrm{T}}, r)$ distributions in Pb+Pb collisions to those measured in pp collisions for $126 < p_{\mathrm{T}}^{\mathrm{jet}} < 158$ GeV and $200 < p_{\mathrm{T}}^{\mathrm{jet}} < 251$ GeV jets are presented in Figure 5.49. They are shown as a function of r for different p_{T} and centrality selections. In

0–10% central collisions, $R_{D(p_{\mathrm{T}},r)}$ is greater than unity for $r < 0.8$ for charged particles with p_{T}less than 4.0 GeV in both jet selections. For these particles, the enhancement of yields in Pb+Pb collisions compared to those in pp collisions grows with increasing r up to approximately $r = 0.3$, with $R_{D(p_{\mathrm{T}},r)}$ reaching up to two for $1.0 < p_{\mathrm{T}} < 2.5$ GeV. The value of $R_{D(p_{\mathrm{T}},r)}$ is approximately constant for r in the interval 0.3–0.6 and decreases for $r > 0.6$. For charged particles with $p_{\mathrm{T}} > 4.0$ GeV, $R_{D(p_{\mathrm{T}},r)}$ shows a depletion outside the jet core for $r > 0.05$. The magnitude of this depletion increases with increasing r up to $r = 0.3$ and is approximately constant thereafter. For 30–40% mid-central collisions, the enhancement of particles with $p_{\mathrm{T}} < 4.0$ GeV has similar trends to that in the most central collisions, however the depletion of particles with $p_{\mathrm{T}} > 4.0$ GeV is not as strong. For 60–80% peripheral collisions, $R_{D(p_{\mathrm{T}},r)}$ has no significant r dependence and the values of $R_{D(p_{\mathrm{T}},r)}$ are within approximately 50% of unity. The observed behavior inside the jet cone, $r < 0.4$, agrees with the measurement of the inclusive jet fragmentation functions [142, 151, 198], where yields of fragments with $p_{\mathrm{T}} < 4$ GeV are observed to be enhanced and yields of charged particles with intermediate p_{T} are suppressed in Pb+Pb collisions compared to those in pp collisions. Calculations done in Ref. [158] show that the medium response to the jet compensates the energy that is lost by the jet in Pb+Pb collisions even up to $r = 1.0$ from the jet axis. The plateauing and slight decrease seen in Figure 5.49 for the $R_{D(p_{\mathrm{T}},r)}$ distributions in central Pb+Pb collisions beyond $r = 0.6$ from the jet axis suggests that the medium response to the jet is smaller than predicted for $r > 0.6$.

The centrality dependence of $R_{D(p_{\mathrm{T}},r)}$ for two charged-particle p_{T} intervals: 1.6–2.5 GeV and 6.3–10.0 GeV, and two different $p_{\mathrm{T}}^{\mathrm{jet}}$ ranges: 126–158 GeV and 200–251 GeV, is presented in Figure 5.50. For both $p_{\mathrm{T}}^{\mathrm{jet}}$ selections and 1.6–2.5 GeV charged particles, the magnitude of the excess increases for more central events and for r for $r < 0.3$. The magnitude of the excess is approximately a factor of two in the most central collisions for $r > 0.3$. A continuous centrality dependent suppression of yields of charged particles with $6.3 < p_{\mathrm{T}} < 10.0$ GeV is observed. The magnitude of the modification decreases for more peripheral collisions in both p_{T} intervals and $p_{\mathrm{T}}^{\mathrm{jet}}$ selections.

Figure 5.51 shows the p_{T} dependence of $R_{D(p_{\mathrm{T}},r)}$ for selections in r for 126–158 GeV and 200–251 GeV jets in the following centrality intervals: 0–10%, 30–40%, and 60–80%. Interestingly, there is no significant suppression of the yields in Pb+Pb collisions for $r < 0.05$ at all measured p_{T}. For larger r values the yields are enhanced for charged particles with $p_{\mathrm{T}} < 4$ GeV and suppressed for higher p_{T} charged particles in both the 0–10% and 30–40% centrality selections and both $p_{\mathrm{T}}^{\mathrm{jet}}$ ranges presented here. The magnitude of the enhancement increases for decreasing p_{T} below 4 GeV while the suppression is enhanced with increasing p_{T} for mbox4–10 GeV, after which it is approximately constant. At fixed p_{T} the magnitude of the deviation from unity is largest for $0.3 < r < 0.4$ and $0.5 < r < 0.6$. In the 60–80% peripheral collisions, the same

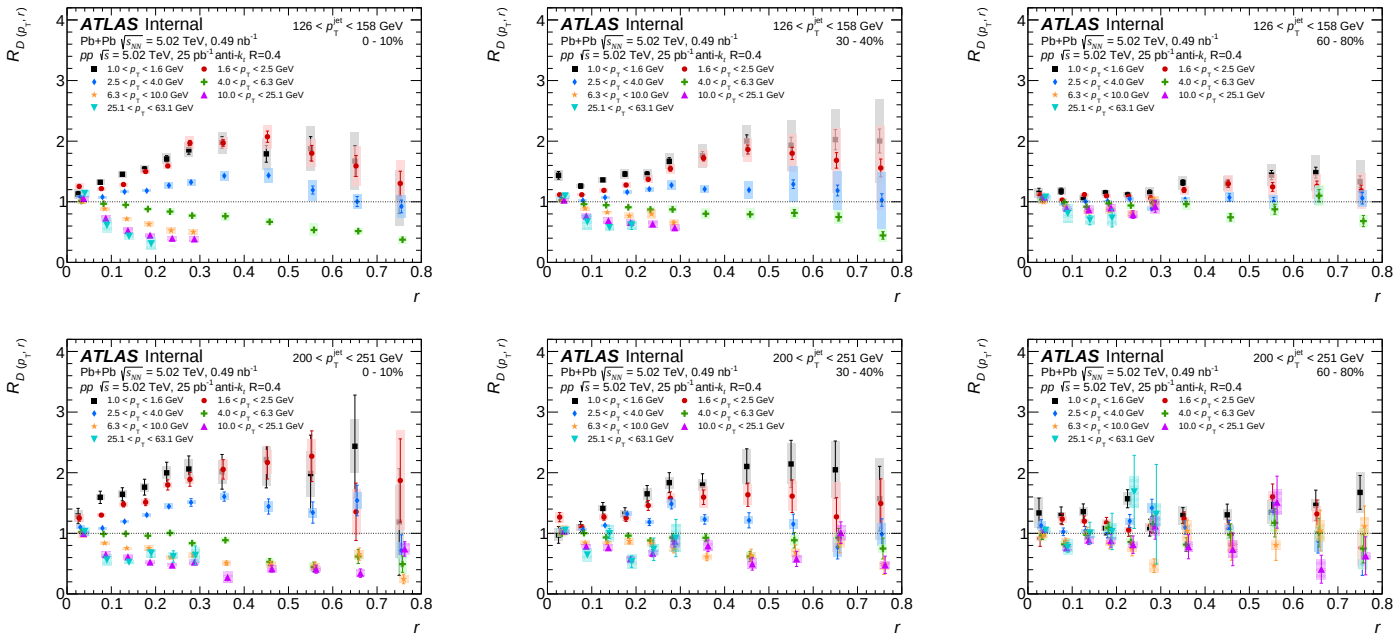

Figure 5.49: Ratios of $D(p_{\mathrm{T}}, r)$ distributions in Pb+Pb and pp collisions as a function of angular distance r for $p_{\mathrm{T}}^{\mathrm{jet}}$ of 126 to 158 GeV (top) and of 200 to 251 GeV (bottom) for seven p_{T} selections. Different centrality selections are shown: 0–10% (left), 30–40% (middle), 60–80% (right). The vertical bars on the data points indicate statistical uncertainties while the shaded boxes indicate systematic uncertainties. The widths of the boxes are not indicative of the bin size and the points are shifted horizontally for better visibility.

trend remains true (but with smaller magnitude modifications) for $126 < p_{\mathrm{T}}^{\mathrm{jet}} < 158$ GeV; for the higher $p_{\mathrm{T}}^{\mathrm{jet}}$ selection the larger uncertainties do not allow a clear conclusion to be drawn for peripheral collisions.

The enhancement of charged particles in the kinematic region of $p_{\mathrm{T}} < 4$ GeV has two common explanations. First, gluon radiation from the hard scattered parton as it propagates through the QGP would lead to extra soft particles [154, 155]. Second, the interactions of a jet with the QGP and its hydrodynamic response could induce a wake that manifests itself as an enhancement of low p_{T} particles [158].

The observed modification at $p_{\mathrm{T}} > 4$ GeV can be explained on the basis of the larger expected energy loss of gluon-initiated jets, resulting in a relative enhancement of quark jets in Pb+Pb collisions compared to pp collisions at a given $p_{\mathrm{T}}^{\mathrm{jet}}$ value [151, 153]. Since gluon jets have a broader distribution of particle transverse momentum with respect to the jet direction compared to quark-initiated jets [227], such an effect could describe the narrowing of the particle distribution around the jet direction for particles with $p_{\mathrm{T}} > 4.0$ GeV that is observed here, though no calculations of this are available.

The $R_{D(p_{\mathrm{T}},r)}$ distributions for low and high p_{T} particles in the different $p_{\mathrm{T}}^{\mathrm{jet}}$ selections are directly overlaid in Figure 5.52. These distributions are for the 0–10% most central collisions, and show a hint of enhancement in $R_{D(p_{\mathrm{T}},r)}$ with increasing $p_{\mathrm{T}}^{\mathrm{jet}}$ for $r < 0.25$ for low p_{T} charged particles. No significant $p_{\mathrm{T}}^{\mathrm{jet}}$ dependence is

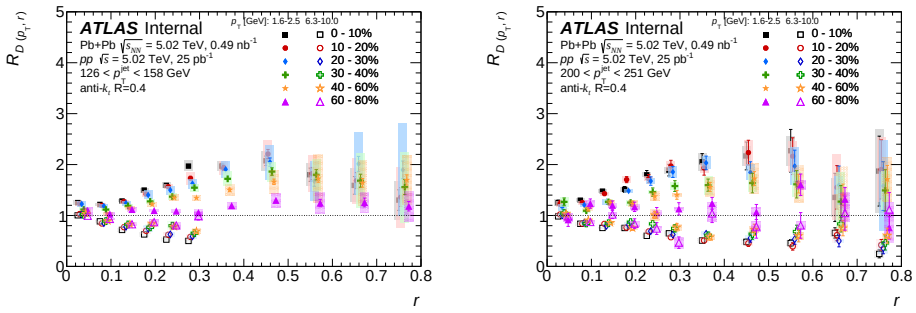

Figure 5.50: The $R_{D(p_{\mathrm{T}},r)}$ distributions for $p_{\mathrm{T}}^{\mathrm{jet}}$ of 126–158 GeV (left) and 200–251 GeV (right) as a function of angular distance r for two p_{T} selections, 1.6–2.5 GeV (closed symbols) and 6.3–10.0 GeV (open symbols), and six centrality intervals. The vertical bars on the data points indicate statistical uncertainties while the shaded boxes indicate systematic uncertainties. The widths of the boxes are not indicative of the bin size and the points are shifted horizontally for better visibility.

seen at larger r values, or for high-p_{T} charged particles at any r. This $p_{\mathrm{T}}^{\mathrm{jet}}$ dependence is further explored by defining an integral over the low p_{T} excess and is discussed in Section 5.5.4.

5.5.3 $\Delta D(p_{\mathrm{T}}, r)$ distributions

In addition to the ratios of the $D(p_{\mathrm{T}}, r)$ distributions, differences between the unfolded charged-particle yields are also evaluated as $\Delta D(p_{\mathrm{T}}, r)$ to quantify the modification in terms of the particle density.

These differences are presented as a function of r for different p_{T} selections in 0–10% central collisions in Figure 5.53. These distributions show an excess in the charged-particle yield density for Pb+Pb collisions compared to pp collisions for charged particles with $p_{\mathrm{T}} < 4.0$ GeV. This ranges from 0.5 to 4 particles per unit area per GeV for 1–1.6 GeV charged particles in 126–158 GeV jets for 0–10% central Pb+Pb collisions and increases with increasing $p_{\mathrm{T}}^{\mathrm{jet}}$. The largest excess for charged particles with $p_{\mathrm{T}} < 4.0$ GeV is within the jet cone. For large r values, the difference decreases, but remains positive. A depletion for higher p_{T} particles of approximately 0.5 particles per unit area per GeV is seen for 126–158 GeV jets in 0–10% central Pb+Pb collisions. The magnitude of this depletion increases for higher $p_{\mathrm{T}}^{\mathrm{jet}}$. A minimum in the $\Delta D(p_{\mathrm{T}}, r)$ distributions for charged particles with $4.0 < p_{\mathrm{T}} < 25.1$ GeV at $0.05 < r < 0.10$ is observed. The magnitudes of the excesses and deficits discussed here are dependent on the selected charged-particle p_{T}.

5.5.4 p_{T} integrated distributions

Motivated by similar studies of the enhancement of soft fragments in jet fragmentation functions in Pb+Pb compared to pp collisions from Ref. [151], the unfolded $D(p_{\mathrm{T}}, r)$ distributions are integrated for charged particles with p_{T} ¡ 4 GeV to construct the quantities $\Theta(r)$ and $P(r)$ defined as:

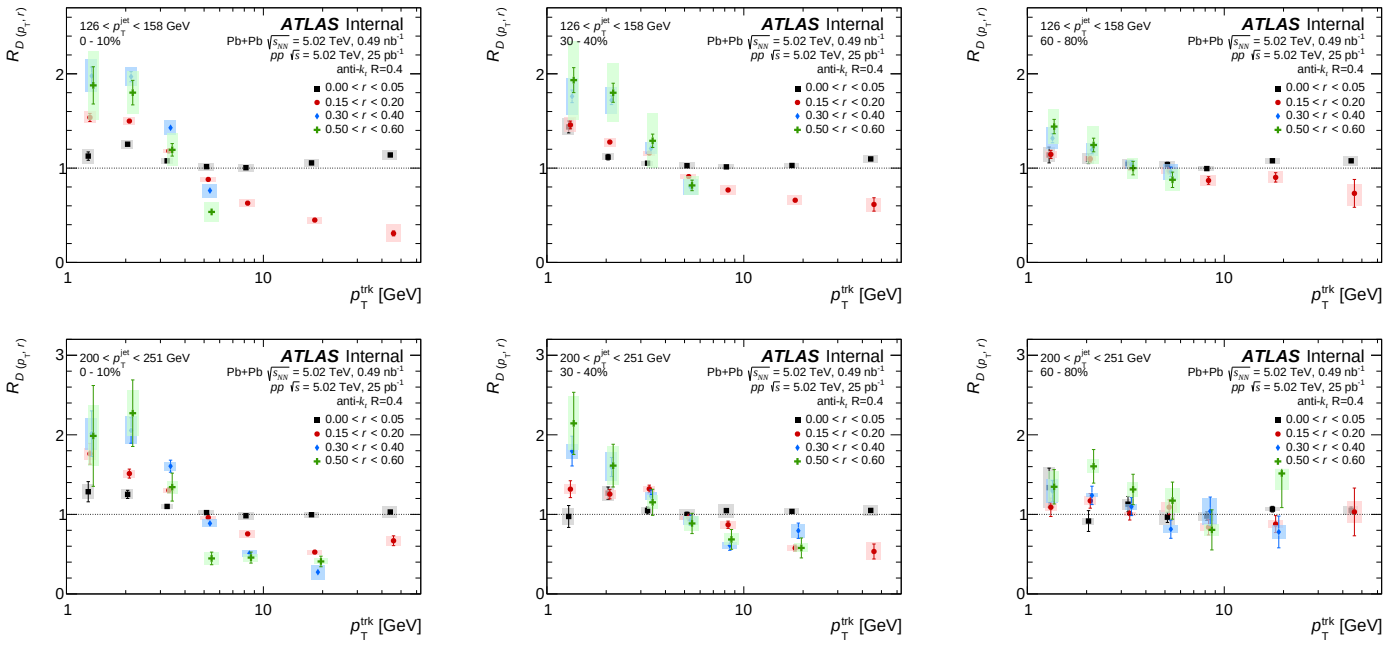

Figure 5.51: $R_{D(p_{\mathrm{T}},r)}$ as a function of p_{T} for 0–10% (left), 30–40% (middle), and 60–80% (right) Pb+Pb collisions in two different $p_{\mathrm{T}}^{\mathrm{jet}}$ selections: 126–158 GeV (top) and 200–251 GeV (bottom). The different colors indicate different angular distances from the jet axis. The vertical bars on the data points indicate statistical uncertainties while the shaded boxes indicate systematic uncertainties. The widths of the boxes are not indicative of the bin size and the points are shifted horizontally for better visibility.

$$\Theta(r) = \int_{1\ \mathrm{GeV}}^{4\ \mathrm{GeV}} D(p_{\mathrm{T}}, r)\mathrm{d}p_{\mathrm{T}}$$
$$P(r) = \int_{0}^{r}\int_{1\ \mathrm{GeV}}^{4\ \mathrm{GeV}} D(p_{\mathrm{T}}, r')\mathrm{d}p_{\mathrm{T}}\mathrm{d}r'$$

The $\Theta(r)$ values are integrated over the charged-particle p_{T} interval of 1–4 GeV to provide a summary look at the p_{T} region of enhancement discussed above. The $P(r)$ values further add a running integral over r and provide information about the jet shape. Both of these quantities are compared between the pp and Pb+Pb systems to give the following distributions:

$$\Delta_{\Theta(r)} = \Theta(r)_{\mathrm{Pb+Pb}} - \Theta(r)_{pp}$$
$$R_{\Theta(r)} = \frac{\Theta(r)_{\mathrm{Pb+Pb}}}{\Theta(r)_{\mathrm{pp}}}$$
$$R_{P(r)} = \frac{P(r)_{\mathrm{Pb+Pb}}}{P(r)_{pp}}$$

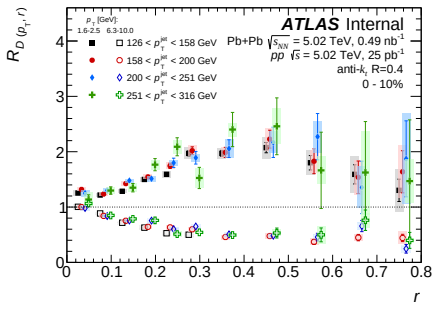

Figure 5.52: $R_{D(p_{\mathrm{T}},r)}$ as a function of r for 0–10% collisions for charged particles with $1.6 < p_{\mathrm{T}} < 2.5$ GeV (closed symbols) and $6.3 < p_{\mathrm{T}} < 10.0$ GeV (open symbols) for different $p_{\mathrm{T}}^{\mathrm{jet}}$ selections. The vertical bars on the data points indicate statistical uncertainties while the shaded boxes indicate systematic uncertainties. The widths of the boxes are not indicative of the bin size and the points are shifted horizontally for better visibility.

These integrated quantities are intended to provide aggregate information about the angular distance with respect to the jet axis, magnitude, and $p_{\mathrm{T}}^{\mathrm{jet}}$ dependence of the low-p_{T} charged-particle excess discussed above. The ratio quantities are useful for comparisons to other Pb+Pb measurements; $\Delta_{\Theta(r)}$ is comparable to $\Delta D(p_{\mathrm{T}}, r)$, however it is integrated over charged-particle p_{T} in the 1–4 GeV interval [151].

Figure 5.54 shows the $\Delta_{\Theta(r)}$ distributions as a function of r for the following centrality intervals: 0–10%, 30–40%, and 60–80%. In the most central collisions, a significant $p_{\mathrm{T}}^{\mathrm{jet}}$ dependence to $\Delta_{\Theta(r)}$ is observed; for $r < 0.4$ (particles within the jet cone) $\Delta_{\Theta(r)}$ increases with increasing $p_{\mathrm{T}}^{\mathrm{jet}}$. The value of $\Delta_{\Theta(r)}$ decreases in more peripheral collisions where the $p_{\mathrm{T}}^{\mathrm{jet}}$ dependence is also no longer significant.

Figure 5.55 shows the $R_{\Theta(r)}$ and $R_{P(r)}$ distributions as a function of r for the 0–10%, 30–40%, and 60–80% centrality intervals. The $R_{\Theta(r)}$ distributions in the most central collisions show a maximum for $r \sim 0.4$ and a flattening or a decrease for larger r. However, since $R_{\Theta(r)}$ remains at or above unity for the full range of r values presented, $R_{P(r)}$ shows no suppression with increasing r over the entire measured range. A slow increase in $R_{P(r)}$ is clearly observed in 30–40% central collisions. In more peripheral collisions the magnitude of the excess is reduced and the trends in $R_{\Theta(r)}$ are less clear, though $R_{P(r)}$ is still seen to be above unity. The flattening of the $R_{P(r)}$ distributions at large distances suggests that while wider jets have a softer fragmentation and contain more particles with less p_{T} in Pb+Pb compared to pp collisions [161, 163], this effect plateaus for jets with radius larger than 0.6.

These measurements show that the excess of particles with $p_{\mathrm{T}} < 4.0$ GeV observed in [151] extends outside the $R = 0.4$ jet cone. The measured dependence of $R_{D(p_{\mathrm{T}},r)}$ suggests that the energy lost by jets through the jet quenching process is being transferred to particles with $p_{\mathrm{T}} < 4.0$ GeV at larger radial distances from the jet axis. This is qualitatively consistent with theoretical calculations [202]. Additionally,

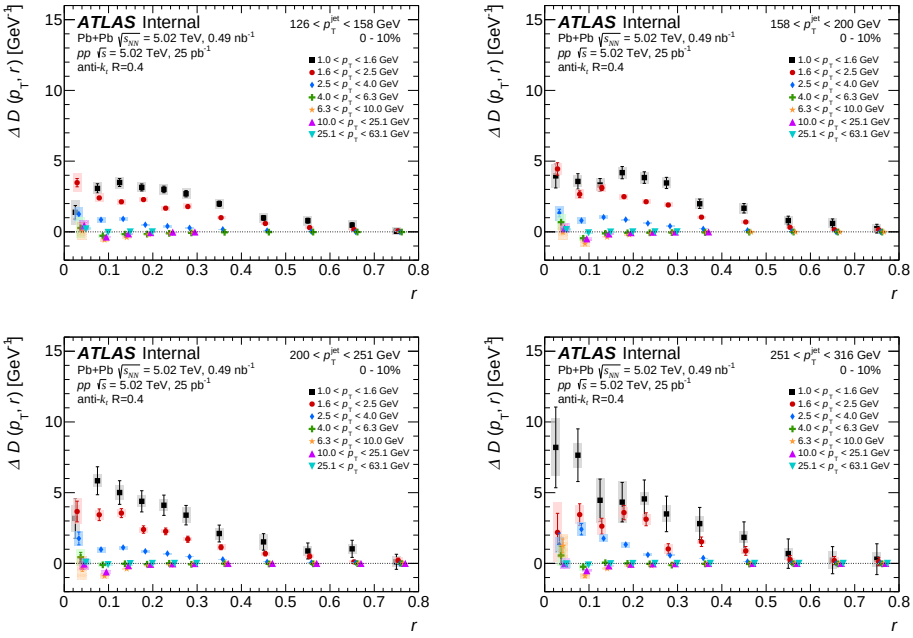

Figure 5.53: $\Delta D(p_{\mathrm{T}}, r)$ as a function of r in central collisions for all p_{T} ranges in four $p_{\mathrm{T}}^{\mathrm{jet}}$ selections: 126–158 GeV, 158–200 GeV, 200–251 GeV, and 251–316 GeV. The vertical bars on the data points indicate statistical uncertainties while the shaded boxes indicate systematic uncertainties. The widths of the boxes are not indicative of the bin size and the points are shifted horizontally for better visibility.

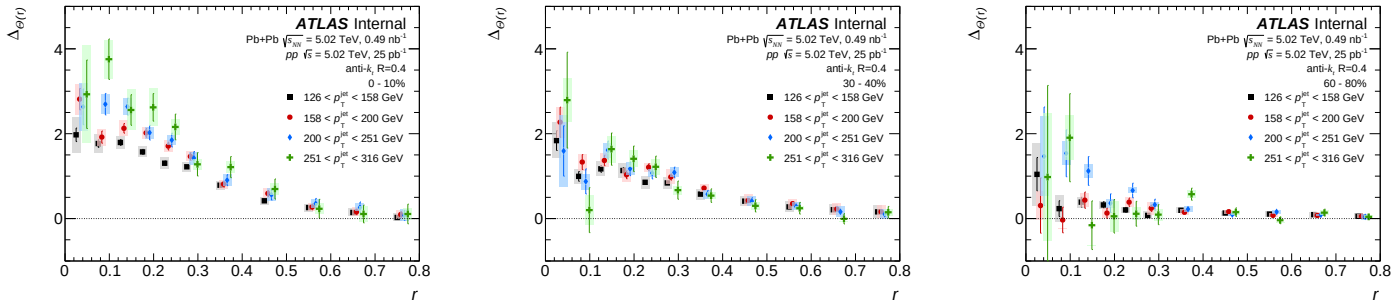

Figure 5.54: $\Delta_{\Theta(r)}$ as a function of r for charged particles with p_{T} ¡ 4 GeV in four $p_{\mathrm{T}}^{\mathrm{jet}}$ selections: 126–158 GeV, 158–200 GeV, 200–251 GeV, and 251–316 GeVand three centrality selections: 0–10% (left), 30–40% (middle) and 60–80% (right). The vertical bars on the data points indicate statistical uncertainties while the shaded boxes indicate systematic uncertainties. The widths of the boxes are not indicative of the bin size and the points are shifted horizontally for better visibility.

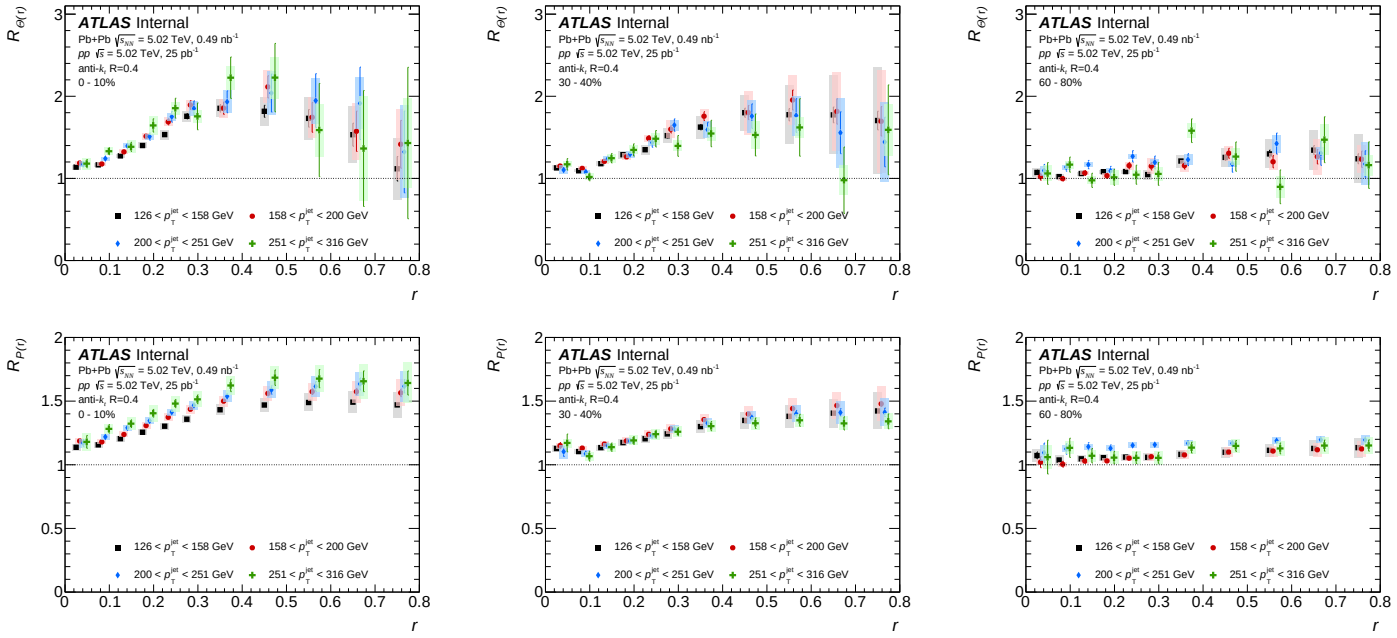

Figure 5.55: $R_{\Theta(r)}$ (top) and $R_{P(r)}$ (bottom) as a function of r for charged particles with $p_{\mathrm{T}} < 4$ GeV ranges in four $p_{\mathrm{T}}^{\mathrm{jet}}$ selections: 126–158 GeV, 158–200 GeV, 200–251 GeV, and 251–316 GeV and three centrality selections: 0–10% (left), 30–40% (middle) and 60–80% (rights). The vertical bars on the data points indicate statistical uncertainties while the shaded boxes indicate systematic uncertainties. The widths of the boxes are not indicative of the bin size and the points are shifted horizontally for better visibility.

these observations are in agreement with the previous measurement of jet fragmentation functions [151, 157, 169, 198] and may indicate the dependence of the response of the hot dense matter to the momentum of a jet passing through it.

Chapter 6

SUMMARY

This thesis presents a measurement of the yields of charged particles, $D(p_{\mathrm{T}}, r)$, inside and around $R = 0.4$ anti-k_t jets with $|y^{\mathrm{jet}}|$ <1.7 up to a distance of $r = 0.8$ from the jet axis. The yields are measured in intervals of $p_{\mathrm{T}}^{\mathrm{jet}}$ from 126 to 316 GeV in Pb+Pb and pp collisions at 5.02 TeV as a function of charged-particle p_{T} and the angular distance r between the jet axis and charged particle.

The results show a broadening of the $D(p_{\mathrm{T}}, r)$ distribution for low p_{T} particles inside the jet in central Pb+Pb collisions compared to those in pp collisions while for higher p_{T} particles angular distributions are narrower in Pb+Pb collisions compared to pp collisions. These modifications are centrality dependent and decrease for more peripheral collisions. The $R_{D(p_{\mathrm{T}},r)}$ distributions for charged particles with $p_{\mathrm{T}} < 4$ GeV are above unity and grow with increasing angular separation up to $r \sim 0.3$, showing weak to no dependence on r in the interval $0.3 < r < 0.6$ followed with a small decrease in the enhancement for $0.6 < r < 0.8$. For charged particles with $p_{\mathrm{T}} > 4$ GeV, a suppression in $R_{D(p_{\mathrm{T}},r)}$ is observed, and the distributions decrease with increasing r for $0.05 < r < 0.3$, with no r dependence for $r > 0.3$. For all charged-particle p_{T} values, the $R_{D(p_{\mathrm{T}},r)}$ values are greater than or equal to unity for $r < 0.05$. Between $0.1 < r < 0.25$, a statistically significant trend of increasing $R_{D(p_{\mathrm{T}},r)}$ with increasing $p_{\mathrm{T}}^{\mathrm{jet}}$ is observed for low-p_{T} particles. No significant $p_{\mathrm{T}}^{\mathrm{jet}}$ dependence is seen for particles with $p_{\mathrm{T}} > 4$ GeV.

While there have been a variety of measurements and models that describe the jet shape, this measurement is the first to describe both the radial and momentum dependence of charged particles inside and outside the jet cone. In particular, observations made in this thesis can help constrain models of jet energy loss that distinguish the modifications of jet due to the presence of the plasma from the response of the medium to the jet.

At the time of writing this thesis, preliminary results from this analysis have been shown at both the

Hard Probes 2018 Conference in Aix-le-Bains, France, and the Quark Matter Conference 2018 in Venice, Italy. The full analysis is currently in the process of approval from the ATLAS Collaboration and will be published in Physical Review C.

REFERENCES

[1] M. K. Gaillard et al. *The Standard model of particle physics*. Rev. Mod. Phys. **71** (1999), S96. arXiv: hep-ph/9812285 (cit. on p. 1).

[2] Wikimedia Commons. *Standard Model of Elementary Particles*. URL: https://en.wikipedia.org/wiki/Standard_Model (cit. on p. 2).

[3] Particle Data Group. *Review of Particle Physics*. Phys. Rev. D **86** (2012), 010001 (cit. on pp. 1, 3).

[4] D. J. Gross et al. *Ultraviolet Behavior of Non-Abelian Gauge Theories*. Phys. Rev. Lett. **30** (1973), 1343 (cit. on p. 4).

[5] D. J. Gross et al. *Asymptotically Free Gauge Theories - I*. Phys. Rev. D **8** (1973), 3633 (cit. on p. 4).

[6] A. Deur et al. *High precision determination of the Q^2 evolution of the Bjorken Sum*. Phys. Rev. D **90** (2014), 012009. arXiv: 1405.7854 [nucl-ex] (cit. on p. 4).

[7] J. H. Kim et al. *A Measurement of $\alpha_s(Q^2)$ from the Gross-Llewellyn Smith sum rule*. Phys. Rev. Lett. **81** (1998), 3595. arXiv: hep-ex/9808015 (cit. on p. 4).

[8] G. Altarelli et al. *Determination of the Bjorken sum and strong coupling from polarized structure functions*. Nucl. Phys. B **496** (1997), 337. arXiv: hep-ph/9701289 (cit. on p. 4).

[9] H. W. Kendall. *Deep inelastic scattering: Experiments on the proton and the observation of scaling*. Rev. Mod. Phys. **63** (July 1991), 597 (cit. on p. 4).

[10] A. L. Kataev et al. *Improved fits to the xF_3 CCFR data at the next-to-next-to-leading order and beyond*. Phys. Part. Nucl. **34** (2003), 20. arXiv: hep-ph/0106221 (cit. on p. 4).

[11] S. Alekhin et al. *Parton Distribution Functions and Benchmark Cross Sections at NNLO*. Phys. Rev. D **86** (2012), 054009. arXiv: 1202.2281 [hep-ph] (cit. on p. 4).

[12] S. Alekhin et al. *ABM news and benchmarks*. PoS DIS **2013** (2013), 039. arXiv: 1308.5166 [hep-ph] (cit. on p. 4).

[13] J. Blumlein et al. *Non-singlet QCD analysis of deep inelastic world data at* $O(\alpha_s^3)$. Nucl. Phys. B **774** (2007), 182. arXiv: hep-ph/0607200 (cit. on p. 4).

[14] H1 Collaboration. *Three- and Four-jet Production at Low x at HERA*. Eur. Phys. J. C **54** (2008), 389. arXiv: 0711.2606 [hep-ex] (cit. on p. 4).

[15] ZEUS Collaboration. *Forward-jet production in deep inelastic ep scattering at HERA*. Eur. Phys. J. C **52** (2007), 515. arXiv: 0707.3093 [hep-ex] (cit. on p. 4).

[16] ZEUS Collaboration. *Multi-jet cross-sections in charged current* $e^{\pm}p$ *scattering at HERA*. Phys. Rev. D **78** (2008), 032004. arXiv: 0802.3955 [hep-ex] (cit. on p. 4).

[17] ZEUS Collaboration. *Inclusive dijet cross sections in neutral current deep inelastic scattering at HERA*. Eur. Phys. J. C **70** (2010), 965. arXiv: 1010.6167 [hep-ex] (cit. on p. 4).

[18] ZEUS Collaboration. *Inclusive-jet cross sections in NC DIS at HERA and a comparison of the* k_t *anti-*k_t *and SIScone jet algorithms*. Phys. Lett. B **691** (2010), 127. arXiv: 1003.2923 [hep-ex] (cit. on p. 4).

[19] H1 Collaboration. *Jet Production in ep Collisions at High* Q^2 *and Determination of* α_s. Eur. Phys. J. C **65** (2010), 363. arXiv: 0904.3870 [hep-ex] (cit. on p. 4).

[20] E. D. Bloom et al. *High-Energy Inelastic* $e-p$ *Scattering at* 6° *and* 10°. Phys. Rev. Lett. **23** (1969), 930 (cit. on p. 4).

[21] M. Breidenbach et al. *Observed Behavior of Highly Inelastic Electron-Proton Scattering*. Phys. Rev. Lett. **23** (1969), 935 (cit. on p. 4).

[22] J. D. Bjorken. *Asymptotic Sum Rules at Infinite Momentum*. Phys. Rev. **179** (1969), 1547 (cit. on p. 4).

[23] K. Nishijima. *BRS invariance, asymptotic freedom and color confinement (a review)*. Czech. J. Phys. **46** (1996), 1 (cit. on p. 4).

[24] K. G. Wilson. *Confinement of quarks*. Phys. Rev. D **10** (1974), 2445 (cit. on p. 4).

[25] W. Buchmuller. *Fine and Hyperfine Structure of Quarkonia*. Phys. Lett. B **112** (1982), 479 (cit. on p. 4).

[26] J. Kogut et al. *A quantitative approach to low-energy quantum chromodynamics*. Nucl. Phys. B **114** (1976), 199 (cit. on p. 4).

[27] N. Isgur et al. *Flux-tube model for hadrons in QCD*. Phys. Rev. D **31** (1985), 2910 (cit. on p. 4).

[28] M. Faber et al. *Casimir scaling from center vortices: Towards an understanding of the adjoint string tension*. Phys. Rev. D **57** (1998), 2603 (cit. on p. 4).

[29] G. S. Bali. *Casimir scaling of* SU(3) *static potentials*. Phys. Rev. D **62** (2000), 114503 (cit. on p. 4).

[30] J. B. Kogut. *The lattice gauge theory approach to quantum chromodynamics*. Rev. Mod. Phys. **55** (1983), 775 (cit. on p. 4).

[31] D. Zwanziger. *No Confinement without Coulomb Confinement*. Phys. Rev. Lett. **90** (2003), 102001 (cit. on p. 4).

[32] A. Jaffe et al. *Yang-Mills and Mass Gap*. URL: http://www.claymath.org/millennium-problems/yangmills-and-mass-gap (cit. on p. 4).

[33] E. V. Shuryak. *Quantum chromodynamics and the theory of superdense matter*. Phys. Rep. **61** (1980), 71 (cit. on p. 4).

[34] BRAHMS Collaboration. *Quark–gluon plasma and color glass condensate at RHIC? The perspective from the BRAHMS experiment*. Nucl. Phys. A **757** (2005), 1 (cit. on pp. 4, 7).

[35] PHENIX Collaboration. *Formation of dense partonic matter in relativistic nucleus-nucleus collisions at RHIC: Experimental evaluation by the PHENIX collaboration*. Nucl. Phys. A **757** (2005), 184. arXiv: nucl-ex/0410003 (cit. on p. 4).

[36] STAR Collaboration. *Experimental and theoretical challenges in the search for the quark–gluon plasma: The STAR Collaboration's critical assessment of the evidence from RHIC collisions*. Nucl. Phys. A **757** (2005), 102 (cit. on pp. 4, 5).

[37] PHOBOS Collaboration. *The PHOBOS perspective on discoveries at RHIC*. Nucl. Phys. A **757** (2005), 28. arXiv: nucl-ex/0410022 [nucl-ex] (cit. on p. 4).

[38] PHENIX Collaboration. *Transverse energy production and charged-particle multiplicity at midrapidity in various systems from* $\sqrt{s_{NN}} = 7.7$ *to* 200 *GeV*. Phys. Rev. C **93** (2016), 024901. arXiv: 1509.06727 [nucl-ex] (cit. on p. 5).

[39] ALICE Collaboration. *Measurement of transverse energy at midrapidity in Pb-Pb collisions at* $\sqrt{s_{NN}} =$ 2.76 *TeV*. Phys. Rev. C **94** (2016), 034903. arXiv: 1603.04775 [nucl-ex] (cit. on p. 5).

[40] CMS Collaboration. *Measurement of the pseudorapidity and centrality dependence of the transverse energy density in PbPb collisions at* $\sqrt{s_{NN}} = 2.76$ *TeV*. Phys. Rev. Lett. **109** (2012), 152303. arXiv: 1205.2488 [nucl-ex] (cit. on p. 5).

[41] Z. Jiang et al. *Pseudorapidity and Initial-energy Densities in p+p and Heavy-ion Collisions at RHIC and LHC*. Acta Phys. Pol. B **12** (Jan. 2019), 261. arXiv: 1806.05750 [nucl-th] (cit. on p. 5).

[42] F. Karsch. *Lattice QCD at high temperature and density*. Lect. Notes Phys. **583** (2002), 209. arXiv: hep-lat/0106019 (cit. on p. 5).

[43] HotQCD Collaboration. *Equation of state in $(2+1)$-flavor QCD*. Phys. Rev. D **90** (2014), 094503. arXiv: 1407.6387 [hep-lat] (cit. on p. 5).

[44] J. W. Harris et al. *The Search for the quark - gluon plasma*. Ann. Rev. Nucl. Part. Sci. **46** (1996), 71. arXiv: hep-ph/9602235 (cit. on p. 5).

[45] Z. Fodor et al. *Critical point of QCD at finite T and mu, lattice results for physical quark masses*. JHEP **04** (2004), 050. arXiv: hep-lat/0402006 (cit. on p. 5).

[46] ALICE Collaboration. *Production of light nuclei and anti-nuclei in pp and Pb-Pb collisions at energies available at the CERN Large Hadron Collider*. Phys. Rev. C **93** (2016), 024917. arXiv: 1506.08951 [nucl-ex] (cit. on p. 5).

[47] S. Borsanyi et al. *Is there still any T_c mystery in lattice QCD? Results with physical masses in the continuum limit III*. JHEP **09** (2010), 073. arXiv: 1005.3508 [hep-lat] (cit. on p. 5).

[48] PHENIX Collaboration. *Single identified hadron spectra from $\sqrt{s_{NN}} = 130$ GeV Au+Au collisions*. Phys. Rev. C **69** (2004), 024904. arXiv: nucl-ex/0307010 (cit. on p. 5).

[49] BRAHMS Collaboration. *Centrality dependent particle production at $y = 0$ and $y \sim 1$ in Au+Au collisions at $\sqrt{s_{NN}} = 200$ GeV*. Phys. Rev. C **72** (2005), 014908. arXiv: nucl-ex/0503010 (cit. on p. 5).

[50] PHOBOS Collaboration. *Identified hadron transverse momentum spectra in Au+Au collisions at $\sqrt{s_{NN}} = 62.4$ GeV*. Phys. Rev. C **75** (2007), 024910. arXiv: nucl-ex/0610001 (cit. on p. 5).

[51] ALICE Collaboration. *Centrality dependence of π, K, and p production in Pb-Pb collisions at $\sqrt{s_{NN}} = 2.76$ TeV*. Phys. Rev. C **88** (2013), 044910. arXiv: 1303.0737 [hep-ex] (cit. on p. 5).

[52] W. Busza et al. *Heavy Ion Collisions: The Big Picture, and the Big Questions*. Ann. Rev. Nucl. Part. Sci. **68** (2018), 339. arXiv: 1802.04801 [hep-ph] (cit. on pp. 5, 7).

[53] J. C. Collins et al. *Superdense Matter: Neutrons or Asymptotically Free Quarks?* Phys. Rev. Lett. **34** (1975), 1353 (cit. on pp. 5, 7).

[54] U. Heinz et al. *Collective flow and viscosity in relativistic heavy-ion collisions*. Ann. Rev. Nucl. Part. Sci. **63** (2013), 123. arXiv: 1301.2826 [nucl-th] (cit. on p. 5).

[55] M. Gyulassy. "The QGP discovered at RHIC". *Structure and dynamics of elementary matter*. 2004, 159. arXiv: nucl-th/0403032 (cit. on p. 5).

[56] A. Ster et al. *The Reconstructed final state of Pb+Pb 158 GeV/A reactions from spectra and correlation data of NA49, NA44 and WA98*. Nucl. Phys. A **661** (1999), 419. arXiv: hep-ph/9907338 (cit. on p. 6).

[57] A. M. Poskanzer et al. *Centrality dependence of directed and elliptic flow at the SPS*. Nucl. Phys. A **661** (1999), 341. arXiv: nucl-ex/9906013 (cit. on p. 6).

[58] C. Pinkenburg et al. *Elliptic flow: Transition from out-of-plane to in-plane emission in Au+Au collisions*. Phys. Rev. Lett. **83** (1999), 1295. arXiv: nucl-ex/9903010 (cit. on p. 6).

[59] ATLAS Collaboration. *Measurement of the azimuthal anisotropy of charged particles produced in* $\sqrt{s_{NN}} = 5.02$ *TeV Pb+Pb collisions with the ATLAS detector*. Eur. Phys. J. C **78** (2018), 997. arXiv: 1808.03951 [nucl-ex] (cit. on pp. 6, 49, 79).

[60] PHENIX Collaboration. *Elliptic Flow of Identified Hadrons in Au+Au Collisions at* $\sqrt{s_{NN}} = 200$ *GeV*. Phys. Rev. Lett. **91** (2003), 182301 (cit. on p. 6).

[61] CMS Collaboration. *Non-Gaussian elliptic-flow fluctuations in PbPb collisions at* $\sqrt{s_{NN}} = 5.02$ *TeV*. Phys. Lett. B **789** (2019), 643. arXiv: 1711.05594 [nucl-ex] (cit. on p. 6).

[62] ALICE Collaboration. *Anisotropic flow of charged particles in Pb-Pb collisions at* $\sqrt{s_{NN}} = 5.02$ *TeV*. Phys. Rev. Lett. **116** (2016), 132302. arXiv: 1602.01119 [nucl-ex] (cit. on p. 6).

[63] M. Connors et al. *Jet measurements in heavy ion physics*. Rev. Mod. Phys. **90** (2018), 025005. arXiv: 1705.01974 [nucl-ex] (cit. on p. 6).

[64] PHENIX Collaboration. *Enhanced Production of Direct Photons in Au+Au Collisions at* $\sqrt{s_{NN}} = 200$*GeV and Implications for the Initial Temperature*. Phys. Rev. Lett. **104** (2010), 132301. arXiv: 0804.4168 [nucl-ex] (cit. on p. 6).

[65] ALICE Collaboration. *Direct photon production in Pb–Pb collisions at* $\sqrt{s_{NN}} = 2.76$ *TeV*. Phys. Lett. B **754** (2016), 235. arXiv: 1509.07324 [nucl-ex] (cit. on p. 6).

[66] PHENIX Collaboration. *Detailed measurement of the* e^+e^- *pair continuum in* $p + p$ *and Au+Au collisions at* $\sqrt{s_{NN}} = 200$ *GeV and implications for direct photon production*. Phys. Rev. C **81** (2010), 034911. arXiv: 0912.0244 [nucl-ex] (cit. on p. 6).

[67] A. M. Poskanzer et al. *Methods for analyzing anisotropic flow in relativistic nuclear collisions*. Phys. Rev. C **58** (1998), 1671. arXiv: nucl-ex/9805001 (cit. on p. 6).

[68] D. Teaney et al. *Flow at the SPS and RHIC as a quark gluon plasma signature*. Phys. Rev. Lett. **86** (2001), 4783. arXiv: nucl-th/0011058 (cit. on p. 6).

[69] T. Hirano et al. *Hadronic dissipative effects on elliptic flow in ultrarelativistic heavy-ion collisions*. Phys. Lett. B **636** (2006), 299. arXiv: nucl-th/0511046 (cit. on p. 6).

[70] ALICE Collaboration. *Higher harmonic anisotropic flow measurements of charged particles in Pb-Pb collisions at* $\sqrt{s_{NN}} = 2.76$ *TeV*. Phys. Rev. Lett. **107** (2011), 032301. arXiv: 1105.3865 [nucl-ex] (cit. on pp. 6, 7).

[71] H. Niemi et al. *Event-by-event fluctuations in a perturbative QCD + saturation + hydrodynamics model: Determining QCD matter shear viscosity in ultrarelativistic heavy-ion collisions*. Phys. Rev. C **93** (2016), 024907. arXiv: 1505.02677 [hep-ph] (cit. on pp. 6, 7).

[72] S. A. Voloshin et al. *Collective phenomena in non-central nuclear collisions*. Landolt-Bornstein **23** (2010), 293. arXiv: 0809.2949 [nucl-ex] (cit. on p. 7).

[73] M. Gyulassy et al. *New forms of QCD matter discovered at RHIC*. Nucl. Phys. A **750** (2005), 30. arXiv: nucl-th/0405013 (cit. on p. 7).

[74] A. D. Linde. *Phase transitions in gauge theories and cosmology*. Rept. Prog. Phys. **42** (1979), 389 (cit. on p. 8).

[75] LIGO/VIRGO Collaboration. *GW170817: Observation of Gravitational Waves from a Binary Neutron Star Inspiral*. Phys. Rev. Lett. **119** (2017), 161101. arXiv: 1710.05832 [gr-qc] (cit. on p. 8).

[76] S. Han et al. *Tidal deformability with sharp phase transitions in (binary) neutron stars*. Phys. Rev. D **99** (2019), 083014. arXiv: 1810.10967 [nucl-th] (cit. on p. 8).

[77] J.-E. Christian et al. *Signals in the tidal deformability for phase transitions in compact stars with constraints from GW170817*. Phys. Rev. D **99** (2019), 023009. arXiv: 1809.03333 [astro-ph.HE] (cit. on p. 8).

[78] E. R. Most et al. *Signatures of Quark-Hadron Phase Transitions in General-Relativistic Neutron-Star Mergers*. Phys. Rev. Lett. **122** (2019), 061101. arXiv: 1807.03684 [astro-ph.HE] (cit. on p. 8).

[79] A. Bauswein et al. *Equation-of-state dependence of the gravitational-wave signal from the ring-down phase of neutron-star mergers*. Phys. Rev. D **86** (2012), 063001. arXiv: 1204.1888 [astro-ph.SR] (cit. on p. 8).

[80] A. Bauswein et al. *Identifying a First-Order Phase Transition in Neutron-Star Mergers through Gravitational Waves*. Phys. Rev. Lett. **122** (2019), 061102. arXiv: 1809.01116 [astro-ph.HE] (cit. on p. 8).

[81] A. S. Kronfeld. *Twenty-first Century Lattice Gauge Theory: Results from the QCD Lagrangian*. Ann. Rev. Nucl. Part. Sci. **62** (2012), 265. arXiv: 1203.1204 [hep-lat] (cit. on p. 8).

[82] R. Glauber. *Lectures in theoretical physics, ed. WE Brittin and LG Dunham*. Interscience, New York **1** (1959), 315 (cit. on p. 8).

[83] H. D. Vries et al. *Nuclear charge-density-distribution parameters from elastic electron scattering*. At. Data Nucl. Data Tables **36** (1987), 495 (cit. on p. 9).

[84] M. L. Miller et al. *Glauber Modeling in High-Energy Nuclear Collisions*. Ann. Rev. Nucl. Part. Sci. **57** (2007), 205 (cit. on pp. 9–11, 24).

[85] B. Alver et al. *The PHOBOS Glauber Monte Carlo*. (2008). arXiv: 0805.4411 [nucl-ex] (cit. on p. 9).

[86] D. Kharzeev et al. *Hadron production in nuclear collisions at RHIC and high density QCD*. Phys. Lett. B **507** (2001), 121. arXiv: nucl-th/0012025 (cit. on p. 11).

[87] A. Bialas et al. *Multiplicity Distributions in Nucleus-Nucleus Collisions at High-Energies*. Nucl. Phys. B **111** (1976), 461 (cit. on p. 11).

[88] D. Perepelitsa et al. *Centrality determination in* $\sqrt{s_{NN}} = 5.02$ *TeV Pb+Pb collision data in 2015*. ATL-COM-PHYS-2016-1287 (cit. on p. 11).

[89] SESAM Collaboration. *Observation of string breaking in QCD*. Phys. Rev. D **71** (2005), 114513. arXiv: hep-lat/0505012 (cit. on p. 12).

[90] OPAL Collaboration. *Experimental properties of gluon and quark jets from a point source*. Eur. Phys. J. C **11** (1999), 217. arXiv: hep-ex/9903027 (cit. on p. 12).

[91] SLAC-LBL Collaboration. *Evidence for Jet Structure in Hadron Production by* e^+e^- *Annihilation*. Phys. Rev. Lett. **35** (1975), 1609 (cit. on p. 12).

[92] SLAC-LBL Collaboration. *Hadron Production by* e^+e^- *Annihilation at Center-of-mass Energies Between* 2.6 *GeV and* 7.8 *GeV*. Phys. Rev. D **26** (1982), 991 (cit. on p. 12).

[93] PLUTO Collaboration. *Jet Analysis of the* Υ *(9.46) Decay Into Charged Hadrons*. Phys. Lett. B **82** (1979), 449 (cit. on p. 12).

[94] PLUTO Collaboration. *Evidence for Gluon Bremsstrahlung in e^+e^- Annihilations at High-Energies*. Phys. Lett. B **86** (1979), 418 (cit. on p. 12).

[95] A. H. Mueller. *Jets at LEP and HERA*. J. Phys. G **17** (1991), 1443 (cit. on p. 12).

[96] G. Kramer et al. *Jet Cross-Sections in e^+e^- Annihilation*. Fortsch. Phys. **37** (1989), 161 (cit. on p. 12).

[97] T. Sjostrand et al. *A Brief Introduction to PYTHIA 8.1*. Comput. Phys. Commun. **178** (2008), 852. arXiv: 0710.3820 [hep-ph] (cit. on p. 13).

[98] G.-Y. Qin et al. *Jet quenching in high-energy heavy-ion collisions*. Int. J. Mod. Phys. E **24** (2015), 1530014. arXiv: 1511.00790 [hep-ph] (cit. on pp. 13, 17, 55).

[99] A. D. Martin et al. *Parton distributions for the LHC*. Eur. Phys. J. C **63** (2009), 189. arXiv: 0901.0002 [hep-ph] (cit. on p. 14).

[100] A. Majumder et al. *The Theory and Phenomenology of Perturbative QCD Based Jet Quenching*. Prog. Part. Nucl. Phys. **66** (2011), 41. arXiv: 1002.2206 [hep-ph] (cit. on p. 14).

[101] Particle Data Group. *Review of Particle Physics*. Chin. Phys. C **40** (2016), 100001 (cit. on p. 15).

[102] D. Britzger et al. *Determination of the strong coupling constant using inclusive jet cross section data from multiple experiments*. Eur. Phys. J. C **79** (2019), 68. arXiv: 1712.00480 [hep-ph] (cit. on p. 15).

[103] Particle Data Group. *Review of Particle Physics*. Phys. Rev. D **98** (2018), 030001 (cit. on p. 15).

[104] M. Hirai et al. *Determination of nuclear parton distribution functions and their uncertainties at next-to-leading order*. Phys. Rev. C **76** (2007), 065207. arXiv: 0709.3038 [hep-ph] (cit. on p. 16).

[105] D. de Florian et al. *Nuclear parton distributions at next to leading order*. Phys. Rev. D **69** (2004), 074028. arXiv: hep-ph/0311227 (cit. on p. 16).

[106] K. J. Eskola et al. *EPS09: A New Generation of NLO and LO Nuclear Parton Distribution Functions*. JHEP **04** (2009), 065. arXiv: 0902.4154 [hep-ph] (cit. on p. 16).

[107] S. J. Brodsky et al. *Shadowing and antishadowing of nuclear structure functions*. Phys. Rev. Lett. **64** (1990), 1342 (cit. on p. 16).

[108] European Muon Collaboration. *The ratio of the nucleon structure functions F2N for iron and deuterium*. Phys. Lett. B **123** (1983), 275 (cit. on p. 16).

[109] O. Hen et al. *New data strengthen the connection between short range correlations and the EMC effect*. Phys. Rev. C **85** (2012), 047301. arXiv: 1202.3452 [nucl-ex] (cit. on p. 16).

[110] K. Saito et al. *Effect of the Fermi Motion on Nuclear Structure Functions and the EMC Effect*. Z. Phys. A **322** (1985), 299 (cit. on p. 16).

[111] ATLAS Collaboration. *Centrality and rapidity dependence of inclusive jet production in* $\sqrt{s_{NN}} = 5.02$ *TeV p+Pb collisions with the ATLAS detector*. Phys. Lett. B **748** (2015), 392. arXiv: 1412.4092 [hep-ex] (cit. on pp. 16, 61, 94).

[112] ALICE Collaboration. *Centrality dependence of charged jet production in p+Pb collisions at* $\sqrt{s_{NN}} = 5.02$ *TeV*. Eur. Phys. J. C **76** (2016), 271. arXiv: 1603.03402 [nucl-ex] (cit. on p. 16).

[113] CMS Collaboration. *Measurement of inclusive jet production and nuclear modifications in pPb collisions at* $\sqrt{s_{NN}} = 5.02$ *TeV*. Eur. Phys. J. C **76** (2016), 372. arXiv: 1601.02001 [nucl-ex] (cit. on pp. 16, 17).

[114] R. D. Weller et al. *One fluid to rule them all: viscous hydrodynamic description of event-by-event central p+p, p+Pb and Pb+Pb collisions at* $\sqrt{s} = 5.02$ *TeV*. Phys. Lett. B **774** (2017), 351. arXiv: 1701.07145 [nucl-th] (cit. on p. 17).

[115] CMS Collaboration. *Jet momentum dependence of jet quenching in PbPb collisions at* $\sqrt{s_{NN}} = 2.76$ *TeV*. Phys. Lett. B **712** (2012), 176. arXiv: 1202.5022 [nucl-ex] (cit. on p. 16).

[116] ATLAS Collaboration. *Measurement of the nuclear modification factor for inclusive jets in Pb+Pb collisions at* $\sqrt{s_{NN}} = 5.02$ *TeV with the ATLAS detector*. Phys. Lett. B **790** (2019), 108. arXiv: 1805.05635 [nucl-ex] (cit. on pp. 16, 24, 25, 49, 53, 55).

[117] CMS Collaboration. *Measurement of transverse momentum relative to dijet systems in PbPb and pp collisions at* $\sqrt{s_{NN}} = 2.76$ *TeV*. JHEP **01** (2016), 006. arXiv: 1509.09029 [nucl-ex] (cit. on pp. 16, 55).

[118] R. Baier et al. *Radiative energy loss of high energy quarks and gluons in a finite-volume quark-gluon plasma*. Nucl. Phys. B **483** (1997), 291 (cit. on p. 18).

[119] M. Gyulassy et al. *Jet quenching in thin quark gluon plasmas. 1. Formalism*. Nucl. Phys. B **571** (2000), 197. arXiv: hep-ph/9907461 (cit. on p. 18).

[120] U. A. Wiedemann. *Gluon radiation off hard quarks in a nuclear environment: Opacity expansion*. Nucl. Phys. B **588** (2000), 303. arXiv: hep-ph/0005129 (cit. on p. 18).

[121] P. B. Arnold et al. *Photon emission from ultrarelativistic plasmas*. JHEP **11** (2001), 057. arXiv: hep-ph/0109064 (cit. on p. 18).

[122] X.-F. Guo et al. *Multiple scattering, parton energy loss and modified fragmentation functions in deeply inelastic eA scattering*. Phys. Rev. Lett. **85** (2000), 3591. arXiv: hep-ph/0005044 (cit. on p. 18).

[123] R. Atkin. *Review of jet reconstruction algorithms*. J. Phys. Conf. Ser. **645** (2015), 012008 (cit. on p. 18).

[124] UA1 Collaboration. *Hadronic jet production at the CERN proton-antiproton collider*. Phys. Lett. B **132** (1983), 214 (cit. on p. 18).

[125] G. C. Blazey et al. "Run II jet physics". *QCD and weak boson physics in Run II. Proceedings, Batavia, USA, March 4-6, June 3-4, November 4-6, 1999*. 2000, 47. arXiv: hep-ex/0005012 (cit. on p. 18).

[126] G. P. Salam et al. *A practical seedless infrared-safe cone jet algorithm*. JHEP **05** (2007), 086. arXiv: 0704.0292 [hep-ph] (cit. on pp. 18, 19).

[127] S. Catani et al. *Longitudinally invariant K_t clustering algorithms for hadron hadron collisions*. Nucl. Phys. B **406** (1993), 187 (cit. on p. 18).

[128] M. Cacciari et al. *The anti-k_t jet clustering algorithm*. JHEP **0804** (2008), 063. arXiv: 0802.1189 [hep-ph] (cit. on pp. 18, 20, 50).

[129] Y. L. Dokshitzer et al. *Better jet clustering algorithms*. JHEP **08** (1997), 001. arXiv: hep-ph/9707323 (cit. on p. 18).

[130] G. P. Salam. *Towards Jetography*. Eur. Phys. J. C **67** (2010), 637. arXiv: 0906.1833 [hep-ph] (cit. on p. 19).

[131] PHENIX Collaboration. *Suppression of hadrons with large transverse momentum in central Au+Au collisions at $\sqrt{s_{NN}} = 130$ GeV*. Phys. Rev. Lett. **88** (2002), 022301. arXiv: nucl-ex/0109003 (cit. on pp. 21, 22).

[132] STAR Collaboration. *Transverse momentum and collision energy dependence of high p_T hadron suppression in Au+Au collisions at ultrarelativistic energies*. Phys. Rev. Lett. **91** (2003), 172302. arXiv: nucl-ex/0305015 [nucl-ex] (cit. on p. 22).

[133] PHENIX Collaboration. *Suppressed π^0 Production at Large Transverse Momentum in Central Au+Au Collisions at $\sqrt{s_{NN}} = 200$ GeV*. Phys. Rev. Lett. **91** (2003), 072301. arXiv: nucl-ex/0304022 (cit. on p. 22).

[134] PHOBOS Collaboration. *Pseudorapidity dependence of charged hadron transverse momentum spectra in $d+$Au collisions at $\sqrt{s_{NN}} = 200$ GeV*. Phys. Rev. C **70** (2004), 061901. arXiv: nucl-ex/0406017 [nucl-ex] (cit. on p. 22).

[135] ALICE Collaboration. *Suppression of Charged Particle Production at Large Transverse Momentum in Central Pb-Pb Collisions at* $\sqrt{s_{NN}} = 2.76$ *TeV*. Phys. Lett. B **696** (2011), 30. arXiv: 1012.1004 [nucl-ex] (cit. on p. 22).

[136] CMS Collaboration. *Study of high-*p_{T} *charged particle suppression in PbPb compared to pp collisions at* $\sqrt{s_{NN}} = 2.76$ *TeV*. Eur. Phys. J. C **72** (2012), 1945. arXiv: 1202.2554 [nucl-ex] (cit. on p. 22).

[137] CMS Collaboration. *Charged-particle nuclear modification factors in PbPb and pPb collisions at* $\sqrt{s_{NN}} = 5.02$ *TeV*. JHEP **04** (2017), 039. arXiv: 1611.01664 [nucl-ex] (cit. on pp. 22, 55).

[138] ATLAS Collaboration. *Measurement of nuclear modification factor* R_{AA} *in Pb+Pb collisions at* $\sqrt{s_{NN}} = 5.02$ *TeV with the ATLAS detector at the LHC*. Tech. rep. ATLAS-CONF-2017-012 (cit. on p. 22).

[139] ISR Collaboration. *Large transverse momentum* π^0 *production in* $\alpha\alpha$*, dd and pp collisions at the CERN ISR*. Phys. Lett. B **185** (1987), 213 (cit. on p. 22).

[140] E. Wang et al. *Interplay of soft and hard processes and hadron* p_T *spectra in* pA *and* AA *collisions*. Phys. Rev. C **64** (2001), 034901. arXiv: nucl-th/0104031 (cit. on p. 22).

[141] PHENIX Collaboration. *Measurement of Direct Photons in Au+Au Collisions at* $\sqrt{s_{NN}} = 200$ *GeV*. Phys. Rev. Lett. **109** (2012), 152302. arXiv: 1205.5759 [nucl-ex] (cit. on p. 22).

[142] ATLAS Collaboration. *Measurement of jet* p_{T} *correlations in Pb+Pb and pp collisions at* $\sqrt{s_{NN}} = 2.76$ *TeV with the ATLAS detector*. Phys. Lett. B **774** (2017), 379. arXiv: 1706.09363 [hep-ex] (cit. on pp. 22–24, 55, 105).

[143] STAR Collaboration. *Dijet imbalance measurements in Au+Au and pp collisions at* $\sqrt{s_{NN}} = 200$ *GeV at STAR*. Phys. Rev. Lett. **119** (2017), 062301. arXiv: 1609.03878 [nucl-ex] (cit. on pp. 23, 24).

[144] ATLAS Collaboration. *Observation of a Centrality-Dependent Dijet Asymmetry in Lead-Lead Collisions at* $\sqrt{s_{NN}} = 2.76$ *TeV with the ATLAS Detector at the LHC*. Phys. Rev. Lett. **105** (2010), 252303. arXiv: 1011.6182 [hep-ex] (cit. on pp. 23, 55).

[145] CMS Collaboration. *Studies of jet quenching using isolated-photon+jet correlations in PbPb and pp collisions at* $\sqrt{s_{NN}} = 2.76$ *TeV*. Phys. Lett. B **718** (2013), 773. arXiv: 1205.0206 [nucl-ex] (cit. on pp. 23, 55).

[146] CMS Collaboration. *Observation and studies of jet quenching in PbPb collisions at nucleon-nucleon center-of-mass energy = 2.76 TeV*. Phys. Rev. C **84** (2011), 024906. arXiv: 1102.1957 [nucl-ex] (cit. on pp. 23, 24, 38, 55).

[147] ALICE Collaboration. *Full Jet Reconstruction in* 2.76 *TeV pp and Pb-Pb collisions in the ALICE experiment*. J. Phys. Conf. Ser. **446** (2013), 012006. arXiv: 1304.5945 [nucl-ex] (cit. on pp. 24, 25).

[148] ATLAS Collaboration. *Measurements of the Nuclear Modification Factor for Jets in Pb+Pb Collisions at* $\sqrt{s_{NN}} = 2.76$ *TeV with the ATLAS Detector*. Phys. Rev. Lett. **114** (2015), 072302. arXiv: 1411.2357 [hep-ex] (cit. on pp. 24, 31, 40, 55, 97).

[149] CMS Collaboration. *Measurement of inclusive jet cross sections in pp and PbPb collisions at* $\sqrt{s_{NN}} =$ 2.76 *TeV*. Phys. Rev. C **96** (2017), 015202. arXiv: 1609.05383 [nucl-ex] (cit. on pp. 24, 31–33, 35, 36, 55).

[150] ALICE Collaboration. *Measurement of jet spectra in Pb-Pb collisions at* $\sqrt{s_{NN}} = 2.76$ *TeV with the ALICE detector at the LHC*. Nucl. Phys. A **910-911** (2013), 421. arXiv: 1208.6169 [nucl-ex] (cit. on p. 24).

[151] ATLAS Collaboration. *Measurement of jet fragmentation in Pb+Pb and pp collisions at* $\sqrt{s_{NN}} = 5.02$ *TeV with the ATLAS detector*. Phys. Rev. C **98** (2018), 024908. arXiv: 1805.05424 [nucl-ex] (cit. on pp. 24, 26–28, 55, 61, 62, 70, 72, 80, 84, 99, 105–107, 109, 112).

[152] J. Adam et al. *Measurement of jet suppression in central Pb-Pb collisions at* $\sqrt{s_{NN}} = 2.76$ *TeV*. Phys. Lett. B **746** (2015), 1. arXiv: 1502.01689 [nucl-ex] (cit. on p. 24).

[153] M. Spousta et al. *Interpreting single jet measurements in Pb+Pb collisions at the LHC*. Eur. Phys. J. C **76** (2016), 50. arXiv: 1504.05169 [hep-ph] (cit. on pp. 27, 37–40, 106).

[154] Y.-T. Chien et al. *Jet Quenching from QCD Evolution*. Phys. Rev. D **93** (2016), 074030. arXiv: 1509.02936 [hep-ph] (cit. on pp. 27, 106).

[155] Z.-B. Kang et al. *Inclusive production of small radius jets in heavy-ion collisions*. Phys. Lett. B **769** (2017), 242. arXiv: 1701.05839 [hep-ph] (cit. on pp. 27, 106).

[156] J. Casalderrey-Solana et al. *A Hybrid Strong/Weak Coupling Approach to Jet Quenching*. JHEP **10** (2014), 019. arXiv: 1405.3864 [hep-ph] (cit. on pp. 27, 34).

[157] CMS Collaboration. *Jet properties in PbPb and pp collisions at* $\sqrt{s_{NN}} = 5.02$ *TeV*. JHEP **05** (2018), 006. arXiv: 1803.00042 [nucl-ex] (cit. on pp. 27, 29, 55, 112).

[158] Y. Tachibana et al. *Full jet in quark-gluon plasma with hydrodynamic medium response*. Phys. Rev. C **95** (2017), 044909. arXiv: 1701.07951 [nucl-th] (cit. on pp. 30, 32–34, 55, 105, 106).

[159] ALICE Collaboration. *Measurement of charged jet suppression in Pb-Pb collisions at* $\sqrt{s_{NN}} = 2.76$ *TeV*. JHEP **03** (2014), 013. arXiv: 1311.0633 [nucl-ex] (cit. on pp. 31, 36, 55).

[160] CMS Collaboration. *Modification of jet shapes in PbPb collisions at* $\sqrt{s_{NN}} = 2.76$ *TeV*. Phys. Lett. B **730** (2014), 243. arXiv: 1310.0878 [nucl-ex] (cit. on pp. 34, 37, 55).

[161] Z. Hulcher et al. *Resolution Effects in the Hybrid Strong/Weak Coupling Model*. JHEP **03** (2018), 010. arXiv: 1707.05245 [hep-ph] (cit. on pp. 34–37, 109).

[162] J. Casalderrey-Solana et al. *Angular Structure of Jet Quenching Within a Hybrid Strong/Weak Coupling Model*. JHEP **03** (2017), 135. arXiv: 1609.05842 [hep-ph] (cit. on pp. 34, 35, 55).

[163] P. M. Chesler et al. *On the Evolution of Jet Energy and Opening Angle in Strongly Coupled Plasma*. JHEP **05** (2016), 098. arXiv: 1511.07567 [hep-th] (cit. on pp. 34, 109).

[164] P. M. Chesler et al. *Jet quenching in strongly coupled plasma*. Phys. Rev. D **90** (2014), 025033. arXiv: 1402.6756 [hep-th] (cit. on p. 34).

[165] J. Casalderrey-Solana et al. *Out of Medium Fragmentation from Long-Lived Jet Showers*. Phys. Lett. B **710** (2012), 175. arXiv: 1111.0310 [hep-ph] (cit. on p. 34).

[166] T. Hirano et al. *Elliptic flow in Pb+Pb collisions at* $\sqrt{s_{NN}} = 2.76$ *TeV: hybrid model assessment of the first data*. Phys. Rev. C **84** (2011), 011901. arXiv: 1012.3955 [nucl-th] (cit. on p. 35).

[167] ATLAS Collaboration. *Measurement of the jet radius and transverse momentum dependence of inclusive jet suppression in lead-lead collisions at* $\sqrt{s_{NN}} = 2.76$ *TeV with the ATLAS detector*. Phys. Lett. B **719** (2013), 220. arXiv: 1208.1967 [hep-ex] (cit. on pp. 36, 53).

[168] J. Rusnak. *Inclusive spectrum of charged jets in central Au+Au collisions at* $\sqrt{s_{NN}} = 200$ *GeV by STAR*. PoS **EPS-HEP2013** (2013), 191 (cit. on p. 36).

[169] CMS Collaboration. *Measurement of jet fragmentation in PbPb and pp collisions at* $\sqrt{s_{NN}} = 2.76$ *TeV*. Phys. Rev. C **90** (2014), 024908. arXiv: 1406.0932 [nucl-ex] (cit. on pp. 37, 55, 112).

[170] J.-P. Blaizot et al. *Medium-induced QCD cascade: democratic branching and wave turbulence*. Phys. Rev. Lett. **111** (2013), 052001. arXiv: 1301.6102 [hep-ph] (cit. on p. 38).

[171] J. Casalderrey-Solana et al. *New picture of jet quenching dictated by color coherence*. Phys. Lett. B **725** (2013), 357. arXiv: 1210.7765 [hep-ph] (cit. on p. 38).

[172] R. Baier et al. *Quenching of hadron spectra in media*. JHEP **09** (2001), 033. arXiv: hep-ph/0106347 (cit. on p. 39).

[173] ATLAS Collaboration. *Measurement of inclusive jet charged-particle fragmentation functions in Pb+Pb collisions at* $\sqrt{s_{NN}} = 2.76$ *TeV with the ATLAS detector*. Phys. Lett. B **739** (2014), 320. arXiv: 1406.2979 [hep-ex] (cit. on pp. 40, 55).

[174] L. Evans et al. *LHC Machine*. JINST **3** (2008), S08001 (cit. on p. 41).

[175] ATLAS Collaboration. *The CERN Accelerator Complex*. URL: https://cds.cern.ch/record/1260465 (cit. on p. 42).

[176] ATLAS Collaboration. *The ATLAS Experiment at the CERN Large Hadron Collider*. JINST **3** (2008), S08003 (cit. on pp. 44, 45, 47).

[177] ATLAS Collaboration. *The ATLAS Insertable B-Layer: from construction to operation*. JINST **11** (2016), C12036. arXiv: 1610.01994 [physics.ins-det] (cit. on p. 44).

[178] ATLAS Collaboration. *The ATLAS Insertable B-Layer Technical Design Report*. CERN-LHCC-2010-013 (cit. on p. 44).

[179] ATLAS Collaboration. *The upgraded Pixel detector and the commissioning of the Inner Detector tracking of the ATLAS experiment for Run-2 at the Large Hadron Collider*. PoS EPS-HEP2015 (2015), 261. arXiv: 1608.07850 [physics.ins-det] (cit. on p. 45).

[180] ATLAS Collaboration. *Measurement of flow harmonics with multi-particle cumulants in Pb+Pb collisions at* $\sqrt{s_{NN}} = 2.76$ *TeV with the ATLAS detector*. Eur. Phys. J. C **74** (2014), 3157. arXiv: 1408.4342 [hep-ex] (cit. on p. 48).

[181] ATLAS Collaboration. *Performance plots for pp and Pb+Pb collisions at* $\sqrt{s_{NN}} = 5.02$ *TeV*. URL: https://atlas.web.cern.ch/Atlas/GROUPS/PHYSICS/PLOTS/HION-2015-001/ (cit. on pp. 48–50, 52).

[182] ATLAS Collaboration. *Study of photon-jet momentum correlations in Pb+Pb and pp collisions at* $\sqrt{s_{NN}} = 5.02$ *TeV with ATLAS*. Tech. rep. ATLAS-CONF-2016-110. 2016 (cit. on p. 49).

[183] ATLAS Collaboration. *Measurement of the pseudorapidity and transverse momentum dependence of the elliptic flow of charged particles in lead-lead collisions at* $\sqrt{s_{NN}} = 2.76$ *TeV with the ATLAS detector*. Phys. Lett. B **707** (2012), 330. arXiv: 1108.6018 [hep-ex] (cit. on p. 49).

[184] ATLAS Collaboration. *ATLAS Event Displays from 2010 Heavy Ion Collisions*. URL: https://twiki.cern.ch/twiki/bin/view/AtlasPublic/EventDisplayHeavyIonCollisions (cit. on pp. 50, 52).

[185] A. Angerami et al. *Performance of Jet Reconstruction in Heavy Ion Collisions*. ATL-PHYS-INT-2012-058 (cit. on pp. 50, 61).

[186] B. Cole et al. *Jet Fragmentation in Heavy Ion Collisions*. ATL-COM-PHYS-2012-628 (cit. on p. 50).

[187] M. Cacciari et al. *FastJet User Manual*. Eur. Phys. J. C **72** (2012), 1896. arXiv: 1111.6097 [hep-ph] (cit. on p. 49).

[188] ATLAS Collaboration. *Measurement of the azimuthal anisotropy for charged particle production in* $\sqrt{s_{NN}} = 2.76$ *TeV lead-lead collisions with the ATLAS detector*. Phys. Rev. C **86** (2012), 014907. arXiv: 1203.3087 [hep-ex] (cit. on p. 51).

[189] R. Wigmans. *Modern Particle Physics*. Oxford, UK: Oxford University Press, 2000 (cit. on p. 51).

[190] ATLAS Collaboration. *Jet energy measurement and its systematic uncertainty in proton-proton collisions at* $\sqrt{s} = 7$ *TeV with the ATLAS detector*. Eur. Phys. J. C **75** (2015), 17. arXiv: 1406.0076 [hep-ex] (cit. on pp. 52, 84).

[191] A. Puri. *Cross calibration factors and their uncertainties for application to 2015 heavy ion jets*. ATL-COM-PHYS-2016-1253 (cit. on pp. 52, 94, 97).

[192] ATLAS Collaboration. *Jet energy scale and its uncertainty for jets reconstructed using the ATLAS heavy ion jet algorithm*. Tech. rep. ATLAS-CONF-2015-016. 2015 (cit. on pp. 52, 97).

[193] ALICE Collaboration. *Measurement of jet suppression in central Pb-Pb collisions at* $\sqrt{s_{NN}} = 2.76$ *TeV*. Phys. Lett. B **746** (2015), 1. arXiv: 1502.01689 [nucl-ex] (cit. on p. 55).

[194] ATLAS Collaboration. *Measurement of photon–jet transverse momentum correlations in 5.02 TeV Pb+Pb and pp collisions with ATLAS*. Phys. Lett. B **789** (2019), 167. arXiv: 1809.07280 [nucl-ex] (cit. on p. 55).

[195] ATLAS Collaboration. *Measurement of the jet fragmentation function and transverse profile in proton-proton collisions at a center-of-mass energy of* 7 *TeV with the ATLAS detector*. Eur. Phys. J. C **71** (2011), 1795. arXiv: 1109.5816 [hep-ex] (cit. on p. 55).

[196] ALICE Collaboration. *Medium modification of the shape of small-radius jets in central Pb-Pb collisions at* $\sqrt{s_{NN}} = 2.76$ *TeV*. JHEP **10** (2018), 139. arXiv: 1807.06854 [nucl-ex] (cit. on p. 55).

[197] CMS Collaboration. *Shape, transverse size, and charged-hadron multiplicity of jets in pp collisions at* $\sqrt{s} = 7$ *TeV*. JHEP **06** (2012), 160. arXiv: 1204.3170 [hep-ex] (cit. on p. 55).

[198] ATLAS Collaboration. *Measurement of jet fragmentation in Pb+Pb and pp collisions at* $\sqrt{s_{NN}} = 2.76$ *TeV with the ATLAS detector at the LHC*. Eur. Phys. J. C **77** (2017), 379. arXiv: 1702.00674 [hep-ex] (cit. on pp. 55, 105, 112).

[199] CMS Collaboration. *Decomposing transverse momentum balance contributions for quenched jets in PbPb collisions at* $\sqrt{s_{NN}} = 2.76$ *TeV*. JHEP **11** (2016), 055. arXiv: 1609.02466 [nucl-ex] (cit. on p. 55).

[200] I. Vitev et al. *A theory of jet shapes and cross sections: from hadrons to nuclei*. JHEP **11** (2008), 093. arXiv: 0810.2807 [hep-ph] (cit. on p. 55).

[201] G. Ovanesyan et al. *An effective theory for jet propagation in dense QCD matter: jet broadening and medium-induced bremsstrahlung*. JHEP **06** (2011), 080. arXiv: 1103.1074 [hep-ph] (cit. on p. 55).

[202] J.-P. Blaizot et al. *Angular structure of the in-medium QCD cascade*. Phys. Rev. Lett. **114** (2015), 222002. arXiv: 1407.0326 [hep-ph] (cit. on pp. 55, 109).

[203] M. A. Escobedo et al. *Event-by-event fluctuations in the medium-induced jet evolution*. JHEP **05** (2016), 008. arXiv: 1601.03629 [hep-ph] (cit. on p. 55).

[204] ATLAS Collaboration. *ATLAS HI Trigger*. URL: {https://twiki.cern.ch/twiki/bin/view/AtlasProtected/TrigHIRecommendedTriggers2015} (cit. on p. 57).

[205] ATLAS Collaboration. *Performance of the ATLAS Trigger System in 2015*. Eur. Phys. J. C **77** (2017), 317. arXiv: 1611.09661 [hep-ex] (cit. on p. 57).

[206] A. M. Sickles et al. *Jet Fragmentation in Pb+Pb Collisions at 5.02 TeV - Supporting Note*. ATL-COM-PHYS-2016-1721 (cit. on pp. 58, 63–67, 73, 74, 79).

[207] P. Nason. *A New method for combining NLO QCD with shower Monte Carlo algorithms*. JHEP **11** (2004), 040. arXiv: hep-ph/0409146 (cit. on p. 58).

[208] T. Sjostrand et al. *An Introduction to PYTHIA 8.2*. Comput. Phys. Commun. **191** (2015), 159. arXiv: 1410.3012 [hep-ph] (cit. on p. 58).

[209] ATLAS Collaboration. *ATLAS Run 1 Pythia8 tunes*. Tech. rep. ATL-PHYS-PUB-2014-021. 2014 (cit. on p. 58).

[210] R. D. Ball et al. *Parton distributions with LHC data*. Nucl. Phys. B **867** (2013), 244. arXiv: 1207.1303 [hep-ph] (cit. on p. 59).

[211] X.-N. Wang et al. *HIJING: A Monte Carlo model for multiple jet production in pp, pA and AA collisions*. Phys. Rev. D **44** (1991), 3501 (cit. on pp. 59, 72).

[212] GEANT4 Collaboration, S. Agostinelli et al. *GEANT4: A simulation toolkit*. Nucl. Instrum. Meth. A **506** (2003), 250 (cit. on p. 59).

[213] ATLAS Collaboration. *The ATLAS Simulation Infrastructure*. Eur. Phys. J. C **70** (2010), 823. arXiv: 1005.4568 [physics.ins-det] (cit. on p. 59).

[214] ATLAS Collaboration. *Tracking Recommendations for ICHEP 2016*. URL: https://twiki.cern.ch/twiki/bin/view/AtlasProtected/TrackingCPICHEP2016 (cit. on pp. 62, 98).

[215] ATLAS Collaboration. *Tracking Recommendations for ICHEP 2016*. URL: https://twiki.cern.ch/twiki/bin/view/AtlasProtected/TrackingCPICHEP2016 (cit. on pp. 68, 98).

[216] T. Bold et al. *Measurement of W boson production in Pb+Pb collisions at* $\sqrt{s_{NN}} = 5.02$ *TeV - Supporting Note*. ATL-COM-PHYS-2016-828 (cit. on p. 68).

[217] ATLAS Collaboration. *Measurement of jet fragmentation in 5.02 TeV proton-lead and proton-proton collisions with the ATLAS detector*. Nucl. Phys. A **978** (2018), 65. arXiv: 1706.02859 [hep-ex] (cit. on pp. 68, 103).

[218] B. Cole et al. *Supporting note for measurement of inclusive jet charged particle fragmentation functions in Pb+Pb collisions*. ATL-COM-PHYS-2012-1653 (cit. on p. 80).

[219] G. D'Agostini. *A Multidimensional unfolding method based on Bayes' theorem*. Nucl. Instrum. Meth. A **362** (1995), 487 (cit. on p. 84).

[220] T. Adye. *Unfolding algorithms and tests using RooUnfold*. PHYSTAT 2009 Workshop Proceedings (2011). arXiv: 1105.1160 [physics.data-an] (cit. on p. 84).

[221] G. D'Agostini. *A Multidimensional unfolding method based on Bayes' theorem*. Nucl. Instrum. Meth. A **362** (1995), 487 (cit. on p. 84).

[222] G. Choudalakis et al. *Characteristic dip in average transverse energy density and multiplicity around the axis of Anti-kT jets*. ATL-COM-PHYS-2010-139 (cit. on p. 87).

[223] ATLAS Collaboration. *JES Uncertainties 2015*. URL: https://twiki.cern.ch/twiki/bin/view/AtlasProtected/JetUncertainties2015ICHEP2016 (cit. on p. 94).

[224] ATLAS Collaboration. *JER Uncertainty Provider*. URL: https://twiki.cern.ch/twiki/bin/view/AtlasProtected/JetEnergyResolutionProvider (cit. on p. 97).

[225] A. Angerami et al. *Jet energy scale determination for heavy ion jet reconstruction: JES for HI jets*. ATL-COM-PHYS-2014-329 (cit. on p. 97).

[226] ATLAS Collaboration. *Properties of jet fragmentation using charged particles measured with the ATLAS detector in pp collisions at* $\sqrt{s} = 13$ *TeV*. (2019). arXiv: 1906.09254 [hep-ex] (cit. on p. 98).

[227] OPAL Collaboration. *A Model independent measurement of quark and gluon jet properties and differences*. Z. Phys. C **68** (1995), 179 (cit. on p. 106).